FORCES ON A WHIRLING CENTRIFUGAL PUMP-IMPELLER

Thesis by
Dimitri Suhayl Chamieh
Division of Engineering and Applied Science

In Partial Fulfillment
of the Requirements for the Degree of
Doctor of Philosophy

California Institute of Technology
Pasadena, California

1983

(Submitted February 21, 1983)

ACKNOWLEDGEMENTS

I would like to express my deepest gratitude and appreciation to my thesis advisor, Professor Allan Acosta, for his invaluable guidance, support and assistance during the course of the present work. His concern for the welfare of this writer as well as his friendship were mostly needed and appreciated throughout my education at Caltech. My most sincere thanks go also to Professors Christopher Brennen and Thomas Caughey for their continuous encouragements and help in this researh work.

Special thanks go to George Yamamoto for his help on various intricate machine drawings during the design stages of the experimental apparatus and to Mike Gerfen for the numerous machinings and technical advice given in the lab. Their help was mostly appreciated in carrying this experimental work to success. Thanks are due too to E. Daly, J. Fontana, L. Johnson and N. Keidel for their assistance.

I would also like to thank my colleagues Joseph Katz, Kean Khoon Ooi and Elias Awad for valuable discussions and technical help.

Several students helped in the data collecting and data processing. I am especially grateful to Ronald Franz and Belgacem Jery for their patient help in the lab. I wish also to thank the other people in the lab such as the likes of Albert Charles, Keith Warfield, WenMei Chen, Doug Atkins and Chelvakumar. Finally my most heartfelt thanks go to Pang Chen for his assistance in the development of the computer program subroutines.

I wish to thank Cecilia Lin for her patient help in preparing the majority of the graphs in this thesis. The assistance of Susan Berkley, Rennie Dudek and

Barbara Hawk in administrative matters is also appreciated. The help of Jean Anderson of the Aeronautic Library is also appreciated.

I would like to acknowledge the financial support of the Institute and of the National Administration Space Agency (contract No. NAS8-33108). This work was also made possible by a Byron-Jackson Fellowship. The author is deeply indebted to all of these sources.

I wish to express my deepest and most sincere love to Fran LaValle for her unceasing patience and constant encouragement. Finally my warmest love go to my parents Eliana and Suhayl for their loving care and unconditional backing during all of these years.

ABSTRACT

The present work is an experimental and theoretical investigation of the possible forces of fluid dynamic origin that can act on a turbomachine rotor particularly when it is situated off its normal center position. An experimental facility, the Rotor Force Test Facility, has been designed and constructed in order to measure these kinds of forces acting on a centrifugal pump impeller when the latter is made to whirl in a slightly eccentric circular orbit. The rotor speed, eccentric orbital radii and whirl speed could be varied independently. The scope of the present experimental work consists of measuring quasi-steady forces on the impeller as it whirls slowly about the axis of the pump rotation. These forces are due to interaction between the impeller and volute; they are decomposed into force components relative to the geometric center of the volute and to those proportional to displacement from this center. These latter are interpreted as stiffness matrices. These matrices were measured on two widely differing volute types and both were found to have the property of being skew-symmetric. It can be shown that a stiffness matrix of this type can lead to dynamic instability of the impeller shaft system in certain circumstances. This new experimental finding may explain some operational problems of "high speed" hydraulic machinery.

In the theoretical part of this thesis, a somewhat more physical model of a rotor pump is proposed other than has been used heretofore in most works namely an actuator disk having infinitely many blades. As a simplification it is assumed that the flow field is irrotational. Forces and stiffness matrices are calculated on this basis but the stiffness matrix so found does not reveal the skew-symmetric property of the experiments.

TABLE OF CONTENTS

LIST OF FIGURES

Fig. 4.10. Direction of average volute force of Fig. 4.9 expressed in Volute A coordinate system. Open and closed symbols represent data for Volutes A and B respectively.

Fig. 4.11. Normalized average volute force components of Figs. 4.9 and 4.10 are shown for Impeller X, Volutes A and B and for face seal clearances of 0.79 mm. Rotor speeds in rpm and their corresponding symbols are shown in brackets.

Fig. 4.12. Normalized force matrix coefficients as defined in text for Impeller X, Volute A and face seal clearances of 0.14 mm. Shaft speed = 600 rpm:△,▲; 800 rpm:○,●; 1000 rpm:□,■. Values of K^*_{XX}, K^*_{XY} and K^*_{YX} are represented by open symbols; values of K^*_{YY} by closed symbols. Comparison is made with Colding-Jorgensen's [29] theoretical stiffness matrix calculations with a volute angle of 86°.

Fig. 4.13. Normalized force matrix coefficients as defined in text for Impeller X, Volute A and face seal clearances of 0.14 mm. Shaft speed = 1200 rpm ($\omega > 0$):◇,◆; 1200 rpm ($\omega < 0$):◁,◀; 2000 rpm:▽,▼. Values of K^*_{XX}, K^*_{XY} and K^*_{YX} are represented by open symbols; values of K^*_{YY} by closed symbols.

Fig. 4.14. Normalized force matrix coefficients as defined in text for Impeller X, Volute A and face seal clearances of 0.79 mm. Shaft speed = 600 rpm:△,▲; 800 rpm:○,●. Values of K^*_{XX}, K^*_{XY} and K^*_{YX} are represented by open symbols; values of K^*_{YY} by closed symbols. The normalized static pressure force matrix for a shaft speed of 600 rpm is shown by the symbols +, //, × and ✱.

Fig. 4.15. Normalized force matrix coefficients as defined in text for Impeller X, Volute B and face seal clearances of 0.79 mm. Shaft speed = 800 rpm:○,●; 1200 rpm:◇,◆. Values of K^*_{XX}, K^*_{XY} and K^*_{YX} are represented by open symbols; values of K^*_{YY} by closed symbols.

Fig. 4.16. The normalized average volute force is shown as a function of shaft speed for various auxiliary experiments conducted for Impeller X, Volute A and face seal clearances of 0.14 mm.

Fig. 4.17. The normalized average volute force is shown as a function of shaft speed for various auxiliary experiments conducted for Impeller X, Volute A and face seal clearances of 0.79 mm. Numbers in brackets represent flow coefficients when sufficient quantities of liquid flowing through the front and back face seal gaps could be detected in the pump loop.

Fig. 4.18. Normalized force matrix coefficients as defined in text for the various auxiliary experiments described in Fig. 4.16 for Impeller X, Volute A and face seal clearances of 0.14 mm. The data when the impeller was removed are presented by the symbol x for any of the four normalized force matrix coefficients.

Fig. 4.19. Locus of equilibrium positions of Impeller X within Volute A for face seal clearances of 0.14 mm for various flow rates. Solid line indicates experimental data of Domm and Hergt [33] for a volute angle of 86.3°.

LIST OF SYMBOLS

a	inverse cotangent of volute angle
$\underline{a_B}$	acceleration relative to blades
$\underline{a_i}$	accelerations in regions i = I, II or III of Fig. A.1
a_k, a'_k } b_k, b'_k }	arbitrary coefficients in the Fourier expansion of the velocity potential φ and acceleration potential Ψ
$\underline{a_N}$	rotor center acceleration vector
$\underline{a_\infty}$	$-\underline{a_N}$
b_2	impeller outlet width
c	$\int_{r_1}^{r_2} dr/(r\cos^2\beta(r))$
d_2	impeller outlet diameter
$\underline{e}$	deflection vector of the external balance
$\underline{e_r}, \underline{e_\Psi}$	unit vectors, respectively parallel and normal to the axes of whirl
f_{max}	maximum frequency range of (external balance signals) spectral analysis
$\underline{f}$	impeller instantaneous force vector for a zero run (rotor speeds less than 30 rpm)
i	$\sqrt{-1}$
k	stiffness
k_a, k_b	diagonal elements of $[K_S]$
m	rotor mass
$\underline{n}$	unit vector normal to contours C_1 and C_3
p	static pressure measurement in volute
p_{td}	downstream total pressure
r	radial coordinate
r_1	impeller inlet radius
r_2	impeller outlet radius

t	time
w_d	disturbance complex velocity, $u_d - iv_d$
w_i	disturbance complex velocity, $u_i - iv_i$
w_t	$w_d + w_i$
w_2	impeller outlet width including the shrouds
x, y	impeller axes
x_i	external balance flexure element signals for a zero run (rotor speeds less than 30 rpm); i = 1, 2 or 3
z, z_o	$x + iy$ and $x_o + iy_o$ respectively
A	flexure width dimension (Fig. 2.14)
A_k	k'th coefficient of the Glauert-Birbaum series
A_V	maximum area of the volute
$[A(\omega/\Omega)]$	generalized hydrodynamic force matrix
A_2	impeller discharge area = $\pi d_2 b_2$
$[C]$	damping matrix
C_p	pressure coefficient = $(p - p_{td})/\frac{1}{2}\rho U_2^2$
C_u, C_d	calibration slopes of upstream and downstream pressure transducers respectively
C_z	contour surrounding the volute
C_1	contour at the impeller entrance ($r = r_1$)
C_3	contour enclosing the impeller ($r = r_2$)
$\underline{F}$	impeller total force; components F_X and F_Y
F_A	magnitude of inertia (acceleration) force
$\underline{F_A}$	acceleration force vector
$\underline{F_B}$	body force vector
F_D	magnitude of damping force
$\underline{F_H}$	$[A(\omega/\Omega)]. (X,Y)$

$\underline{F_K}$ average impeller force vector due to eccentricity only ($= \underline{F_\varepsilon} - \underline{F_0}$); components F_{KX} and F_{KY}

F_N normalizing force = $\rho U_2^2 A_2 R_2$

$\underline{F_0}$ radial force or average volute force vector; magnitude F_0 and components F_{0X} and F_{0X}

$\underline{F_S}$ source-vortex force vector

$\underline{F_V}$ volute force vector

$\underline{F'_V}$ damping force due to motion of actuator impeller in unbounded medium; components F'_{V_r} and F'_{V_ψ}

$\underline{F_\varepsilon}$ averaged displaced impeller force vector

$\underline{F_\omega}$ fundamental harmonic component of $\underline{F} - \underline{f}$

H total head rise across pump, (meters of water)

K Stepanoff's parameter as defined by Eqs. 1.2 and 1.3

[K] hydrodynamic stiffness matrix or force matrix; components K_{ij} with i,j = X,Y

[KP] static pressure hydrodynamic force matrix; components KP_{ij} with i,j = X,Y

$[K_S]$ stiffness matrix of the external balance system

[KT] total stiffness matrix; components KT_{ij} with i, j = x, y

K_V, K_{VR} kernel function and its regular part, respectively

M mass of the rotating part

[M] inertia matrix

M_a impeller added mass

N main shaft speed (rpm)

N_S dimensionless specific speed = $N\sqrt{Q}/(gH)^{3/4}$

ΔP_t total head rise across the pump

Q volume flow rate

Q_{des} volume flow rate at design

Q_η volume flow rate at best efficiency

S_H, S_V	slope of calibration for the horizontal and vertical flexures respectively
U_B, V_B	basic flow components
U_o, V_o	$U_B - U_\infty$ and $V_B - V_\infty$ respectively
U_1, V_1	upstream flow velocity components
U_2	impeller tip speed
U_∞, V_∞	downstream infinity velocity contributions
$\underline{V}$	velocity relative to impeller axes (xy)
$\underline{V_I}$	induced velocity at impeller center
$\underline{V_N}$	rotor center velocity vector
V_r, V_ϑ	absolute velocity components in $\zeta = re^{i\vartheta}$ plane
$\underline{V_\infty}$	$-\underline{V_N}$
$\underline{W}$	relative velocity vector
W_T	total complex velocity, $U_T - iV_T$
X,Y	axes of volute; also impeller center position within the volute axes
X',ξ	dummy variables
X^H	$(X_1 + X_2 - x_1 - x_2)\, S_H$
X_i	external balance load cell signal; i = 1, 2 or 3
Y^V	$(X_3 - x_3)\, S_V$
α	index line angle
β, $\beta(r)$	rotor blade angle
γ, γ_1	vorticity distributions
Γ	inlet swirl circulation
Γ'	vortex strength
Γ_2	$2\pi\Omega\, r_2^2 - Q\tan\beta$
δ,δ_o	components of equation of log spiral volute
$\underline{\delta}$	instantaneous impeller center position with respect to the center of whirl

$\underline{\delta^e}$	locus of equilibrium points of impeller inside the volute
$\underline{\delta^N}$	displacement of impeller center with respect to whirl orbit center due to the purely hydrodynamic force, $\underline{F} - \underline{f}$
$\underline{\delta^o}$	average value of $\underline{\delta^N} = [K_S]^{-1}\ \underline{F_0}$
$\underline{\delta_V}$	distance between the volute center and the center of whirl
$\underline{\delta_\omega}$	fundamental harmonic component of $\underline{\delta^N}$
$\underline{\varepsilon}$	eccentricity vector
ε	eccentricity of impeller or whirl orbit radius
ζ	$re^{i\vartheta}$
η, κ	real constants
ϑ	angular position measured from the tongue; also polar coordinate
$\Delta\vartheta$	angular difference subtended by one blade
ϑ_M	total angle subtented by volute
λ, λ'	dummy variables
ρ	density of water
τ	angular position of the cutwater with respect to the horizontal line of Fig. 3.3
φ'	potential velocity
φ	pump flow coefficient = Q/A_2U_2
Φ	acceleration potential
ψ	angular position of eccentricity with respect to the cutwater axis of the volute
Ψ	pump total head coefficient = $\Delta P_t/\rho U_2^2$
ω	radian frequency of whirl motion
Ω	radian frequency of impeller rotation

Subscripts

1	inlet
2	discharge
c	quadrature component (or cosine terms)
d	downstream
o	average values
s	in-phase component (or sine terms)
u	upstream

Superscripts

.	first derivative with respect to time
..	second derivative with respect to time
_	complex conjugate
*	dimensionless quantity
-1	inverse quantity

Special Notation

$\underline{Z}$	vector quantity
[Z]	matrix/tensor quantity

Chapter 1

INTRODUCTION

1.1. Historical Background

The word turbomachine is now used generally to describe rotating machines whose function is to change the energy level of a flowing medium primarily by momentum exchange. A pump or compressor increases the total head or pressure of the fluid whereas a turbine decreases it and so extracts energy from the flow. The history of such machines goes back as far as the Archimedes Spiral used to pump water from one level to another. But it was not until a century or so ago that rapid progress was made in the state of the art coupled with the development of the electric motor, electric generator and steam turbine. In these intervening years the design of turbomachinery and the various mechanical elements surrounding the rotor such as the casing, interstage seals, shaft support bearings, motors, etc has become quite intricate. Yet many aspects of design and manufacturing remain the exclusive property of the various private companies concerned with specific application requirements usually being satisfied from "catalog" data. Ordinarily this is sufficient for commercial service.

However as the need for more efficient, compact, reliable and economic turbomachines has developed, economic competition has become more dependent on fine details. Sometimes only a one or two percent difference in efficiency is sufficient to result in a lost order (this is more true for irrigation pumps and hydraulic turbines than for boiler feed pumps where reliability is the primary factor). Recently a significant engineering step was taken in the creation of the world's highest power-to-weight ratio turbomachine (see Ek [36]), namely the High Pressure Fuel Turbopump of the Space Shuttle. This machine absorbs

77,000 hp yet weighs only 760 pounds! A variety of problems emerged in the development of this device such as destructive rotor whirl (see next section). Although most of these problems were not new to the engineering community, the risk of an aborted mission was far too great to risk ad-hoc fixes. More research was therefore needed in order to understand the behaviour of the various components of this system in particular and of other turbomachines in general despite all of the current industrial understanding of the state of the art and the excellent reference books available on the general subject of turbomachine design (e.g. Wislicenus [66], Stepanoff [63]).

In the following sections we describe one of the major problems encountered during turbomachine operation, namely rotor whirl. We then discuss its probable causes with particular emphasis on the effect of the flow through the rotor and its immediate surroundings (such as the diffuser, volutes, etc.). We finally present the goals of the present research which deal with the measurements and estimates of quasi-steady hydrodynamic forces acting on the whirling rotor of a pump.

1.2. General Description of Turbomachine Rotor Whirl

When a new engineering design is introduced, e.g., the Space Shuttle Main Engine, or even when an established design is operated under unusual conditions such as part-loading or overspeed, rotor structural problems manifest themselves mainly through rotor shaft vibrations and may cause heavy damage. One important aspect of these vibrations is rotor whirl. Rotor whirl occurs when the rotor of a machine operates off-center or follows a path or orbit; a dynamically unstable regime is then said to occur if this orbit is increasing in size with time. One can resolve the forces acting on the whirling turbomachine rotor into forces normal and tangential to the whirl path for every instant of time (see for example Thompson [64]). The tangential force is the driving or damping force; a

positive value (in the direction of orbital motion) excites whirl while a negative one is stabilizing and damps the motion (see Giberson [37]). The simplest case of rotor whirl is the synchronous one in which the rotor center whirls at the speed of shaft rotation. The driving force in synchronous whirl is usually mass unbalance (see Vance et al [65]) and the amplitude of oscillations can be controlled by balancing and operation away from the critical speeds (see next section for definitions). However in many applications of rotating equipment such as the Space Shuttle's engines, steam turbines, multistage compressors etc, subsynchronous whirl has been observed; here the orbital frequency of vibration is less than shaft speed. Rotor whirl is not always damaging; every rotor-shaft system has a built-in degree of flexibility and there is no cause for concern if rotor oscillations do not exceed a certain tolerance level. When this margin is exceeded, however, rotor whirl may become dangerous since rubbing can occur if the minimum clearance is exceeded leading to seal failures, reduction of efficiency, large bearing forces and mechanical destruction. This can even cause explosions in the case of liquid oxygen pumps.

Examples of Rotor Whirl. The occurrence of problems related to the Space Shuttle Main Engine was first made available to the public in a series of newspaper articles in early 1978. According to a Los Angeles Times article (by G. Alexander, L.A. Times, Part 1, Page 4, April 1, 1978), a special panel of engineers was convened in april 1978 to investigate problems plaguing the Space Shuttle liquid propelled rocket engines; this panel recommended that the space agency (NASA) "devote more time and effort to ground tests of the engines even if this delayed the flight tests". In tests at the space agency's Mississipi facility, the engines experienced "cracks, fractures, leaks and looseness". Most of these problems occurred in the rotating machinery, i.e., the four high speed, turbine-driven pumps that deliver the liquid hydrogen and liquid oxygen propellants to the combustion chamber under high pressure. Examples of the difficulties

encountered then were "high, vibration-induced stresses in the High Pressure Fuel Turbopump (HPFTP) turbine blades, major leakages through shaft seals in the High Pressure Oxygen Turbopump (HPOTP), inability of the fuel (hydrogen) pump to operate at the inlet propellant pressures for which it was designed and low efficiencies".

The article did not mention that a severe rotor whirl was encountered in the HPFTP. Typical values during early testing of the HPFTP showed a forward precession of the shaft at less than shaft speed at a frequency typically 0.5 to 0.56 of the shaft speed with bearing loads rapidly increasing in a nonlinear manner until a destructive limit cycle was attained (see Ek [36]). The roots of these problems were never completely understood.

Rotor whirl problems are not just limited to the Space Shuttle. Many conventional machines from re-injection compressors in the North Sea oilfields to boiler feed-pumps are also affected. The Electric Power Research Institute (EPRI) has identified power trip-outs due to turbine rotor whirl as a significant contributor to power plant downtime. To dramatize this effect we will quote two further examples from field experiences at the Phillips Petroleum Company (see Doyle [34]). The first of these occurred at the Ekofisk oilfield in the North Sea. In this compressor facility, gas is received at 68 bars and is boosted through two parallel compressor trains to 625 bars. Each train consists of two 15,000 kW units in series. Each casing contains 8 stages with back-to-back impeller construction. A whirling phenomenon developed in which the rotors experienced large amplitude vibrations. Early testing consisted of adjusting seal clearances, adding seal grooves, adjusting lube oil temperatures and testing numerous bearing configurations to no avail. After a great loss in operating time, the problem was finally solved by the installation of squeeze-film dampers on the bearings, coupled with an increase in the shaft diameter and a decrease in the bearing

span. The second example is that of the Hewett Gas Plant in England. This plant consists of six identical 3,000 kW centrifugal compressor units pumping gas from wells located 17 miles offshore. All compressors were located on shore. These consisted of single stage back-to-back parallel flow impellers, operating at 13,750 rpm with five-lobe pressure-pad journal bearings. Some of the units started to experience whirl at a frequency about two thirds of the running speed with amplitudes large enough to cause damage. Yet other identical units did not develop any problems. Many changes including rebalancing of the units were made, all yielding temporary relief. Lost time in maintainance was great. Even though all units are still in operation today, their reliability is doubtful. Furthermore it is not known why among six identical units under identical conditions of operation some experience rotor whirl while others do not.

These kinds of problems were addressed at the first workshop on Rotordynamic Instability Problems in High-Performance Turbomachinery [25]; Organisers Childs, Hendrichs and Vance state in their preface that "Although techniques have been developed to cope with units that prove to be unstable, the degree of understanding is completely inadequate to design stable high-performance turbomachinery."

1.3. Possible Causes of Rotor Whirl

It is well known that the operation of a turbomachine at a speed close to or equal to the critical frequencies of its rotating parts causes severe oscillations or rotor whirl. Indeed the concept of critical speed was originally called "whirl speed", and the textbooks by Den Hartog [32] and Bevan [9] remain basic references on the subject. For illustration we quote a simple example from Bevan; here a single rotor of mass m is attached in the middle of a vertical shaft of negligeable mass and lateral stiffness k. The whole assembly rotates around the vertical axis. By equating the radial outward centrifugal force (due to an initial

horizontal deflection) to the inward elastic pull exerted by the shaft, one can show the rotor deflection will grow infinitely large as the shaft speed approaches $\sqrt{k/m}$. This particular speed is called the "first critical speed". Bevan goes on to show that the critical speeds are those of the free transverse vibrations of the same shaft.

The first critical speed appeared to be an unsurmountable barrier for the pioneer turbomachine designers as it was then believed to be the highest limit of rotor operation. However in 1895, Gustave De Laval became the first person to demonstrate experimentally that a steam turbine was capable of sustained operation above the lowest lateral flexural resonance speed, or first critical. Designers were then free to increase operating speeds and utilize all the potential benefits of higher speeds. However as the pressure and delivery flow ratings of turbomachines were then increased, serious nonsynchronous whirling problems have appeared in some machines which were designed to operate above the first shaft flexural critical speed. We find it convenient to discuss these new causes of whirl by classifying them as mechanically-induced and fluid dynamically-induced.

Mechanically-Induced Sources of Whirl. We will describe three major causes of mechanically-induced rotor whirl. First rotating shafts with non-isotropic stiffness and inertia caused, for example, by a keyway anchoring the rotor onto the shaft, can excite rotor whirl: as the shaft rotates the amount of deflection changes creating a parametric exciting effect. We refer the reader to the work of Crandall and Brosens [30] for an in-depth stability analysis on the subject. Secondly internal damping caused by multipiece shafts as well as pressed fits and collars on the shaft create a rotating internal hysteresis that promotes rotor whirl provided the rotor speed is above the shaft critical (see Newkirk [54] and Kimball [47]). The whirl speed is then equal to the first critical of the

system. Finally rotor whirl can occur when a rub is initiated between the stationary and rotating parts of a turbomachine. Many analyses of this phenomenon are reported, e.g. [8,23,26,32,35]. These findings are summarized in a recent article by Goggin [38] in which he presented various field experiences involving rub-induced instabilities. Control of rotor whirl was then achieved through alignment or avoided through minor speed increases. In his experiments, half-rotor speed forward whirl has been observed most frequently.

Fluid Dynamic Sources of Whirl. In general rotor whirl of fluid dynamic origins can be traced back to journal bearings, various seals (e.g. neck ring or interstage seals) and also to the presence of the rotor in the flow. Journal bearing and seal forces are somewhat similar. As an example of journal bearing effects we mention "oil whip" (see Hori [42]) which is excited by fluid film bearing forces when the shaft speed reaches at least twice the first critical speed. Adams [2] built a test rig for for the testing of journal bearing forces due to shaft whirl; however he has no published experimental results so far. An excellent survey of past theoretical and experimental works on seal forces and their rotordynamic coefficients (i.e stiffness, damping and inertia effects) was presented by Childs et al [24,27]. These authors also describe an experiment that has the capabilities of measuring these dynamic coefficients by whirling various seal configurations; however their experiments are still incomplete at the time of writing.

Recently it has been increasingly recognized that hydrodynamic effects due to the presence of the rotor itself, in addition to the seals and bearings, can cause serious rotor whirl. Such problems have been experienced not only in steam turbines (Alford [5] and Pollman et al [58]) but also in large compressors (Thompson [64] and Doyle [34]) and in high speed pumps (Ek [36]). Here the flow through the turbomachine rotor and its surroundings induces a fluid dynamic force on the rotor shaft that may be a cause for rotor whirl. Unfortunately

there have been few attempts to measure these fluid dynamic forces as well as to develop theoretical models for them. The conventional area of fluid mechanic research in turbomachines has concentrated on the internal flows of non-whirling stages. This literature is truly vast in the extent and we cite only the references [1,11,12] which are experimental in nature, the references [28,46,49] which are theoretical in nature and the recent explosion in the number of numerical treatments of internal fluid flows (Japikse [45]). This thesis is concerned with the measurement and estimates of the radial or rotordynamic forces caused by the flow trough an impeller. In the next section we discuss previous works and introduce rotordynamic coefficients due to the presence of the rotor in the flow.

1.4. Steady and Unsteady Forces Due to the Presence of the Rotor

The Steady-State Radial Force. Many impellers discharge flow into casing channels of gradually increasing area called "volutes". These volutes are designed to "match" the impeller for certain modes of operation (rotational speeds and through-flow rates) called "design conditions". Generally at the design condition the unit has its best efficiency point and the volute is so matched to the impeller to minimize flow disturbances at the entrance or tongue of the volute. Any departure of the impeller from these operating modes are referred to as "off-design conditions". Among the problems with which a pump designer must cope is the steady unbalanced radial load on the impeller caused by the nonuniformity of the static pressures and velocities within the volute, particularly at off-design conditions. Lawaczek [50] in 1913 modified a conventional volute to reduce high bearing temperatures caused by a high radial load. He installed a vane within the volute and corrected the problem. Later "double volutes" were used to balance these steady impeller forces for all flow rates. This result brings out the importance of the volute. Previously the

impeller was thought to be responsible for all the work on the flow and the volute's influence on this work was limited to the losses . Yet as the influential paper by Worster [67] shows, the two parts, impeller and volute, do not act independently of each other. Worster goes on to show that the volute and impeller are matched to each other at the best efficiency point of the combination. This best efficiency point is determined by the volute characteristic and thus the best efficiency point of the complete pump can be changed by changing the volute design. When the impeller and volute are "matched" together the pressure distribution around the impeller at the inlet of the volute diffuser is uniform. When the flow rate is different from this design value, the pressure distribution at the impeller discharge is not uniform. As a result of this nonuniformity each portion of the impeller discharge tends to operate at a different flow rate and therefore produces a different total head rise. Fluid losses from mismatched volute and flow angles then ensue. Similar findings on somewhat simplified volutes were also reported by Bowerman and Acosta [12]. In his excellent literature search on the influence of the volute and its various parameters on the flow characteristics of a pump, Caignaert [16] emphasizes the importance of volute geometry: in particular the separate effects of volute cross-sections, volute angles at the cutwater, volute inlet widths and volute base diameters on through-flow velocities and pressure distributions are described in detail.

But the mismatch resulting from operation away from the volute design also has the effect of causing the previously mentioned radial force to be exerted on the impeller. Figure 1.1 shows a schematic of a pump within a volute casing. For a given impeller/volute geometry, flow rate and rotational speed, an instantaneous force $\underline{F}$ (not shown in Fig. 1.1) is exerted on the rotor system. this force is the sum of the steady radial force (shown as $\underline{F_o}$ in Fig. 1.1) and of a dynamic (or unsteady) force due flow disturbances at the rotor speed due to impeller blades

passing the volute entrance.

Thus a first step in any rotordynamic analysis is the evaluation of the steady-state radial force $\underline{F_0}$. The literature dealing with this force is quite extensive. Many of the earlier references are based on the semi-empirical relation quoted by Stepanoff [63]:

$$F_0 = K \Delta P_t d_2 w_2 \tag{1.1}$$

where ΔP_t represents the total head rise across the pump while d_2 is the impeller outlet diameter and w_2 is the impeller outlet width, including the shrouds. K is a parameter depending on the type of volute casing used and on flow rate. For single volute (i.e. increasing area single casing volute) pumps:

$$K = 0.36 \left[1 - (Q/Q_\eta)^2 \right] \tag{1.2}$$

where Q is the flow rate and Q_η the design flow rate. Notice the maximum thrust occurs at shutoff (when Q = 0). For a concentric casing (i.e circular constant cross-sectional area volute) pumps Stepanoff expresses the parameters as

$$K = 0.36 \, (Q/Q_\eta) \ . \tag{1.3}$$

Here the radial force is zero at zero capacity.

Others have also measured radial forces. Agostinelli et al [4] measured bearing reactions of centrifugal pumps of different specific speeds with single volutes, double volutes and concentric casings; Iversen et al [44] measured radial forces as well as discharge pressure distributions for an impeller volute configuration. Biheller [10] measured radial forces on the impeller of a

centrifugal pump with volute, semi-volute and fully concentric casing in order to derive an equation enabling prediction of expected forces based only on pump geometry, operating speed and capacity. Theoretical calculations of the radial force are discussed in Chapter 5.

The radial force is thus an important parameter to know so that shaft stiffness, radial wear-ring clearances and bearing loads can be properly determined. It seems somewhat surprising, however, that given this important component there is little data to guide the designer. The work of Stepanoff and the prementioned references apply only to a very special line of pumps. But for design reasons one may wish to change the geometric proportions, employ diffuser vanes, offset scrolls, etc, all of which necessitate further laboratory testing. For example even in the recent detailed reference book by Balje [7], or in the older but influential books by Wislicenus [66] and Kovats [48], no information on this impeller-volute interaction is to be found.

Hydrodynamic Stiffness Matrix. Colding-Jorgensen [29] first introduced the concept of hydrodynamic stiffness matrices in order to express steady rotor forces, other than the previously defined radial force, for the case of having the impeller not centered in the volute. He solved a theoretical case that is documented in Chapter 5. Here even at design flow we may still expect a hydraulic force to be exerted on the impeller caused by the distortion of the streamlines within the volute from the diplacement from the geometric center.

The displacement of the impeller from the geometric center of the volute can arise from many sources, e.g., manufacturing tolerances, weight, vibrational disturbances, unbalanced forces or blade cut-water forces etc. In this situation the hydraulic forces caused by the relative displacement of the impeller and volute may be likened to act like a "spring". The explanation is simple: let us suppose that at the well-matched condition at the design point there is no volute force

on the impeller at all; we should expect then that if the impeller is moved from the center a hydraulically-caused force proportional to this distance should develop. This is, plainly, a different type of force than the previously described radial force. For a fixed eccentric position (having radial coordinates ε and ψ) of the rotor with the axes shown in Fig 1.2, one can define a hydrodynamic stiffness matrix [K] as follows:

$$\underline{F_K} = \underline{F_\varepsilon} - \underline{F_0} = [K] \begin{pmatrix} \varepsilon\cos\psi \\ \varepsilon\sin\psi \end{pmatrix} . \tag{1.4}$$

where $\underline{F_\varepsilon}$ is the new steady impeller force for the displaced position and $\underline{F_0}$ is the corresponding radial force of Fig 1.1 for the same mode of operation. It is customary to represent [K] in the form

$$[K] = \begin{bmatrix} K_{XX} & K_{XY} \\ K_{YX} & K_{YY} \end{bmatrix} . \tag{1.5}$$

In components the force $\underline{F_K}$ can be written

$$F_{KX} = K_{XX} .X + K_{XY} .Y$$

$$F_{KY} = K_{YX} .X + K_{YY} .Y \tag{1.6}$$

where X and Y represent the displacement of the impeller from its concentric position. To interpret this formula suppose that the rotor is displaced along the X-axis (that is Y=0); then $F_{KX} = K_{XX}.X$, which is a purely outward force. But at the same time the other term of Eq. 1.6 yields a force in the Y-direction perpendicular to the displacement, namely $K_{XY}.Y$. Alternatively we can arrange X=0 so

then there is a radial force $K_{YY}.Y$ and a force perpendicular to the displacement $K_{YX}.X$.

This kind of behaviour is typical of any elastic system such as a shaft weakened on one side by a keyway, bending of an angle with unequal legs, etc. But for all elastic systems it is known $K_{XY} = K_{YX}$. When this concept is applied to the fluid dynamic force of a displaced rotor the terms K_{XY} and K_{YX} will be referred to as the "hydrodynamic cross-coupling coefficients", and it will be shown that they are responsible for the force tangential to the whirl orbit (section 1.2). The matrix [K] will then be called the hydrodynamic stiffness matrix.

In a real pump the hydrodynamic stiffness matrix is part of a total stiffness matrix [KT] that also include the stiffness of the shaft, seals and bearings and it is similarly defined to be

$$[KT] = \begin{bmatrix} KT_{XX} & KT_{XY} \\ KT_{YX} & KT_{YY} \end{bmatrix} . \qquad (1.7)$$

In general, KT_{XX} and KT_{YY} are assumed to be caused mainly by the elastic stiffness of the impeller shaft and bearings and the hydrodynamic stiffness coefficients K_{XX} etc. are neglected. The exceptions are few, in particular Alford [5] for axial flow machines and Thompson [64] for centrifugal compressors include an aerodynamic cross-coupling coefficient in the elastic matrix of Eq. 1.7.

Documentation of hydrodynamic stiffness forces and matrices is exceedingly sparse as we have mentioned. For centrifugal pumps, for example, only very limited experimentation by Domm and Hergt [33] and Hergt and Krieger [39] can be found in the literature. Domm and Hergt measured forces on an impeller for

two equal eccentricities (but different angular positions) for various flow rates. Their results were not interpreted using the concept of hydrodynamic stiffness matrices. Hergt and Krieger measured forces on an impeller for three different flow rates but for various eccentricities and angular positions. One of their conclusions is that the forces seemed to be proportionnal to the eccentricity for the three flow rates tested but there was still no attempt to deduce stiffness matrices. Besides Colding-Jorgensen [29], Chamieh [20], Allaire et al [6] and Sato and Allaire [60] calculated hydrodynamic stiffness matrices using very simple impeller flow models. their results along with the description of different impeller models are discussed in Chapter 5.

Hydrodynamic Damping and Inertia Matrices. Let us now suppose that we move the impeller center of Fig. 1.2 on a given trajectory. There will be two main frequencies of interest, the rotational speed of the shaft Ω and the whirl speed ω of the displaced center. Also assume that these two quantities are constant. The total force $\underline{F}$ acting on the impeller can be decomposed again into steady and unsteady components. The steady components are the radial force $\underline{F_0}$ and the "spring force" $\underline{F_K}$ defined earlier. The unsteady components are now subharmonics and superharmonics of the rotor speed and of the whirl speed. The latter, along with spring force $\underline{F_K}$, can be written symbolically as a generalized force $\underline{F_H}$, where

$$\underline{F_H} = [A(\omega / \Omega)] \cdot \begin{bmatrix} X \\ Y \end{bmatrix} . \qquad (1.8)$$

$[A(\omega / \Omega)]$ is a generalized hydrodynamic force matrix which depends implicitely on whirl speed. When $\omega = 0$, the case of the non-whirling displaced impeller should be recovered. The quantity $[A(\omega / \Omega)]$ can be determined if forces acting on a rotor for a given impeller volute configuration are measured for a given

rotor speed Ω, whirl orbit and variable whirl speed ω. It may also be possible to decompose $\underline{F_H}$ into a series of polynomial expansions in powers of ω or, alternatively, time derivatives of the displacement vector

$$\underline{F_H} = [K]\begin{Bmatrix} X \\ Y \end{Bmatrix} + [C]\begin{Bmatrix} \dot{X} \\ \dot{Y} \end{Bmatrix} + [M]\begin{Bmatrix} \ddot{X} \\ \ddot{Y} \end{Bmatrix} + \text{higher harmonics} \quad . \tag{1.9}$$

Here $(\dot{X},\dot{Y})$ represent the rotor center velocity and $(\ddot{X},\ddot{Y})$ the rotor center acceleration. The terms [C] and [M] can then be called the hydrodynamic damping and inertia matrices respectively as they are in the corresponding representation of annular seal forces [24,27].

The hydrodynamic force expressed in Eq. 1.8 or 1.9 should then include all factors of importance to shaft stability or critical speed computations. The coefficient matrices [K], [C] and [M] of Eq. 1.9 should then be independent of frequency ω but will depend upon the impeller-casing geometry, rotation speed and volumetric flow rate. Up to the present time we are aware of only one experiment in which these coefficients (or more properly, [A] of Eq. 1.8) were measured, namely that of Ohashi and Shoji [57]. Their test impeller was installed in a large 'vaneless" diffuser with the result that stiffness term [K] in Eq. 1.9 was very small and could not be detected. A summary of their results is that [C] provided a positive damping but that this result depended somewhat on flow coefficient.

1.5. Goals of the Present Research

We have seen how little is known of the fluid dynamic forces acting on a turbomachine rotor due to the impeller through-flow. Whether these forces are stabilizing or destabilizing for rotor dynamics is simply not known. We propose herein to measure these overall impeller forces and express them in terms of an appropriate force matrix and to determine the effect of whirl frequency on this

matrix.

Our main intent at the time the present experiments were initiated was to be able to contribute to the understanding of the fluid dynamic mechanisms causing the severe whirl problem encountered in the High Pressure Fuel Turbopump (HPFTP) of the Space Shuttle (Ek [36]). Therefore we chose to model one of the two double suction impellers of the HPFTP having a dimensionless specific speed of about $N_S = 0.6$ (see nomenclature). Other turbomachines such as axial pumps, compressors or turbines may also be subject to the same effect but the present work is strictly concerned with radial flow machines and for this purpose a special test facility was designed, constructed and installed in the Dynamic Pump Test Facility at the Institute [14,21]. This work is to be carried out in several stages; in the first stage, forces are to be measured on a centrifugal pump impeller made to whirl at a low speed on a given circular orbit. The second stage of this work is to measure these impeller forces over a wide range of whirl speed/impeller speed ratios. The present thesis is concerned with only the first stage of work; the forces then are the essentially "quasi-static" ones previously described. The design of this apparatus, the 'Rotor Force Test Facility", is described in the next three chapters together with the means of collecting and analysing the obtained data and the calibration of the force-measuring devices. These experimental results are then expressed in the light of existing knowledge of radial forces and hydrodynamic stiffness matrices. To our knowledge these are the first such measurements to be made. Chapter 5 introduces several theoretical impellers flow-models that have been used in the past to estimate volute-impeller forces and damping forces together with a new simplified actuator model. Finally these findings are summarized in Chapter 6 where it is concluded that the structure of the experimentally-measured stiffness matrix could result in a shaft whirl if damping is insufficient.

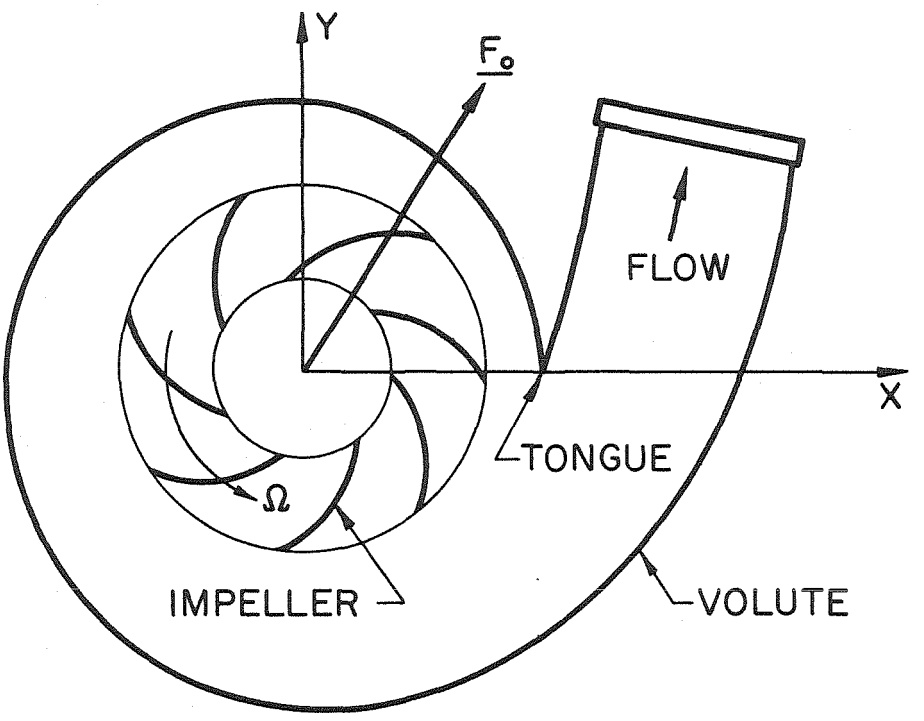

Fig. 1.1. Schematic of a pump concentrically located within a volute (see also text).

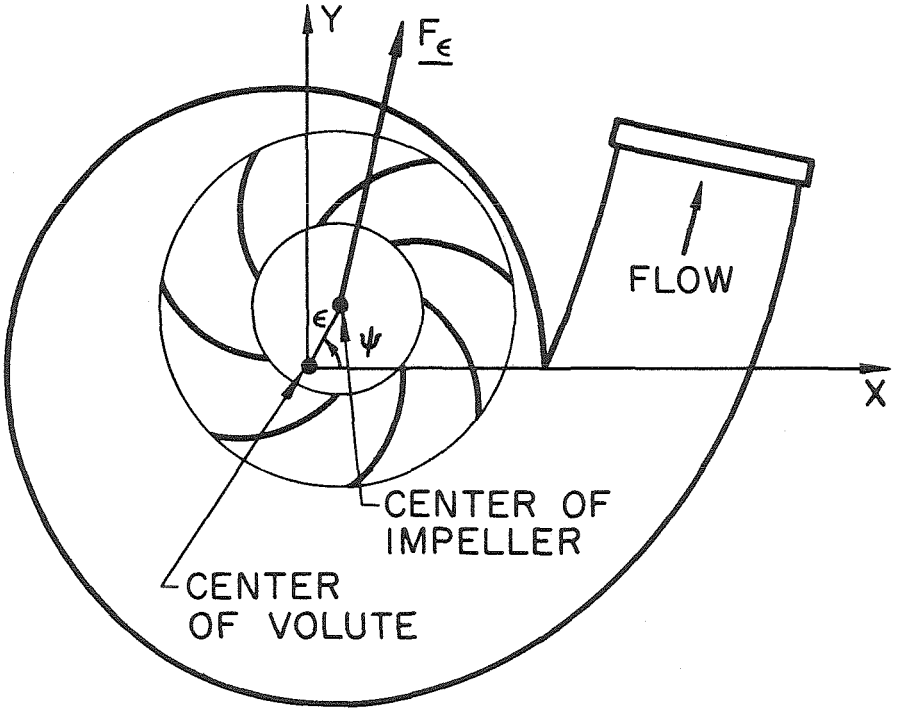

Fig. 1.2. Schematic of a pump eccentrically located within a volute (see also text).

Chapter 2

EXPERIMENTAL FACILITY

2.1. Basic Design Requirements

The main objective of this research is a critical examination of the hydrodynamic forces which influence the dynamics of a centrifugal pump rotor system. Basically it is intended to construct a facility which will have sufficient flexibility to measure the various sources of steady and unsteady fluid dynamic forces acting on the rotor of a pump. In addition it should be designed such that various geometries of impeller, volute, stator, blade-tip clearance, etc, might be used to examine different basic mechanisms responsible for these forces. As mentioned earlier in section 1.5, we are interested primarily in the investigation of centrifugal pumps that model one of the two double-suction impellers of the HPFTP and other generically similar machines. Fortunately, a testing facility that provided the basic hydraulic circuits already existed; this closed loop system, the Dynamic Pump Test Facility (DPTF), is geared for continuous pump operation and will be described in section 2.3 along with the modifications that were made for it.

One of our design objectives was to investigate a large number of volute configurations. One design approach was to make them of lightweight fiberglass construction but this would necessitate mounting them in a pressure housing to reduce the pressure differences across the walls of these volutes. The other concept was to use conventional pump construction which would have, it was believed, interfered with instrumentation. But this proved to be very expensive and the first approach was subsequently adopted. The pressure housing was then mounted on the existing base of the DPTF and permitted easy installation

of various impellers and volutes without disturbing the rest of the system. It will be described with great detail in section 2.6.3.

Another design objective was to use as much of the existing equipment of the DPTF without major modifications. In particular an existing 20 hp motor (see also section 2.6.1) with a maximum rotative speed of 1750 revolutions per minutes (rpm) was to be used to power the rotor pump. This maximum power rating along with the 0.6 specific speed line of pumps used (which is representative of many centrifugal pump applications) and their expected radius dictated having a maximum rotor shaft speed of 3500 rpm; this was achieved by altering the gearing ratios of an existing gear box (section 2.6.1) and coupling it between the main motor and the drive shaft. A constraint for the system is an eight inch distance between the centerline of the pipings of the DPTF and its existing base; for that reason the maximum radius for any pump volute system was chosen to be less than eight inches. The maximum pressure rise across the pump was then calculated to be around 70 psi (4.82×10^5 N/m^2). In addition the minimum pressure necessary to eliminate cavitation was estimated to be around 25 psig. The pressure housing was then designed for a pressure of 150 psi (1.036×10^6 N/m^2) in order to be able to accommodate in the future lower specific speed pumps having a higher total head rise. This design pressure was also consistent with the pump loop capabilities and allowed sufficient flexibility in setting the datum pressure of the system which was necessary, for example, in cavitation experiments.

Two possible methods were then considered in order to measure impeller forces:

(i) Displace the impeller and measure forces directly on the rotor

(ii) Displace the volute and measure forces on the volute housing.

Method (i) was adopted for it seemed easier for the quasi-steady forces and essential for rapidly whirling impellers. The next objective was to measure and distinguish the coefficient matrices [K], [C] and [M] of Eq. 1.9. For this purpose the impeller must be whirled on some controllable eccentric path. The simplest such path is a circular one. A mechanism that was able to impose circular orbits of whirl with variable eccentricity ranging from zero to 1/16 inch (1.59 mm) was first conceived. But this seemed too difficult to manufacture with adequate tolerance and for that reason a single eccentric setting was adopted in order to have a better controlled experiment. This preliminary setting was intended to be 0.0500 inches but was determined to be 0.0495 inches (1.26 mm) after fabrication. It is thought that this value of eccentricity would yield significant "stiffness" forces with respect to the radial forces (section 1.4) based on the experimental findings of Domm and Hergt [33] and Hergt and Krieger [39].

Before we present the newly designed system we would emphasize care must be taken to measure fluid dynamic forces due to the presence of the rotor only and to the flow through the rotor. Seal and bearing forces are not wanted in this work and for this reason it was necessary to eliminate their effect on the force measuring system. Such a system was proposed which will be described in section 2.2. Furthermore the entire rotor bearing support system operates well below its first critical frequency for all unsteady force measurements.

All the previous requirements are now realized in the schematic diagram shown in Fig. 2.1 in which forces on an impeller (1) are to be determined. This new facility will be called the "Rotor Force Test Facility" or RFTF. A volute or diffuser-volute system surrounds the impeller (not shown in the sketch). Flow and pressure parameters across the pump are provided through the piping circuits of the DPTF (also not shown). The rotor angular speed of rotation (Ω) is

provided by a main motor drive (4) through shaft $A_1A_2A_3A_4$. Section A_1A_2 of this main shaft is orbited around line B_1B_2 (stationary) on a circular path of known eccentricity ε at a known angular whirl speed ω. A separate motor drives the eccentric mechanism responsible for the whirl (both are not shown in the sketch). The radial misalignment between sections A_1A_2 and A_3A_4 of the main shaft is permitted by a flexible coupling (2). The dynamometers systems (D1 and D2) used to measure impeller forces are described in detail in the subsequent sections.

2.2. Preliminary Design of the Force Measuring Assembly

The forces acting on the rotor may be measured in two ways:

(a) in a frame rotating with the rotor

(b) in a stationary frame.

Both methods have their advantages. In (a) no intermediate members interfere with the direct sensing of the impeller forces and the rotating mass of the measuring system (shown as D1 in Fig. 2.1) can be quite small thereby permitting a relatively high frequency response. However, the signals must be led from a rotating member to external stationary equipment (a slip ring assembly (3) is indicated in Fig. 2.1 for this purpose). An external force measuring system or dynamometer does not have this problem but it must accept support loads of the drive system and eccentric mechanism as well as the forces exerted on the impeller or rotor. Such a dynamometer will clearly be more massive but it is in a way more straightforward than an internal rotating one. The external type was adopted by Hergt and Krieger [39], for example.

In the beginning phases of the design study for the force measuring system, both methods (a) and (b) were considered to be quite feasible, but the internal rotating dynamometer would require more development time than an external

one would. For that reason it was proposed to implement first an external dynamometer (method b) which would be intended primarily to measure forces at a low frequency compared to shaft speed and to make provision for the subsequent installation of a rotating dynamometer. Thus two stages of work were contemplated, a first one with external dynamometer which would measure primarily external volute forces and a second stage which would in principle be able to measure all forces and moments acting on the impeller up to blade rate frequencies. The present thesis as previously mentioned is concerned only with the first stage of work.

Whichever force measuring system is adopted it is clear that three forces and three moments are required to restrain and position the impeller in its whirling orbit. It would be extremely usefull to measure all of these but in the present context of impeller or rotor-volute interactions, it is plain that only one force is really essential for this purpose, namely the vector force $\underline{F_H}$ of Eq. 1.8 acting on the impeller center. The thrust, torque and in-plane moments acting on the impeller (or impeller support mechanism) are not essential for this purpose. Thus at the outset it was decided to react out these components by floating the entire eccentric drive mechanism (symbolically represented in the dotted lines of Fig. 2.1) by a set of parallel flexures, one end of which restrains the eccentric mechanism (impeller and bearings, etc) and the other is grounded. The "floating" end of the flexure fixture must be restrained by a force and a moment. For practical reasons, three force cells are to be used for this purpose, one in the vertical direction and two in the horizontal direction displaced vertically from each other (as is common practice in the design of external force balances used in experimental fluid mechanics). Thus it can be seen that the axis of this external dynamometer (D2 in Fig. 2.1) will of necessity be that about which the impeller whirls or line B_1B_2 in Fig. 2.1 rather than of the volute center as is depicted in Fig. 1.2. This turns out, however, not to present any difficulty.

In the beginning of this work we did not have a very clear idea of the magnitude to be expected of the impeller forces as a function of eccentricity. For this reason the external dynamometer was sized to accept the largest steady radial force to be estimated from Stepanoff's formula (Eq. 1.1). These design features of the external dynamometer and that of the entire RFTF will be described more completely following a brief description of the pump test facility and the test pump parameters to be chosen.

2.3. Dynamic Pump Test Facility

The Rotor Pump Test Facility (RFTF) as described in the previous sections has been incorporated as a part of another existing facility, the Dynamic Pump Test Facility (DPTF). The DPTF is shown in Fig. 2.2 before any changes were made. This facility was described in great detail by Ng [55] and Braisted [13]. It is basically a closed pump loop that provides steady and unsteady pressure and flow rate controls necessary for the impeller to be tested. It was originally designed to obtain transfer functions of several cavitating inducers (refs. [13,15,55,56]).

Figure 2.3 shows the DPTF after the addition of the RFTF. The DPTF was slightly modified due to the fact that our preliminary testings dealt only with steady state-flows and steady-state pressure drops across the pump. Consequently only the turbine flowmeter (25) was used to determine the flow rate. The 3.5 MW laser station (Fig. 2.2) previously used to measure velocity profiles was removed along with the downstream LDV measuring station. A straight piece of piping (29) replaced the downstream electro- magnetic flowmeter (17) which was needed for another experiment. The siren phase-lock drive (22,24) was dismantled along with the shaft that connected the upstream and downstream fluctuator valves (21). These siren valves were responsible for the pressure and mass disturbances introduced during the study of dynamic transfer functions. Lastly the sintered bronze component of each fluctuator valve (Fig. 2.2 of Ng [55]) was

removed in order to minimize friction in the loop.

A brief description of parts of the DPTF used during experimentation is in order. Distilled water was used in the system and metal corrosion was prevented by addition of a sodium chromate solution. The water was deaerated frequently in order to get rid of dissolved air that might resurface at low pressure points of the pump loop and interfere with experimentation. Direction of the flow is clockwise as seen in Fig. 2.3. Only the turbine flowmeter (25) was used to measure flow rate (ref. [55]). Its output was calibrated to give flow rates directly in gallons per minutes (gpm), and was read by a voltmeter. The silent valve (27) was used to regulate these flow rates. It is a throttling system that allows preset flow rates to be accurately maintained in the loop (see also [55]). A plastic bladder consisting of an inner tube and located inside the reservoir assembly (23) was used to fix the static datum pressure of the system. Pressures upstream and downstream of the rotor were measured independently using a set of two Statham pressure transducers and also a mercury manometer (see also Chapter 3 for pressure calibrations). Finally water temperature was maintained at 70° F during each test run. A heat exchanger located inside the reservoir assembly and using chilled water provided the necessary cooling.

Fig. 2.4 provides recent photographs of the entire facility.

2.4. Test Model Impeller(s)

As mentioned earlier we modelled one of the two double suction impellers of the HPFTP (section 1.2; also see Ek [36]). A six-inch diameter seven vane centrifugal pump was originally designed for the present experimental work using the methods described by Stepanoff [63], Lazarkiewicz and Troskolanski [51], and Sabersky, Acosta and Hauptmann [59]. However the Byron-Jackson Company of Commerce, California offered us a pump impeller of comparable characteristics. Impeller X is a five-bladed centrifugal pump with an outer diameter of 162 mm

(6.375 in.) and a discharge angle of 25 degrees. A machine drawing of the final product is shown in Fig. 2.5 and two photographs are included as Fig. 2.6. This impeller was cast in bronze and has a specific speed of 0.57. All data presented in this thesis were obtained using Impeller X.

2.5. Pump Volutes

A well-matched trapezoidal cross-section volute (Volute A) was designed to be used with Impeller X. Design procedures are described in Lazarkiewicz and Troskolanski [51]. Figures 2.7a,b are machine drawings showing the main dimensions of Volute A and cross-sections at selected points around the circumference of the base circle. We will also refer to Fig. 2.10 for a photograph of Volute A. The largest area of this volute is $A_V = 20.75$ cm^2 (3.22 in^2). The cross-sectional area at any angle, θ, starting from the cutwater, is $A_V\theta°/360$. In the machine drawing of Fig 2.7b, station 0 represents the cutwater while each subsequent station (I, II, etc) represents angular increments of 45 degrees thereof. This volute was fabricated in-house. A wooden pattern was fabricated, fiberglassed and finally gel-coated to increase waterproofing and durability of the material. The ratio of the base circle diameter to impeller diameter is 1.13, a higher than average value yet useful as we intend to use "tight" volutes for comparison in future experimentation.

A deliberately mismatched circular volute was also fabricated out of fiberglass for use with Impeller X. Volute B is the "largest" such collector that could be fitted in our pump housing. It has a 5.42 cm (2.25 in.) constant circular cross-section and is shown in Fig. 2.8.

2.6. Description of the Rotor Force Test Facilty

The existing base (38) of Fig. 2.3 upon which the DPTF was mounted was extended to accommodate the addition of the RFTF. The new components that make up the RFTF consist of a pump housing permitting a variety of different designs of pump volutes, an eccentric drive mechanism, and an external balance to measure steady-state impeller forces. These components and others are described in what follows.

2.6.1. *Main Motor, Gear Box and Shafting* . It will be recalled that an existing 20 hp motor was available in the system. This open loop SCR variable speed d.c. motor (1 in Fig. 2.3) was manufactured by Sabina Electric and had a top speed of 1750 rpm. The rotation speed was increased by means of a gear box (3) with a step-up ratio of two (manufacturer: Vi-Star Gear Co, Inc.) to bring the maximum possible rotor shaft speed of 3500 rpm. A shafting system made out of several parts connected the pump impeller to the motor. The first section (symbolized by A_1A_2 in Fig. 2.1) was made out of stainless steel and is an integral part of the eccentric drive mechanism (section 2.6.4). End A_1 was tapered to accept the rotating dynamometer of section 2.2 (or a dummy balance when the external dynamometer was used) upon which the impeller was mounted. In order to account for the misalignment between the rotor center and the volute center (section A_2A_3 in Fig. 2.1), a twelve inch long double flexing full-floating shaft Thomas coupling (7,8 in Fig. 2.3) was incorporated between the gear box and the eccentric drive. A section of shafting made out of steel was used to connect this flexible coupling to the gear box (see also Fig. 2.3). Provision was made to extend this shaft through and beyond the gear box in order to allow for instrumentation, such as a slip ring assembly or an optical encoder, to be mounted on it. The gear box and the motor drive were then connected through a shaft fitted with a coupling (2 in Fig. 2.3) in case some misalignment was present between these two units. Finally the shafting system is hollow starting from the

impeller all the way to the gear box assembly to permit wiring from the internal balance (section 2.2) to go through to the slip-ring assembly (4).

2.6.2. *Pump Speed Magnetic Pick-up* . To measure the rotor shaft speed, a magnetic pick-up transducer was placed 1/8 in. (3.18 mm) from a sixty-four tooth steel wheel (6) mounted on the pump shaft between the gear box and the flexible coupling. The rotor speed was read in rpm on an HP 5302A universal counter. To obtain that, the number of voltage pulses per second had to be multiplied by the factor 60/64 before feeding it into the frequency counter. This was done through a frequency divider/multiplier manufactured by Shapiro Scientific Instruments, Anaheim, California. The sixty-four tooth gear was used because its signal will be used in the future to set the whirl speed at some known fraction of the shaft speed using digital instrumentation.

2.6.3. *Pump Housing* . As mentioned in section 2.1 a large "container" stressed for 150 psig was designed according to the ASME Boiler and Pressure Vessel Code of 1977 with a recommended safety factor of two. This casing is numbered (13) in Fig. 2.3, and will accommodate several impeller-volute configurations. Figure 2.9 is a machine drawing of the cross-section of the working part of the RFTF along with two elevation views. This pump housing (1) is shown here with an enclosed impeller (5) and volute (2) configuration. It is a hollow flooded cylindrical 356-T6 aluminum casting with a cover plate machined out of Al 2024. This assembly contains the inlet connection (3), the pump inlet bell (4) which guides the inlet flow through the rotor and a flange that discharges flow from the volute. The housing is equipped with several drain and vent valves to insure proper flooding. Provision was also made in the housing casting to accept three optical displacement probes (7) and to permit internal static pressure measurement tubes to be led to outside instrumentation.

Figure 2.10 is a photograph of the housing after removal of the cover plate. One can clearly see the volute and impeller and the housing exit flange.

2.6.4. *Eccentric Drive Mechanism* . An eccentric drive mechanism may be seen in the cross-section of assembly drawing Fig. 2.9. It consists of the previously mentioned stainless steel inner shaft (10), in addition to a set of inner bearings (13) enclosed between this shaft and an inner bearing carrier (9) and a set of outer bearings (12) enclosed between the inner bearing carrier and an outer bearing carrier (8). The centerlines of the two bearing pairs are eccentric to each other in the inner bearing carrier (1.26 mm) so that rotation of the sprocket (11) causes the orbiting motion. This sprocket is mounted on the inner bearing carrier and is driven via a chain or belt by an external motor whose rotative speed is a fraction of shaft speed. It is this inner bearing carrier that was originally conceived (section 2.1) to have a variable eccentricity. Although this was quite feasible, we did not opt for it in the present work. The outer bearing carrier may be mounted rigidly to the pump housing or it may be mounted on a flexure face (14) connected to the pump housing (through the force-measuring parts of the external balance system of section 2.2). Finally all elements were machined out of stainless steel.

The eccentric drive and its internal bearing system are water sealed from the pump housing by means of two face seals (22,23). It should be noted failure of the inner face seals (22) will result in the flooding of the inner bearing carrier. Therefore these face seals are designed not to run eccentrically otherwise they do not seal.

Figure 2.11 shows a photograph of the eccentric drive dismounted from the RFTF. Impeller X can be seen mounted at one end of the shaft.

2.7. External Dynamometer

The goals of the external dynamometer as mentioned in section 2.2 are to measure steady forces (acting on the rotor of a pump) at a low frequency compared to shaft speed. We also mentioned using three force cells (one in the vertical direction and two in the horizontal directions) in order to restrain the floating end of the entire impeller-eccentric drive mechanism. Many possible methods of measuring the forces were investigated. In one method, the three force cells would act as elastic restraints while displacements of the floating impeller-ecentric drive mechanism would be measured either optically or mechanically and calibrated accordingly to give the corresponding forces. In another method, strain gauges would be mounted on these elastic restraints and direct readouts would yield the appropriate forces. In yet another method, the possibility of having positive position force feedback controls was briefly investigated; each force cell would then consist of a ferrous element surrounded by a magnetic coil that would react proportionally to the imposed force. The method of strain gauged force cells was finally adopted since it was the most direct and cost-effective method to measure impeller forces; the force cell characteristics and their strain gauge elements will be described subsequently in this section under the heading of "External Balance Measuring Elements".

The external balance thus described was intended to be used with relatively small whirl speeds in order to measure steady and quasi-steady forces (section 2.2). For this purpose a small 1/75 hp d.c. motor manufactured by the Bodine Electric Company was selected and mounted on the flexure face (14 of Fig. 2.9) of the floating assembly so that all chain drive forces are internal to the system. This motor produces a steady whirl speed of 3 rpm in either the forward or backward direction and it is shown in the photographs of Fig. 2.12. The purpose of a small whirl speed instead of merely displacing the impeller center to a fixed eccentric position inside the volute was to allow continuous sampling of the

forces at all locations of the shaft around the circular orbit. This will be discussed later under the section on "Instrumentation".

Axial Flexures. The eccentric drive mechanism was supported by a flexure assembly to permit only translating motions perpendicular to the rotor shaft. Three identical stainless steel axial flexures (16 in Fig. 2.9), made to a carefully controlled gauge length, are mounted at equally spaced positions around the circumference of the flexure face (14) in order to maintain the floating unit in this configuration. These axial flexures also react out the hydrostatic thrust on the eccentric drive, any moment acting on the impeller and the component of torque due to the angular misalignment of the drive shaft. Each flexure is 8.750 inches (222.25 mm) long and is bolted axially to the pump housing (ground) at one end and to the floating flexure face at the other. They are hexagonal in cross-section (1.125 inches or 28.58 mm is the closest dimension) except for two circular cross-sections of 0.25 inches (6.35 mm) in diameter near each end as shown in Fig. 2.9. Calibration of the force balance assembly (Chapter 3) proved these circular areas to be small enough to minimize radial coupling yet strong enough to resist the tensile load caused by pressurizing the pump housing.

External Balance Measuring Elements. We now fully describe the strain-gauged force cells briefly mentioned at the onset of this section. These elements (15) are mounted radially between the floating flexure face (14) and ground as shown in the right elevation view of Fig 2.9. They are designed to allow radial forces of up to 150 lbf (667.2 N); this was calculated using Stepanoff's formula (Eq. 1.1) based on the worst possible operating conditions of shut-off (no flow through the pump) at the maximum shaft speed of 3500 rpm. The balance system, since it is not infinitely rigid, was caged in order to prevent contact between the rotor and the volute. For this purpose, a circular gap of 16 mils (0.41 mm) was provided around the flexure face to permit floating without

contact with ground. This gap is shown in the top photograph of Fig. 2.13 and it brought the maximum possible eccentric distance between rotor and volute centers to 1.67 mm (counting the imposed eccentricity of 1.26 mm).

All the previous requirements on maximum loading and displacements are now gathered together as we require the stiffness of the external balance to be around 10,000 lbf/in (1.75×10^6 N/meter) in both horizontal and vertical directions. The load cells were then designed as bending elements rather than tension members because of the low value of this stiffness. Among various designs of bending members, a proof-ring concept design was finally adopted. Aluminum 2024 was selected as material instead of steel in order to limit the size of these force cells. Aluminum is also easier to machine and has good heat dissipation properties thus reducing the wait time for the strain gauges to come to thermal equilibrium. Two of the three strain-gauged flexures were then mounted horizontally (Figs. 2.9 and 2.12) equally spaced from the shaft center for measurement of the horizontal force and torque; the other was mounted vertically to measure vertical force. In order to prevent interactions due to motions in the axial and radial directions, each flexure axis was thinned down to 0.040 in. (1.02 mm) at four places in two different perpendicular planes. Figure 2.14 is a machine drawing representing a typical load cell element. Four strain gauges were then mounted on each load cell (as shown in Fig. 2.14) and wired in a full bridge. These strain gauges were Denfoil all purpose high temperature platinum foil gauges type AP1832NE with a 350 $\pm$ 1 ohms resistance and a gauge factor of 4.66 $\pm$ 1 % (catalog data). The high gauge factor was necessary to get good sensitivities; in fact the smallest force reading that could be detected by each load cell was around 0.01 lbf (0.044 N). Semi-conductor strain gauges having much higher sensitivities were not considered for this project in order to minimize time and temperature related drifts. Finally gaging was done by the Able Corporation of Anaheim, California.

To summarize all of the above the external balance consisted of three strain-gauged aluminum flexures and was used with the entire impeller-eccentric drive mechanism floating on soft spring supports attached to the ceiling (Fig. 2.12). This spring, with a stiffness of 80 lbf/in (1.4×10^4 N/m), cancelled the dead-weight of the floating assembly while a turnbuckle attached to it could be adjusted to maintain the uniform gap of 16 mils (0.41 mm); this insured the whirl orbit centerline would coincide with the volute centerline when the pump was not in operation.

Miscellaneous Items.

(i) A connection had to be provided between the flooded pump housing (stationary) and the eccentric drive mechanism (floating) in order to avoid water leaks out of the system. A set of soft neoprene bellows (17) was mounted as shown schematically in Fig. 2.9. Various problems arose at first such as loading hysteresis phenomena and nonrelaxation during calibration of the external balance. Many bellows configurations were tested until a satisfactory one was found. It involves using thin neoprene (3/32 in. or 2.38 mm) and gluing it on well rounded surfaces (fillets) .

ii) Static calibrations of the internal balance were accomplished by hanging weights via a system of gears and pulleys. Calibration results and the data aquisition system will be fully described in the next chapter.

iii) The whole rotor/shafting/eccentric drive unit is shown in its bolted position in Fig. 2.9. By tightening the axial flexures (16) on to the floating flexure table (14) then removing various bolts (18) and spacers (19) the unit can be made to float. Adjusting the spring assembly turnbuckle will yield the desired centering effect.

iv) The first critical speed of the external balance was around 20 Hz. It was believed that the system could then measure dynamic signals of up to 80 percent of this first critical. This might be useful in the future for the probing of the dynamic forces other than the quasi-steady forces as described in section 1.4.

2.8. Impeller Face Seals

In order to control leakage flows from the volute into the inlet and the back of the pump-housing sections, two sets of radial face seals (20,21) were installed as shown in Fig. 2.9. These face seals were selected rather than the usual radial wear rings as these would interfere with the measurement of radial forces. Two sets of clearances were investigated with the radial face seals. One was considered a normal clearance in which both face seals are backed 0.14 mm (5.5 mils) from Impeller X; inlet leakage was then estimated to be around two percent of the design flow rate. The other clearance is a deliberately large maximum clearance of 0.79 mm (31 mils) where inlet leakage losses are about twelve percent of the design flow rate. No experiments were made with the seals in contact as we do not want rubbing between a stationary and a rotating part of the turbomachine to occur since this was described in section 1.3 to be a source for rotor whirl.

2.9. Instrumentation

The basic unit around which the data processing was accomplished is the Shapiro Digital Signal Processor (SDSP) manufactured by Shapiro Scientific Instruments, Anaheim, California. Originally this device was driven by a clean external reference signal and sampled eight channels of input data up to 128 times per reference signal cycle. These samples are stored in buffers which number 128 times the number of channels. It proceeds to accumulate the sampled values for up to 10,000 cycles; the result is finally an average cycle of data

for each channel represented by up to 128 digital values per channel. These values are then transmitted to a central computer at Caltech for digital processing. The present SDSP can sample reference signals up to 40 Hz.

However the present investigation deals only with the measurement of steady-state radial and displacement-related forces. This dictated the use of the 3 rpm motor of section 2.7 as the reference signal for the SDSP in order to average out higher frequency-related forces. This low frequency of 0.05 Hz was below the reference frequency range of the SDSP, thereby dictating some modifications. An optical encoder was mounted to the shaft of the 3 rpm motor as shown in the bottom photograph of Fig. 2.12. This Rotaswitch shaft encoder, with the capability of emiting a square wave output of 1024 times the whirl frequency, was indexed to emit a sharp voltage outburst for every whirl cycle. This signal always corresponded to a given unchanged position of the rotor center on the orbit path and was used as a "start" position for sampling runs. The SDSP was then phase-locked to the optical encoder and a switch was added to provide encoder triggering as well as the previous external reference signals. A detailed explanation of the various data acquisition techniques can be found in Chapter 3.

Three Vishay Strain Gauge Conditioning Amplifiers were purchased to power each strain gauge bridge of the external balance measuring elements. Each one of these instruments contained a variable d.c. power supply, a variable amplifier bank with gains from 1 to 11,000 and six low-pass active Butterworth filters. Finally we refer to [13] and [55] for any additional instrumentation dealing with the DPTF.

2.10. Comparison with other Existing Test Rigs

The present set-up is hereby compared with two recent test rigs designed by Ohashi and Shoji et al [57] and by Adams et al [2] respectively. The goals of the former one are similar to ours and they are the measurement of fluid dynamic forces acting on a whirling centrifugal pump (see also section 1.4). However their apparatus is quite different from the present one. Their eccentric drive mechanism is somewhat simpler and permitted various eccentric setting but they measured the forces using load cells mounted on the bearing closest to the impeller (see Fig. 2 of [57]). Furthermore the omission of a volute in their testings raises questions regarding the relevance of the results with respect to complete turbomachines. We believe that the present test rig is carefully designed to accept complete pump impeller systems and for more fundamental measurements. Furthermore the proximity of ball bearings to the load cells of Ohashi et al's experiment might prove to be a source of noise in the analysis of the load cell response; no such effects are expected to arise in the measuring systems of section 2.2.

The test rig of Adams et al's is quite similar to ours (Fig. 23 of [2]). It will be used, however, for an entirely different purpose which is the measurement of fluid annulus forces in journal bearings. Some operational problems due to tolerances have arisen since a variable eccentric mechanism was used. There is no published data on their experiments at the time of this writing.

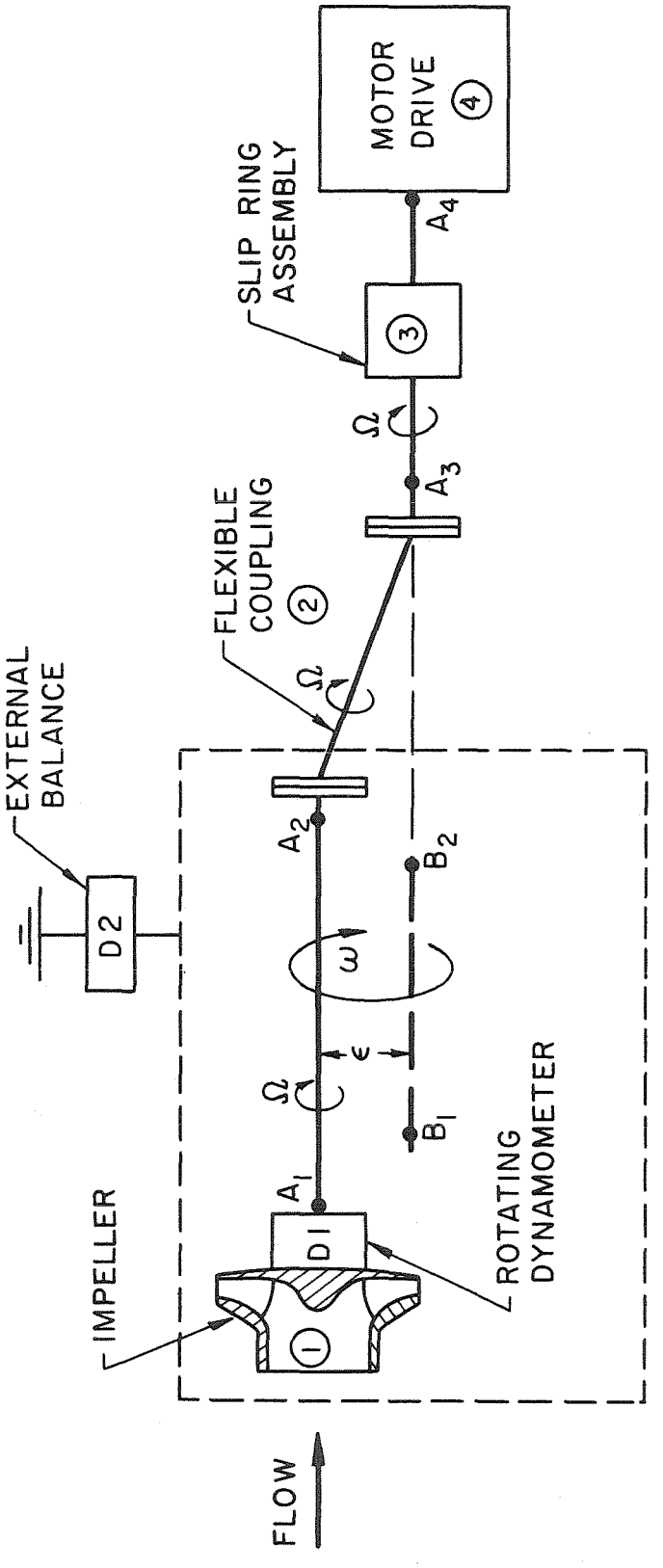

Fig. 2.1. Schematic drawing of the Rotor Force Test Facility (see also text).

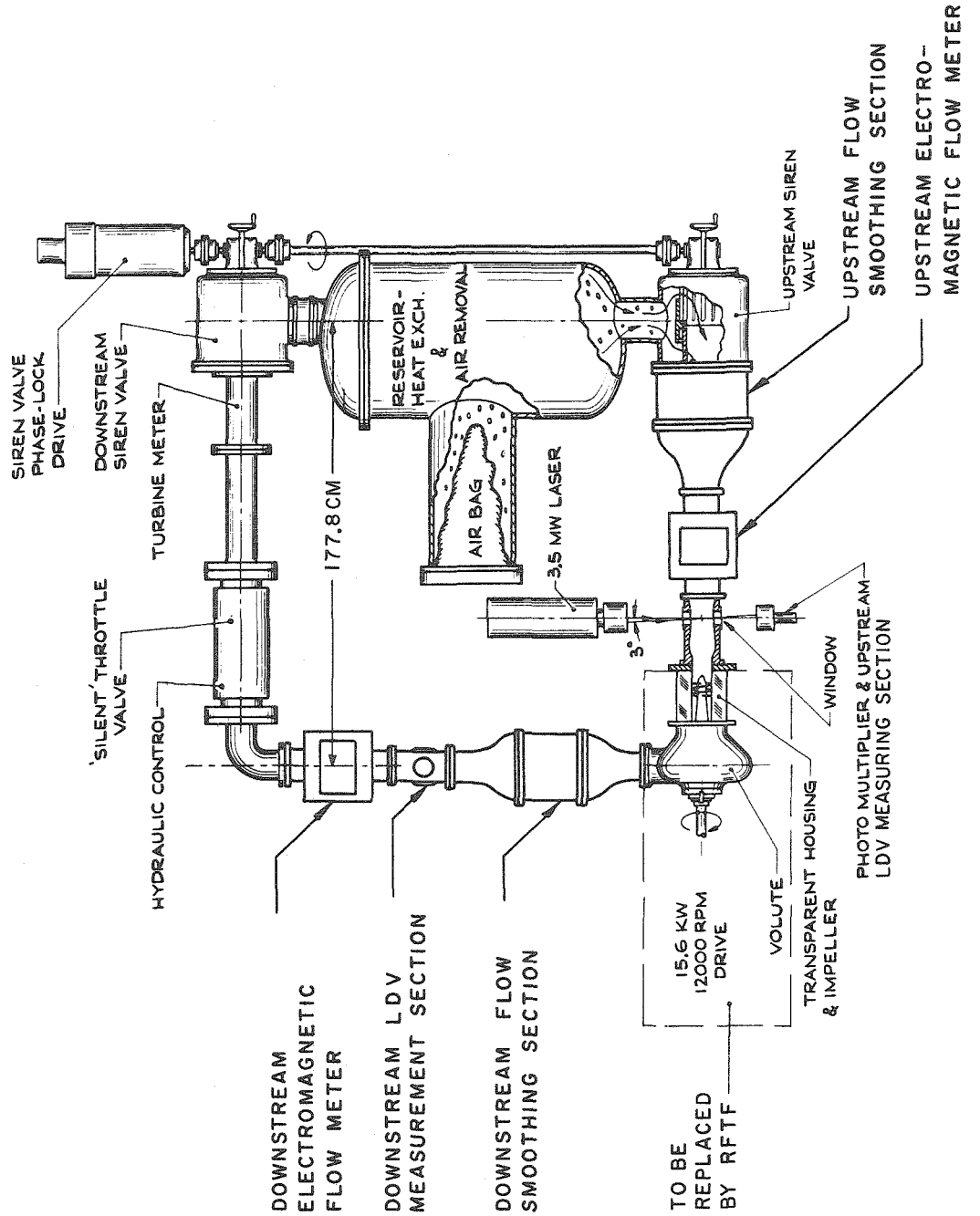

Fig. 2.2. Schematic plan view of the Dynamic Pump Test Facility, before the addition of the Rotor Force Test Facility (RFTF).

SEE POCKET INSERT AT END OF THESIS

Fig. 2.3. The Dynamic Pump Test Facility after the addition of the Rotor Force Test Facility.

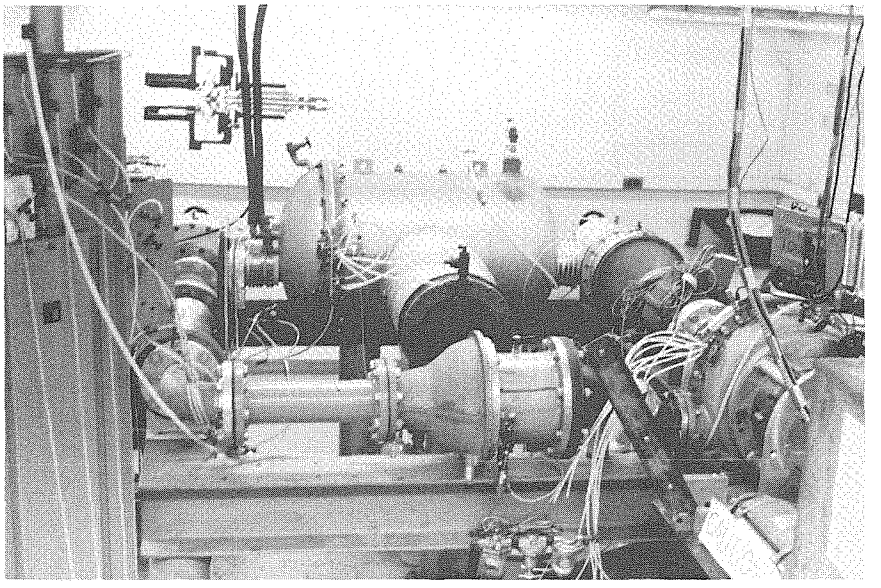

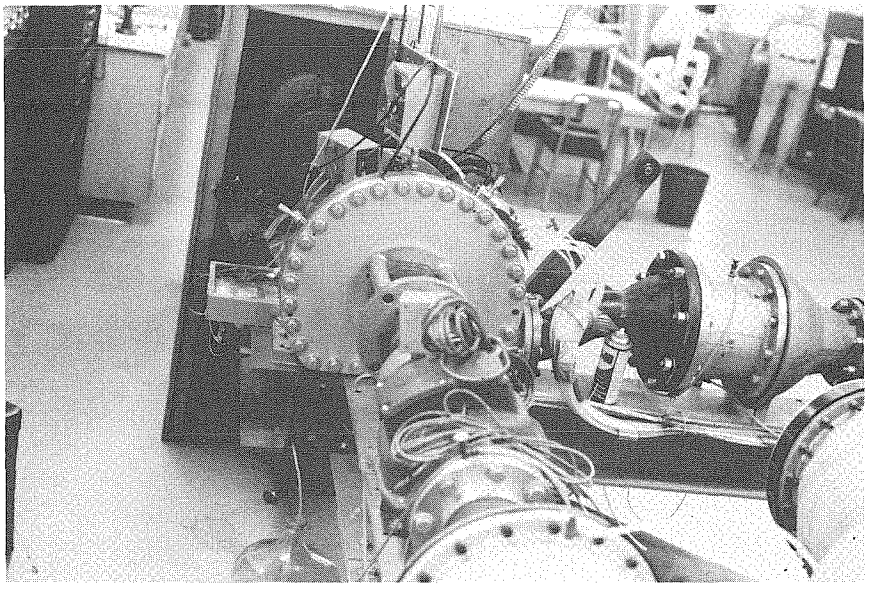

Fig. 2.4. Photographs of the current test facility of Fig. 2.3.

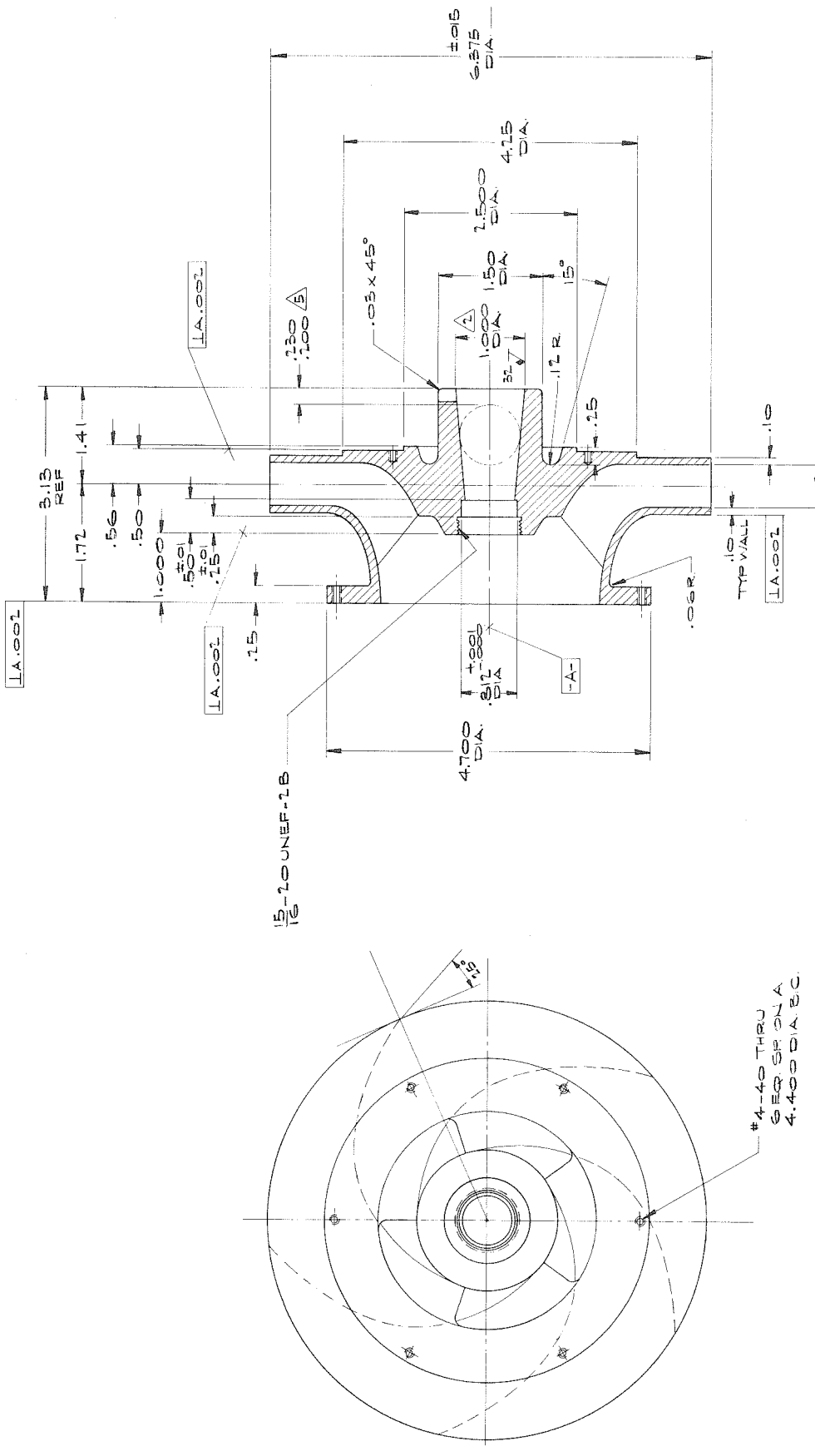

Fig. 2.5. Machine drawing of impeller X.

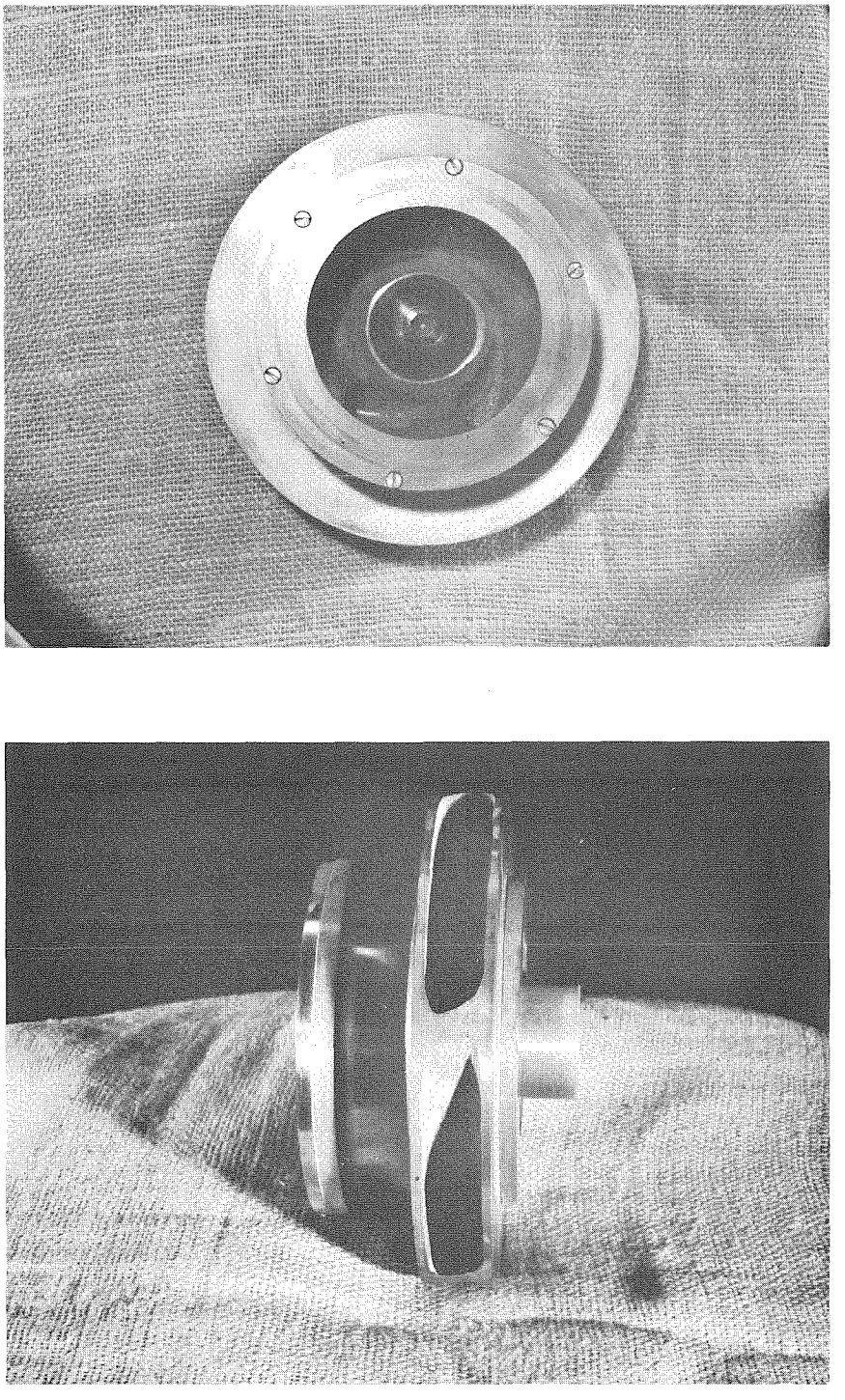

Fig. 2.6. Photographs of Impeller X.

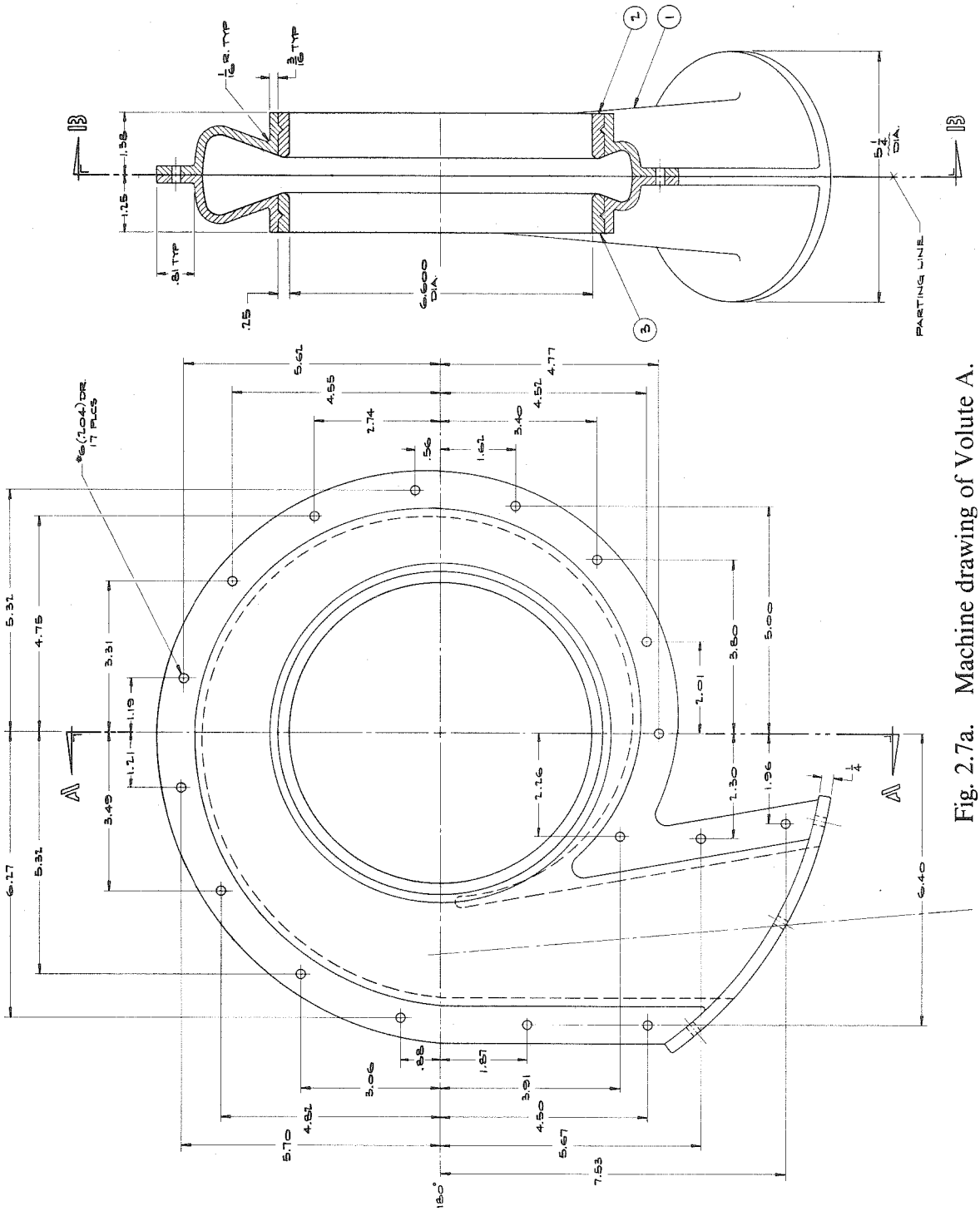

Fig. 2.7a. Machine drawing of Volute A.

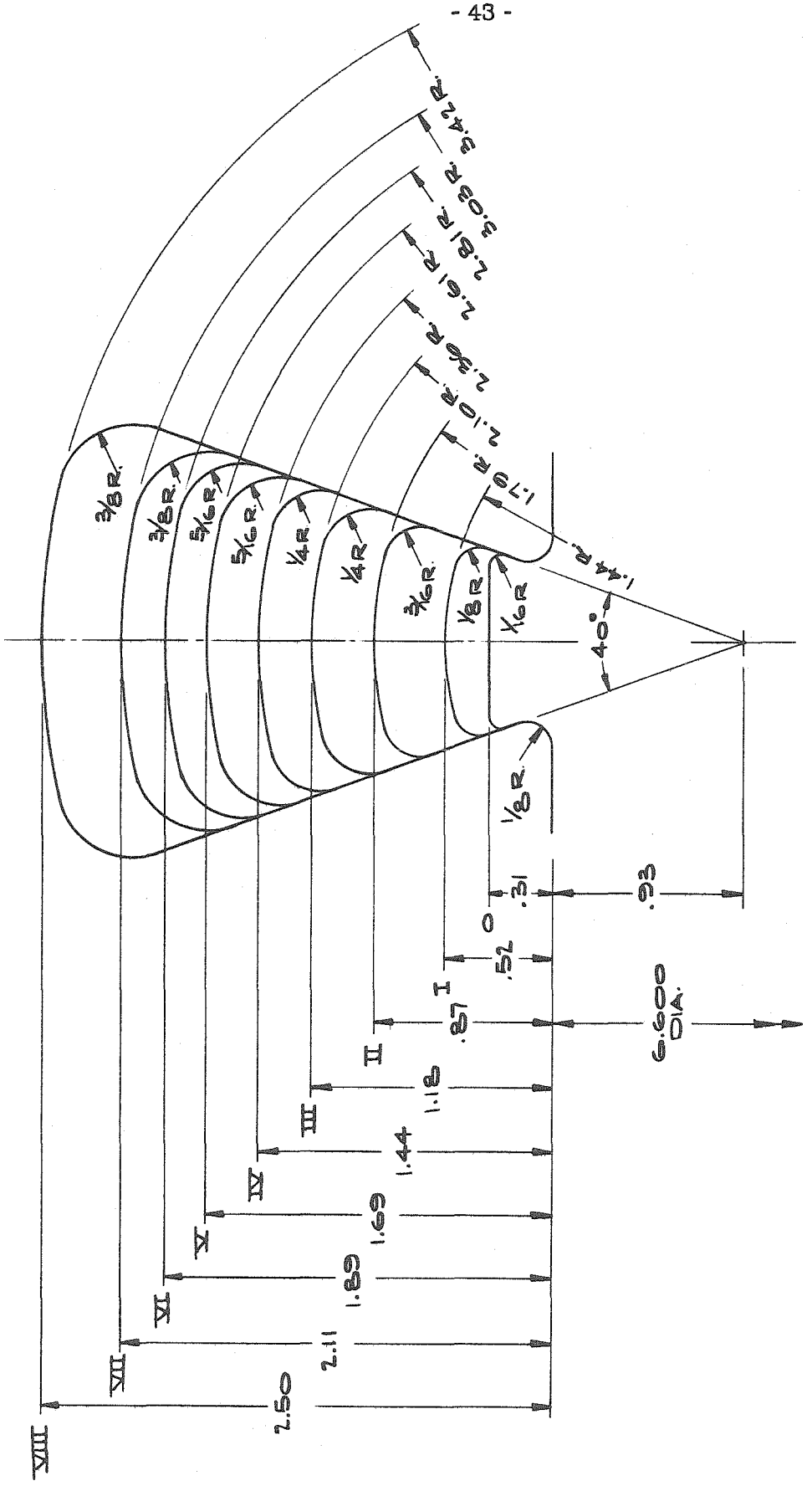

Fig. 2.7b. Cross-sections of Volute A as shown in Fig. 2.7a (see also text).

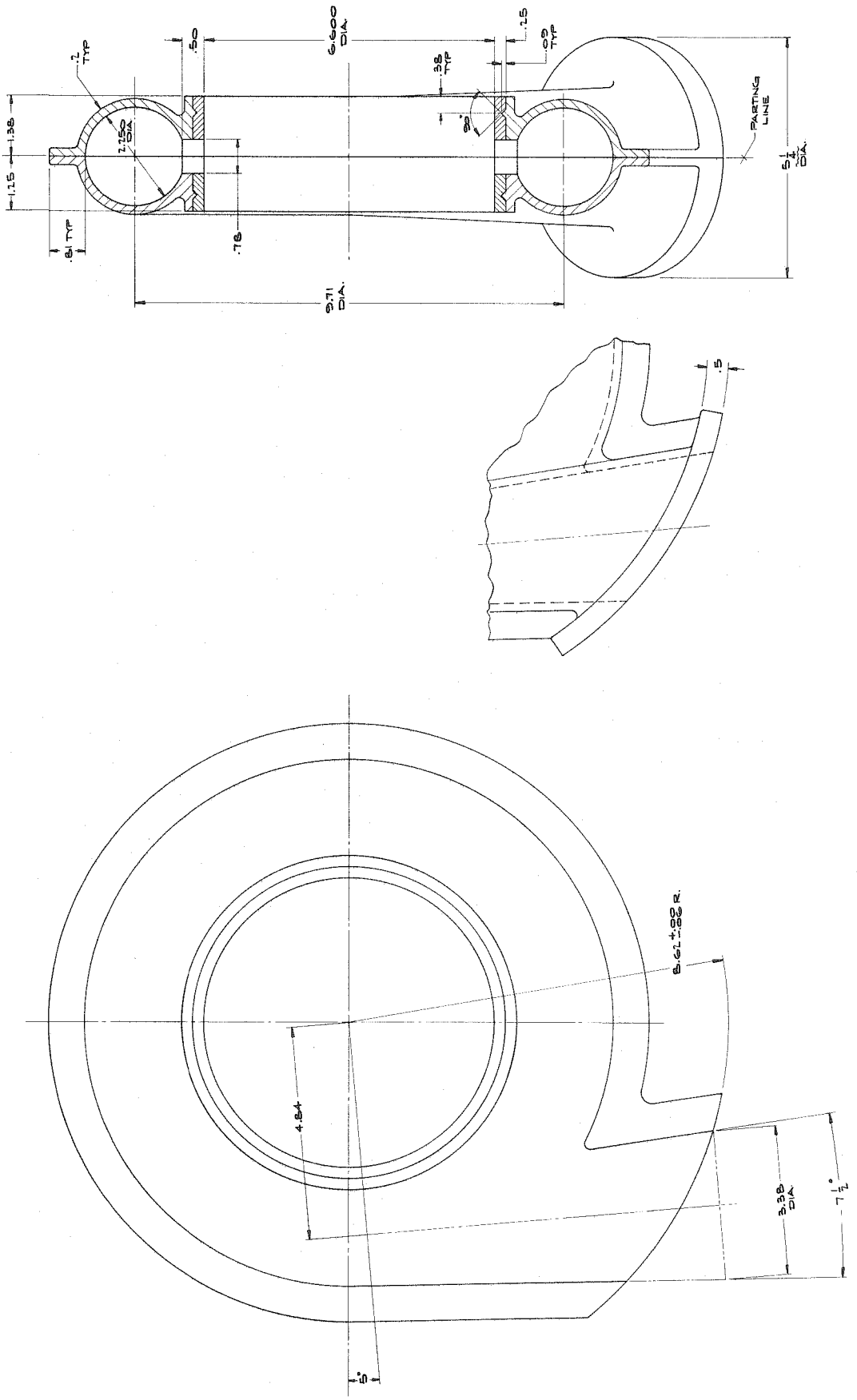

Fig. 2.8. Machine drawing of Volute B.

SEE POCKET INSERT AT END OF THESIS

Fig. 2.9. Machine drawing of the impeller, volute, internal balance, eccentric drive, pump housing and external balance assembly of the Rotor Force Test Facility. Pump housing (1); volute (2); inlet connection (3); inlet bell (4); impeller (5); internal balance (6); proximity probes (7); eccentric drive mechanism: outer bearing carrier (8), inner bearing carrier (9), main shaft (10), orbiting motion sprocket (11) and bearings (12,13); external balance: flexure face (14), flexure elements (15) and axial flexures (16); bellows (17); bolts linking floating system and ground (18); spacers (19); impeller front face seals (20) and back face seals (21); eccentric drive inner face seals (22) and outer face seals (23).
Note: The system is shown in its caged position. Removal of bolts (18) and spacers (19) will make unit float (see also text).

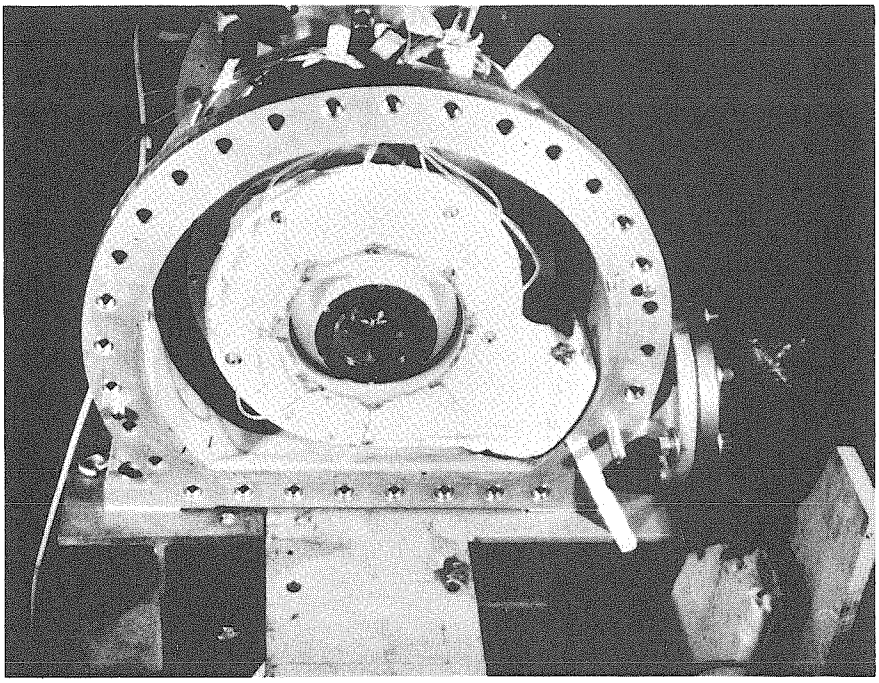

Fig. 2.10. The pump housing, Volute A and Impeller X.

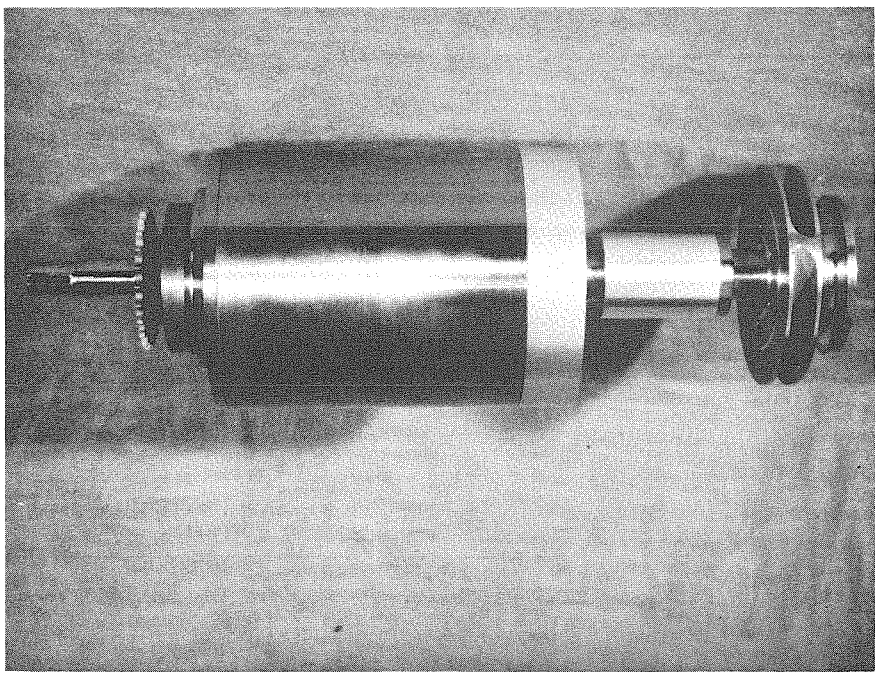

Fig. 2.11. The eccentric drive disassembled from the Rotor Force Test Facility. Impeller X can be seen mounted at the end of the drive shaft.

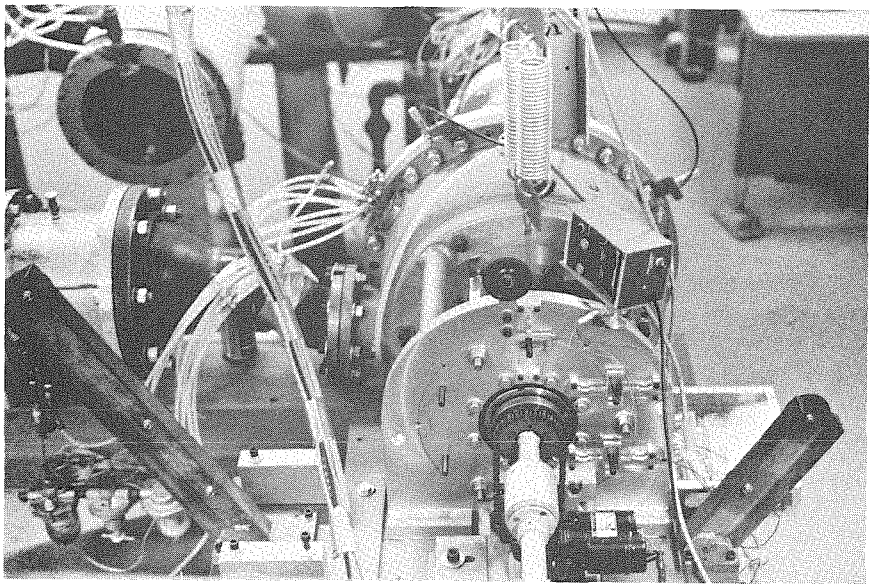

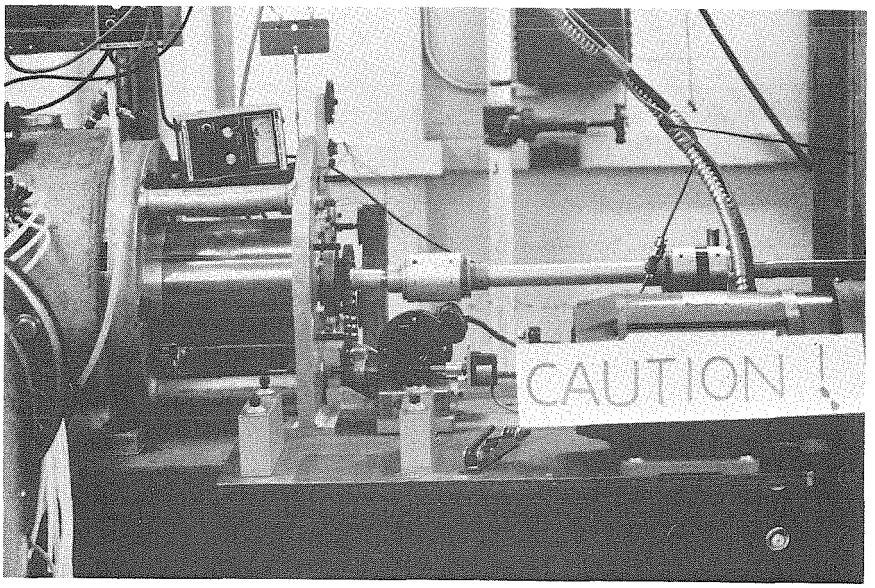

Fig. 2.12. Photographs of the Rotor Force Test Facility.

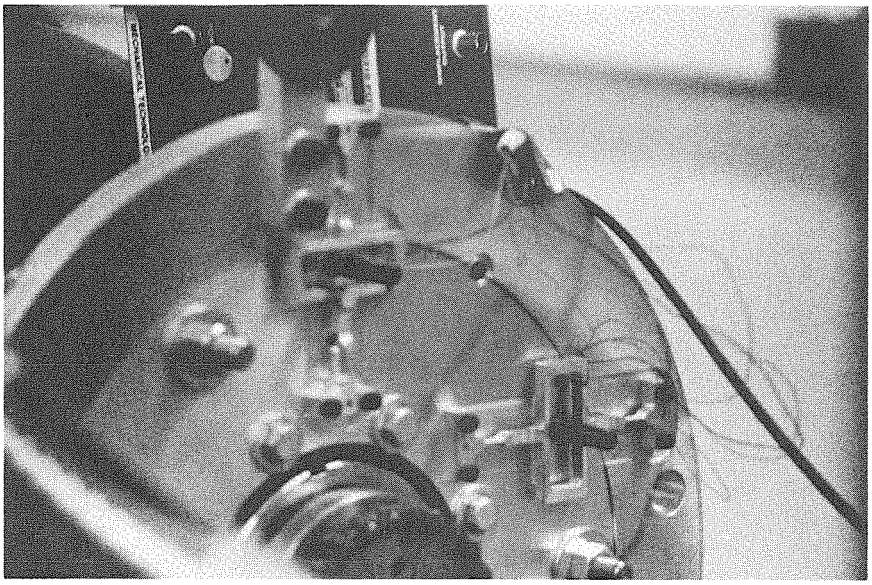

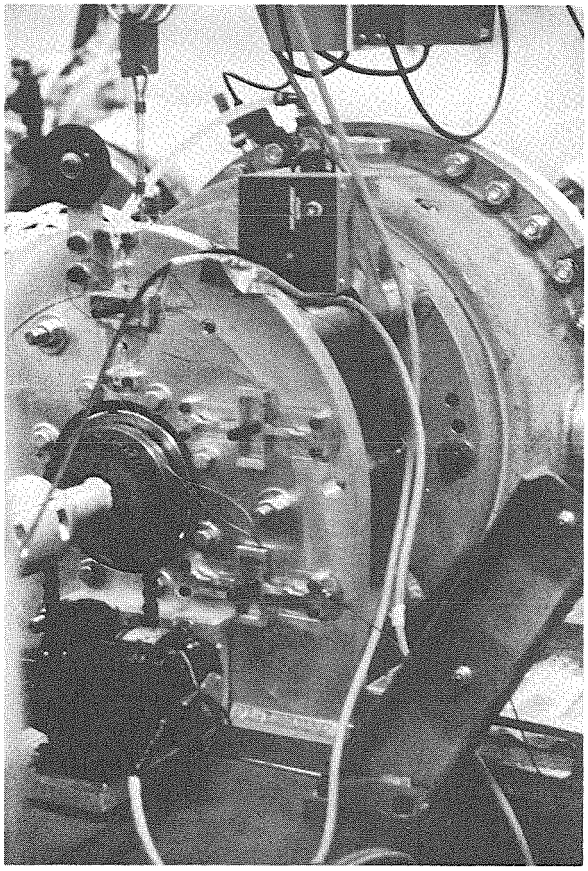

Fig. 2.13. Close-up of the External Balance load cell elements showing the gap between the floating flexure face and ground.

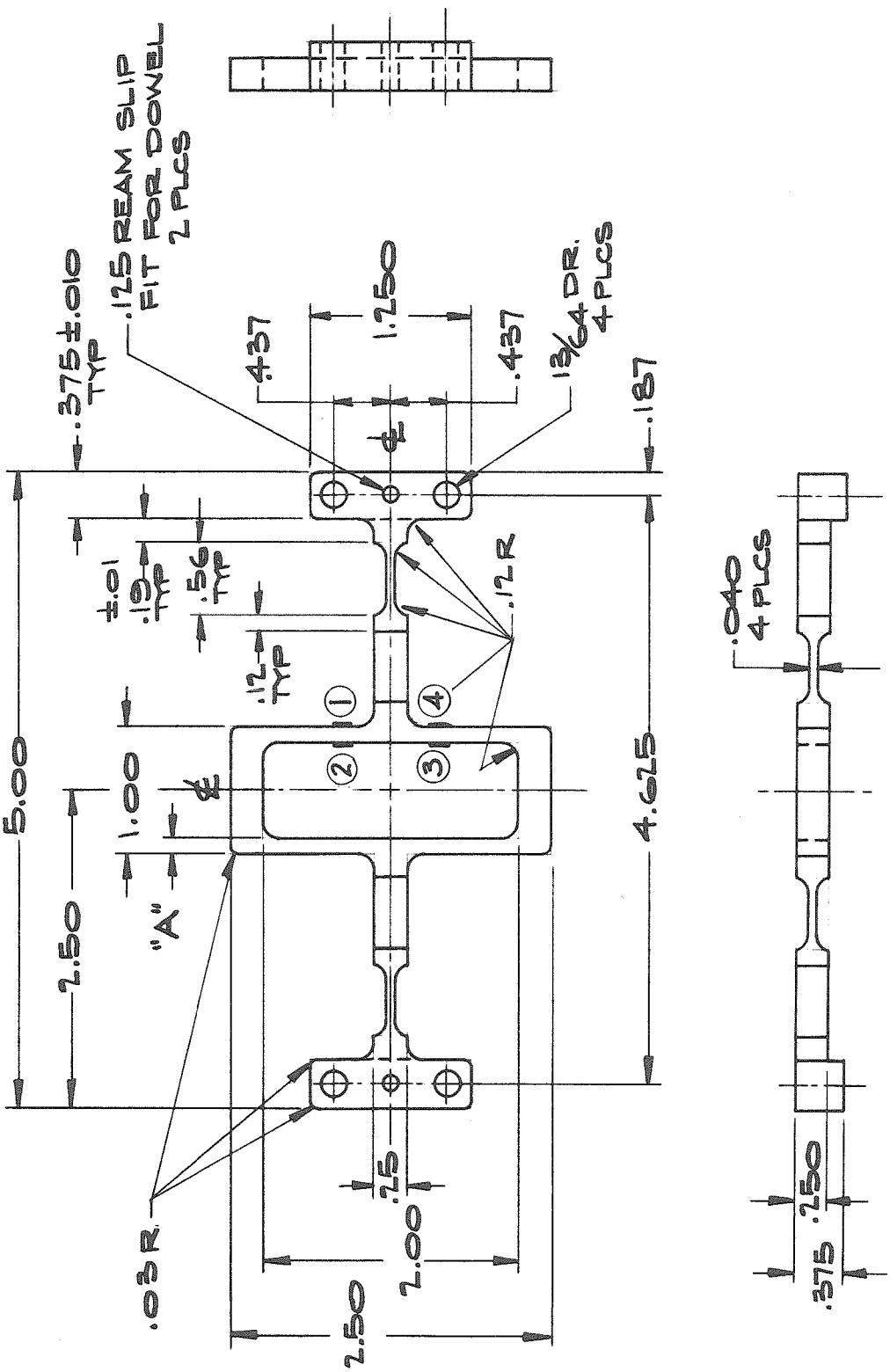

Fig. 2.14. Machine drawing of the External Balance load cell elements. 1, 2, 3 and 4 show positions where strain gauges were mounted.

Chapter 3

EXPERIMENTAL PROCEDURES AND DATA REDUCTION TECHNIQUES

3.1. Introduction

In this chapter we discuss the experimental procedures and data reduction techniques used during the course of the present studies. It will be recalled that the experimental objectives are the measurement of steady and quasi-steady fluid dynamic impeller forces for a given centrifugal pump impeller located inside a volute casing. These forces are interpreted as a radial force at the center of the volute and a force proportional to the displacement from this center. These second type of forces are presented in the form of hydrodynamic stiffness matrices as defined in section 1.4. In addition static pressure distributions around the volute periphery are numerically integrated to determine the static pressure component of these forces.

We have tested an impeller, denoted as Impeller X, along with two different volutes (sections 2.4 and 2.5). The first volute (A) was tested with two face seal clearances (see section 2.8) of 0.14mm and 0.79mm; the second volute (B) was tested with a 0.79mm face seal clearance only. As described in the previous chapter, the whirl speed was maintained at 3 rpm for data sampling purposes except for a few experiments in which the whirl motor was stopped and the impeller locked in a fixed eccentric position. These experiments were designed to check our quasi-steady whirl assumptions and required a slightly modified measurement technique that will be described in Chapter 4. Rotor speeds and impeller flow rates were held steady while collecting data on a given test run. Rotor speeds of 600, 800, 1000, 1200, 2000 and 2400 rpm were tested along with flow rates ranging from shut-off (zero flow rate) to the maximum the pump loop

would allow (around 330 gpm at 2400 rpm). The results will be given in dimensionless form. In what follows we define some pump characteristics, present pressure and force calibration data and explain the experimental and data reduction techniques.

3.2. Pump Flow Coefficient

The flow coefficient φ of a centrifugal pump such as Impeller X is a dimensionless term usually defined on the basis of quantities at the outer radius by the flow rate through the pump over impeller tip speed times impeller discharge area (see also nomenclature). This was calculated using the flow rate Q measured using the turbine flowmeter of section 2.3. and the rotor speed N measured using the pump speed magnetic pick-up of section 2.6.2. It is customary to show force results plotted versus flow coefficient and we have done so in the presentation of data in Chapter 4.

3.3. Total Head Coefficient and Pressure Calibration Techniques

The total head coefficient Ψ of a pump is a dimensionless quantity usually defined as the total pressure rise across the pump over twice the dynamic head based on impeller tip speed (see also nomenclature). Two Statham pressure transducers were used to measure the static pressure rise across the pump. These are described in section 2.5.2 of Ng [55] along with their signal conditioning systems (Burr-Brown 3620L/16 operational amplifiers). The upstream pressure transducer was mounted on section (20) of Fig. 2.3 while the downstream pressure transducer was fitted to the screen barrel (31). These two sections had a different cross-sectional area necessitating a small dynamic head correction in order to obtain the total pressure rise across the pump. Both pressure transducers were calibrated against a precise Heise pressure gauge prior to each test run. Figure 3.1 shows a typical 0-15 psi (0-1.03 x 10^5 N/m^2) calibration curve for each pressure transducer. The output signal (in volts) was fairly proportional to

the static pressure (in psi). Two calibration slopes C_u and C_d were defined for the upstream and downstream pressure transducers respectively (units: psi/volts). The output signal of each transducer was then fed to the Shapiro Digital Signal Processor (SDSP) of section 2.9 and averaged over a test run. The natural frequency of the pressure transducers as supplied by the manufacturers is around 10,000 Hz in air. The catalog data did not provide a cross-section of these pressure transducers but it was estimated that their natural frequency in water would still be much higher than the 0.05 Hz sampling rate frequency (whirl speed). Therefore we were confident about their use in our experiment.

3.4. Dimensionless Radial Force and Stiffness Matrix

The radial force vector $\underline{F_0}$ as defined in section 1.4 is non-dimensionalized by the dynamic head based on impeller tip speed times the discharge area of the impeller. The dimensionless radial vector force $\underline{F_0^*}$ is then defined as

$$\underline{F_0^*} = \underline{F_0} / F_N \tag{3.1}$$

where F_N is the normalizing force, namely

$$F_N = \rho U_2^2 A_2 / 2 \quad . \tag{3.2}$$

Similarly the hydrodynamic stiffness matrix [K] of section 1.4 is non-dimensionalized by the normalizing force divided by the radius of the impeller (= F_N/r_2). Dimensionless hydrodynamic stiffness matrix [K*] for Impeller X is then defined as

$$[K^*] = [K] / (\rho U_2^2 A_2 / 2 r_2) \quad . \tag{3.3}$$

In Chapter 4 where $\underline{F_0^*}$ and [K*] are plotted usually versus flow rate φ, there has

been a name change from radial forces to average volute forces and from hydrodynamic stiffness matrices to hydrodynamic force matrices. This was done in anticipation of the damping and acceleration matrices to be measured in the near future.

3.5. Calibration of the External Balance

Static calibration of the external balance force measuring elements (section 2.7) was conducted prior to each group of test runs. Each of the three strain gauge bridges was powered by a constant 10 v.d.c supply from the Vishay Conditioning Amplifiers (section 2.9). Amplification was set to obtain approximatively one volt signal for each ten lbf (4.54 kgf) loading in either the vertical or horizontal directions. Calibrations were then performed by known forces applied by systems of wires, pulleys and weights. The top photograph of Fig. 2.12 shows calibration set-up rigs on which some of the pulleys were mounted. The vertical load cell was calibrated independently from the two horizontal ones in both tension and compression. The two signals from the horizontal load cells were added to provide the total horizontal force which was then calibrated in tension and compression. A typical calibration curve for the vertical load cell is provided in Fig. 3.2 over a loading range of -15 to +15 lbf (-6.81 to +6.81 kgf). The two horizontal load cells exhibited a similar type of behaviour and therefore are not shown on the graph. Linearity of calibrations was within one percent over the maximum range of loading (-20 to +20 kgf). In addition the horizontal/vertical interaction was also found to be less than one percent for the worst case. As an illustrative example, the slope of calibration in Fig. 3.2 is about 10.13 lbf/volt. The equivalent slope of calibration of the horizontal load cells (not shown here) was about 9.98 lbf/volt. Departure from linearity of the results as well as the maximum interaction were found to be less than 0.7 percent.

High calibration linearity and low interactions seemed to justify the use of the axial flexures and neoprene bellows of section 2.7 and the proper floating procedures. In fact the neoprene bellows were designed such that the slope of calibration would be insensitive to the hydrostatic pressure inside the bellows chamber. To illustrate that point the bellows chamber pressure for the calibrations of Fig. 3.2 was 8 psig (5.5×10^4 N/m^2); when increased to 13 psig (8.9×10^4 N/m^2), the slopes of calibration were only increased to 10.14 lbf/volt for the vertical load cell and to 9.99 lbf/volt for the horizontal ones.

3.6. Experimental Techniques

A standard routine was followed during experimentation; the external balance was first calibrated maintaining the same bellows chamber pressure expected during test runs. The three preamplified strain gauge bridge signals were then filtered using 10 Hz low pass Butterworth filters before being fed into three SDSP channels. These 10 Hz filters eliminated high frequency noise that could saturate the SDSP (having a 10 volts maximum input). The validity of their use is justified later in this chapter. Other signals monitored were those of the two Statham pressure transducers of section 3.3. The SDSP was used well under its maximum capacity of eight channels, 128 sampled points per reference signal and 10,000 cycles of sampled data. In fact each of the five input channels was sampled at 32 equally spaced positions of each rotation of the eccentricity. Furthermore this sampling was continued for 15 rotations in order to obtain averages for each of the 32 geometric positions. This represents an optimum data collecting time of 5 minutes for one set of data. The strain gauge bridge signals were balanced (zeroed) for a given fixed impeller eccentric position and angular orientation within the volute prior to each test run. Finally flow rates and rotor speeds were visually recorded every 60 sec and averaged after each test run (see section 3.9 on drift errors).

The unfiltered signals of the external balance load cells were also recorded on magnetic tape and processed through a digital spectrum analyser. The major peak was observed at the 3 rpm whirl frequency. Much smaller peaks also occurred at higher harmonics of this whirl frequency. The largest observed magnitude of the second harmonic was always less than ten percent of the fundamental indicating that the impeller forces at the small eccentricity employed vary quite sinusoidally around the circular eccentric orbit and that this variation can be accurately represented by a stiffness matrix. More data on this spectral analysis can be found in Chapter 4.

Finally linearity of the stiffness matrix with respect to the imposed eccentricity has been assumed in view of the experimental data of Hergt and Krieger [39] described in section 1.4.

3.7. Data Reduction

We wish now to extract average volute forces (radial forces) and hydrodynamic force matrices (stiffness matices) from data collected from the external balance load cells. Let us first show that damping and acceleration forces are negligible. In here we approximate the magnitudes of these forces by

$$F_D \approx \rho Q \varepsilon \omega \tag{3.4}$$

for the damping force and by

$$F_A \approx M \varepsilon \omega^2 \tag{3.5}$$

for the acceleration force. ε represents eccentricity (1.26mm), ω is the whirl speed (3rpm), ρ is the density of water at 70° F (62.4 lbm/ft), Q is flow rate (maximum of 500 gpm used) and M is the mass of the rotating part (maximum

of 140 lb used). Substitutions of these values yields $F_D \approx 2.8 \times 10^{-3}$ lbf (1.27×10^{-3} kgf) and $F_A \approx 1.8 \times 10^{-3}$ lbf (8.2×10^{-4} kgf). Hence damping and acceleration forces are, in theory, negligible. As a result the force $\underline{F_H}$ of Eq. 1.9 can be assumed to be a "stiffness force" only, that is,

$$F_H \approx [K] \begin{bmatrix} X \\ Y \end{bmatrix} . \tag{3.6}$$

Here we neglected higher harmonics in view of the spectral analysis of the force signals (section 3.6 and later section 4.2). We now proceed to calculate the stiffness matrix [K].

The geometry and notation of the impeller shaft location, external balance load cells and volute position are shown in Fig. 3.3 (viewed from the pump inlet). The center of the volute and the center of whirl are made to coincide through proper floating procedures (section 2.7) such that $\underline{\delta_V}$ is minimized; ideally $\underline{\delta_V}$ should be zero before any test run. The flexure system, though quite stiff, has some deflection due to the hydrodynamic forces on the impeller; indeed this deflection $\underline{e}$ is monitored by the external balance elements. One consequence of this is that the actual position of the shaft center is a combination of the 1.26mm eccentricity plus the deflection of the flexure system. All of the data on impeller forces were corrected for this effect. If $\underline{\varepsilon}$ is the instantaneous shaft center due to the imposed eccentricity of 1.26mm and $[K_S]$ is the stiffnesss matrix of the flexure system (measured by loading under conditions of no motion), then the actual instantaneous position of the shaft is

$$\underline{\delta} = \underline{\varepsilon} + \underline{e}; \quad \underline{e} = [K_S]^{-1}\underline{F} \tag{3.7}$$

where $\underline{F}$ is the instantaneous force acting on the rotor (and therefore on the

floating assembly) for a particular test run due to the Ω and ω motions. The design value of $[K_S]$ as explained in section 2.7 was to have been around 10,000 lbf/in in the vertical and horizontal directions but this was later measured to be

$$[K_S] = \begin{bmatrix} k_a & 0 \\ 0 & k_b \end{bmatrix} = \begin{bmatrix} 11{,}000 & 0 \\ 0 & 8{,}300 \end{bmatrix} \text{ lbf/in} \quad . \tag{3.8}$$

We now proceed to eliminate the tare forces due to the whirling of the eccentric mass and to the non-isotropic stiffness of the rotating flexible coupling by substracting data from two properly zeroed test runs. The first run is one in which hydrodynamic impeller forces are to be actually determined (rotor speeds of 600 rpm and higher). The other run features low rotor speeds of less than 30 rpm and was thus called a "zero run". This procedure was justified because (i) impeller forces will be seen to increase quadratically with rotor speed and because (ii) no perceptible forces could be measured using this technique when the impeller was removed and whirling experiments were initiated (see "No Impeller" results in Chapter 4). Letting $\underline{f}$ be the total force acting on the impeller for a "zero run" , then the net instantaneous displacement due to a purely hydrodynamic force $(\underline{F} - \underline{f})$ is

$$\underline{\delta^N} = \underline{\varepsilon} + [K_S]^{-1}(\underline{F}-\underline{f}) \quad . \tag{3.9}$$

We now express $\underline{F}$ and $\underline{f}$ into components in the horizontal and vertical coordinates of the external balance as shown in Fig 3.3. We then have

$$\underline{F} = \begin{bmatrix} X_1 + X_2 \\ X_3 \end{bmatrix} \tag{3.10a}$$

and

$$\underline{f} = \begin{Bmatrix} x_1 + x_2 \\ x_3 \end{Bmatrix} . \qquad (3.10b)$$

X_i or x_i being the amplified averaged voltage signal (in volts) from each of the three measuring load cells for any of the 32 orbital positions sampled. Here i=1, 2 represent the two horizontal load cells while i=3 represents the vertical one. The whole set of signals, (X_i, x_i), is now decomposed in a Fourier series with the whirl speed ω as basic frequency. X_{io} and x_{io} will then denote the averaged values for the 32 orbital positions while (X_{is}, x_{is}) and (X_{ic}, x_{ic}) are respectively the in-phase and quadrature components of the first harmonic of these signals with respect to the "start" position of sampling or index line of Fig. 3.3 (see also section 2.9). We now decompose the net displacement $\underline{\delta^N}$ of Eq. 3.9 into a similar Fourier series in ω. The average volute force $\underline{F_0}$ can now be associated with the mean position of the shaft center and the first harmonic $\underline{F_\omega}$ of $(\underline{F} - \underline{f})$ can be associated with the first harmonic of $\underline{\delta^N}$, $\underline{\delta_\omega}$. The hydrodynamic force matrix, [K] is then equal to

$$\underline{F_\omega} = [K]\underline{\delta_\omega} . \qquad (3.11)$$

We now proceed to give expressions for each component of this matrix. For simplicity first set

$$X_j^H = (X_{1j} + X_{2j} - x_{1j} - x_{2j}) \cdot S_H \qquad (3.12a)$$

and

$$Y_j^V = (X_{3j} - x_{3j}) \cdot S_V \tag{3.12b}$$

where j = o, s and c denote average, fundamental in-phase and fundamental in-quadrature elements respectively. S_H and S_V are the respective slopes of calibration for the horizontal and vertical external balance load cell elements expressed in lbf/volt. Also let α be the index line angle measured from the horizontal line of Fig. 3.3 and τ be the volute's cutwater angular position. The dimensionless average volute force $\underline{F_0^*}$ and hydrodynamic force matrix $[K^*]$ can then be expressed in the volute coordinates (X,Y) as they are seen to make up the hydrodynamic steady-state impeller force $\underline{F_\varepsilon}$ of section 1.4, namely,

$$\underline{F_\varepsilon^*} = \underline{F_0^*} + [K^*] \cdot \frac{\underline{\delta_\omega}}{r_2} \tag{3.13a}$$

Here

$$\underline{F_0^*} = F_0^* e^{i\Theta} = \begin{bmatrix} F_{0X}^* \\ F_{0Y}^* \end{bmatrix} = \frac{1}{F_N} \begin{bmatrix} X_o^H \cos\tau - Y_o^Y \sin\tau \\ X_o^H \sin\tau + Y_o^Y \cos\tau \end{bmatrix} \tag{3.13b}$$

and

$$[K^*] = \begin{bmatrix} K_{XX}^* & K_{XY}^* \\ K_{YX}^* & K_{YY}^* \end{bmatrix} \tag{3.13c}$$

with

$$K^*_{XX} = \frac{r_2}{\varepsilon F_N} \frac{S[sY_s^V - cX_s^H] + C[cX_c^H - sY_c^V] + P\left(\frac{s^2}{\varepsilon k_a} + \frac{c^2}{\varepsilon k_b}\right)}{\left[1 - \frac{\sin\alpha}{\varepsilon}\left(\frac{X_s^H}{k_a} - \frac{Y_c^V}{k_b}\right) + \frac{\cos\alpha}{\varepsilon}\left(\frac{X_c^H}{k_a} + \frac{Y_s^V}{k_b}\right) + \frac{P}{\varepsilon^2 k_a k_b}\right]}$$

$$K^*_{XY} = \frac{r_2}{\varepsilon F_N} \frac{S[cX_s^H - sY_c^V] + C[cX_s^H - sY_s^V] - scP\left(\frac{1}{\varepsilon k_a} - \frac{1}{\varepsilon k_b}\right)}{\left[1 - \frac{\sin\alpha}{\varepsilon}\left(\frac{X_s^H}{k_a} - \frac{Y_c^V}{k_b}\right) + \frac{\cos\alpha}{\varepsilon}\left(\frac{X_c^H}{k_a} + \frac{Y_s^V}{k_b}\right) + \frac{P}{\varepsilon^2 k_a k_b}\right]}$$

$$K^*_{YX} = \frac{r_2}{\varepsilon F_N} \frac{-S[sX_s^H + cY_c^V] + C[sX_c^H + cY_c^V] - scP\left(\frac{1}{\varepsilon k_a} - \frac{1}{\varepsilon k_b}\right)}{\left[1 - \frac{\sin\alpha}{\varepsilon}\left(\frac{X_s^H}{k_a} - \frac{Y_c^V}{k_b}\right) + \frac{\cos\alpha}{\varepsilon}\left(\frac{X_c^H}{k_a} + \frac{Y_s^V}{k_b}\right) + \frac{P}{\varepsilon^2 k_a k_b}\right]}$$

$$K^*_{YY} = \frac{r_2}{\varepsilon F_N} \frac{S[sX_c^H + cY_c^V] + C[sX_s^H + cY_s^V] + P\left(\frac{c^2}{\varepsilon k_a} + \frac{s^2}{\varepsilon k_b}\right)}{\left[1 - \frac{\sin\alpha}{\varepsilon}\left(\frac{X_s^H}{k_a} - \frac{Y_c^V}{k_b}\right) + \frac{\cos\alpha}{\varepsilon}\left(\frac{X_c^H}{k_a} + \frac{Y_s^V}{k_b}\right) + \frac{P}{\varepsilon^2 k_a k_b}\right]}$$

where $s = \sin\tau$, $c = \cos\tau$, $S = \sin(\alpha + \tau)$, $C = \cos(\alpha + \tau)$ and $P = X_c^H Y_s^V - X_s^H Y_c^V$.

One last point of interest is to determine the locus of equilibrium points ($\underline{\delta^e}$) inside the volute for which the steady state-hydrodynamic force $\underline{F_\varepsilon}$ is zero. From Eq. 3.13a

$$\underline{\delta^e} = \begin{bmatrix} X/r_2 \\ Y/r_2 \end{bmatrix} = [K_S]^{-1} \frac{\underline{\delta^o}}{r_2} - [K^*]^{-1} \underline{F_0^*} \qquad (3.14)$$

where $\underline{\delta}^{o}$ is the average value of $\underline{\delta}^{N}$ (=$[K_S]^{-1}\underline{F}_0$).

$\underline{F}_0^*$ and its components, along with $[K^*]$ and $\underline{\delta}^{e}$ are plotted in Chapter 4.

3.8. Computer Programs

The SDSP is linked to a PDP-10 central computer. After test runs are completed all of the data are accumulated on files before being processed. Fig. 3.4 shows a self-explanatory flow diagram leading to the calculation of the desired quantities. STDFO is the master program designed to read data files along with other various inputs and print results in their most convenient forms. Its various tasks include conversions of hexadecimal numbers (as stored by SDSP) into decimal forms, subtractions of "zero run" test values from actual test runs values , along with decompositions of all signals into Fourier series with whirl speed as basic frequency.

3.9. Experimental Errors

Drift Errors. Rotor speeds and pump flow rates were read by digital voltmeters and showed negligible drifts or oscillations. In an effort to further reduce these errors, readings of these values were initiated for every three cycles of whirl (equivalent to one minute actual time) and only average values were used in STDFO. Usually rotor speeds drifted no more than ± 5 rpm about their mean computed value, representing an error less than one percent for the slowest speed of 600 rpm. Similarly flow rates were read to within ± 0.25 gpm again representing errors of the order of one percent for the slowest flow rate tested (other than for shut-off operation).

Index Location. The index angle α as documented in Fig. 3.3 was located using an oscilloscope in order to detect the sharp voltage outburst for each whirl cycle. This was done by rotating the whirl motor back and forth until a satisfactory position was found. The rotor orbital angular position was then measured.

We feel this angle was accurately determined to within ± 3 degrees. This type of error cannot affect the magnitude of the forces but affects their phase angle in relation to the volute's cutwater (i.e the individual magnitudes of the components of the hydrodynamic force matrix).

Filter Characteristics. Each strain gauge signal was filtered using a 10 Hz Butterworth low pass filters (section 3.6). Their sine wave response (output/input), as supplied by the manufacturers, is equal to one for the sampling frequency of 0.05 Hz. However their step response (or time lag) is about 0.13 sec, which corresponds to about 2.4 degrees angular lag. This error affects the system in the same way the index angle does.

Machining and Manufacturing Errors. Machining and manufacturing errors are indeed very small. Among those that affect our dimensionless hydrodynamic impeller forces are the eccentricity and outer radius and width of the impeller. The set eccentricity was measured to be 0.0495 ± 0.0002 in. with a relative error of 0.4 percent. Impeller dimensions were also found to have a relative error less than 0.2 percent. An important source of error somewhat independent of manufacturing was the locating of the volute coordinates with respect to the external balance coordinates (angle in Fig. 3.3). This was done to within 2 degrees and affects measurements the same way the index angle does.

Calibration Errors. These are the errors in judging the slopes of calibration of the pressure transducers (C_u, C_d) and of the external balance load cell elements (S_H, S_V). It was felt that the accuracy of these slopes was well within a one percent relative error. Measurements of the stiffness of the flexure system (k_a and k_b) were conducted with a relative error of five percent but this was toned down by the fact that it barely affects the hydrodynamic force matrix results of Eq. 3.13c since it enters as a correction term because the load cell elements are not infinitely rigid. This correction amounts to less than ten percent of the total

magnitudes of each coefficient of $[K^*]$ for the maximum load encountered during experimentation.

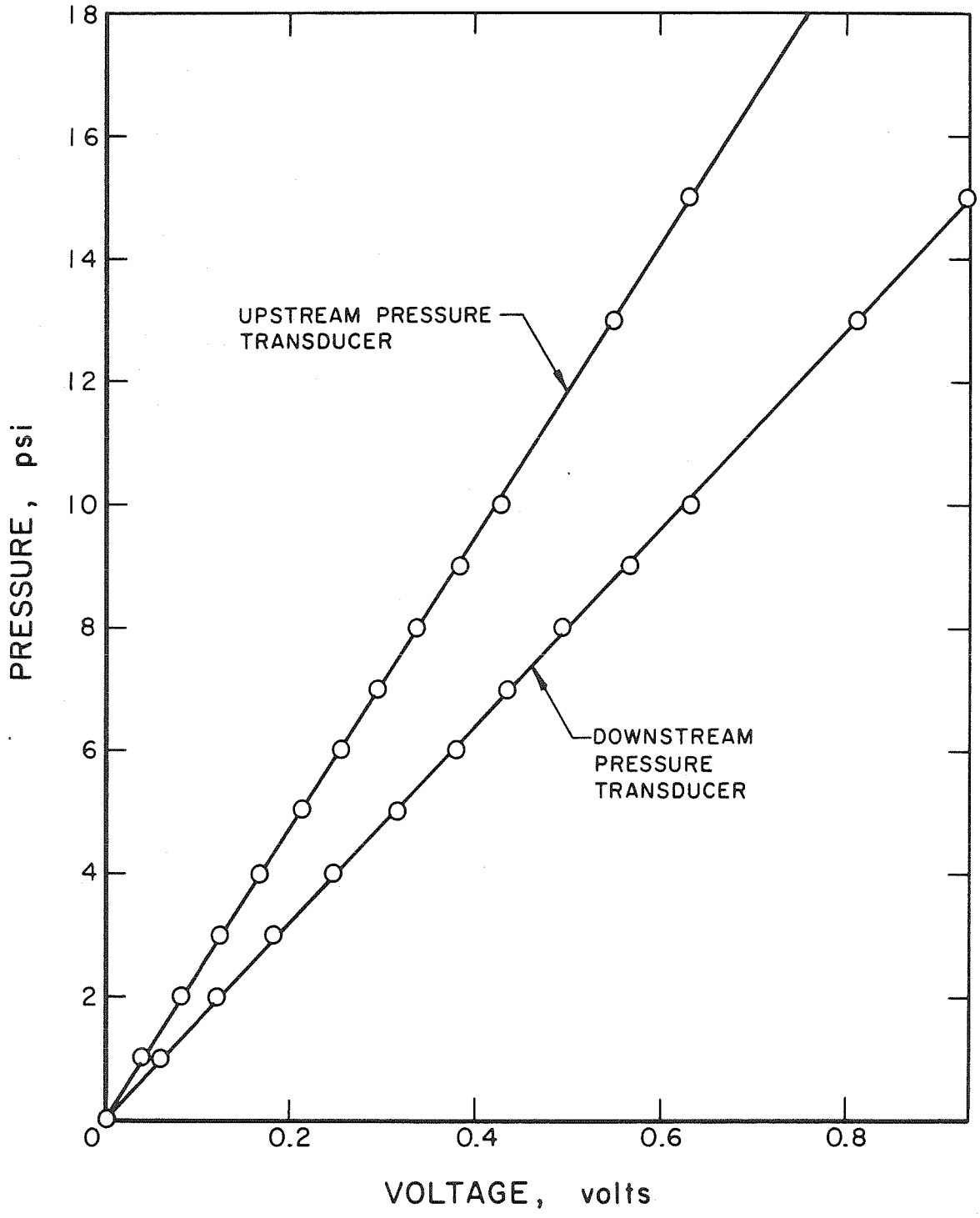

Fig. 3.1. Typical calibration curves for the two pressure transducers.

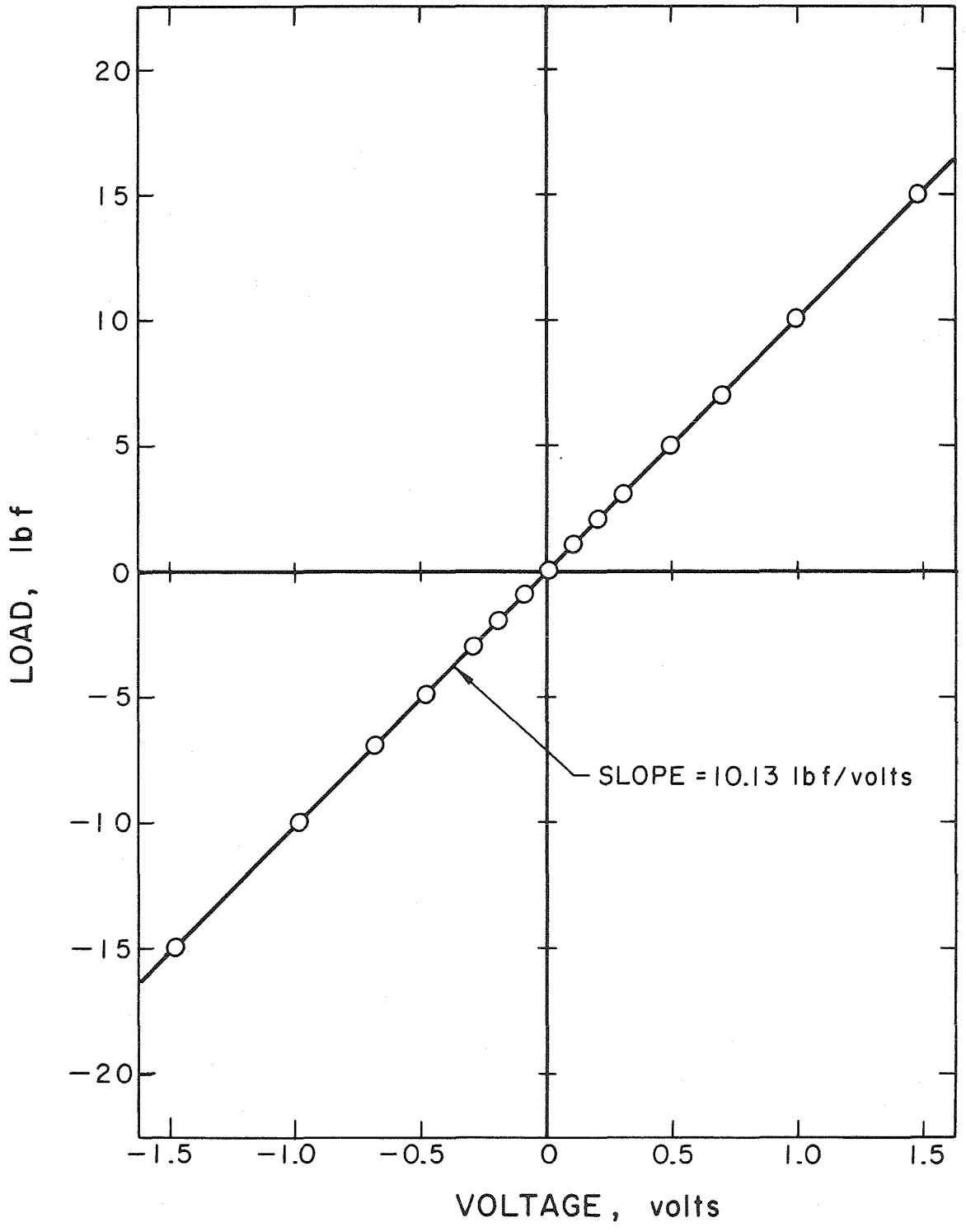

Fig. 3.2. Typical calibration curve for the vertical load cell of the external balance (No. 3 in Fig. 3.3). Bellows chamber pressure of 8 psig, 10 volts d.c. bridge excitation and amplification of 171 times the original signal.

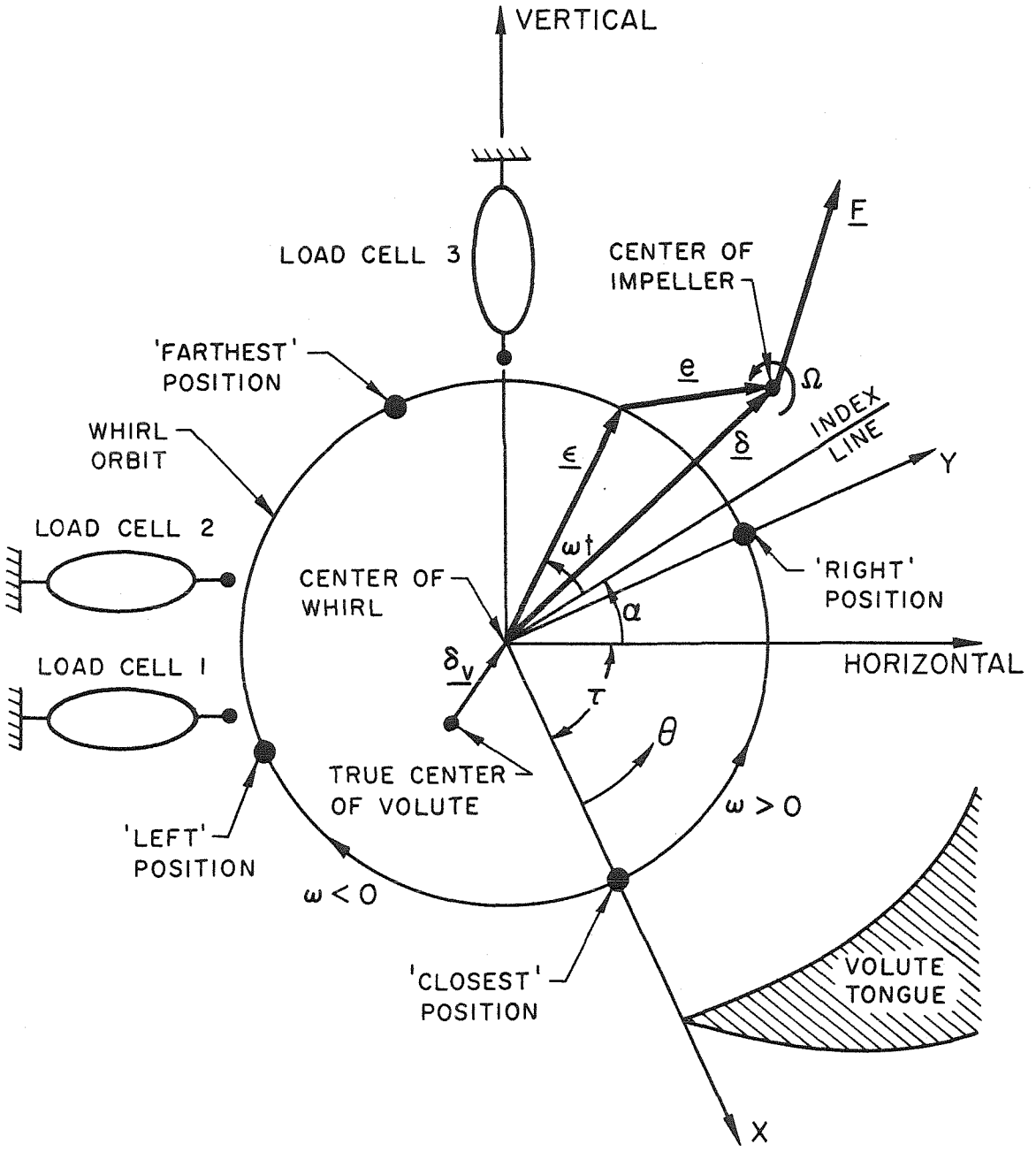

Fig. 3.3. Schematic of forces and locations within the impeller-volute system as seen from the inlet.

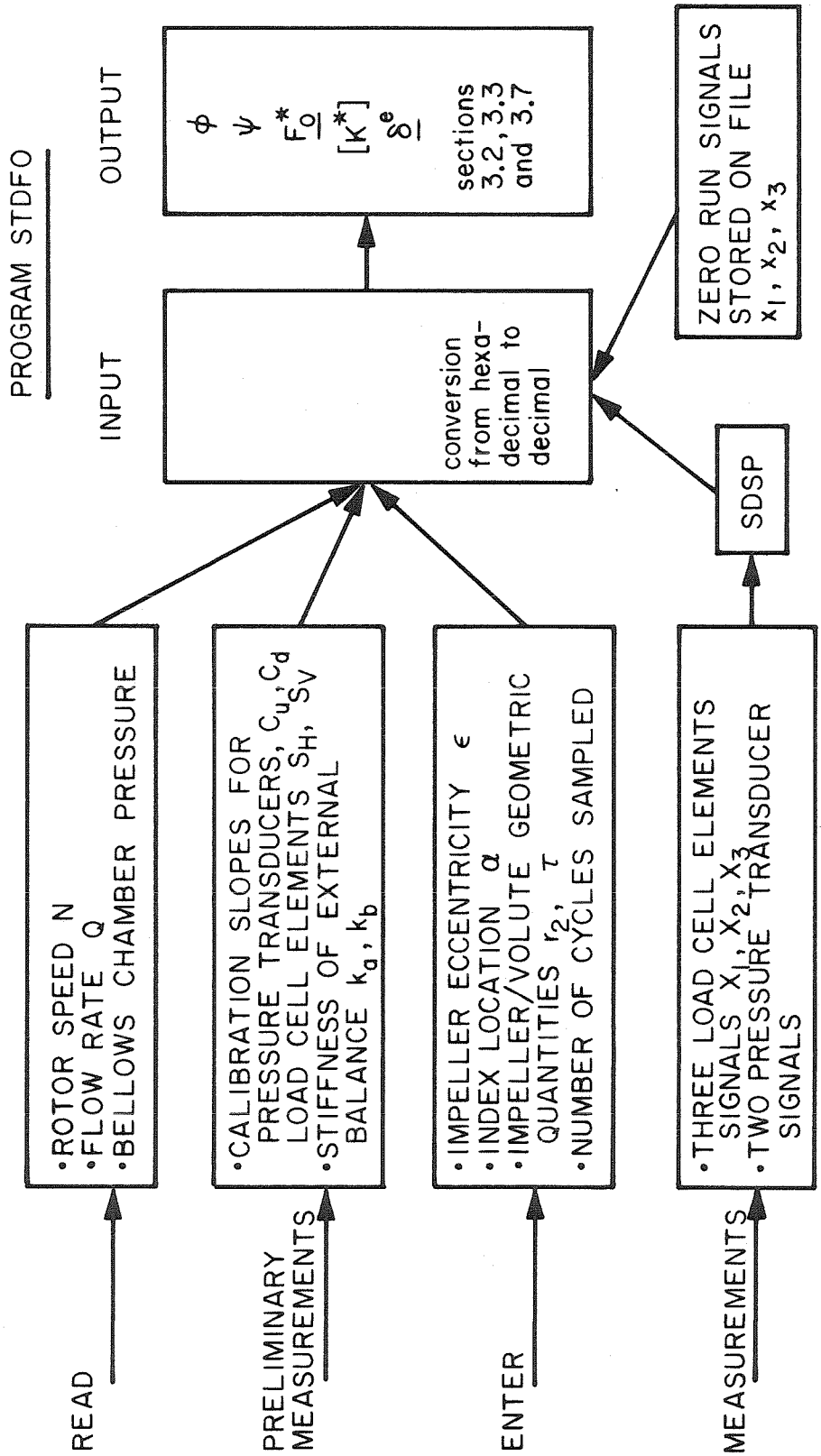

Fig. 3.4. Flow chart of the various inputs in order to get steady hydrodynamic impeller forces and various pump and volute characteristics.

Chapter 4

EXPERIMENTAL RESULTS AND DISCUSSIONS

4.1. Introduction

All experimental results derived from the present course of studies are presented in this chapter. The main features of the various plots and figures are pointed out. An in-depth discussion is also included in each section to describe the corresponding result.

4.2. Spectral Analysis

As mentioned in the previous chapter the external balance load cell signals were recorded on magnetic tape and processed through a digital spectrum analyser in order to investigate their content. A four-channel HP-3960 instrumentation recorder was used to tape the three unfiltered signals simultaneously. In order to reduce the relative noise generated by the recording equipment, these signals were preamplified to the maximum recorder input band using the tape recorder built-in amplifiers, then calibrated by recording a known sine wave from a signal generator. The range of frequencies of interest was under 150 Hz which proved satisfactory for the present measurements as the frequency response of the HP recorder was fairly flat up to 5 kHz. The power spectra of the load cell signals were then computed and plotted by a Spectral Dynamic Corporation Model SD360 digital signal processor. The system has an internal digitizer so that analog data can be loaded directly from the tape recorder. The sampling rate depends on the predetermined frequency; 2048 points are sampled during a basic time unit equal to $500/f_{max}$ where f_{max} is the highest frequency in the analysis range. Thus a sample is taken every $(0.5/2.048f_{max})$ seconds or approximately four points during a cycle of the highest frequency. In

order to accurately observe harmonics of the whirl speed (ω = 0.05 Hz) as well as the fundamental (and maybe higher higher harmonics) of the rotor speed, Ω, it was necessary to use the smallest frequency range available on the signal processor(0-10 Hz range). Therefore a preliminary taping of a rotor speed of 300 rpm (5 Hz) was initiated and analysed. Figures 4.1 and 4.2 present the power spectra of horizontal load cell No. 1 as defined in Fig. 3.3 and of the vertical load cell (No. 3) respectively. Horizontal load cell No. 2 presented similar findings as load cell No. 1 and therefore will not be documented for the 300 rpm tests. Figure 4.1a,b shows the power spectum of the horizontal load cell for the minimum range of 0-10 Hz. The various harmonics in ω can be clearly distinguished especially on the log plot. The 20 d.b. attenuation between the fundamental and the second harmonic is somewhat typical of all results and could be confirmed by the Fourier decomposition initiated by the master program, STDFO (section 3.8). In fact the maximum amplitude of the second harmonic for any of the load cell signals encountered by STDFO was at most ten percent of the fundamental. Moreover the power spectrum of any dynamometer output failed to show any other major peaks between the whirl speed ω and the rotor speed Ω, i.e., no subharmonics of Ω could be found. These two considerations point out to the validity of the data reduction technique where only the average values (d.c.) and the fundamentals in ω of the three load cell signals are needed to determine average volute forces and hydrodynamic force matrices. Furthermore it is generally agreed (although we cannot prove it) that the absence of harmonics higher than the fundamental implies the linearity of the signals with respect to the eccentricity of the rotor center (ε).

A brief description of other observed peaks is in order. Superharmonics of the rotor speed as well as various natural frequencies of the floating external balance assembly can be seen on the expanded 0-50 Hz frequency range of Figs. 4.1c and 4.2b. These peaks are still present in Fig. 4.3 where a more realistic

rotor speed of 1010 rpm was taped, analysed and plotted for each of the load cell outputs and for a 0-150 Hz frequency range. Among the superharmonics in Ω (denoted by 2Ω, 3Ω,etc.), we would like to point out the predominance of the blade passage frequency peak (5Ω). On the other hand the natural frequencies of the floating system (denoted by 1, 2,... for each graph) represent fixed quantities, independent of rotor speed, that can be theoretically shown to exist. For example the 22 Hz peak of Fig. 4.2 is the calculated natural frequency of motion in the vertical direction of Fig. 3.3. The high frequency noise (100 Hz and higher) present in Fig. 4.3 was not investigated because it is out of the range of interest for this work.

4.3. Performance Characteristic Curves of Impeller X

Figure 4.4 presents the performance characteristics of Impeller X within Volute A for the two face seal clearances of 0.14 and 0.79 mm and for these values the leakage flow back to the inlet of the impeller was about two percent and twelve percent of design flow rate respectively. This plot is quite typical for such impeller/volute configurations and is independent of rotor speed. A noticeable degradation occurs when the seal gaps are increased as the total head coefficient decreases by about 0.04. Figure 4.5 compares the performance characteristics of Impeller X within Volutes A or B for the same maximum seal clearance of 0.79 mm. It is somewhat surprising that the "circular" volute (B) outperforms the "well-matched" volute (A) above the design flow coefficient of Volute A (φ = 0.092). This is a plus for this type of volute widely used for slurry applications as well as in the oil industry field.

It is always desirable to measure complete performance characteristics including efficiency but in the present experiment provision was not made to measure torque in the present apparatus for all volutes; as a result we are unable to report the efficiency for these two volute types. Tests performed by

Byron-Jackson on a sixteen stage pump using Impeller X reveal that the overall pump efficiency was 77 percent at a flow coefficient of 0.080.

4.4. Average Volute Forces; Results and Discussion

The reduced data for the dimensionless average volute force acting on Impeller X due to Volutes A or B are presented in Figs. 4.6 through 4.11; these include the magnitude, direction and individual force components. These forces are also defined by Eq. 3.13b. The data for the "well-matched" volute (A) for a face seal clearance of 0.14 mm are shown in Fig. 4.6. Here F_0^* is plotted versus flow coefficient for various rotor speeds. Some results for both a forward 3 rpm sampling orbit speed ($\omega > 0$) and a reverse orbit speed of 3 rpm ($\omega < 0$) are shown to confirm that this orbit speed had little effect on the results. The non-dimensionalized force data for different shaft speeds (600 up to 2000 rpm) is in substantial agreement though there would appear to be a slight increase in the magnitude of the force coefficient at low flow coefficients when rotor speed was increased. It seems likely that this is a Reynolds number effect. From a practical viewpoint it is clear that the Impeller X and Volute A are well matched at their design flow coefficient of 0.092 since the force on the impeller is virtually zero in this operating stage. The magnitude of the dimensionless force is then seen to vary linearly with flow coefficients above and below design. In fact,

$$F_0^* = 1.69\varphi - 0.15 \tag{4.1}$$

for $\varphi \geq 0.092$ for all rotor speeds and

$$0.155 - 1.6\varphi \leq F_0^* \leq 0.17 - 1.76\varphi \tag{4.2}$$

for $\varphi \leq 0.092$. Here the lower bound applies for rotor speeds of 600, 800 and 1000 rpm while the upper bound is for the rotor speed of 2000 rpm. Values of F_0^*

at shut-off range from 0.155 to 0.17 which is ten to twenty percent higher than the calculated value suggested by Stepanoff [63]. For completeness the direction of this force with respect to a line joining the center to the tongue of the volute is shown in Fig. 4.7. It is surprising that this angle is somewhat independent of rotor speed or flow coefficient and depends only on the position of operation of the rotor with respect to the design flow coefficient of 0.092. In fact this force angle is about -90 degrees for flow coefficients above design, and about +70 degrees for flow coefficients below design. This result should be valuable in the design of shafts and rotor structures for this particular impeller/volute configuration as the line of action of the radial force is constant depending on the side of operation with respect to design.

Also shown in Figs. 4.6 and 4.7 are the experimental results of Agostinelli, Nobles and Mockridge [4] and Iversen, Rolling and Carlson [44] for pumps with specific speeds of 0.61 and 0.36 respectively. The former are in close agreement with the present results since the specific speed of the present Impeller X/Volute A combination is 0.57. The results of Iversen et al for a lower specific speed also appear consistent with the present results. For clarity, another set of experimental results by Domm and Hergt [33] is presented in Fig. 4.8. These results for a similar volute (having a spiral angle of 86.3 degrees) appear to be in substantial disagreement (lower forces by a factor of two or three) with the present results shown in Fig. 4.6. There is unfortunately insufficient data in that report to determine if that discrepancy is due to a different volute design or to different experimental procedures.

Figure 4.8 also presents the dimensionless force components of the average volute force. Included in the plot are the theoretical results of Domm and Hergt [33] and Colding-Jorgensen [29] for volutes with spiral angles of about 86 degrees. These theories are based on the impeller being modeled by a source-

vortex at its centerline and by assuming potential flow throughout the pump stage. Volute A has a similar angle when projected on the radial plane of the impeller. However Volute A is fully three-dimensional and the equivalent spiral angle obtained by unwrapping its area would be about 82 degrees. Under these assumptions the data of Colding-Jorgensen appears more consistent with the experiments than what is actually shown in Fig. 4.8. Unfortunately we cannot initiate a similar "correction" with the results of Domm and Hergt as the theoretical example of reference [33] featured only a volute angle of 86.3 degrees.

We have also investigated the effects on the average volute force due to either an increase in the face seal clearances or due to a volute change. Figures 4.9, 4.10 and 4.11 show data for Volutes A and B for the maximum front and back face seal clearances of 0.79 mm. The magnitudes, directions (and therefore also cartesian components) of the average volute force for Volute A exhibited almost no change for the two face seal clearances at least for the two rotor speeds tested (600 and 800 rpm); this is somewhat surprising because the total head changed significantly. We can only conclude that the flow distribution in the volute is affected by the leakage flow.

Different results were found for the circular Volute (B). Instead of the linearly decreasing force magnitude with decreasing flow rate as predicted by Stepanoff [63] (Eq. 1.3), we observe a flat region for flow coefficients about 0.07 in which the normalized force magnitude is about 0.055. For decreasing flow coefficients below 0.07 the previously predicted linearly decreasing pattern is recovered with an intercept for shut-off at about 0.0155. Manufacturing imperfections and lack of perfect centering might be the cause for the force not vanishing there. Contrary to the findings on volute A, the force angle Θ as documented in Fig. 4.10 is not constant with flow coefficient. Finally we should point out that the two

speeds of 800 and 1200 rpm tested with volute B seemed to be in general agreement with respect to the normalization process.

4.5. Hydrodynamic Force Matrices

Non-dimensional hydrodynamic force matrix coefficients, K_{ij}^*, are presented in Figs. 4.12 through 4.15; these contain all the information on how the forces presented in Figs. 4.6 to 4.11 vary as the position of the impeller center changes provided the change is within the linear region. These coefficients are also given by Eq. 3.13c. Figure 4.12 presents data for Volute A, for face seal clearances of 0.14 mm, for various flow rates and for rotor speeds of N = 600, 800 and 1000 rpm. We observe that the variation with N^2 is consistent with that anticipated by the non-dimensionalization and that the components vary only modestly with flow coefficient, φ, for values above about 0.03. Finally all of the measured K_{ij}^* show a tendency to drop as we approach shut-off but they do not vanish there.

The theoretical results of Colding-Jorgensen [29] based on the source/vortex model of the impeller which are also depicted in Fig. 4.12 exhibit substential disagreement with the measurements. This model will be discussed in Chapter 5. The diagonal components K_{XX}^* and K_{YY}^* are about one third of those of the present experiment. The off-diagonal or "cross-coupling" terms also differ from the present values and the calculated values of K_{YX}^* exhibit a change in sign unlike its experimental counterpart.

It is worthwhile to examine closely the structure of the $[K^*]$ matrix before presenting the remaining force matrix data; in fact the hydrodynamic force matrix of Fig. 4.12 implies that the fluid forces will tend to excite a whirl motion of the impeller. This force matrix can be presented approximately in the form

$$[K^*] = \begin{bmatrix} 2.0 & -0.9 \\ 0.9 & 2.0 \end{bmatrix} \tag{4.3}$$

over the range $0.04 < \varphi < 0.14$. It is therefore a combination of a diagonal and a skew-symmetric matrix. The former will simply reduce the structural stiffness matrix and in many cases this hydrodynamic effect will be small. The skew-symmetric or cross-coupling terms are much more important. Since K^*_{XY} and K^*_{YX} are of opposite sign, their effect is to tend to destabilize the rotor. This is easy to show; suppose that the impeller of Fig. 1.2 lies on the X-axis of the volute (Y=0). It now experiences an upward Y-force equal to $0.9X/r_2$ (in dimensionless form); if the impeller is now moved to the positive Y-axis (since the impeller is pushed that way) a negative X-force equal to $-0.9Y/r_2$ (in dimensionless form) is developed. The new result is that the impeller center tends to be pushed around the center of the volute. In short, if the impeller were made to move in such a motion (slowly), work could be extracted from the impeller, just like a turbine! Presumably if the impeller shaft center were free to move (as it is in actual pumps) rotation or whirl of the shaft center would take place. The rotordynamic consequences of such excitation will, of course, depend on the damping matrix as well (see for example Adams and Padovan [3]). In other words this whirl motion will be suppressed if the damping force due to the whirling motion is sufficient. However since K^*_{XY} and K^*_{YX} are proportional to N^2, it follows that if damping increases more slowly with N, then there will always be a speed above which the excitation will exceed the damping. This is easy to show using the experimental results of Ohashi and Shoji [57] that were briefly discussed in section 1.4. Their test impeller was installed in a large "vaneless" diffuser with the result that the cross coupling stiffness terms K^*_{XY} and K^*_{YX} were very small and could not be detected. However the damping matrix was; in fact positive damping was found resulting in a "negative" tangential force (see also section 1.2). By

equating this negative tangential force (Fig. 8a of [57] for example) to our "positive" tangential force (calculated using K^*_{XY} of Fig. 4.12), inception speed of rotor whirl can be predicted. Disregarding the fact that we are comparing two different pump/volute systems, one can show using these results rotor whirl to occur at $\Omega > 1.1\omega$ for design conditions and at $\Omega > 4\omega$ for shut-off conditions. Here Ω is rotor speed while ω is whirl speed. Hence we see the possibility of non-synchronous whirling when this whirl speed ω is equal to the first critical. Future measurements using the internal balance of section 2.2 will examine the hydrodynamic contributions to the damping and mass matrices in order to extend the kind of results obtained by Ohashi and Shoji et al which will allow more quantitative analysis of hydrodynamically induced whirl. Nevertheless we see from this example that hydrodynamic stiffness due to the flow through the rotor and its surroundings can then be seen to be a possible cause of "rough running" of pumps.

We now examine the effect of parameter variation on the normalized force matrix. We tested higher rotor speeds than in Fig 4.12 and found a slight increase in the magnitudes of K^*_{ij} as shown in Fig. 4.13 for the rotor speeds of 1200 ($\omega > 0$), 1200 ($\omega < 0$) and 2000 rpm. We take this to be some kind of Reynolds number effect. By imposing forward and backward orbital motions (at N = 1200 rpm) it can also be seen how little is the effect of the 3 rpm whirl speed on the force matrix results. Data have also been obtained with face seal clearances of 0.79 mm and the results are shown in Fig. 4.14. These findings are qualitatively similar to that of Fig. 4.12 except that the magnitude of all the components is roughly at most twenty percent larger for the larger clearances.

Results for the circular volute (B) are shown in Fig. 4.15. The force matrix data for this volute are hereby expressed in the coordinates of Volute A since it was difficult to define the cutwater of the circular volute and because

comparison between the two volutes could then be initiated . The results for the circular volute were surprising in the sense that the skew-symmetric effect was even clearer and that, contrary to Volute A, the K_{ij}^* coefficients increased with decreasing flow rate.

In conclusion no change in the experimental parameters altered the skew-symmetric behaviour of the $[K^*]$ matrix. Even the magnitudes of the K_{ij}^* coefficients seemed to be around the same values for different volutes and operating conditions. This is indeed a new finding valuable for any serious rotor-dynamic analysis.

4.6. Auxiliary Experiments

Figures 4.16 and 4.17 present the force coefficient data for a number of tests performed with the objective of assessing the source of the large forces present at conditions of no flow ($\varphi = 0$) for the case of Volute A. Figure 4.16 deals with face seal clearances of 0.14 mm while the larger clearances of 0.79 mm were investigated in Fig. 4.17. All of the normalized data presented appeared to be virtually independent of shaft speed indicating that forces are proportional to the square of tip speed. The lack of any appreciable force in the absence of the impeller (No Impeller points of Fig. 4.16) was one of the main reasons for subtracting the data of a "zero run" from the data of an actual run in Section 3.7 on "data reduction" techniques; this shows the force to be truly due to the presence of the rotor only. Other experiments conducted consisted of testing a solid impeller having the same dimensions of Impeller X and of testing Impeller X with its inlet and/or exit blocked by a sheet of metal. The data for the solid impeller and for Impeller X having its inlet and exit blocked were quite similar for both face seal clearances. We conclude that this force coefficient component (about 0.045) is due to disk friction effects and to the induced pressure gradient acting on the entire exterior surfaces of the impeller. The force coefficient for Impeller

X with its exit blocked was about 0.055 showing that the inlet recirculation effects are somewhat negligible with respect to the force momemtum exchange with the impeller. The data with only the impeller inlet blocked are significantly higher, probably because the outer recirculation effects are greater than in the previous case. This force coefficient was also twenty percent higher for the smaller face seal clearances, the reason of which is not entirely known at this time. Finally the force data for the flow blocked exterior to the impeller (shut-off) are significantly higher still. Here a solid plate was inserted in the flow about three diameters upstream of the impeller. Disturbance of the flow through the impeller was even greater than in all of the previous cases and a substantial inlet vortex swirl could be observed between the solid plate wall and the inlet of the impeller.

For completeness we have plotted in Fig. 4.18 the dimensionless force matrix coefficients, K^*_{ij}, for each of the experiments of Fig. 4.16. The most significant result is the absence of "stiffness" when the impeller was removed (No Impeller points); the highest value of any component was less than three percent of its counterpart for design flow when the impeller was present. This confirms again the fact that the stiffness force so measured is due to the presence of the rotor only. The force matrix of the solid impeller gives a clear idea on how much disk friction accounts for the total force matrix of the actual impeller; results for the solid impeller were four times smaller than for design conditions. For completeness we also give the hydrodynamic force for Impeller X with its inlet and/or exit blocked. Their values were at most twice that of the solid impeller. Finally all matrices remained skew-symmetric at all time.

4.7. Hydrodynamic Centers

The locus of equilibrium positions of Impeller X within Volutes A or B was computed according to Eq. 3.14 and plotted in Figs. 4.19 and 4.20 for the coordinates of Volute A only; when the impeller center coincides with the plotted "hydrodynamic center" the impeller force is zero. The position of the "hydrodynamic center" for Impeller X, for Volute A and for face seal clearances of 0.14 mm is presented as a function of flow coefficient in Fig. 4.19. These equilibrium positions were independent of rotor speed and exhibited a "linear" region between the flow coefficients of 0.055 and 0.122 with the hydrodynamic center and the volute center coinciding at the design flow coefficient of 0.092. An exciting finding is the possibility of having the rotor shaft move on a straight path according to flow coefficient so that the hydrodynamic forces acting on the impeller are minimized. Such a device might be able to prevent failures in high-performance turbomachinery as these operate at high rotor speeds and therefore they exhibit large radial forces. Finally it is seen that these data are consistent with that of Domm and Hergt [33] for a similar volute.

The positions of the hydrodynamic centers of Volutes A and B is also shown in Fig. 4.20 for the larger face seal clearances of 0.79 mm. Volute A exhibited the same previous linear behaviour with all hydrodynamic center positions being slightly shifted upwards towards the second quadrant. The hydrodynamic centers for volute B were less sensitive with flow coefficient and approached the center of the volute as we neared shut-off.

4.8. Static Pressure Measurements in the Volute

Instrumentation. Static pressure distributions within Volute A were measured by means of the static pressure taps shown in Fig. 4.21 for four fixed positions of the eccentricity (the positions "closest", "farthest", "right" and "left" shown in Fig. 3.3) and various flow coefficients. The main intent is a break-up of

the hydrodynamic forces into static pressure forces, disk friction forces and momentum flux forces. A bank of inverted water manometers was used to measure pressure differences for the sixteen taps of Fig. 4.21 and reference them with respect to the downstream total pressure as measured by an accurate Heise gauge. These values were fed to a PDP-10 computer and processed into useful form using a program with initials "CP". The pressure distributions are then presented non-dimensionally using a pressure coefficient, C_P, based on the downstream total pressure and the dynamic head based on impeller tip speed (see nomenclature). C_P is then plotted versus the angle starting from the cutwater of the volute. Finally program "CP" fits various spline curves through these pressure distributions in order to carry a numerical integration to get the forces due to the static pressure only for each of the four impeller positions. These forces are then compared to the actual impeller forces measured simultaneously for the same eccentric position.

Static Pressure Distributions. Typical static pressure distributions in the impeller discharge flow are presented in Figs. 4.22 to 4.25 for various flow coefficients of Impeller X within Volute A and for the larger face seal clearances of 0.79 mm. Each figure represents one of the four eccentric positions of Fig. 3.3 for the fixed rotor speed of 600 rpm. The form and magnitude of the pressure variations are similar to those measured by Iversen et al [44] and to those predicted theoretically by Kurokawa [49]. The most important feature is the static pressure discontinuity that occurs about the cutwater (in here we compare the values of C_P at $\theta=0°$ and $\theta=360°$) particularly at off-design flow coefficients. However at or close to the design value of 0.092, the static pressure is quite uniform around the volute periphery. This is to be expected in view of the discussion in section 1.4 on the radial force. Finally we should emphasize the disagreement between the front pressure taps and the back pressure taps (see Fig. 4.21) measurements particularly at low flow coefficients. This points out

that the flow coming out of the impeller is not symmetrical with respect to the centerline of the volute cross-section.

Static Pressure Forces. Figures 4.26 through 4.29 present the X and Y components of the static pressure forces expressed in the coordinates of Volute A for each of the four eccentric positions and compare them with the total force components on the impeller measured by the external balance for the same impeller location. Note that the static pressure component is not sufficient in itself to explain the measured total force. This is contrary to the results obtained by Iversen et al [44]; they observed significant agreement between these forces. Their static pressure force results are plotted in Fig. 4.26 for comparison. They exhibit the same general trend as ours but are much larger in magnitudes; this is perhaps due to the lower specific speed pump used (0.36 instead of 0.57). On the other hand we conclude that the discrepancy in the forces presented in Figs. 4.26 to 4.29 is due to a difference in net flux of momentum in and out of the volute. Some measure of the order of magnitude of this momentum flux difference can be obtained by evaluation of the momentum flux force at the discharge of the volute; when non-dimensionalized in the same manner as the forces, it has a value of 4.14 φ^2 (in the Y-direction). This is of the same order of magnitude as the forces. We conclude that the non-isotropy of the momentum flux leaving the impeller is an important contributor to the impeller forces.

Static Pressure Force Matrix. We estimated the magnitude of a hydrodynamic force matrix [KP] due to the static pressure force components only. An approximate formula was derived for each non-dimensionalized component that is,

$$KP^*_{XX} = \frac{F^*_{Xc} - F^*_{Xf}}{2\varepsilon/r_2} \qquad (4.4a)$$

$$KP^{*}_{XY} = \frac{F^{*}_{Xr} - F^{*}_{Xl}}{2\varepsilon/r_2} \tag{4.4b}$$

$$KP^{*}_{YX} = \frac{F^{*}_{Yc} - F^{*}_{Yf}}{2\varepsilon/r_2} \tag{4.4c}$$

$$KP^{*}_{YY} = \frac{F^{*}_{Yr} - F^{*}_{Yl}}{2\varepsilon/r_2} \tag{4.4d}$$

where F^{*}_{ij} is the static force component (in the X or Y direction) for each of the four eccentric positions tested . Here i = X, Y represent direction while subscripts c, f, r and l represent the four eccentric positions (closest, farthest, right and left respectively) of Fig. 3.3. ε is the imposed eccentricity and r_2 is the outer radius of Impeller X. The normalized static pressure force matrix for a rotor speed of 600 rpm and for face seal clearances of 0.79 mm is shown in Fig. 4.14. It transpires that the components of this matrix represent only about 20 percent of the magnitude of the corresponding total hydrodynamic force matrix components. In addition we have shown earlier that disk friction contributes to about 25 percent of this matrix. We therefore conclude that the non-isotropy of the momentum flux is the primary contributor to the "stiffness" matrix. This fact emphasizes the need for direct measurement of the forces on the impeller rather than estimating the latter by integrating pressure distributions around the base circle of the volute.

4.9. Additional Measurements

We carried independent experiments in order to check the validity of the Shapiro Digital Signal Processor, computer program STDFO and the continuous data sampling procedures. In these experiments impeller forces were measured for each of the four eccentric positions of Fig. 3.3 for both volutes, face seal clearances and for various flow rates and rotor speeds. The experimental technique was simple; the strain gauge signal conditioning amplifiers were zeroed for any of the four eccentric positions for a low rotor speed (less than 30 rpm) and the corresponding load cell signals were read on digital voltmeters where an average value was selected in case of oscillations. We then bring the rotor speed up to test speed and read the new averaged value. The difference between these two readings is the averaged hydrodynamic impeller force for the given eccentric position. It is then straightforward to calculate an equivalent normalized force matrix using a similar formula to Eq. 4.4. Figure 4.30 shows the magnitude and direction of the average force for the four eccentric positions, Volute A, rotor speed of 1000 rpm, face seal clearances of 0.14 mm and for various flow coefficients. These data are similar in content to the data in Figs. 4.6 and 4.7. Figure 4.31 shows the corresponding calculated force matrix coefficients. These compare nicely to the ones of Fig. 4.12. Finally the calculated force matrix coefficients of Volute B are shown in Fig. 4.32 for a rotor speed of 800 rpm and a face seal clearance of 0.79 mm. Here the agreement is less in magnitudes but the major trends are preserved. In conclusion we are confident that our continuous sampling method is justifiable and yields better data.

4.10. Concluding Remarks

We have presented measurements of the steady-state hydrodynamic forces on a centrifugal pump impeller as a function of position within two geometrically different volutes. These correspond to the forces experienced by the impeller at zero whirl frequency. The hydrodynamic force matrices derived from these

measurements exhibit both diagonal and off-diagonal terms of substantial magnitude. The off-diagonal or cross-coupling terms are of the form which would tend to excite a whirl motion in a rotordynamic analysis of the pump. This may be the cause of "rough running" reported in many pumps.

Static pressure measurements in the impeller discharge flow show that the hydrodynamic force on the impeller contains a substantial component due to the non-isotropy of the net momentum flux leaving the impeller. Moreover a similar breakdown of the contributions to the stiffness matrices reveals that the major component of these matrices results from the non-isotropy of the momentum flux.

Future plans should include direct measurement of the forces due to the momentum flux leaving the impeller and the study of other impeller/volute configurations particularly vaned diffusers. Finally measurement of forces at non-zero whirl frequencies should be initiated in order to obtain a complete picture of the rotordynamic consequences of these hydrodynamic forces.

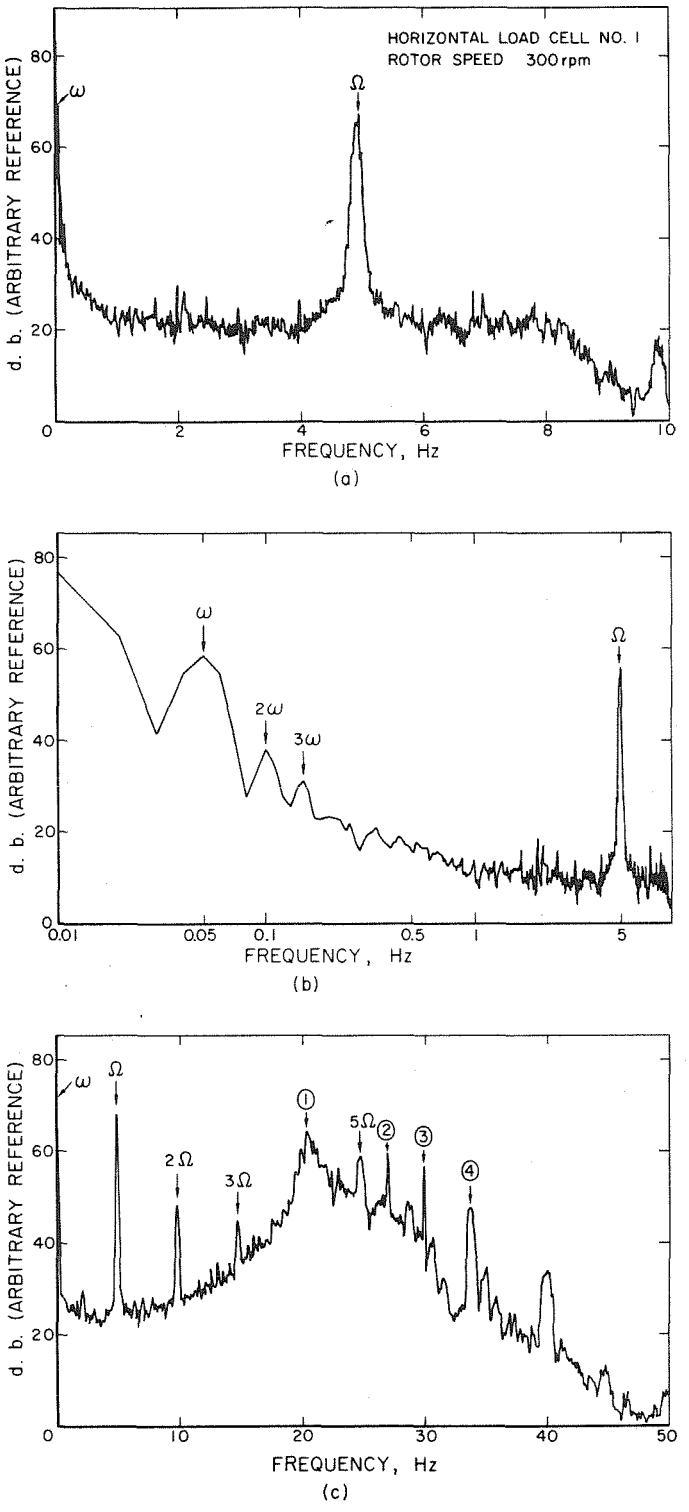

Fig. 4.1. Spectrum of horizontal load cell No. 1 as defined in Fig. 3.3 for a rotor speed of 300 rpm. a) 0-10 Hz, b) 0-10 Hz in a log plot, and c) 0-50 Hz.

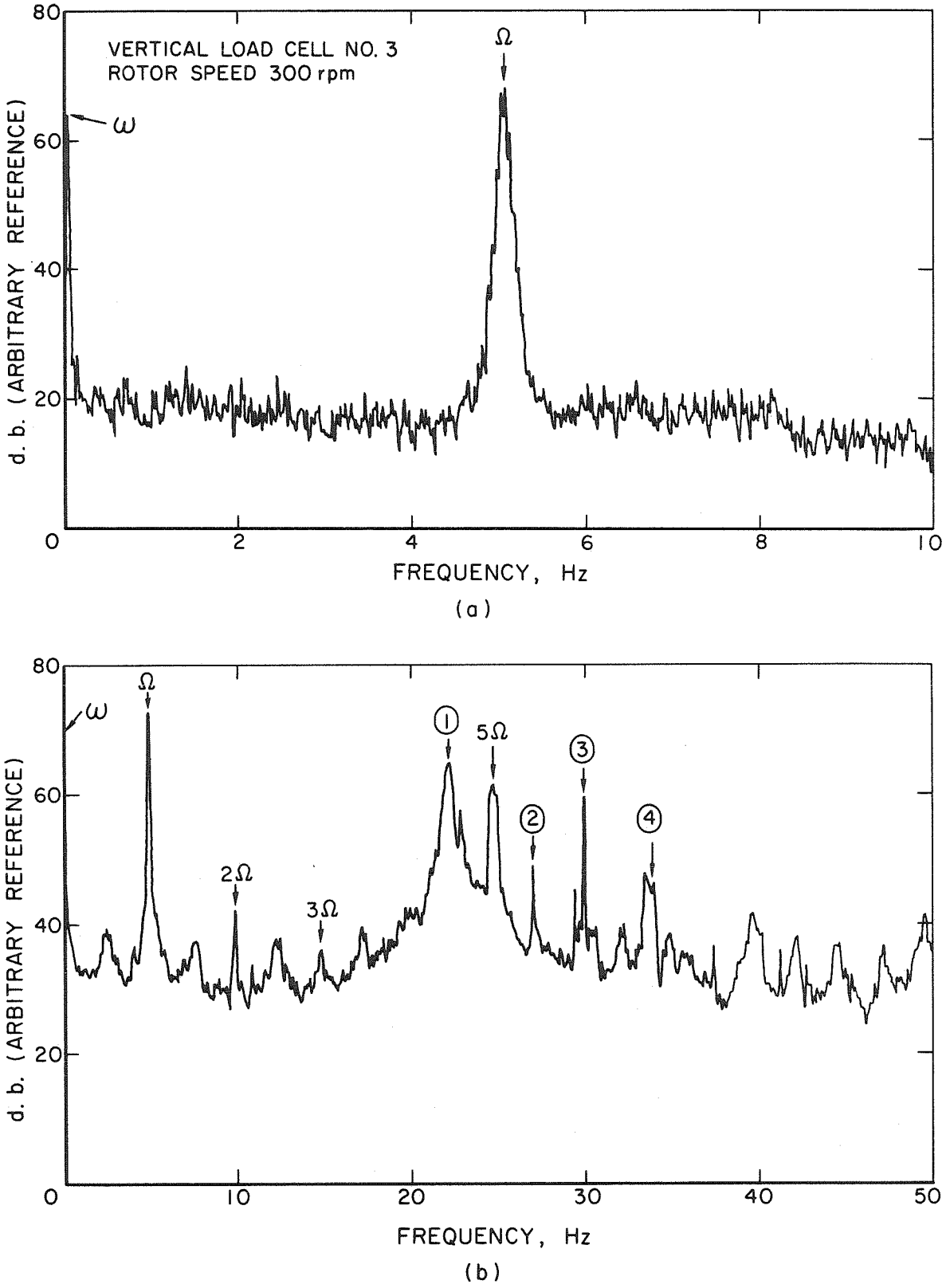

Fig. 4.2. Spectrum of the vertical load cell (No. 3 as defined in Fig. 3.3) for a rotor speed of 300 rpm. a) 0-10 Hz, and b) 0-50 Hz.

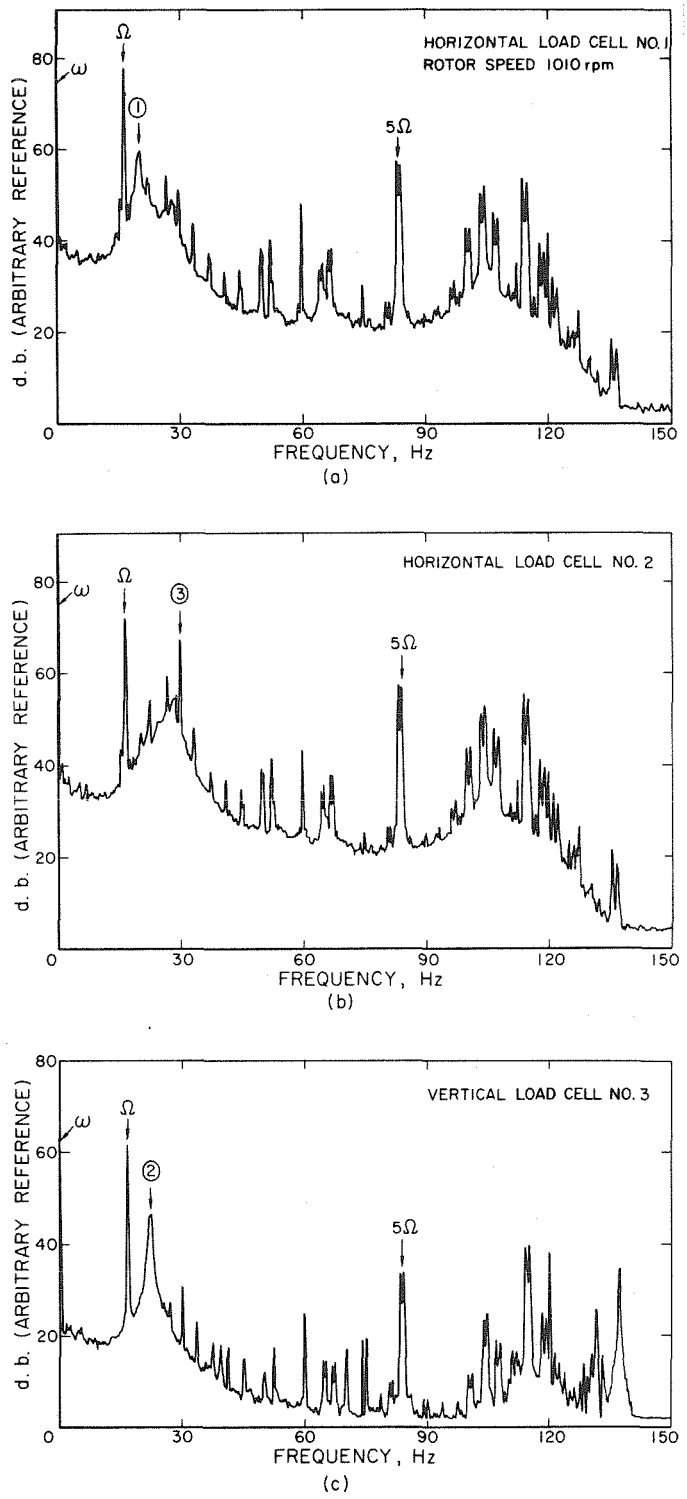

Fig. 4.3. Spectrum of a) horizontal load cell No. 1, b) horizontal load cell No. 2, and c) vertical load cell No. 3 for 0-150 Hz and for a rotor speed of 1010 rpm.

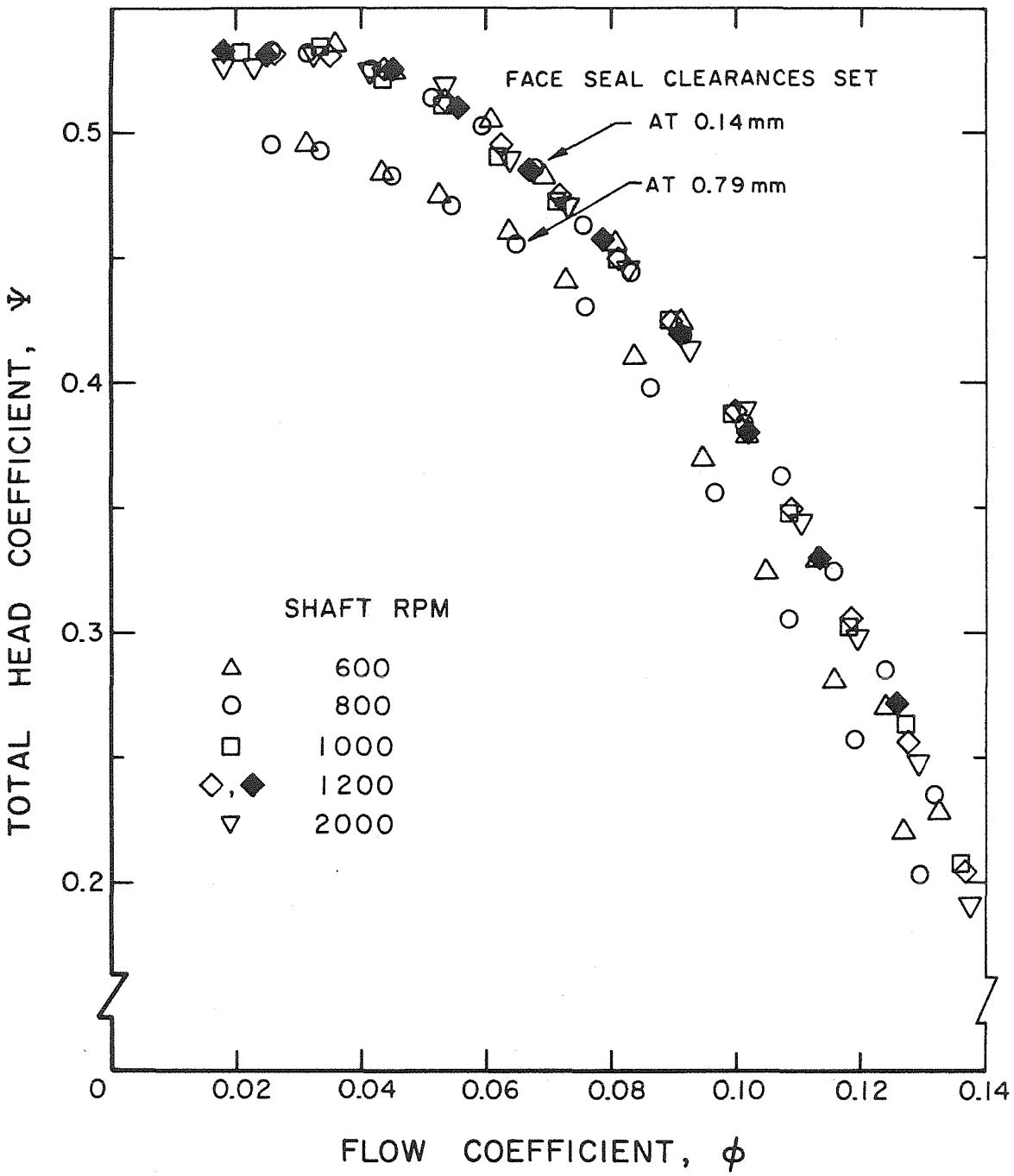

Fig. 4.4. Performance charcteristics of Impeller X inside Volute A for the front and back face seal clearances of 0.14 and 0.79 mm. Open and closed symbols represent data for $\omega > 0$ and $\omega < 0$ respectively.

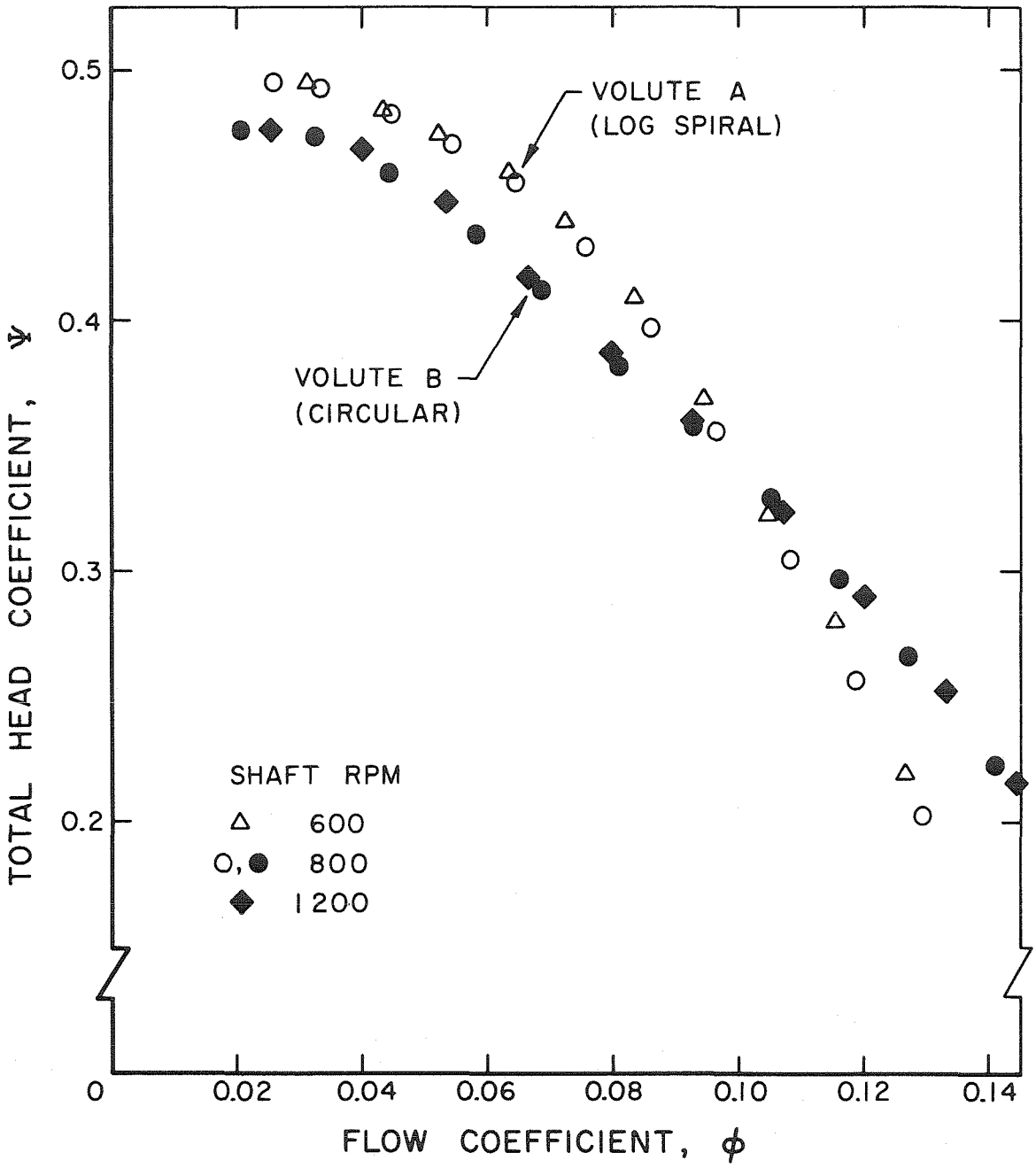

Fig. 4.5. Performance characteristics of Impeller X inside Volute A (open symbols) and Volute B (closed symbols) for the front and back face seal clearances of 0.79 mm.

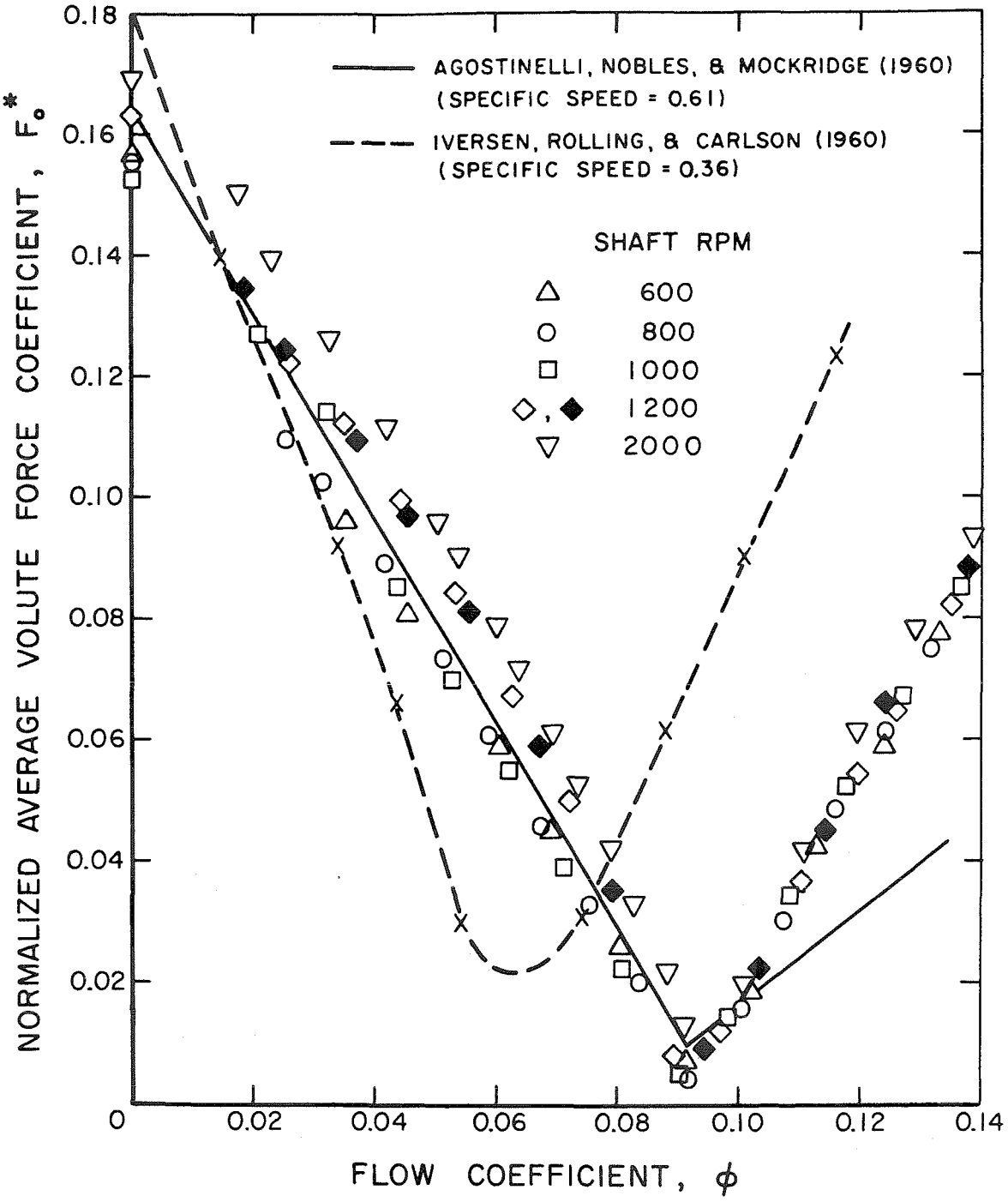

Fig. 4.6. Normalized average volute force for Impeller X, Volute A and face seal clearances of 0.14 mm. Open and closed symbols represent data for $\omega>0$ and $\omega<0$ respectively. Comparison is made with with Iversen et al [44] bearing reactions and Agostinelli et al [4] experimental data.

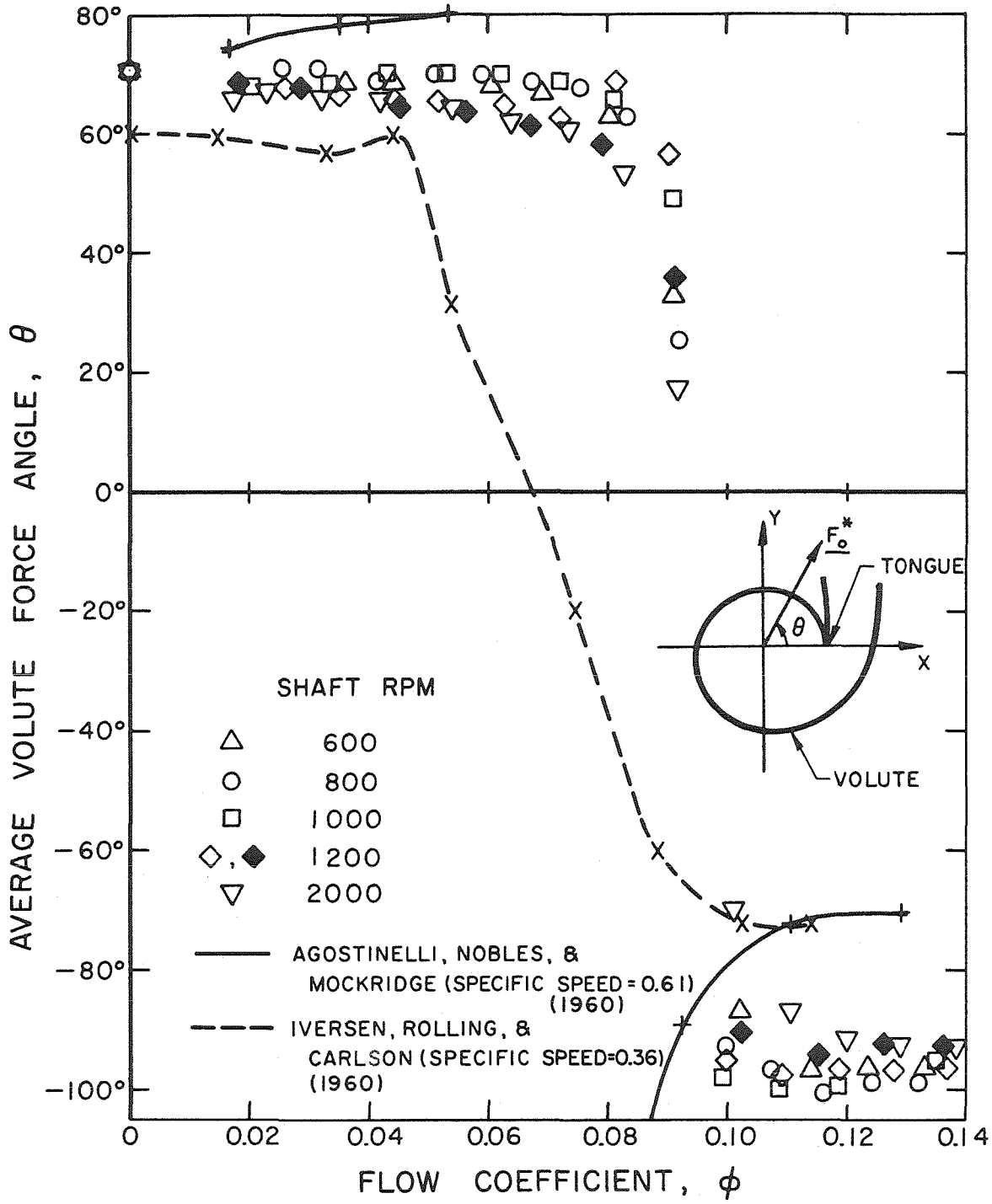

Fig. 4.7. Direction of average volute force plotted in Fig. 4.6 expressed in the volute coordinate system. θ is the angle between the direction of the average force and the line joining the center to the tongue of the volute. Open and closed symbols represent data for $\omega>0$ and $\omega<0$ respectively.

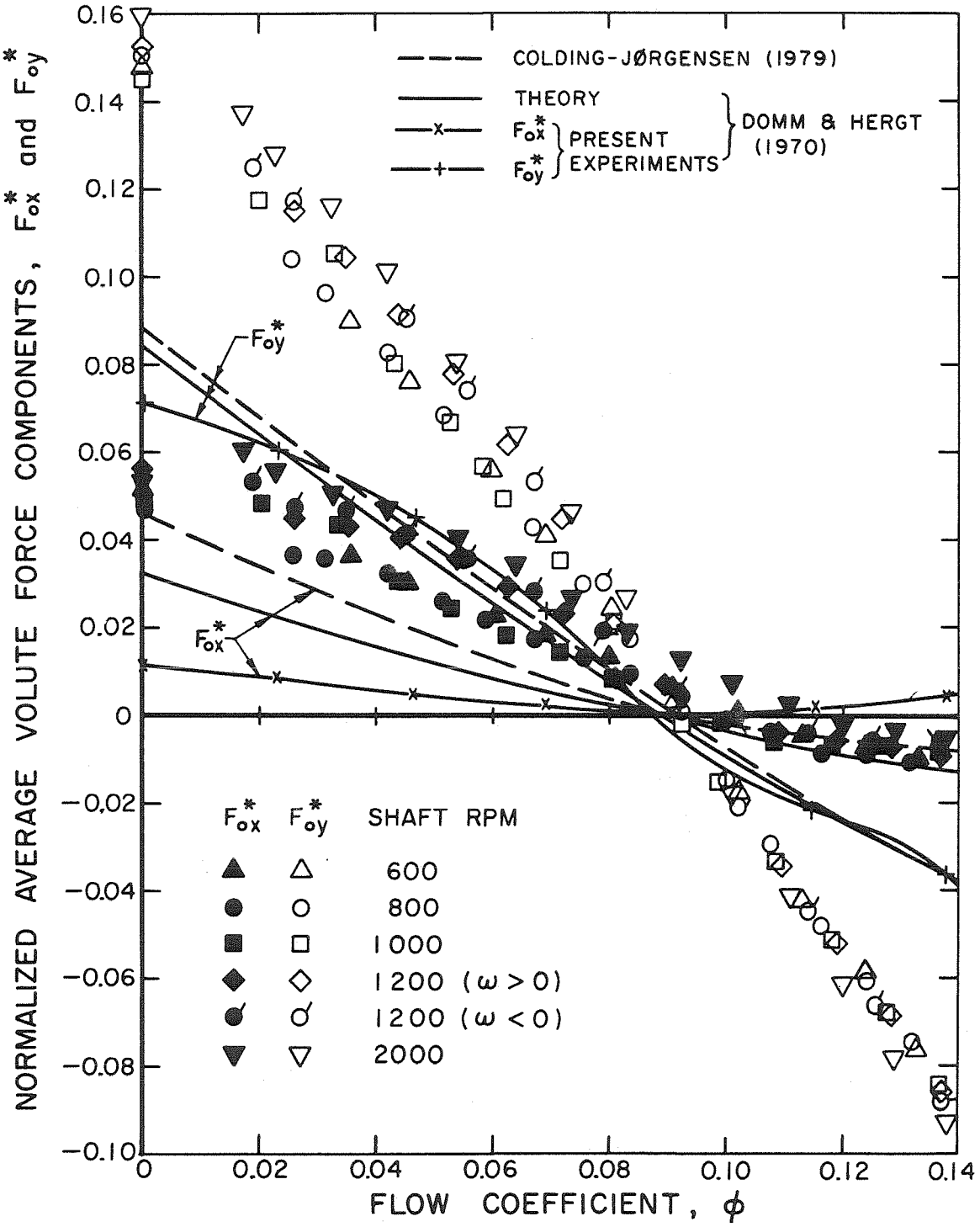

Fig. 4.8. Normalized average volute force components of Figs. 4.6 and 4.7 are shown along with the works of Domm and Hergt [33] and Colding-Jorgensen [29] having volute angles of 86.3° and 86° respectively. Impeller X, Volute A and face seal clearances of 0.14 mm.

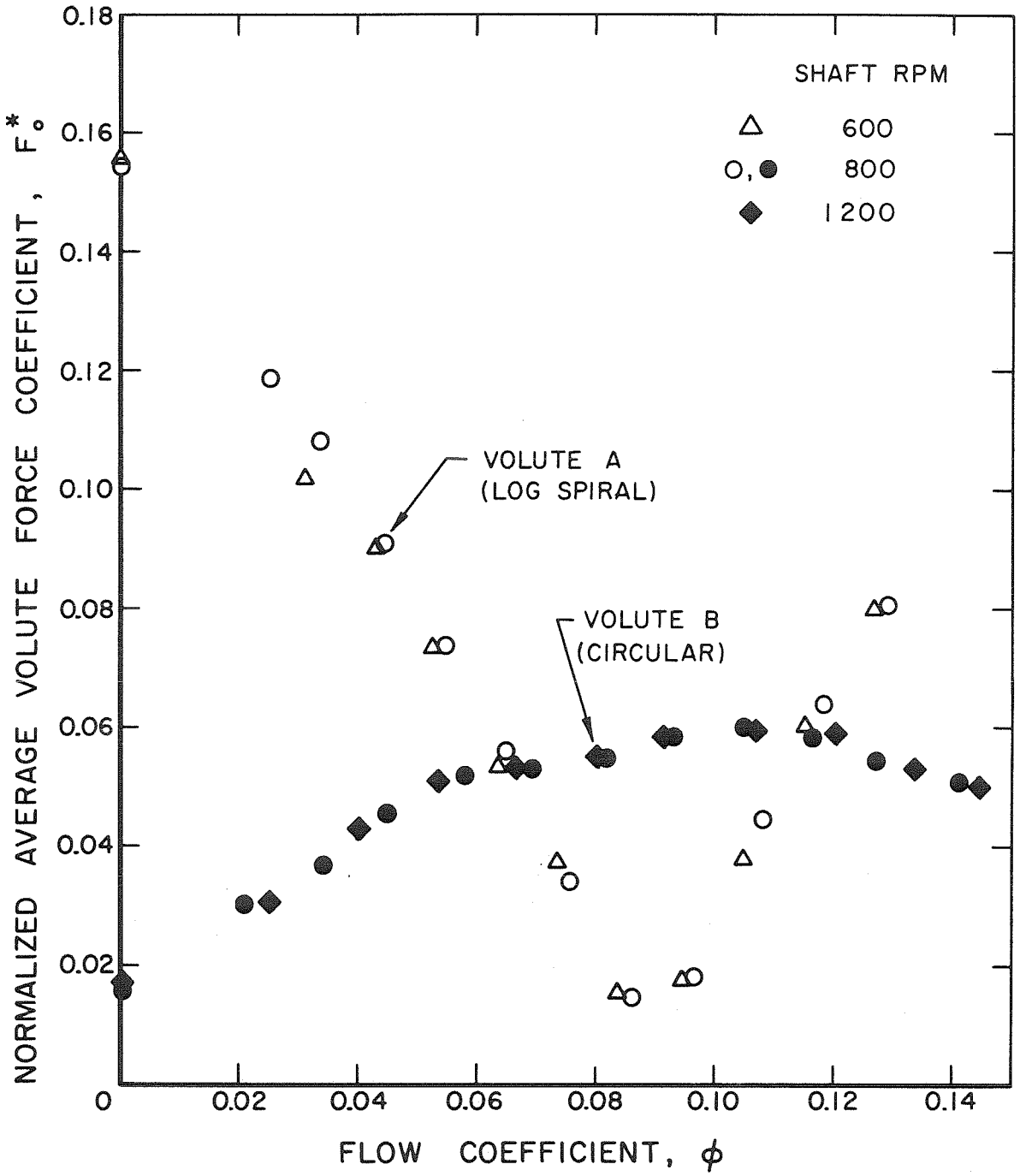

Fig. 4.9. Normalized average volute force for Impeller X and face seal clearances of 0.79 mm. Open and closed symbols represent data for Volutes A and B respectively.

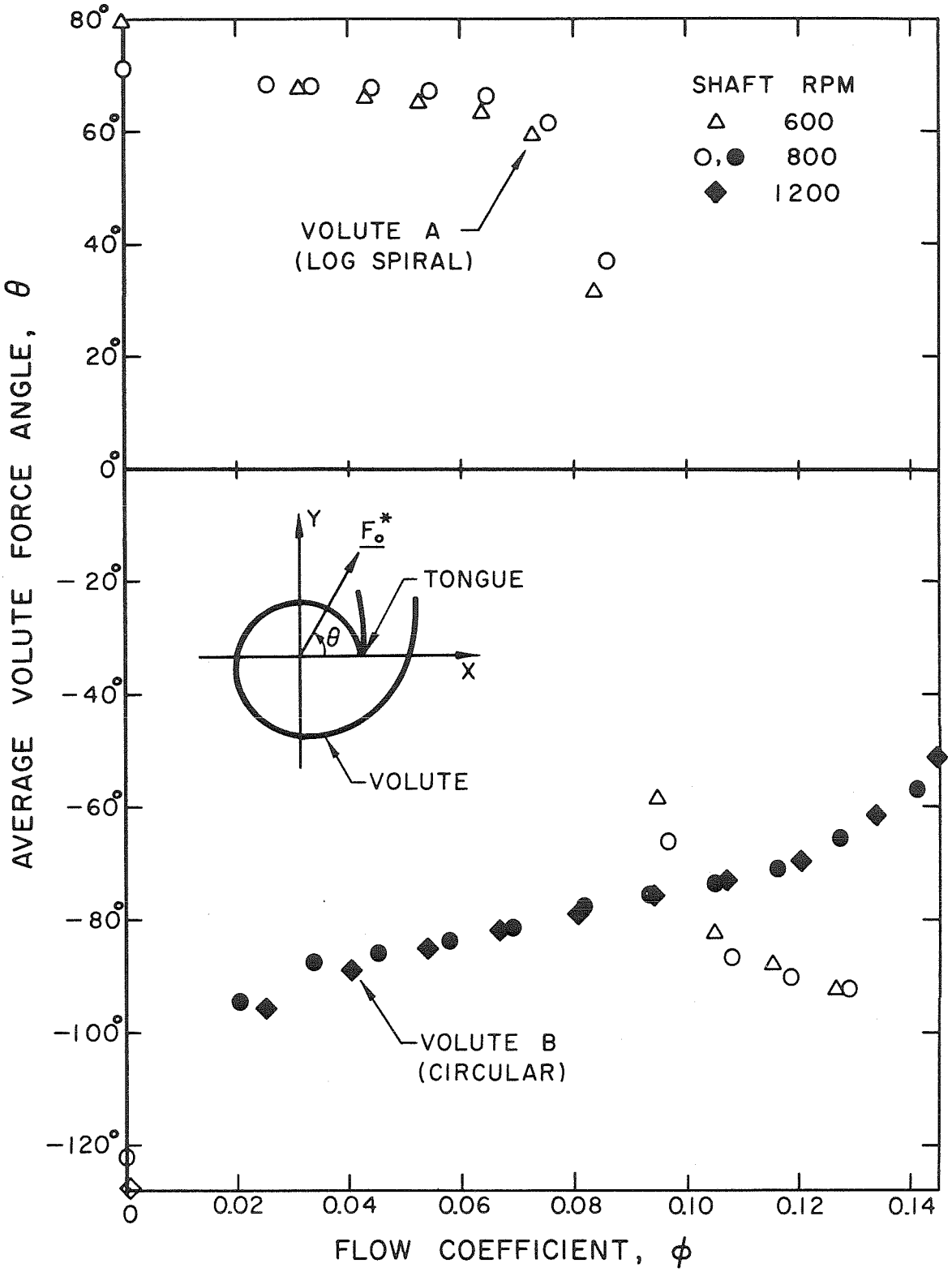

Fig. 4.10. Direction of average volute force of Fig. 4.9 expressed in Volute A coordinate system. Open and closed symbols represent data for Volutes A and B respectively.

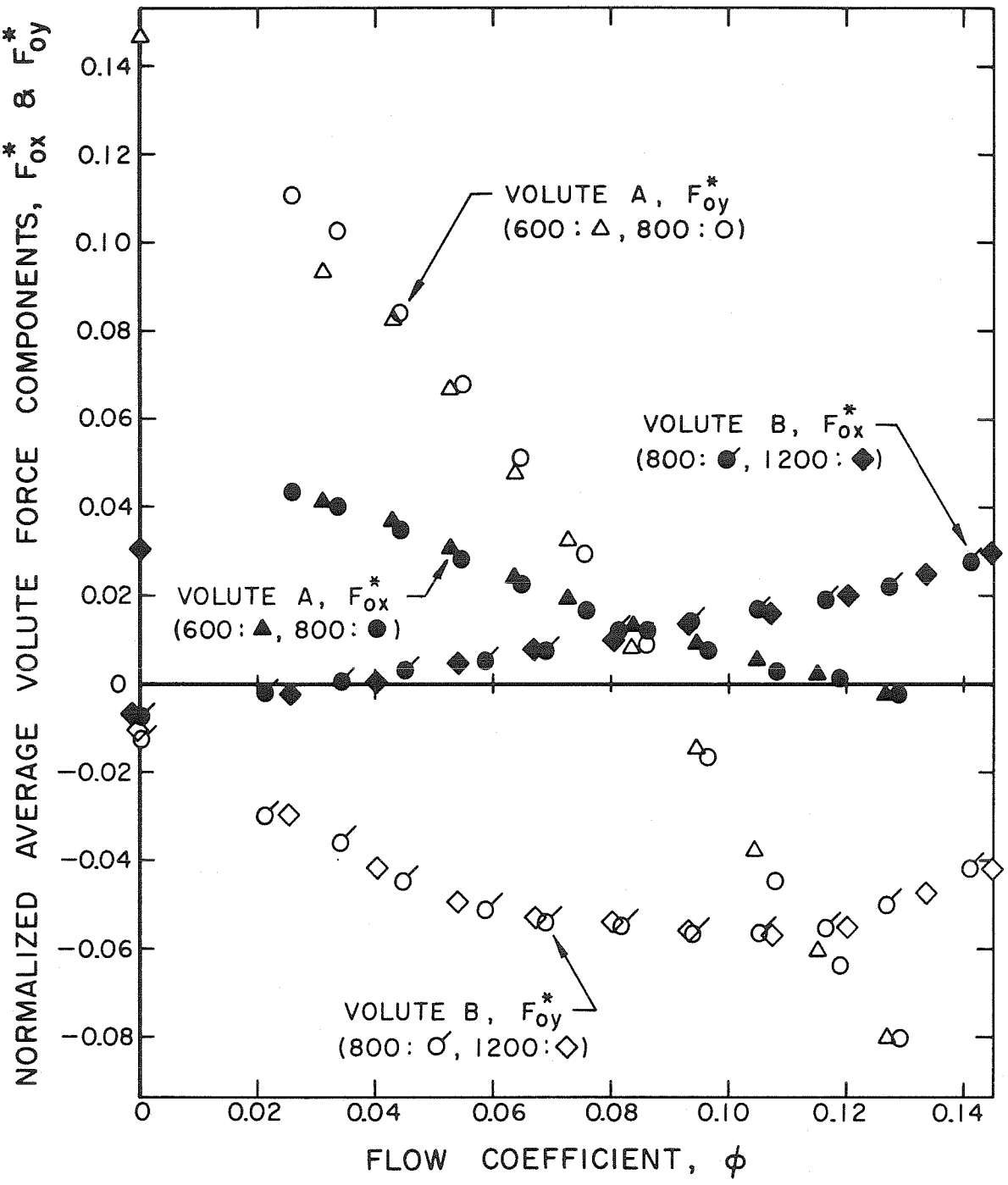

Fig. 4.11. Normalized average volute force components of Figs. 4.9 and 4.10 are shown for Impeller X, Volutes A and B and for face seal clearances of 0.79 mm. Rotor speeds in rpm and their corresponding symbols are shown in brackets.

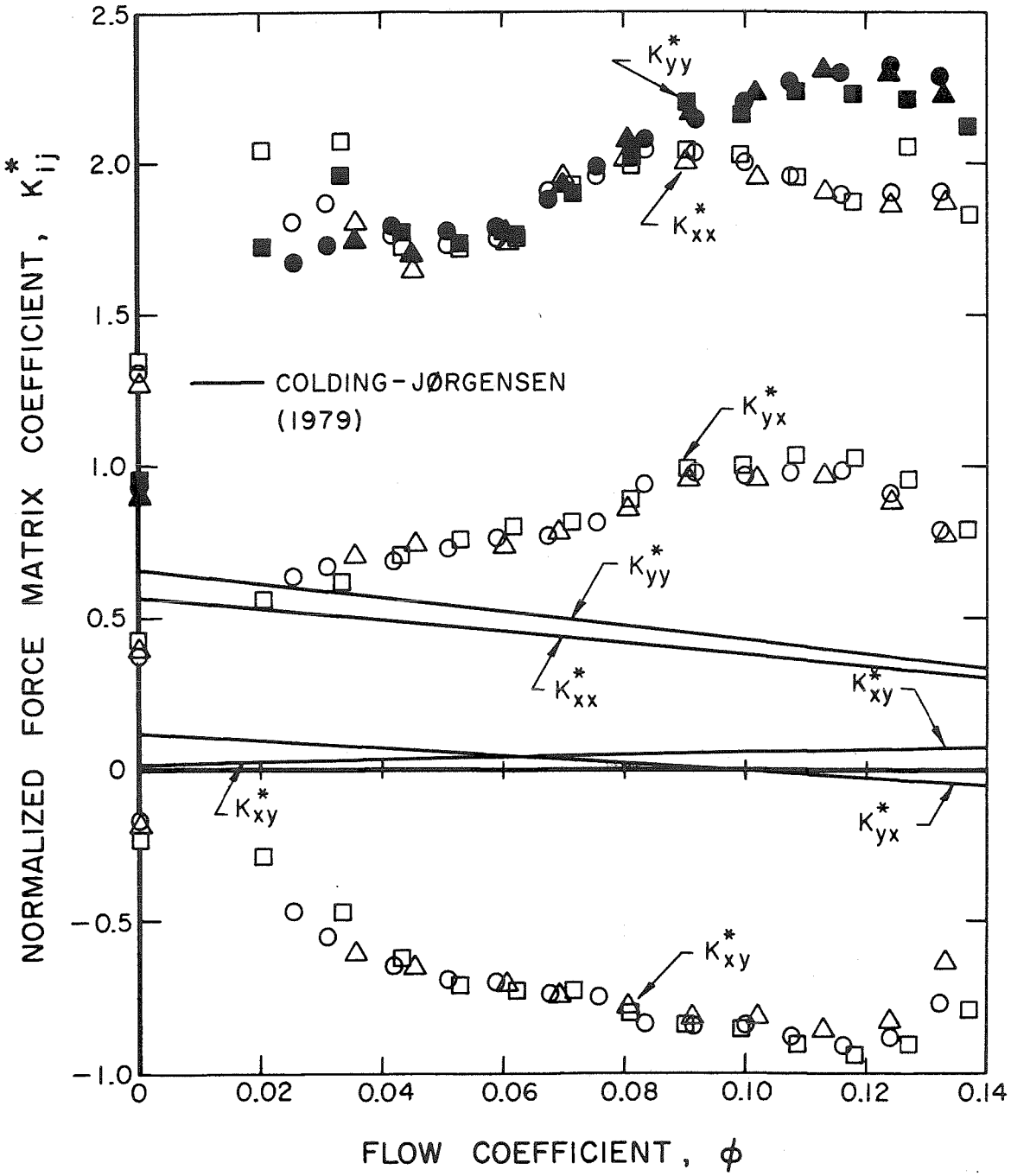

Fig. 4.12. Normalized force matrix coefficients as defined in text for Impeller X, Volute A and face seal clearances of 0.14 mm. Shaft speed = 600 rpm: △ ,▲; 800 rpm: ○,●; 1000 rpm: □,■. Values of K^*_{XX}, K^*_{XY} and K^*_{YX} are represented by open symbols; values of K^*_{YY} by closed symbols. Comparison is made with Colding-Jorgensen's [29] theoretical stiffness matrix calculations with a volute angle of 86°.

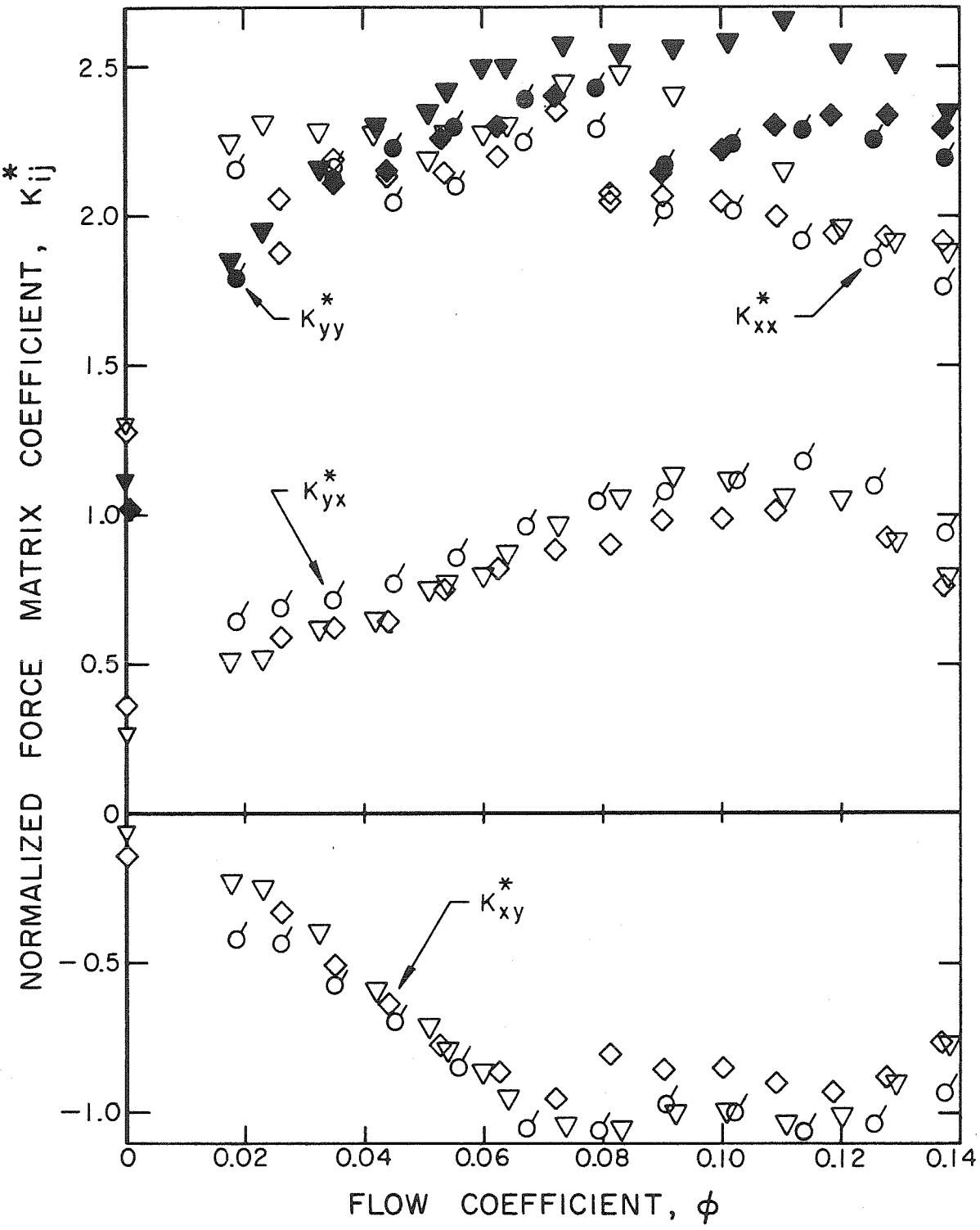

Fig. 4.13. Normalized force matrix coefficients as defined in text for Impeller X, Volute A and face seal clearances of 0.14 mm. Shaft speed = 1200 rpm ($\omega>0$):◇,◆; 1200 rpm ($\omega<0$):○,●; 2000 rpm:▽,▼. Values of K^*_{XX}, K^*_{XY} and K^*_{YX} are represented by open symbols; values of K^*_{YY} by closed symbols.

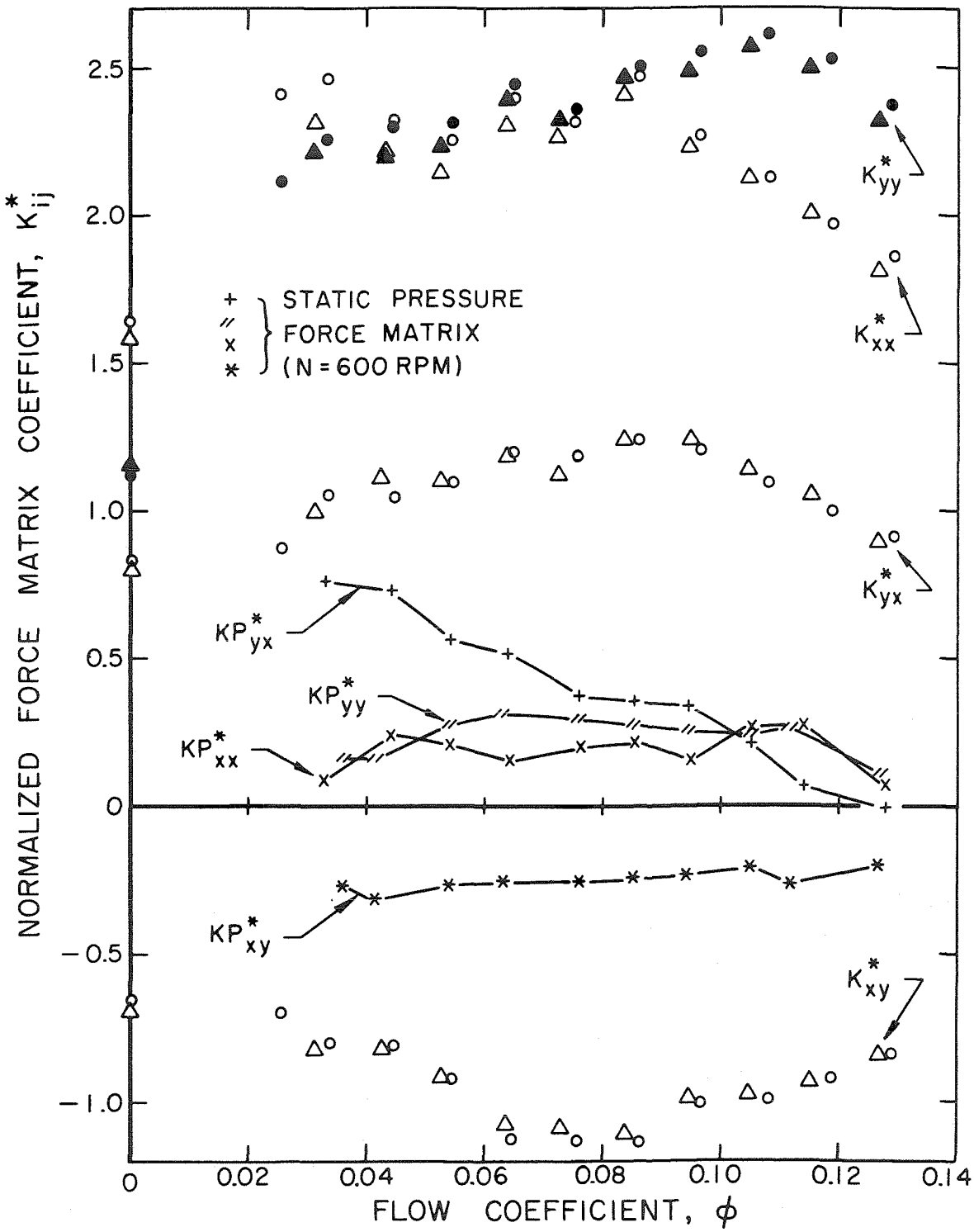

Fig. 4.14. Normalized force matrix coefficients as defined in text for Impeller X, Volute A and face seal clearances of 0.79 mm. Shaft speed = 600 rpm: △,▲; 800 rpm: ○,●. Values of K^*_{XX}, K^*_{XY} and K^*_{YX} are represented by open symbols; values of K^*_{YY} by closed symbols. The normalized static pressure force matrix for a shaft speed of 600 rpm is shown by the symbols +, //, X and ✳.

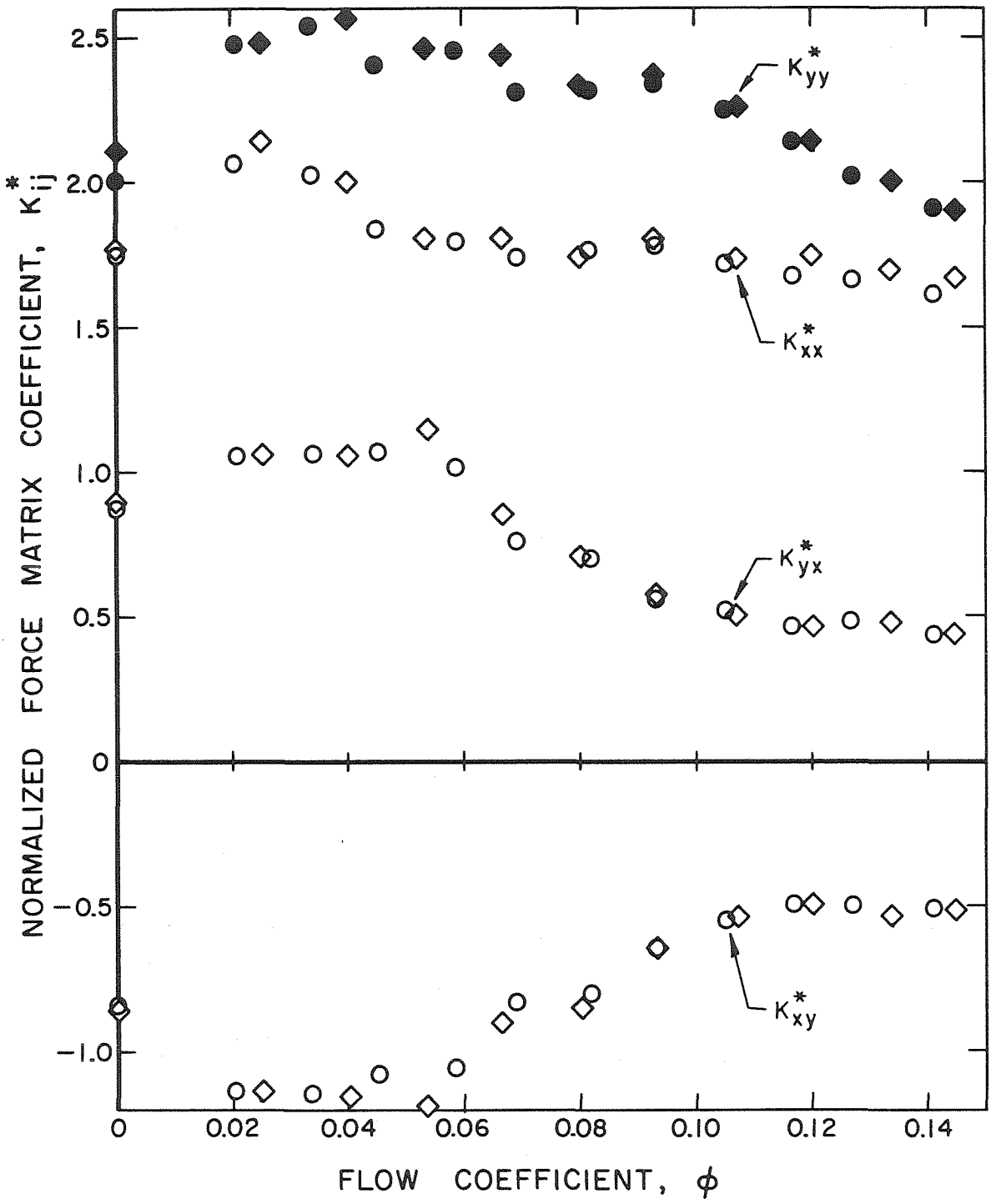

Fig. 4.15. Normalized force matrix coefficients as defined in text for Impeller X, Volute B and face seal clearances of 0.79 mm. Shaft speed = 800 rpm: ○,●; 1200 rpm:◇,◆. Values of K^*_{XX}, K^*_{XY} and K^*_{YX} are represented by open symbols; values of K^*_{YY} by closed symbols.

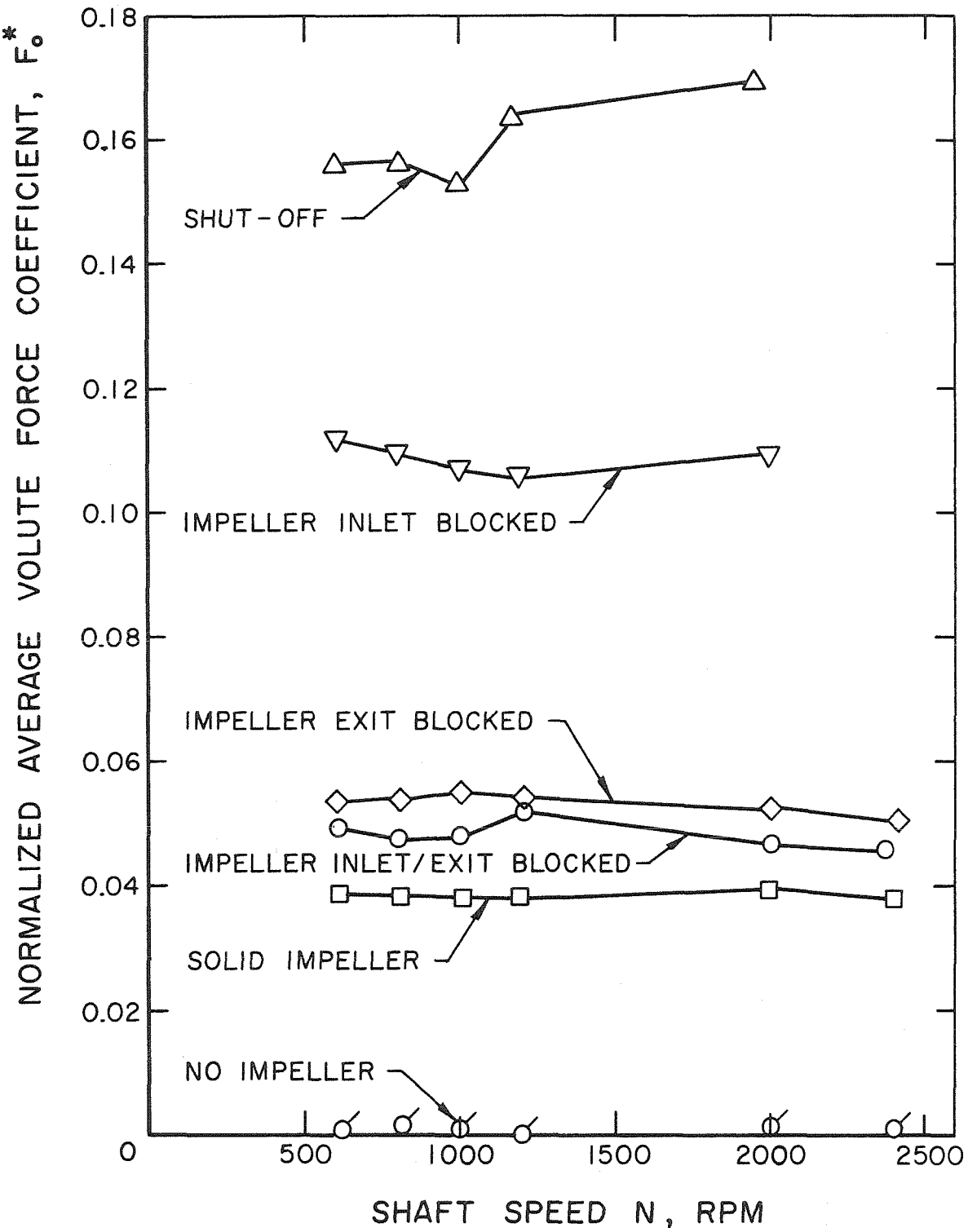

Fig. 4.16. The normalized average volute force is shown as a function of shaft speed for various auxiliary experiments conducted for Impeller X, Volute A and face seal clearances of 0.14 mm.

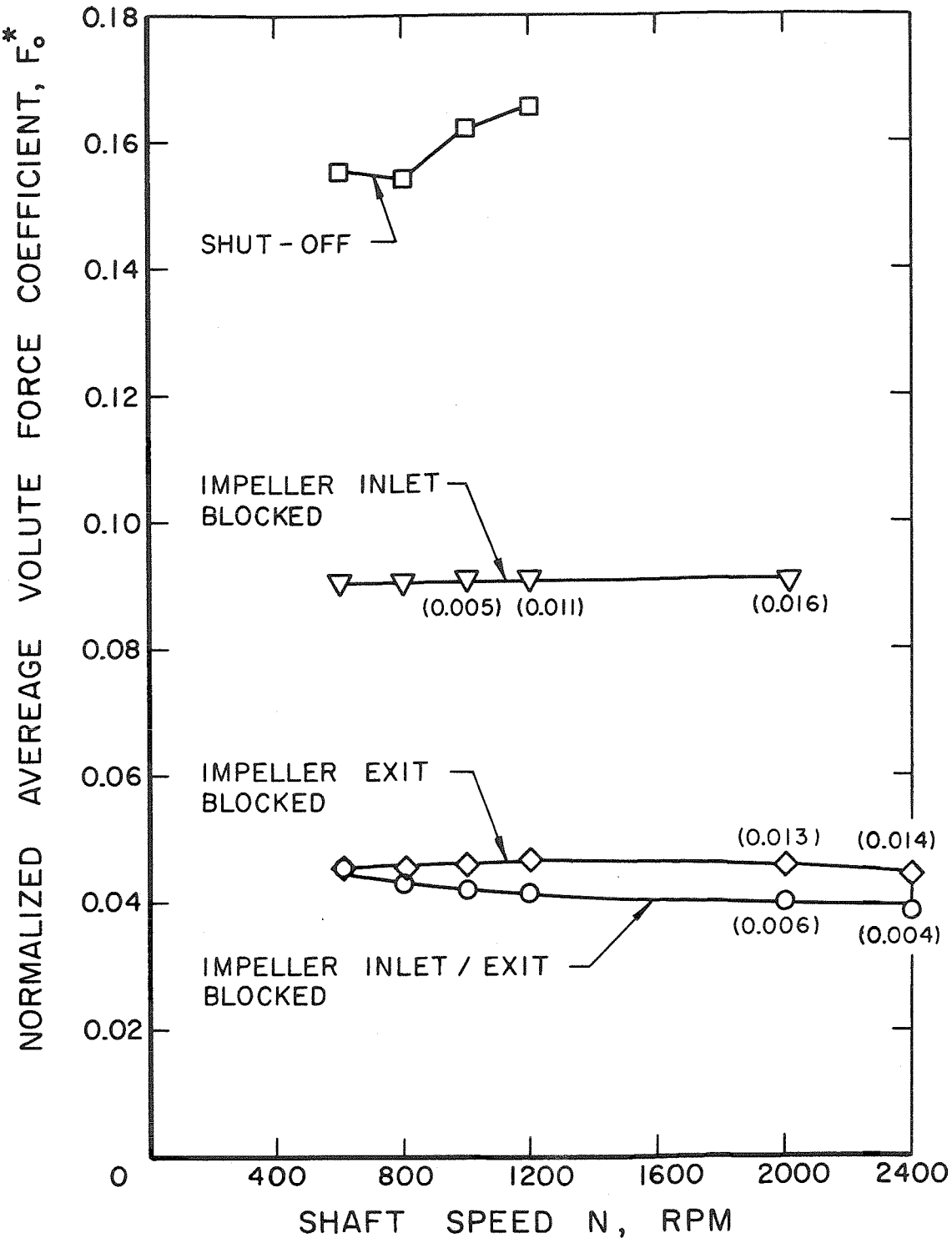

Fig. 4.17. The normalized average volute force is shown as a function of shaft speed for various auxiliary experiments conducted for Impeller X, Volute A and face seal clearances of 0.79 mm. Numbers in brackets represent flow coefficients when sufficient quantities of liquid flowing through the front and back face seal gaps could be detected in the pump loop.

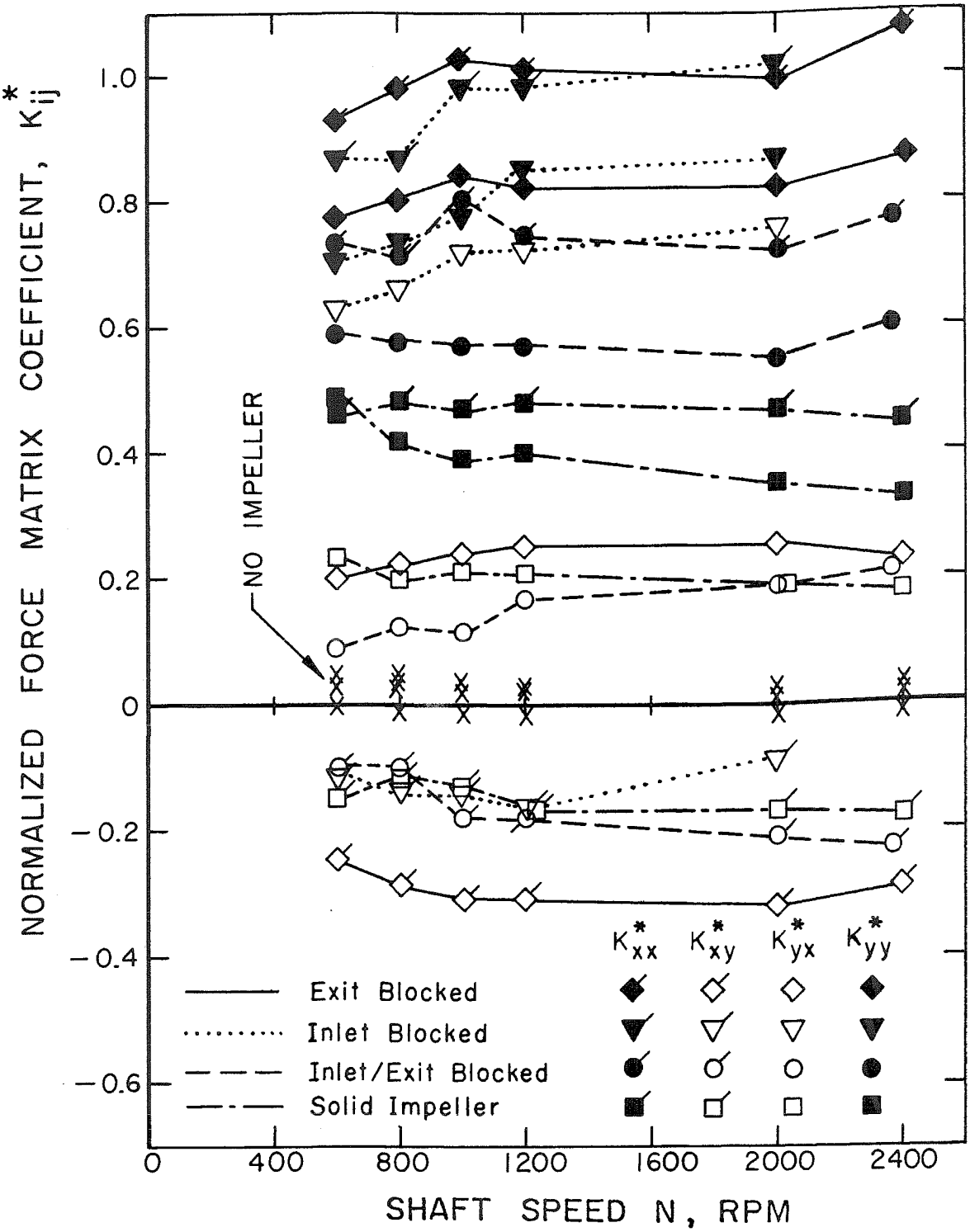

Fig. 4.18. Normalized force matrix coefficients as defined in text for the various auxiliary experiments described in Fig. 4.16 for Impeller X, Volute A and face seal clearances of 0.14 mm. The data when the impeller was removed are presented by the symbol x for any of the four normalized force matrix coefficients.

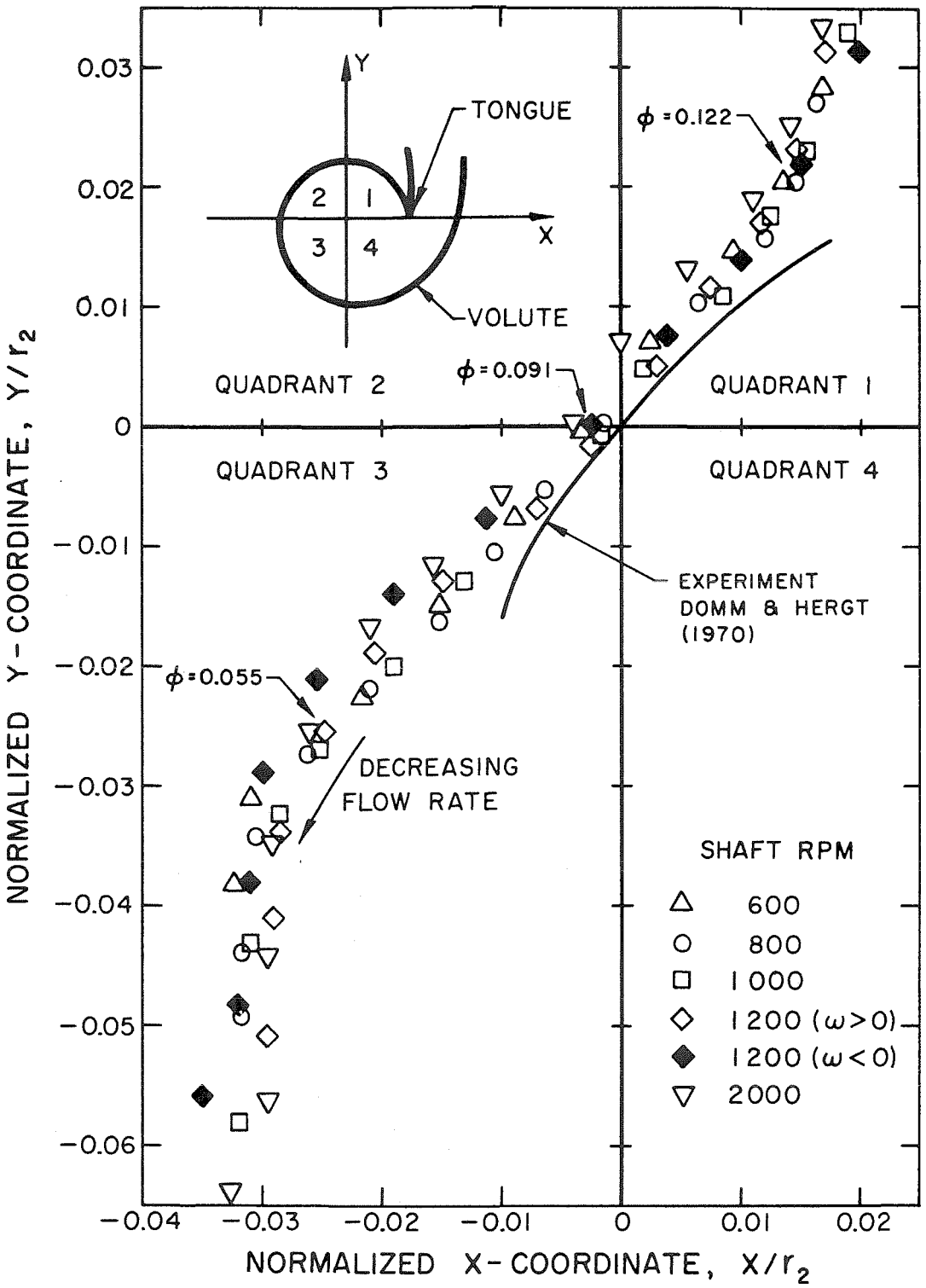

Fig. 4.19. Locus of equilibrium positions of Impeller X within Volute A for face seal clearances of 0.14 mm for various flow rates. Solid line indicates experimental data of Domm and Hergt [33] for a volute angle of 86.3°.

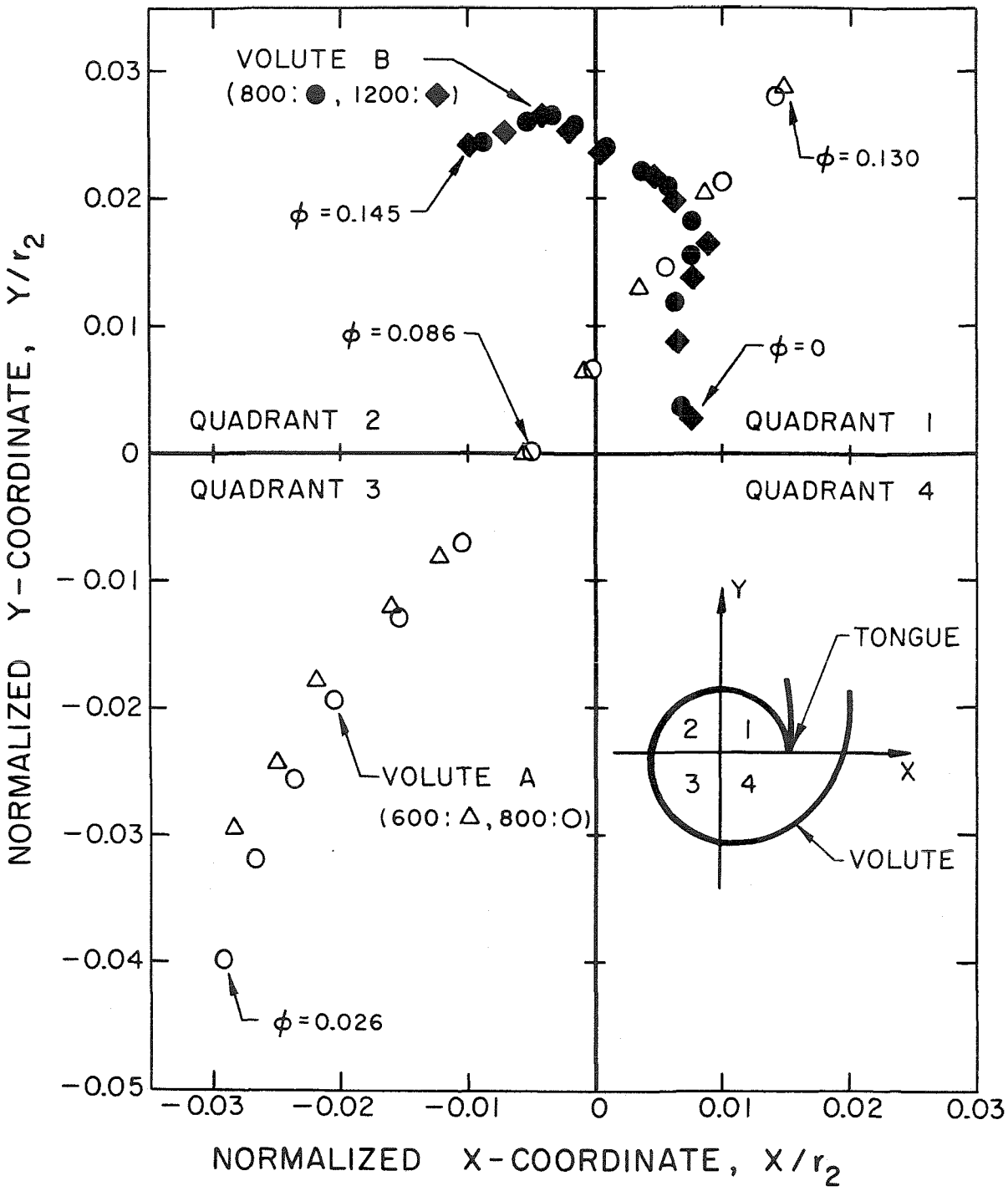

Fig. 4.20. Locus of equilibrium positions of Impeller X within Volutes A and B for face seal clearances of 0.79 mm and for various flow rates. Rotor speeds in rpm and their corresponding symbols are shown in brackets.

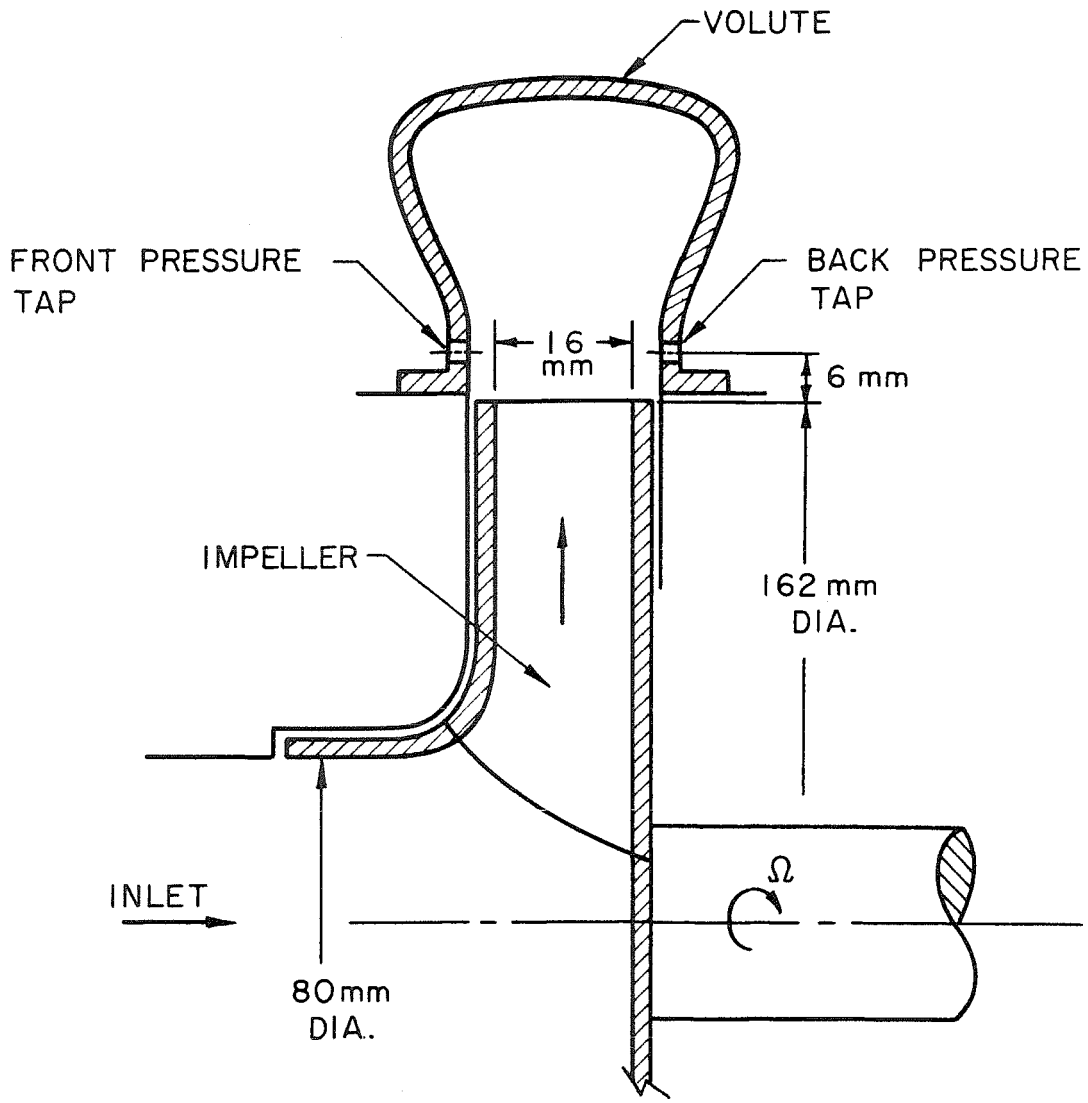

Fig. 4.21. Schematic showing main dimensions and static measurement points within Volute A. There are eight pressure taps more or less equally spaced around the volute circumference on the front and back.

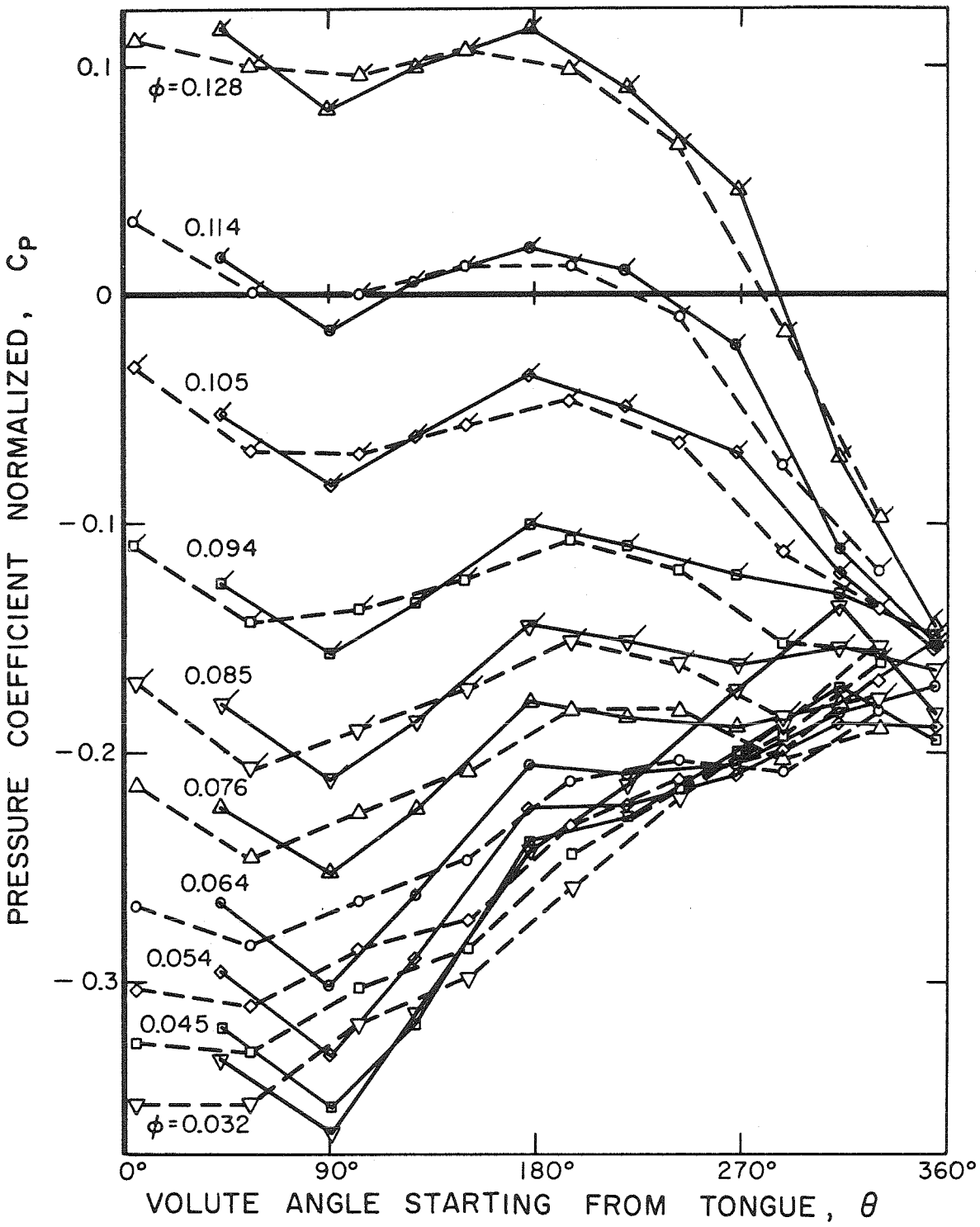

Fig. 4.22. Pressure coefficients for various flow rates for a rotor speed of 600 rpm. Impeller X, Volute A and face seal clearances of 0.79 mm. The shaft center position is at the "closest" point as defined by Fig. 3.3. Solid lines represent the front pressure taps and dashed lines the back pressure taps of Fig. 4.21.

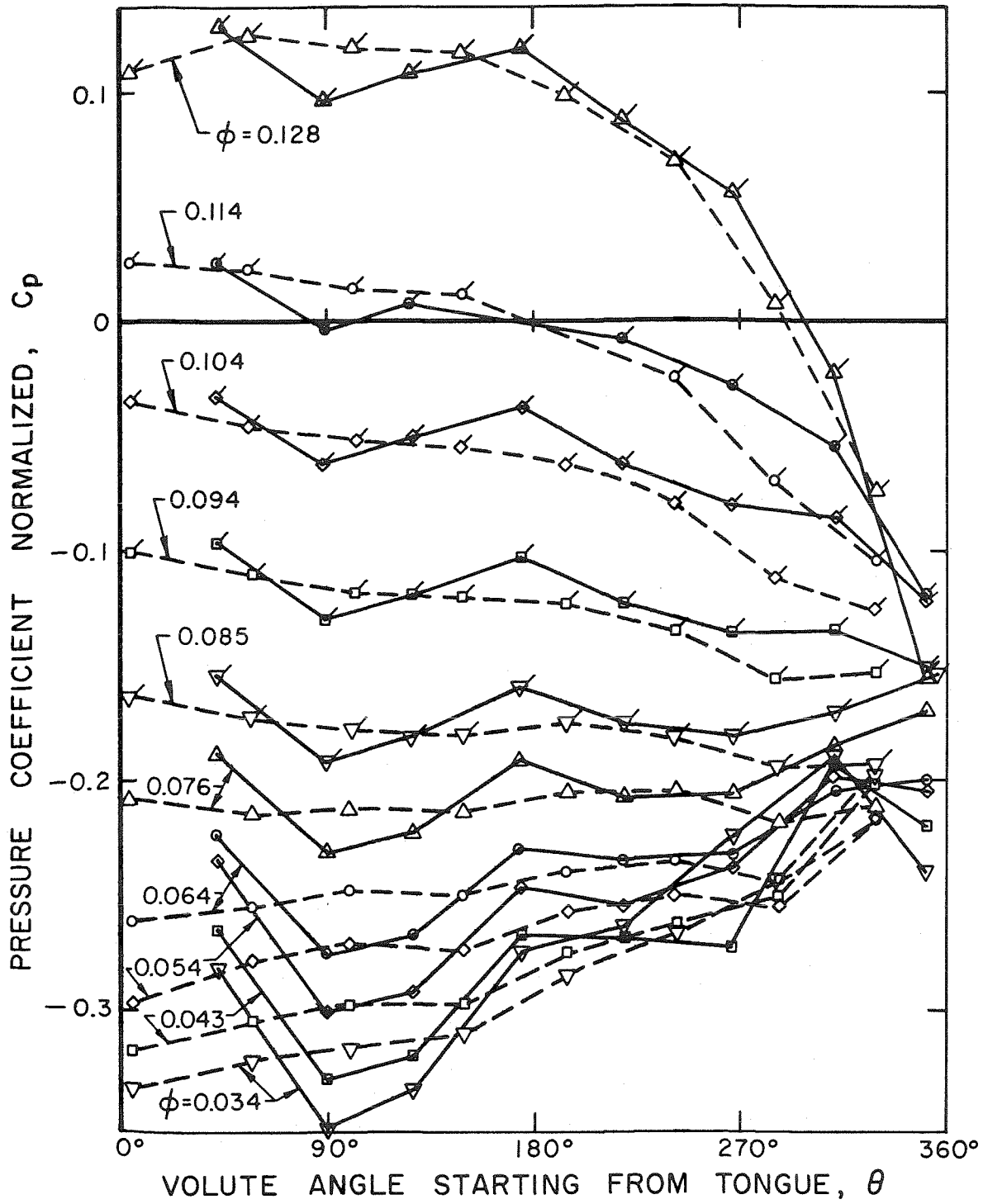

Fig. 4.23. Pressure coefficients for various flow rates for a rotor speed of 600 rpm. Impeller X, Volute A and face seal clearances of 0.79 mm. The shaft center position is at the "farthest" point as defined by Fig. 3.3. Solid lines represent the front pressure taps and dashed lines the back pressure taps of Fig. 4.21.

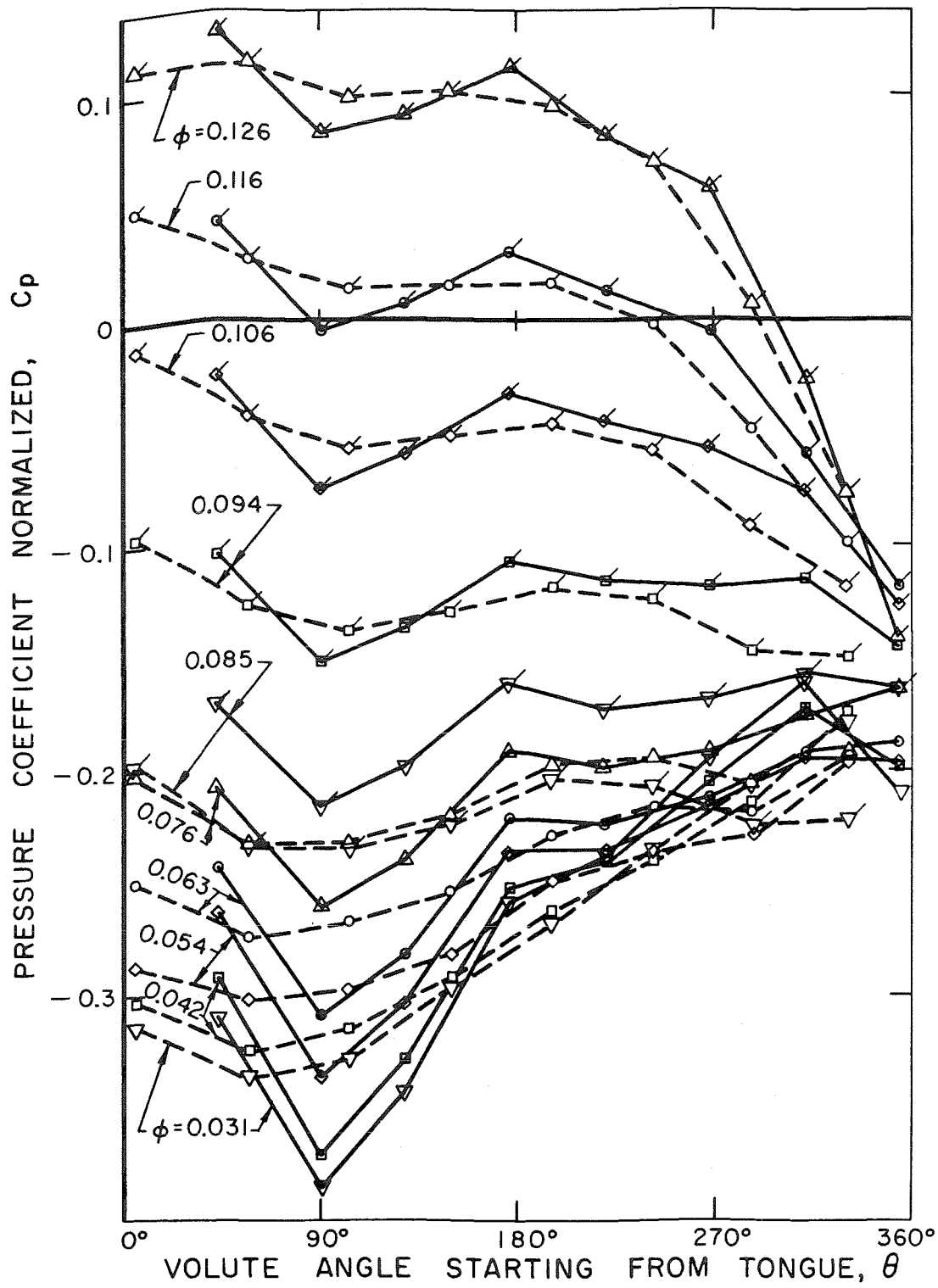

Fig. 4.24 Pressure coefficients for various flow rates for a rotor speed of 600 rpm. Impeller X, Volute A and face seal clearances of 0.79 mm. The shaft center position is at the "right" point as defined by Fig. 3.3. Solid lines represent the front pressure taps and dashed lines the back pressure taps of Fig. 4.21.

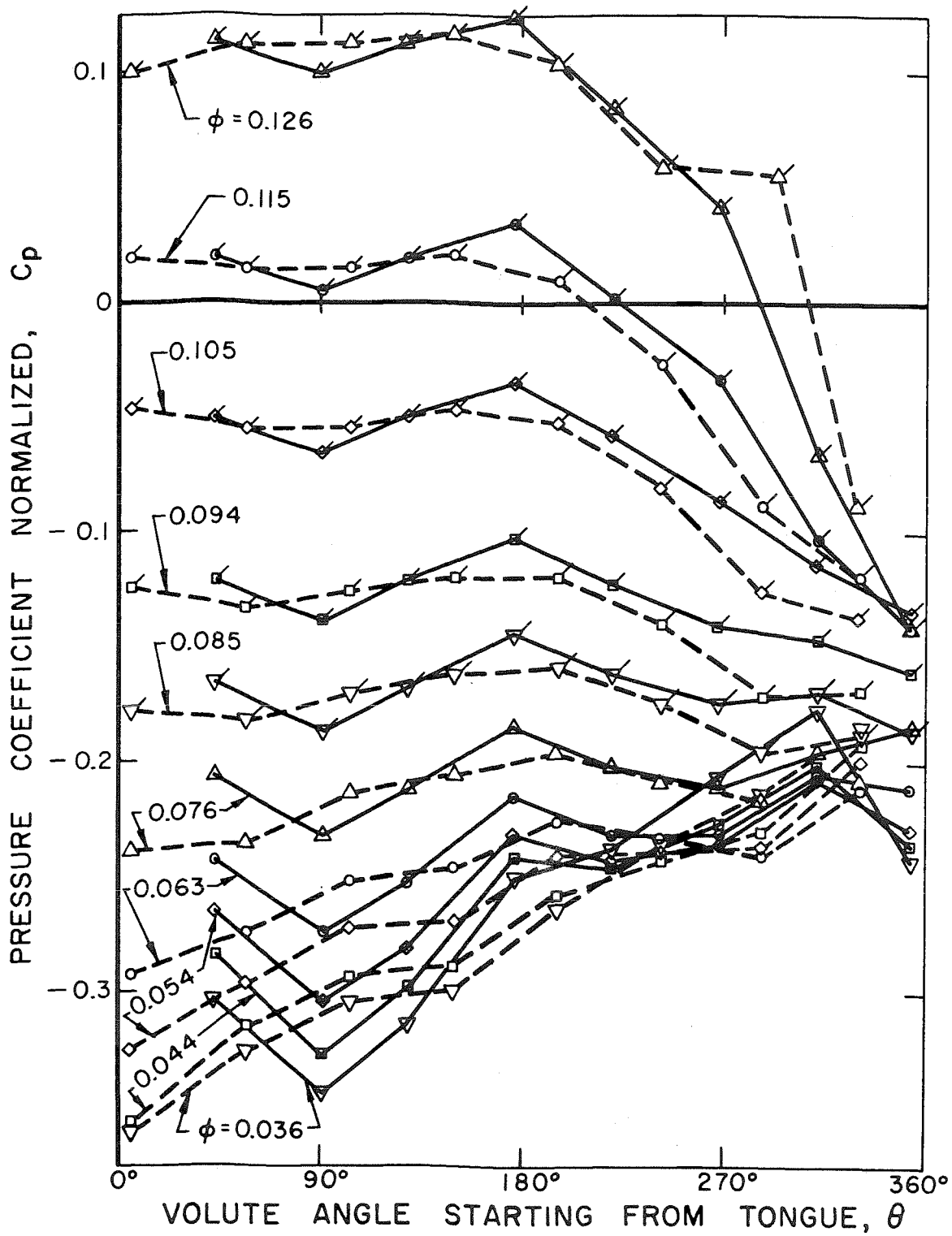

Fig. 4.25. Pressure coefficients for various flow rates for a rotor speed of 600 rpm. Impeller X, Volute A and face seal clearances of 0.79 mm. The shaft center position is at the "left" point as defined by Fig. 3.3. Solid lines represent the front pressure taps and dashed lines the back pressure taps of Fig. 4.21.

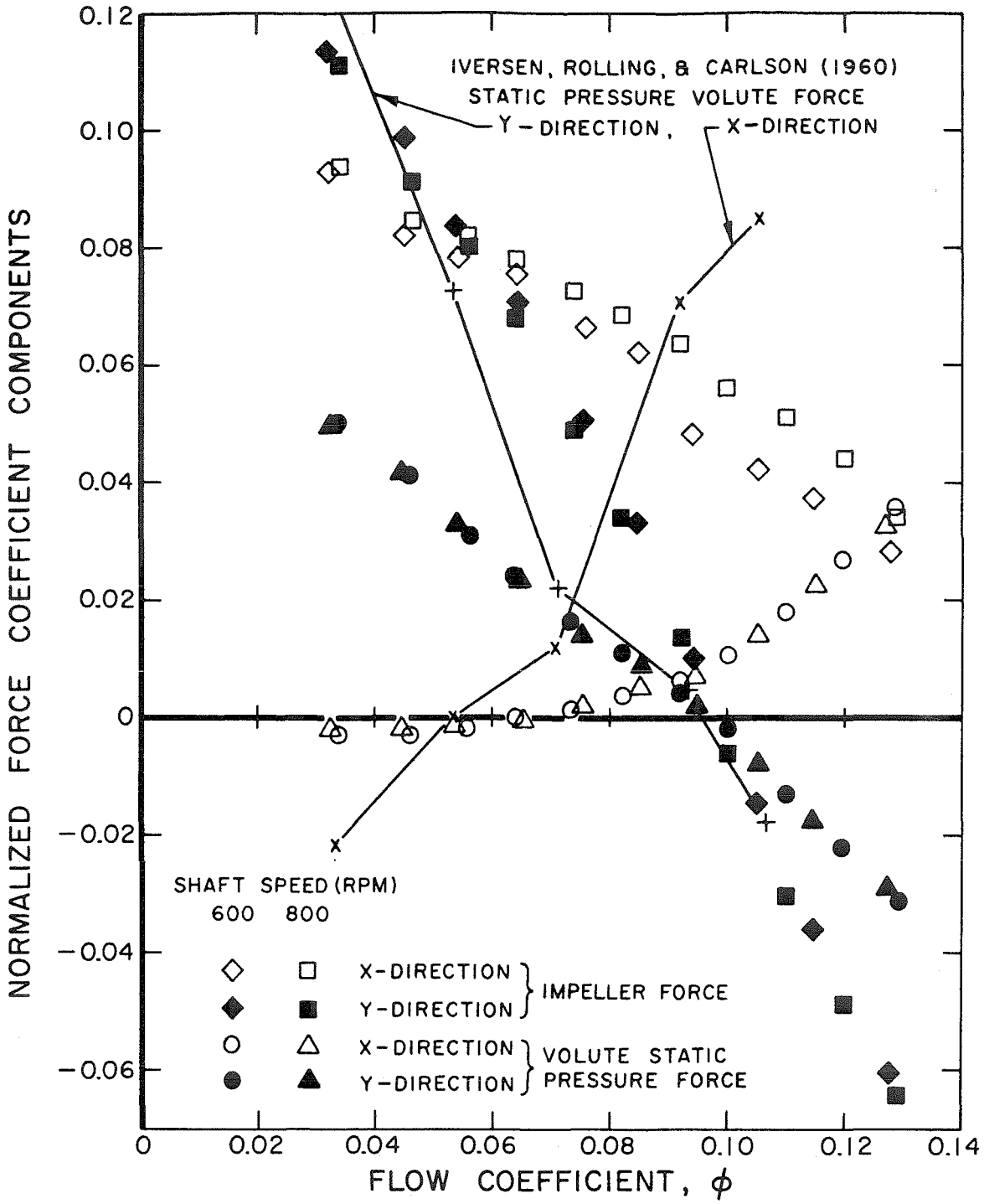

Fig. 4.26. Normalized impeller forces and static pressure forces of Fig. 4.22 for rotor speeds of 600 and 800 rpm for Impeller X, Volute A and face seal clearances of 0.79 mm. The shaft center position is at the "closest" point as defined by Fig. 3.3. Comparison is made with Iversen et al [44] static pressure volute forces.

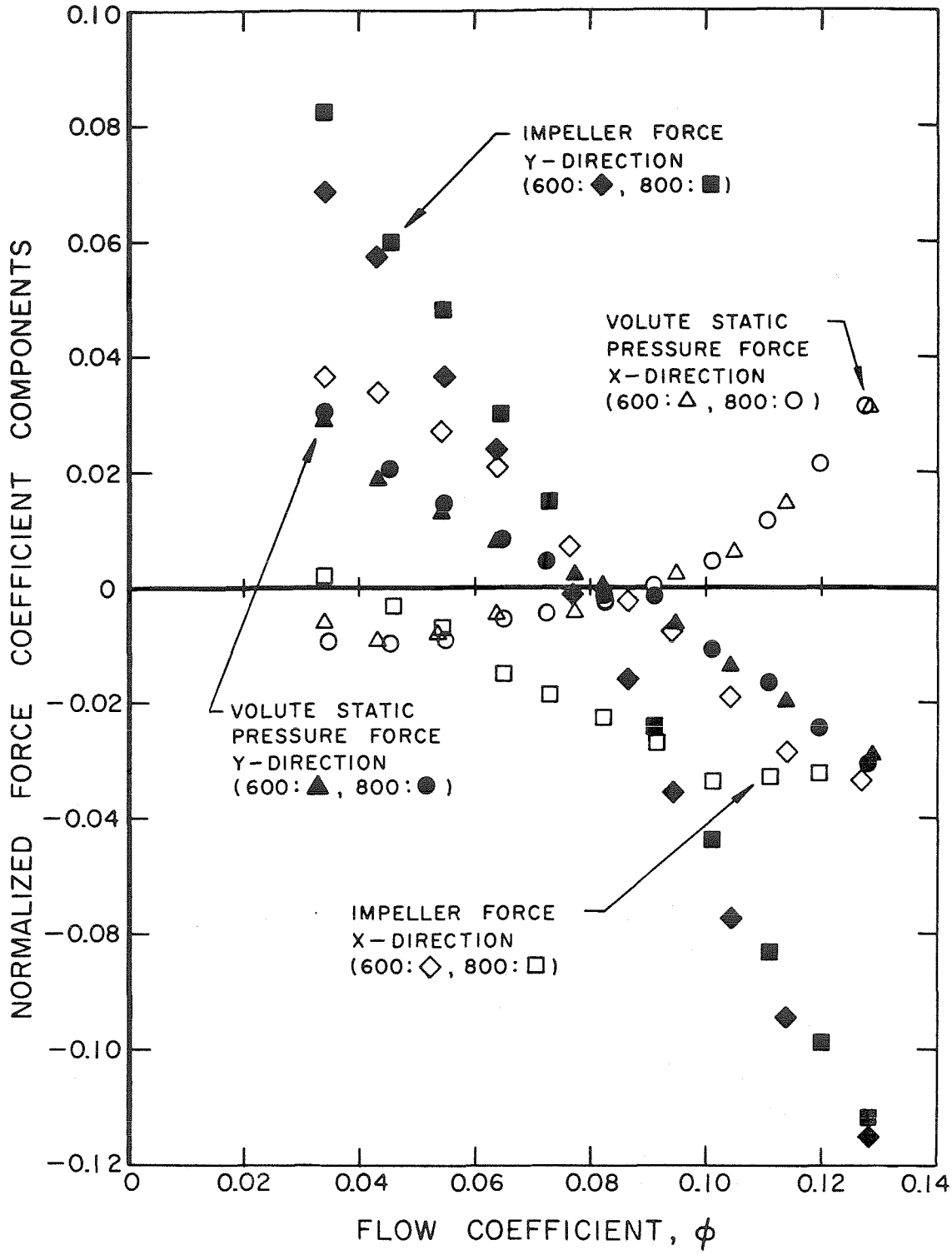

Fig. 4.27. Normalized impeller forces and static pressure forces of Fig. 4.23 for rotor speeds of 600 and 800 rpm for Impeller X, Volute A and face seal clearances of 0.79 mm. The shaft center position is at the "farthest" point as defined by Fig. 3.3. Rotor speeds in rpm and their corresponding symbols are shown in brackets.

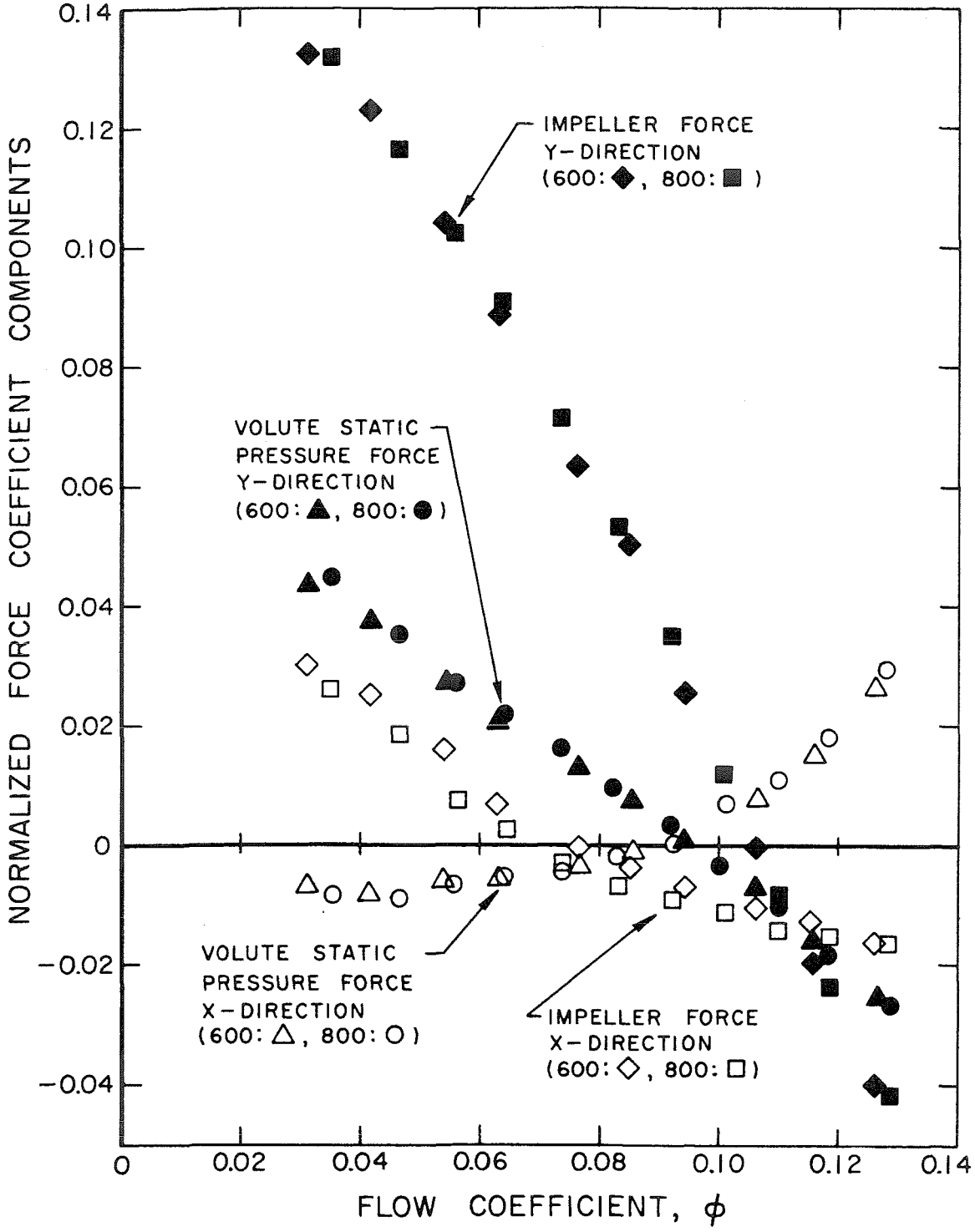

Fig. 4.28. Normalized impeller forces and static pressure forces of Fig. 4.24 for rotor speeds of 600 and 800 rpm for Impeller X, Volute A and face seal clearances of 0.79 mm. The shaft center position is at the "right" point as defined by Fig. 3.3. Rotor speeds in rpm and their corresponding symbols are shown in brackets.

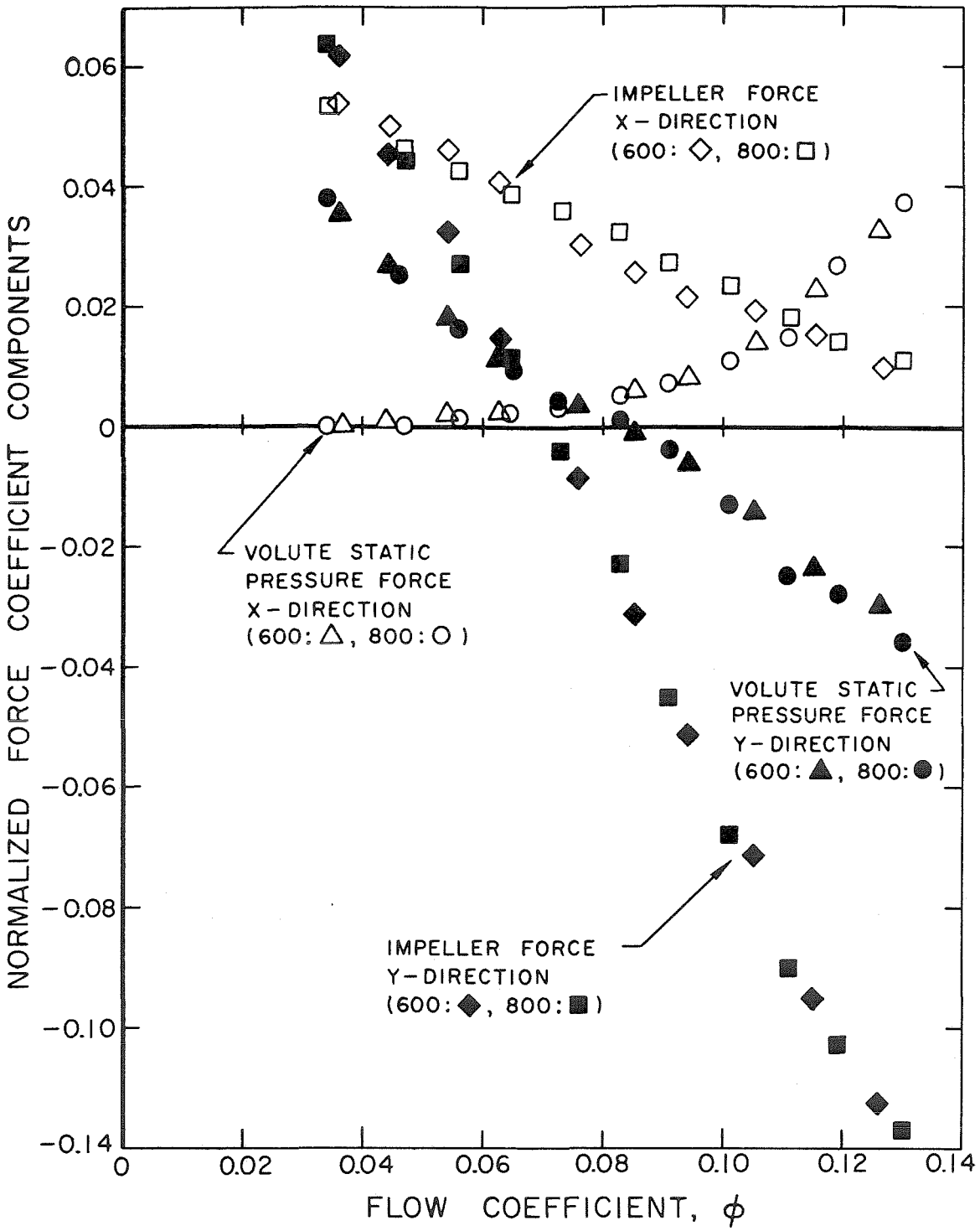

Fig. 4.29. Normalized impeller forces and static pressure forces of Fig. 4.25 for rotor speeds of 600 and 800 rpm for Impeller X, Volute A and face seal clearances of 0.79 mm. The shaft center position is at the "left" point as defined by Fig. 3.3. Rotor speeds in rpm and their corresponding symbols are shown in brackets.

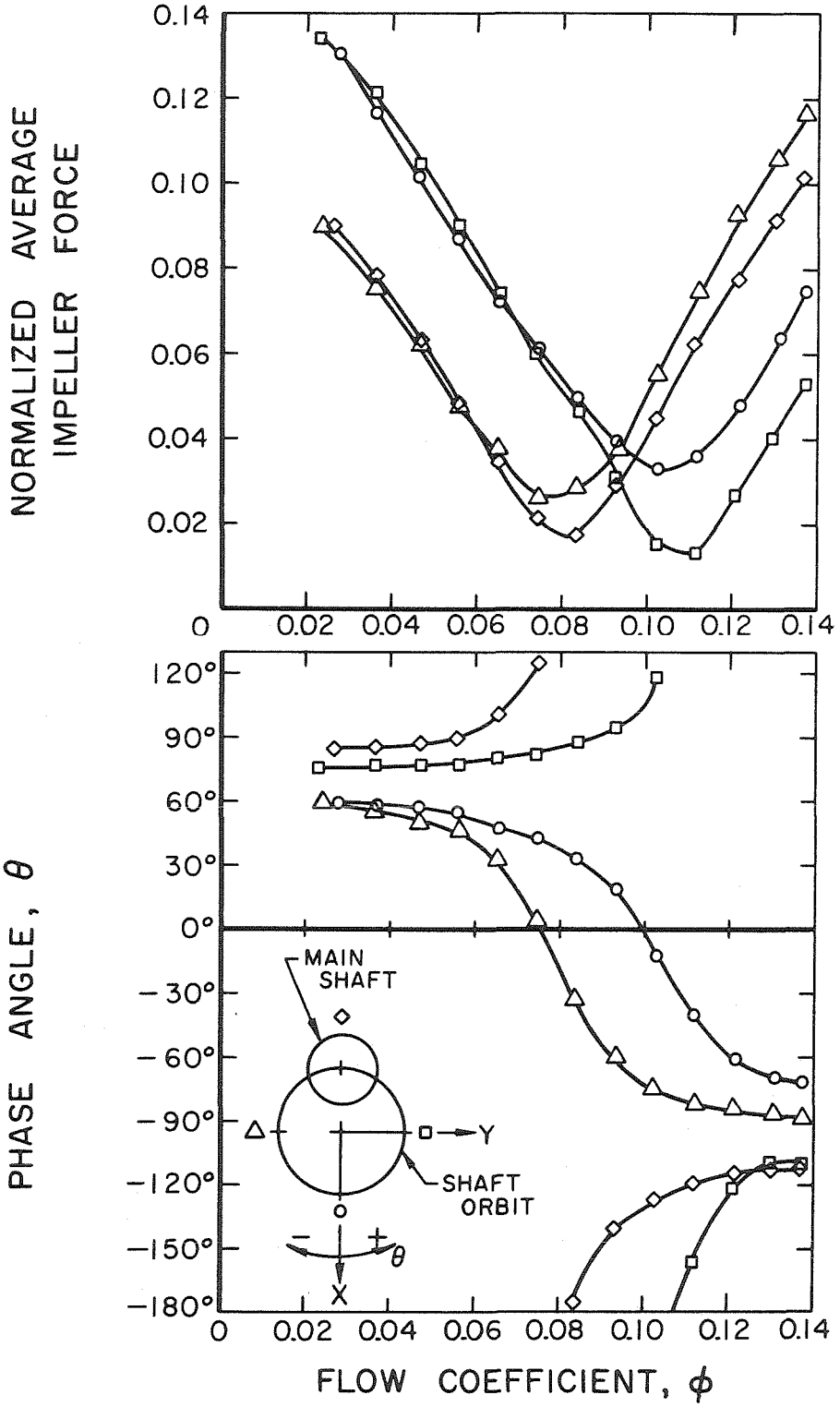

Fig. 4.30. Magnitudes and phase angles of normalized average impeller forces for four eccentric positions defined in Fig. 3.3. (closest: ○; farthest: ◇; right: □; left: △). Impeller X, Volute A, face seal clearances of 0.14 mm and rotor speed of 1000 rpm.

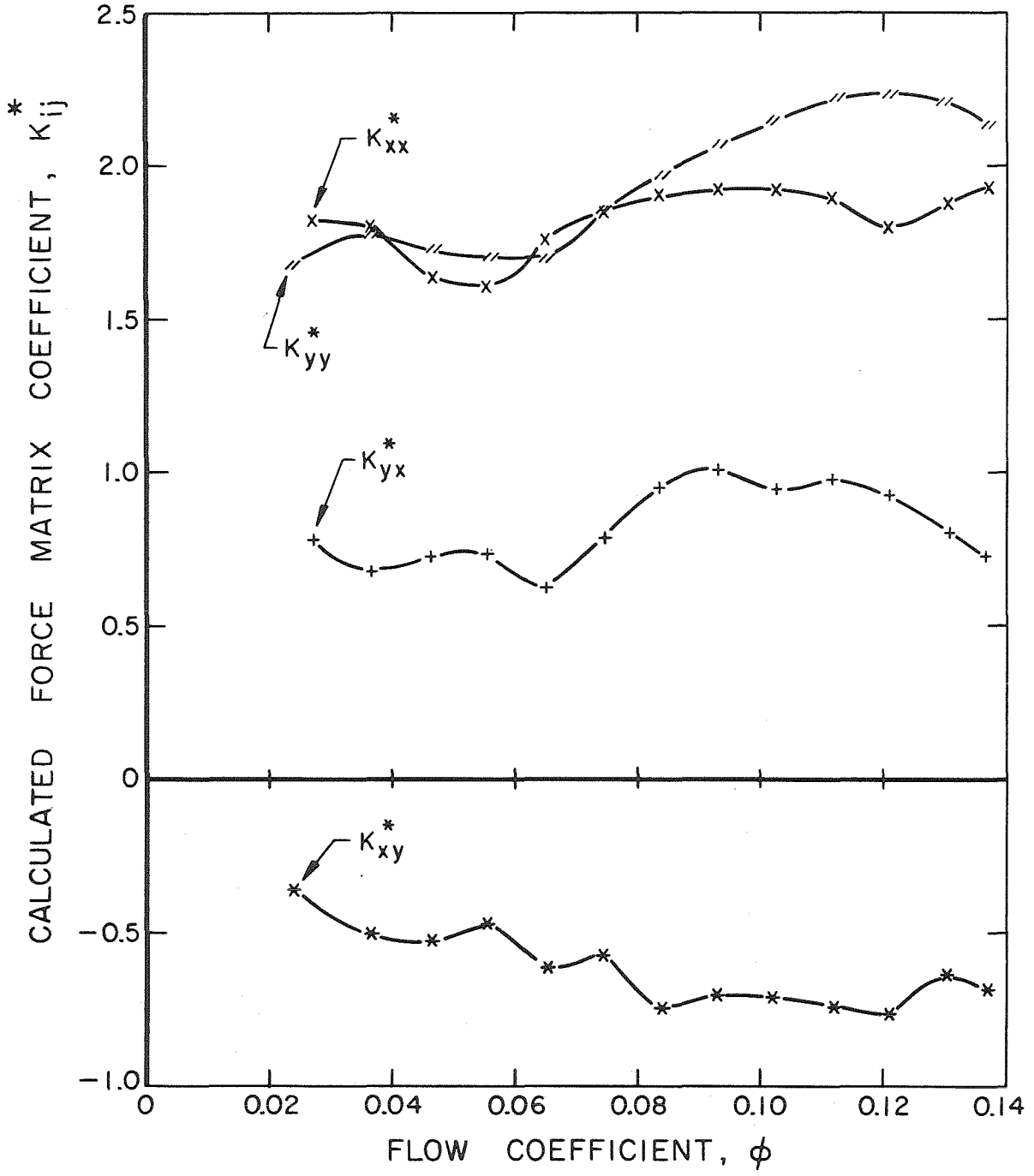

Fig. 4.31. Calculated normalized force matrix coefficients as defined by Eq. 4.4 in text using the volute forces of Fig. 4.30. Impeller X, Volute A, face seal clearances of 0.14 mm and rotor speed of 1000 rpm.

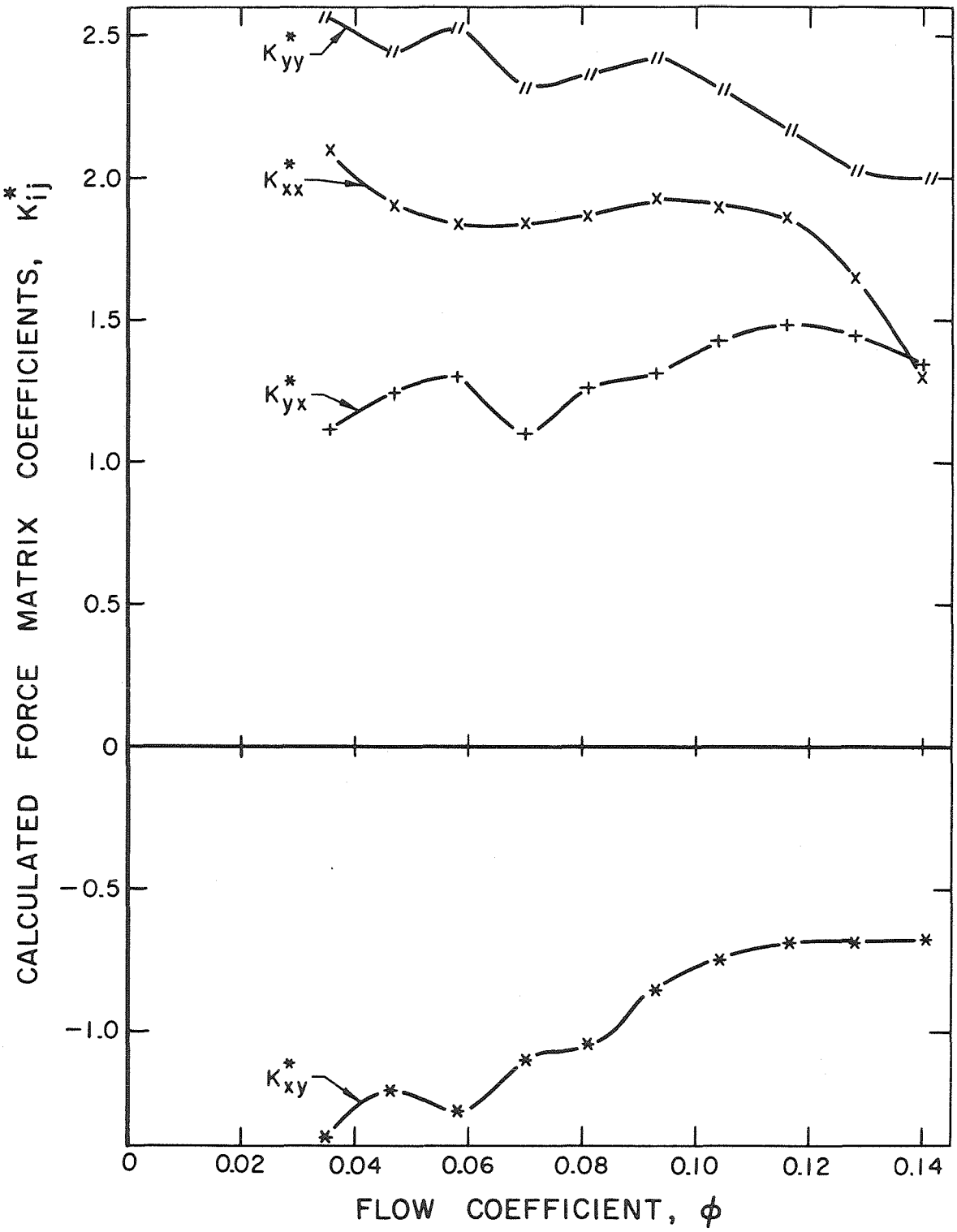

Fig. 4.32. Calculated normalized force matrix coefficients as defined by Eq. 4.4 in text using Impeller X, Volute B (circular), face seal clearances of 0.79 mm and rotor speed of 800 rpm.

Chapter 5

CALCULATIONS OF HYDRODYNAMIC RADIAL FORCES AND STIFFNESS MATRICES OF AN IMPELLER ECCENTRICALLY LOCATED WITHIN A VOLUTE

5.1. Impeller Physical Models-Previous Works

In the previous four chapters we have introduced and discussed an experimental procedure to measure quasi-steady fluid dynamic forces acting on a whirling centrifugal pump impeller. We have shown that the flow through the rotor of such a turbomachine may result in forces acting on the supporting shaft which could contribute to dynamic instability. Engineers generally agree that model and full scale testings are the only ways to predict stable turbomachinery operation. However this can prove to be costly for every new product. It would therefore be beneficial to be able to predict rotor forces using analytical methods. Several rotor-volute models have been created for this purpose. We would like to mention the "one-dimensional" volute flow model of Loret [52] which provides good estimates of off-design volute pressure distributions, and the "quasi-one-dimensional" model of Kurokawa [49] which permits a rotational volute flow and predicts experimental measurements of volute velocity distributions fairly well. By far, however, the most favored approach to analysis of the volute flow distribution is that of two-dimensional potential flows with a vortex singularity distribution to represent the volute. The simplest impeller model used for that purpose is the source-vortex model. This model of a centrifugal pump or compressor stage with a vaneless volute was first suggested by Csanady [31] and represents the impeller by an equivalent source-vortex concentrated at a single point at the rotor center as shown in Fig. 5.1. The source strength Q, representing impeller flow rate, and the vortex strength Γ,

representing impeller circulation, are related to geometric parameters of this impeller. Csanady calculated pressure distributions at the volute contour of a casing with a logarithmic spiral contour using conformal representation methods. However the works of Domm and Hergt [33] and Colding-Jorgensen [29] using the source-vortex model are perhaps best known. Domm and Hergt calculated impeller forces for concentric and eccentric (but fixed) impeller positions with respect to the volute. They distributed vortices on the volute trace and carried out computations with the aid of singularity theory. Here Glauert series were used in accordance with Schlichting's [60] and Hoffmeister's [41] procedures in order to calculate the strength of the unknown volute vorticity distribution. Later Colding-Jorgensen extended these computations by letting the source-vortex representing the impeller have an arbitrary but small eccentricity and velocity in order to calculate radial forces along with stiffness and damping matrices as defined in section 1.4. He used a method developed by Hess [40] in order to calculate his unknown volute singularity distribution. In Chapter 4 we compared these previous works to our measured forces and there concluded that this simple potential flow model was insufficient to predict accurate radial forces (see Fig. 4.8). Colding-Jorgensen's stiffness matrices as shown in Fig. 4.12 also seriously under-predicted our measured stiffness matrices and most important, they do not predict the skew-symmetric property of these matrices.

A much more sophisticated two-dimensional, unsteady lifting-surface computation with volute and finite number of impeller vanes was presented by Imaichi et al [43] and Shoji and Ohashi [62]. Rotor blades were assumed to have no thickness and impeller wakes were represented by a finite number of rotating vortex sheets as shown in Fig. 5.2. Both γ (representing blade vortex distribution) and γ_1 (representing trailing vortex sheet) have to be found in addition to any singularity distribution on the volute when such a device was present.

Imaichi et al calculated radial forces and torque acting on a stationary concentric impeller enclosed within a volute. The intent of their work, however, was the calculation of pressure fluctuations and impeller vanes-volute tongue unsteady reactions rather than of the hydrodynamic forces. Shoji and Ohashi used the same impeller model to calculate forces on a whirling centrifugal pump in an unbounded medium. Their work showed that impeller whirl without a volute results in positive damping (a stabilizing effect). Very recently Sato and Allaire [60] solved the case of an unbounded rotor pump or compressor, with finite thickness and number of blades, undergoing synchronous whirl. The assumption of irrotational potential flow was postulated as no trailing vortex wakes were included in the computations. Finite element computational techniques were used to solve for the flow. A control volume formulation was then used to calculate aerodynamic forces. The computed stiffness matrices differ widely from the present measured ones. The diagonal elements of their computed matrix are about 15 percent of the measured diagonal terms. Furthermore the computed cross-coupling terms predicted backward whirl; this is contrary to what was observed in the present experiment.

However Imaichi et al, Shoji and Ohashi and Sato and Allaire failed to solve the case of a whirling impeller enclosed within a volute due to inherent computational difficulties. We have proposed elsewhere (Chamieh and Acosta [18], Chamieh et al [19] and Chamieh [20]) a model of intermediate complexity; namely to replace the source-vortex of Csanady by an actuator impeller having an infinite number of vanes with the blade angle and dimensions of the actual impeller. Thus as in the original Euler theory, vane-angle geometry is preserved. Therefore the rotor vanes are replaced, in principle, by a set of body forces. Such a model has the advantage that internal losses can be accounted for and apparent mass and damping effects (but not blade to blade effects) can be predicted. Allaire et al [6] have used this model from a kinematic standpoint to

calculate stiffness matrices of a pump in an unbounded flow but the apparent mass effect was neglected. The importance of this latter effect is shown in Appendix A. In what follows, we sketch a theory based on the actuator disk model from which hydrodynamic radial forces and stiffness matrices are calculated. In this theory it is assumed that the flow in the volute space is a potential flow; this is the same assumption inherent in the impeller source-vortex distribution. It is known that the flow external to the impeller must be rotational when volute and impeller are not matched. To this extent a further approximation is inherent in this assumption which should be minimal at the volute design flow. Lastly numerical procedures and numerical results are described and comparisons with experiments are initiated.

5.2. The Concentric Problem-Radial Forces

The Problem. The physical arrangement of the actuator impeller located at the center of a logarithmic volute is shown in Fig. 5.3. As a first step we would like to compute radial forces only and therefore assume zero eccentricity (i.e. impeller and volute have the same set of coordinates). The distances r_1 and r_2 represent the inlet and exit radii of the actual impeller. We assume that the actuator impeller rotates at angular speed Ω as shown and that the relative flow is perfectly guided by the vanes having stagger angle β. To model the incoming flow, a source of strength Q and a prerotation Γ have been placed at the impeller center. The volute is replaced by a log spiral whose equation is

$$\delta = \delta_o e^{a\theta} \quad . \tag{5.1}$$

Here $\theta = 0$ is the leading edge angle and $\theta = \theta_M$ is the trailing edge angle. θ_M is the total angle subtended by the volute. The assumptions of incompressibility and irrotationality inside and outside of the volute are postulated. The flow is considered inviscid and two-dimensional. As pointed out by many early workers,

it is convenient to work with a linear cascade instead of a circular one and this is effected through the transformation

$$z = x + iy = ir_2 \ln(\zeta / r_2) \tag{5.2}$$

The volute thus appears as a straight line with equation (see Fig. 5.4)

$$y = -ax + r_2 \ln(\delta_o / r_2) \tag{5.3}$$

and is represented with a period $r_2\theta_M$. The volute is a streamline and this is represented by a vortex distribution $\gamma(x)$ on the volute trace. Thus the problem to be solved is to determine this vorticity distribution subject to the requirement that the flow leaving the actuator impeller be perfectly guided. Once this is done forces can be determined by the Blasius theorem and later on, for the case of the displaced impeller, the hydrodynamic stiffness matrix can be computed. The first step then is the calculation of the basic flow singularity of a vortex element of the volute satisfying the flow tangency condition of the impeller exit.

Interaction of a Singularity with an Actuator Cascade. Suppose in the upper half z-plane of Fig. 5.4 a singularity is located at $z = z_o$, and let the disturbance velocity due to this singularity be denoted $w_d = u_d - iv_d$. Because of the presence of the actuator cascade, additional velocities $w_i = u_i - iv_i$ (non singular for $y > 0$) will be induced resulting in the complex velocity

$$w_t = w_d + w_i = u_t - iv_t \ . \tag{5.4}$$

In addition to these perturbations, there is a basic uniform flow through the actuator cascade given by

$$U_B = -\Gamma_2/2\pi r_2 \tag{5.5a}$$

with $\Gamma_2 = 2\pi\Omega\, r_2^2 - Q\tan\beta$ and by

$$V_B = Q/2\pi r_2 \tag{5.5b}$$

where Γ_2, Q are the circulation and flow rate respectively leaving the impeller. This basic flow was calculated by satisfying the flow tangency condition

$$\left(\Omega\, r_2 - V_\theta\right)_{r=r_2} = \tan\beta \left(V_r\right)_{r=r_2} \tag{5.6}$$

at the voluteless impeller exit in the radial plane of Fig. 5.3. An equivalent flow tangency condition must be satisfied by the perturbation complex velocity w_t. In the cascade plane of Fig. 5.4 this becomes

$$u_d + u_i = (v_d + v_i)\tan\beta \tag{5.7}$$

at the impeller exit ($y = 0^+$). This is equivalent to requiring

$$\eta u_t + \kappa v_t = 0$$

on $y = 0^+$ with $\eta = 1$ and $\kappa = -\tan\beta$. Thus w_t has to satisfy a mixed boundary condition on $y = 0^+$. This turns out to be neatly handled by the methods described by Cheng and Rott [22]. Assuming that

$$w_d = w_d(z - z_o) \quad ,$$

the induced disturbance w_i is

$$w_i = -\frac{\eta - i\kappa}{\eta + i\kappa}\overline{w_d}(z-\overline{z_o}) \tag{5.8}$$

which is seen merely to be an image of w_d in the cascade plane. This is easy to show; let

$$H(z) = (\eta + i\kappa)w_t \ .$$

Then $\text{Real}\{H(z)\} = \eta u_t + \kappa v_t$ is required to be zero on the real axis. Now set

$$H(z) = (\eta + i\kappa)w_d(z-z_o) - (\eta - i\kappa)\overline{w_d}(z-\overline{z_o}) \ , \tag{5.9}$$

so that on $y = 0$, $H(x,0)$ is the difference of two complex conjugate functions and is therefore purely imaginary. In particular if we have a vortex element

$$w_d = -i\Gamma'/2\pi(z-z_o) \tag{5.10a}$$

then

$$w_i = -i\Gamma' e^{2i\beta}/2\pi(z-\overline{z_o}) \ . \tag{5.10b}$$

The problem shown in Fig 5.4 requires an infinite array of vortex elements; it is instantly recognized that Eqs. 5.10 lead to familiar forms for this repeating sum. We imagine now distributing vortex elements $\gamma(x)$ along the volute trace using Eqs. 5.10a,b as the kernel. In the notation of Fig. 5.4 we get the complex velocity

$$w_t = -\frac{i}{4\pi r_2}\int_{-r_2\theta_M}^{0} \gamma(x_o)dx_o\left[\cot\left(\frac{z-z_o}{2r_2}\right) + e^{2i\beta}\cot\left(\frac{z-\overline{z_o}}{2r_2}\right)\right] . \qquad (5.11)$$

Here $x_o = 0$ is the volute tongue and $x_o = -r_2\theta_M$ is the trailing edge of the volute where we arbitrarily require $\gamma(x_o=-r_2\theta_M) = 0$. $z_o = x_o + iy_o(x_o)$ represents points on the volute trace with y given by Eq. 5.3 .

The second term of Eq. 5.11 is the new contribution of the present model over that of Domm and Hergt [33] and Colding-Jorgensen [29]. There is a slight additional complication as this second term gives a finite contribution U_∞ and V_∞ to the basic velocities of Eqs. 5.5. In order to preserve continuity equation far downstream, we must subtract this effect. V_∞, the downstream contribution of the image sources located at $z = \overline{z_o}$, is given by

$$V_\infty = \frac{\sin 2\beta}{4\pi r_2}\int_{x_o=-r_2\theta_M}^{0} \gamma(x_o)dx_o . \qquad (5.12a)$$

As U_∞ and V_∞ must also satisfy the tangency condition of Eq. 5.7, U_∞ is then given by

$$U_\infty = \frac{(1-\cos 2\beta)}{4\pi r_2}\int_{x_o=-r_2\theta_M}^{0} \gamma(x_o)dx_o . \qquad (5.12b)$$

The complete flow field $W_T = U_T - iV_T$ will then be

$$U_T = u_t + U_B - U_\infty \qquad (5.13a)$$

$$V_T = v_t + V_B - V_\infty \ . \tag{5.13b}$$

To sum up we have solved for the flow field (U_T, V_T) in terms of the unknown vorticity distribution γ. In order to solve for γ, we require no flow through the volute surface. This in turn yields the volute flow tangency condition (see also Eq. 5.3)

$$\frac{dy}{dx} = -a = \frac{V_T}{U_T} \ . \tag{5.14a}$$

Substituting for U_T and V_T gives the integral equation

$$\int_{-1}^{+1} \gamma(\xi) K_V(X',\xi) d\xi = \frac{4(a\Gamma_2 - Q)}{r_2\Theta_M} \tag{5.14b}$$

for the strength of the vortex sheet γ. Here the coordinates of the volute have been appropriately stretched ($\xi = 1 + 2x_o/r_2\Theta_M$ and $X' = 1 + 2x/r_2\Theta_M$) and the terms U_∞, V_∞ have been incorporated into the singular kernel $K_V(X',\xi)$,

$$K_V(X',\xi) = \frac{\sin\left[\frac{\Theta_M}{2}(X'-\xi)\right] + a\sinh\left[\frac{a\Theta_M}{2}(X'-\xi)\right]}{\cosh\left[\frac{a\Theta_M}{2}(X'-\xi)\right] - \cos\left[\frac{\Theta_M}{2}(X'-\xi)\right]} - \left[\sin 2\beta + a\left[1 - \cos 2\beta\right]\right]$$

$$+ \frac{(\cos 2\beta + a\sin 2\beta)\sin\left[\frac{\Theta_M}{2}(X'-\xi)\right] + (a\cos 2\beta - \sin 2\beta)\sinh\left[\frac{a\Theta_M}{2}(X'+\xi) - Y_1\right]}{\cosh\left[\frac{a\Theta_M}{2}(X'+\xi) - Y_1\right] - \cos\left[\frac{\Theta_M}{2}(X'-\xi)\right]} \tag{5.14c}$$

where $Y_1 = 2\ln(\delta_o/r_2) + a\Theta_M$. The next and usual step is to express the γ

distribution in the Glauert-Birbaum series

$$\gamma(\lambda) = A_0 \cot\frac{\lambda}{2} + \sum_{k=1}^{\infty} A_k \sin(k\lambda) \qquad (5.14d)$$

for $\xi = \cos\lambda$ and to solve for the A_k's by any of several now standard methods. This will be discussed under numerical procedures in section 5.4 as we now proceed to calculate the radial force acting on the impeller in terms of the A_k coefficients.

The Radial Force. Our task now is to determine the force $\underline{F}$ on the actuator impeller; it may be readily shown that this force is equal to the negative of the forces on the volute ($\underline{F_V}$) and the source-vortex ($\underline{F_S}$) at the impeller center. To show this, consider a control surface surrounding the system and extending infinitely large. The total force acting on this control surface is equal to the sum of the forces required to maintain the volute, impeller and source-vortex at their respective fixed positions. However the flow as seen from far away ($r \to \infty$) behaves like a source flow of strength Q on top of a vortical flow of constant prerotation. Hence no force is expected on the control surface and

$$\underline{F} = -\underline{F_V} - \underline{F_S} \ . \qquad (5.15)$$

Both volute and source-vortex forces can be found by application of the Blasius theorem.

(i) Volute Force. Consider a control volume C_ζ enclosing the volute (but not the impeller) in the radial plane of Fig. 5.3 (not shown in Fig. 5.3). The complex conjugate of the volute force is given by application of the Blasius theorem, i.e.,

$$\overline{F_V} = -\frac{i\rho}{2} \oint_{C_\zeta} W^2(\zeta) d\zeta \ . \qquad (5.16a)$$

It is somewhat easier to work in the linear plane. C_z is then the transform of C_ζ and is shown in Fig. 5.4. Using the mapping function of Eq. 5.2, we find

$$\overline{F_V} = -\frac{\rho}{2} \oint_{C_z} W_T^2(z) e^{iz/r_2} dz \ . \qquad (5.16b)$$

Here $W_T = U_T - iV_T$ represents the total flow field as given by Eqs. 5.13. It is simpler to write W_T as

$$W_T = w_t + W_o \ ,$$

where w_t is given by Eq. 5.11 and W_o is a combination of the basic flow of Eqs. 5.5 and of U_∞ and V_∞ of Eqs. 5.12. In fact

$$W_o = U_o - iV_o$$

$$= (U_B - U_\infty) - i(V_B - V_\infty)$$

$$= -\Gamma_2/2\pi r_2 - \theta_M \frac{1-\cos 2\beta}{8} \left(A_o + \frac{A_1}{2}\right) - i\left[Q/2\pi r_2 - \theta_M \frac{\sin 2\beta}{8} \left(A_o + \frac{A_1}{2}\right) \right] \qquad (5.17)$$

where Eq. 5.14d has been used to substitute for the vorticity distribution of Eqs. 5.12 . It can be seen that W_o is regular while w_t presents a singular behaviour inside C_z. Hence the complex conjugate of the volute force is

$$\underline{F_V} = \underbrace{-\rho W_o \oint_{C_z} w_t e^{iz/r_2} dz}_{\text{TERM I}} \quad \underbrace{-\frac{\rho}{2} \oint_{C_z} w_t^2 e^{iz/r_2} dz}_{\text{TERM II}} . \tag{5.16c}$$

We evaluate 5.16c term by term using using Eq. 5.11 to express w_t; the first term

$$I = \frac{\rho i W_o}{4\pi r_2} \oint_{C_z} \int_{x_o=-r_2\Theta_M}^{0} \gamma(x_o) dx_o \left[\left\{ \cot\left(\frac{z-z_o}{2r_2}\right) + e^{2i\beta} \cot\left(\frac{z-\overline{z_o}}{2r_2}\right) \right\} e^{iz/r_2} \, dz \right]$$

$$= \frac{\rho i W_o}{4\pi r_2} \int_{x_o=-r_2\Theta_M}^{0} \gamma(x_o) dx_o \oint_{C_z} \left[\cdots \right] .$$

This integral exchange is allowed as contour C_z encloses but does not intersect the path of the integral in x_o. Evaluating the contour integral yields

$$I = -\rho W_o \int_{-r_2\Theta_M}^{0} \gamma(x_o) \, e^{iz_o/r_2} \, dx_o . \tag{5.18a}$$

Further substitutions in order to split the preceding integral in X and Y components of the volute's coordinates yields

$$I = -\frac{\rho r_2 \Theta_M}{2} \left\{ (U_o U_1 + V_o U_2) + i(U_o U_2 - V_o U_1) \right\} \tag{5.18b}$$

with U_o and V_o given by Eq. 5.17. U_1 and U_2 are definite integrals involving the A_k coefficients:

$$U_1 = \int_0^{\pi} \left\{ A_0(1 + \cos\lambda) + \sum_{k=1}^{\infty} A_k \sin\lambda \sin k\lambda \right\} . \cos\left\{ \frac{\Theta_M}{2}(\cos\lambda - 1) \right\}$$

$$. \exp\left\{ \frac{a\Theta_M}{2}(\cos\lambda - 1) - \ln(\delta_o/r_2) \right\} d\lambda \qquad (5.18c)$$

$$U_2 = \int_0^{\pi} \left\{ A_0(1 + \cos\lambda) + \sum_{k=1}^{\infty} A_k \sin\lambda \sin k\lambda \right\} . \sin\left\{ \frac{\Theta_M}{2}(\cos\lambda - 1) \right\}$$

$$. \exp\left\{ \frac{a\Theta_M}{2}(\cos\lambda - 1) - \ln(\delta_o/r_2) \right\} d\lambda \ . \qquad (5.18d)$$

The second term of Eq. 5.16c is harder to evaluate. After substituting for w_t from Eq. 5.11

$$II = \frac{\rho}{32\pi^2 r_2^2} \int_{-r_2\Theta_M}^{0} \int_{-r_2\Theta_M}^{0} \gamma(x_o)\gamma(x'_o) dx_o dx'_o \oint_{C_z} e^{iz/r_2}$$

$$. \left\{ \cot\left[\frac{z - z_o}{2r_2} \right] + e^{2i\beta} \cot\left[\frac{z - \overline{z_o}}{2r_2} \right] \right\} . \left\{ \cot\left[\frac{z - z'_o}{2r_2} \right] + e^{2i\beta} \cot\left[\frac{z - \overline{z'_o}}{2r_2} \right] \right\} . \qquad (5.19a)$$

Here w_t has been split into two integrals with x_o and x'_o as dummy variables and the contour integral has been exchanged with the double integration integrals as it encloses but does not intersect their path. $z_o = x_o + iy_o(x_o)$ and $z'_o = x'_o + iy'_o(x'_o)$ with $y_o(x_o)$ and $y'_o(x'_o)$ being given by Eq. 5.3. Evaluation of the contour integral gives

$$II = \frac{\rho i}{4\pi r_2} \int_{-r_2\theta_M}^{0} \int_{-r_2\theta_M}^{0} \gamma(x_o)\gamma(x'_o)dx_o dx'_o \, e^{iz_o/r_2}$$

$$\cdot \left\{ \cot\left[\frac{z_o - z'_o}{2r_2} \right] + e^{2i\beta} \cot\left[\frac{z_o - \overline{z}'_o}{2r_2} \right] \right\} ,$$

requiring further splitting of this second integral. The only singular term, $\cot\left\{(z_o - z'_o)/2r_2\right\}$, is split into a purely singular part, $2r_2/(z_o - z'_o)$, and a regular part, $\cot\left\{(z_o - z'_o)/2r_2\right\} - 2r_2/(z_o - z'_o)$. We now wish to evaluate three integrals composing term II. The first one

$$IIa = \frac{\rho i}{4\pi r_2} \int_{-r_2\theta_M}^{0} \int_{-r_2\theta_M}^{0} \gamma(x_o)\gamma(x'_o) e^{iz_o/r_2} \cdot \frac{2r_2}{z_o - z'_o} dx_o dx'_o \qquad (5.20a)$$

is equal to

$$\frac{\rho i(1 + ia)}{2\pi(1 + a^2)} \int_{-r_2\theta_M}^{0} \gamma(x_o) dx_o e^{iz_o/r_2} \int_{-r_2\theta_M}^{0} \frac{\gamma(x'_o)dx'_o}{x_o - x'_o} ,$$

which, upon a change in the integrand of $x_o = r_2\theta_M(\cos\lambda - 1)/2$ and $x'_o = r_2\theta_M(\cos\lambda' - 1)/2$ becomes a familiar expression for use of the relation

$$\int_0^{\pi} \frac{\cos k\lambda' \, d\lambda'}{\cos\lambda - \cos\lambda'} = -\pi \frac{\sin k\lambda}{\sin\lambda} . \qquad (5.20b)$$

Further substitutions of γ in terms of the Glauert series of Eq. 5.14d give

$$IIa = \frac{\rho r_2 \Theta_M}{4(1 + a^2)} \left\{ -aS_1 - S_2 + i\left[S_1 - aS_2\right] \right\} . \qquad (5.20c)$$

S_1 and S_2 are definite integrals involving the A_k coefficients

$$S_1 = \int_0^{\pi} \left\{A_0(1 + \cos\lambda) + \sum_{k=1}^{\infty} A_k \sin\lambda \sin k\lambda\right\} . \left\{-A_0 + \sum_{k=1}^{\infty} A_k \cos k\lambda\right\}$$

$$. \cos\left\{\frac{\Theta_M}{2}(\cos\lambda - 1)\right\} . \exp\left\{\frac{a\Theta_M}{2}(\cos\lambda - 1) - \ln(\delta_o/r_2)\right\} d\lambda \qquad (5.20d)$$

and

$$S_2 = \int_0^{\pi} \left\{A_0(1 + \cos\lambda) + \sum_{k=1}^{\infty} A_k \sin\lambda \sin k\lambda\right\} . \left\{-A_0 + \sum_{k=1}^{\infty} A_k \cos k\lambda\right\}$$

$$. \sin\left\{\frac{\Theta_M}{2}(\cos\lambda - 1)\right\} . \exp\left\{\frac{a\Theta_M}{2}(\cos\lambda - 1) - \ln(\delta_o/r_2)\right\} d\lambda \qquad (5.20e)$$

The last two integrals of term II are lengthy but straightforward to evaluate. We will sum up our findings by giving the volute force

$$\underline{F_V} = -\frac{\rho r_2 \Theta_M}{2}(U_o U_1 + V_o U_2) - \frac{\rho r_2 \Theta_M}{4(1+a^2)}(aS_1 + S_2)$$

$$- \frac{\rho r_2 \Theta_M^2}{16\pi}(S_3 + S_5 \cos 2\beta + S_6 \sin 2\beta)$$

$$+ i\left\{ \frac{\rho r_2 \Theta_M}{2}(U_o U_2 - V_o U_1) + \frac{\rho r_2 \Theta_M}{4(1+a^2)}(aS_2 - S_1) \right.$$

$$\left. + \frac{\rho r_2 \Theta_M^2}{16\pi}(-S_4 + S_5 \sin 2\beta - S_6 \cos 2\beta) \right\} . \qquad (5.21)$$

Here U_o, V_o, U_1, U_2, S_1 and S_2 have been previously defined. For completeness S_3, S_4, S_5 and S_6 will be given in Appendix B.

(ii) Source-Vortex Force. The vector force exerted upon the inlet source-vortex is

$$\underline{F_S} = -\rho \underline{V_I}(Q - i\Gamma) \qquad (5.22)$$

where $\underline{V_I}$ is the velocity induced at the impeller center by all disturbances except from the source-vortex itself. In the radial plane of Fig. 5.3, the inner flow ($r < r_1$) can be expanded in a power serie of $\zeta = re^{i\theta}$. The complex velocity of such a flow field is

$$W_1(\zeta) = \frac{Q - i\Gamma}{2\pi\zeta} + B_0 + B_1\zeta + B_2\zeta^2 + \cdots \qquad (5.23)$$

with B_0, B_1, B_2 , ... being complex constants. Obviously

$$\underline{V_I} = \overline{B_0} . \qquad (5.24)$$

It is simpler to work in the cascade plane where

$$W_1(z) = \frac{-\Gamma - iQ}{2\pi r_2} - B_0 ie^{-iz/r_2} - B_1 r_2 i \left[e^{-iz/r_2}\right]^2 - \cdots \quad , \tag{5.25}$$

and only the second term of the series needs to be evaluated. To sum up we need to find the behaviour of Eq. 5.25 at upstream infinity ($y \to -\infty$). The downstream solution of the flow field (W_T of Eq. 5.13) and the upstream solution are linked through the continuity equation requiring the normal velocity $V_T(x,0)$ to be the same across the cascade at $y = -r_2 \ln(r_2/r_1)$. The downstream solution was obtained through the distribution of vorticity on the volute trace (at z_o) and its equivalent source-vortex images in the conjugate plane (at $\overline{z_o}$). To construct the upstream solution we have to disallow all upstream singularities and add "corresponding" disturbances downstream such as $V_T(x,0)$ is preserved. For the example of Eqs. 5.1,a,b the total disturbances that has to be distributed on the volute trace in order to remove upstream singularities and preserve $V_T(x,0)$ is

$$\Gamma'\left\{\left(-\sin 2\beta + i(1 + \cos 2\beta)\right\}\right. . \tag{5.26}$$

In order to have $V_1\left[x, -r_2 \ln(r_2/r_1)\right] = V_T(x,0)$ these total disturbances must be displaced by a constant vector depending on cascade geometry (in our case case equal to $-r_2\theta_M - ir_2\ln(r_2/r_1)$). This fact is ignored in the present calculation as the flow at upstream infinity is independent of this vector. Indeed it can be checked that the current flow field formed by a summation of the disturbances of Eq. 5.26 and of the basic flow of Eqs. 5.5 minus U_∞ and V_∞ of of Eqs. 5.12 gives the right source flow at upstream infinity. By expansion of the complex velocity of this upstream flow one finds

$$B_0 = \frac{\sin 2\beta + i(1 + \cos 2\beta)}{2\pi r_2} \int_{-r_2\Theta_M}^{0} \gamma(x_o)\, e^{iz_o/r_2}\, dx_o \quad . \tag{5.27}$$

This integral is similar to the one of Eq. 4.18a. Thus

$$\underline{F_S} = -\frac{\rho\Theta_M}{4\pi}(Q - i\Gamma)\Big\{ U_1 \sin 2\beta - U_2(1 + \cos 2\beta)$$

$$- i\left[U_2 \sin 2\beta + U_1(1 + \cos 2\beta) \right]\Big\} \tag{5.28}$$

where U_1 and U_2 are defined through Eqs. 5.18c,d. Hence the total force on the impeller is entirely defined.

5.3. The Eccentric Problem-Stiffness Coefficients

We are now concerned with the calculation of the forces on the impeller when it is displaced a distance ε relative to the center of the volute. For convenience we refer all quantities to the impeller center and thus the volute appears displaced as in Fig. 5.5. The method of solution is similar to the one described for the concentric case. The same mapping function of Eq. 5.2 yields a distorted volute shape in the linear cascade plane. In what follows it is assumed $\varepsilon/r_2 << 1$ so that the volute equation is approximately

$$y = -ax + r_2 \ln(\delta_o/r_2) + \frac{\varepsilon r_2}{\delta_o} e^{ax/r_2} \Big\{ \cos(x/r_2 + \psi) - a \sin(x/r_2 + \psi) \Big\} \quad . \tag{5.29}$$

As was done before, vorticity γ is distributed along the preceding volute trace. A further simplifying assumption is postulated, in that impeller and volute operate close to their mutual design flow rate, Q_{des}. This means that for a given flow rate Q, the basic velocities of Eq. 5.5 are linked to the volute angle

represented by a and to $(Q_{des} - Q)$ through

$$V_B / U_B = -a + h + O(h^2) \ , \tag{5.30}$$

where $h = (Q_{des} - Q)/Q_{des} << | a |$. The vorticity γ then becomes of order ε (or h). The flow field is again given by Eq. 5.13 as the vorticity has been distributed back to the original average trace of the volute (Eq. 5.3) with an error of order ε^2. Only the tangency flow condition of Eq. 5.14a bears a change on the expression for γ. We now make use of the distorted shape of Eq. 5.29 to substitute for the expression (dy/dx) in Eq. 5.14a in order to derive the integral equation for the vortex sheet density $\gamma(x)$. We proceed in the now standard way but first set

$$\gamma(x) = \gamma^o(x) + \frac{\varepsilon}{r_2}\left\{\gamma^c(x)\cos\psi + \gamma^s(x)\sin\psi\right\} \tag{5.31}$$

and upon substitution of Eqs. 5.30 and 5.31 into Eq. 5.14a we find the set of integral equations

$$\int_{-1}^{+1} \gamma^o(\xi)\, K_V(X',\xi)d\xi = 4\frac{h\Gamma_2}{r_2\Theta_M} \tag{5.32a}$$

$$\int_{-1}^{+1} \gamma^c(\xi)\, K_V(X',\xi)d\xi = \frac{4(1+a^2)\Gamma_2}{\delta_o\Theta_M}\, e^{\frac{a\Theta_M(X'-1)}{2}}\, \sin\left\{\frac{\Theta_M}{2}(X'-1)\right\} \tag{5.32b}$$

$$\int_{-1}^{+1} \gamma^s(\xi)\, K_V(X',\xi)d\xi = \frac{4(1+a^2)\Gamma_2}{\delta_o\Theta_M}\, e^{\frac{a\Theta_M(X'-1)}{2}}\, \cos\left\{\frac{\Theta_M}{2}(X'-1)\right\} \ . \tag{5.32c}$$

Here $K_V(X',\xi)$ is the same as before in Eq. 5.14c. Solution of these equations is

identical to what was previously done as we express each of the distributions in the Glauert-Birbaum series by

$$\gamma^i(\lambda) = A_0^i \cot\frac{\lambda}{2} + \sum_{k=1}^{\infty} A_k^i \sin(k\lambda) \tag{5.32d}$$

where superscript (i) is either (o), (c) or (s) corresponding to Eq. 5.32a,b,c respectively. We may now proceed to calculate the force on the impeller $\underline{F}$ for the eccentric case. This is again equal to the negative of the forces on the volute and source-vortex at the origin. The previous force calculations still hold. However the force on the volute is somewhat simpler as we drop the definite integrals $S_1, S_2, \cdots, S_6$ due to their dependence on γ^2 which is of order ε^2. Furthermore U_o and V_o of Eq. 5.17 can be substituted by U_B and V_B of Eqs. 5.5a,b with an error of order ε^2 only. Finally all of these forces are now gathered together with the approximation that $\varepsilon/r_2 << 1$ and going directly to the final result it is found that

$$\underline{F} = \underline{F_0} + [K]\begin{bmatrix} -\varepsilon\cos\psi \\ -\varepsilon\sin\psi \end{bmatrix} . \tag{5.33a}$$

Here $\underline{F_0}$ is the radial force (components F_{0X} and F_{0Y}) for the concentric case and is independent of the impeller center angular position ψ. [K] is the "stiffness matrix" of the impeller-volute interaction expressed with respect to the volute (note: this is why we have a minus sign in the vector position). Furthermore,

$$[K] = \begin{bmatrix} K_{XX} & K_{XY} \\ K_{YX} & K_{YY} \end{bmatrix} . \tag{5.33b}$$

The components F_{0X}, F_{0Y} and those of [K] are determined by the coefficients of

the Glauert series of Eq. 5.32d. Defining

$$U_1^i = \int_0^\pi \exp\left[\frac{a\Theta_M}{2}(\cos\lambda - 1) - \ln(\delta_o/r_2)\right] . \cos\left[\frac{\Theta_M}{2}(\cos\lambda - 1)\right]$$

$$. \left[A_0^i(1 + \cos\lambda) + \sum_{k=1}^{\infty} A_k^i \sin\lambda \sin k\lambda \right] d\lambda$$

and

$$U_2^i = \int_0^\pi \exp\left[\frac{a\Theta_M}{2}(\cos\lambda - 1) - \ln(\delta_o/r_2)\right] . \sin\left[\frac{\Theta_M}{2}(\cos\lambda - 1)\right]$$

$$. \left[A_0^i(1 + \cos\lambda) + \sum_{k=1}^{\infty} A_k^i \sin\lambda \sin k\lambda \right] d\lambda \qquad (5.34a)$$

where (i) = (o), (c) or (s) (see Eqs. 5.32a,b,c) and letting

$$L = \frac{Q\,(\tan\beta + \sin 2\beta)}{2\pi r_2} - \frac{\Gamma\,(1 + \cos 2\beta)}{2\pi r_2} - \Omega\, r_2 \qquad (5.34b)$$

and

$$M = -\frac{Q\cos 2\beta}{2\pi r_2} - \frac{\Gamma \sin 2\beta}{2\pi r_2} \qquad (5.34c)$$

then one finds for F_{OX}, F_{OY}, K_{XX}, K_{XY}, K_{YX} and K_{YY}:

$$F_{OX} = \frac{\rho r_2 \Theta_M}{2}\,(LU_1^o + MU_2^o) \qquad (5.35a)$$

$$F_{OY} = \frac{\rho r_2 \Theta_M}{2} (MU_1^c - LU_2^s) \tag{5.35b}$$

and

$$K_{XX} = -\frac{\rho \Theta_M}{2} (LU_1^c + MU_2^s) \tag{5.35c}$$

$$K_{XY} = -\frac{\rho \Theta_M}{2} (LU_1^s + MU_2^s) \tag{5.35d}$$

$$K_{YX} = -\frac{\rho \Theta_M}{2} (MU_1^c - LU_2^s) \tag{5.35e}$$

$$K_{YY} = -\frac{\rho \Theta_M}{2} (MU_1^s - LU_2^s) \ . \tag{5.35f}$$

Concluding Remarks and Non-Dimensionalization. it should be noted that all force results and stiffness coefficients obtained here are expressed per unit width as we are treating a purely two-dimensional model. Non-dimensionalization is then carried for a quick comparison with experimental results. All forces are normalized by the dynamic head based on tip speed ($=\rho\Omega^2 r_2^2/2$) times the impeller discharge area per unit width ($=A_2/b_2$). All stiffnesses are normalized by the dynamic head based on tip speed times the discharge area per unit width over the radius of the impeller ($=r_2$). In conclusion direct comparison with experimental data can be initiated if all force results of Eq. 5.35a are divided by $\pi\rho\Omega^2 r_2^3$ and if all stiffness results of Eq. 5.35b are divided by $\pi\rho\Omega^2 r_2^2$.

5.4. Numerical Procedures-Solution of the Vorticity Distribution

We wish to introduce a general method of solution for any of the Fredholm integral equations encountered in the previous sections of this chapter in order to solve for any vorticity distribution $\gamma(\xi)$. In general

$$\int_{-1}^{+1} \gamma(\xi)\, K_V(X',\xi)\, d\xi = F(X')$$

is the type of equation to be solved with $K_V(X',\xi)$ being given by Eq. 5.14c and $F(X')$ being any arbitrary but continuous function of X'. Solution of this integral equation follows the steps outlined by Mani [53]. These formal steps are as follows:

1. Let $X' = \cos\theta$ and $\xi = \cos\lambda$ so that as X', ξ run from -1 to +1, θ and λ run from π to 0. The kernel $K_V(X',\xi)$ of Eq. 5.14c is also of the form

$$K_V(X',\xi) = \frac{4}{\theta_M(X' - \xi)} + K_{VR}(X',\xi) \quad , \tag{5.36}$$

where K_{VR} is the regular part of K_V once the singularity is removed. K_{VR} contains all the image terms (w_i).

2. Assume for $\gamma(\cos\lambda)$ the usual Glauert-Birbaum airfoil type series of Eqs. 5.14d and 5.32d with the square root singularity at the leading edge ($\xi = 1$ or $\lambda = 0$) and with all terms vanishing at the trailing edge due to the Kutta-Joukowski condition ($\xi = -1$ or $\lambda = \pi$). Then

$$\gamma(\lambda) = A_0 \cot\frac{\lambda}{2} + \sum_{k=1}^{\infty} A_k \sin(k\lambda) \quad .$$

We will truncate this serie at k = N thereby keeping N+1 coefficients to be calculated. N will be determined according to the needs of accuracy.

3. Compute the first N+1 coefficients, i.e. $C_0, \cdots, C_N$, in the Fourier analysis of

$$F(X') = C_0 + \sum_{k=1}^{\infty} C_k \cos(k\theta) \quad . \tag{5.37}$$

4. compute (N+1)(N+2) coefficients in the double Fourier series expansion of

$$K_{VR}(X',\xi) = \sum_{l=0}^{\infty} \sum_{m=0}^{\infty} B_{lm} \cos(l\theta) \cos(m\lambda) \quad . \tag{5.38}$$

Evaluate $B_{00}, B_{01}, \cdots, B_{N,N+1}$.

5. Upon substitution of all the preceding in the integral equation we find the Glauert coefficients to satisfy the following set of simultaneous equations

$$A_0 \left[-\frac{4}{\theta_M}\delta_{r0} + B_{r0} + B_{r1}/2 \right] + A_1 \left[\frac{4}{\theta_M}\delta_{r1} + B_{r0}/2 - B_{r2}/4 \right]$$

$$+ \sum_{n=2}^{N} A_n \left[\frac{4}{\theta_M}\delta_{rn} + B_{r,n-1}/4 - B_{r,n+1}/4 \right] = C_r/\pi \tag{5.39}$$

with r = 0, 1, ..., N. δ_{rn} is the Kronecker delta function equal to zero if $r \neq n$ and equal to one if r = n.

The numerical procedure is straightforward. Select any arbitrary N and solve the simultaneous set of equations defined above to check for the convergence of the A_k coefficients; increase the value of N as needed. Impeller forces and

stiffness matrices can then be calculated by truncating any definite integral involving these coefficients above order N then evaluating it. We now concentrate our attention to the expressions for U_1^i and U_2^i of Eq. 5.34a since these are the end products concerning the Glauert series prior to the actual calculation of the stiffness matrices. It can then be checked that the maximum k = N needed there is equal to 9 provided $A_{k+1} \leq A_k$ for $k \geq 5$; this is due to the presence of the term $(\sin\lambda\sin k\lambda)$ in the integrals in λ from 0 to π. Thus only ten terms $(A_0, A_1, \cdots, A_9)$ of any given Glauert series need to be accurately calculated since a decreasing pattern for these coefficients is expected after the first few terms. The error of truncating U_1^i and U_2^i was then estimated to be much less than than 0.1 percent. The only other difficulty consists of estimating the influence of higher harmonics $(A_{10}, A_{11}, \cdots)$ on the magnitudes of the first ten Glauert coefficients via Eq. 5.39. Values of N=14 (15 terms) and N=19 (20 terms) were then tried with negligeable effects on the magnitudes of the first ten terms (and thus on U_1^i and U_2^i also). Hence we will restrict ourselves to the calculation of the first ten Glauert coefficients for each of the integral equations defined in 5.32a,b,c.

5.5. The Computing Programs and Notes on their Use

The main intent of this theoretical work was the calculation of the hydrodynamic stiffness matrices exclusively. Therefore the methods of section 5.3 were numerically investigated instead of the methods of section 5.2 dealing with the calculation of radial forces only. For this purpose, two computing programs have been developed for the solution of Eqs. 5.32 a,b,c (for $\gamma^o(\xi)$, $\gamma^c(\xi)$ and $\gamma^s(\xi)$) and for the subsequent calculation of the normalized stiffness matrices. The by-product of these calculations was the linearized radial force, as defined by Eq. 5.35a, for flow rates close to design. We should emphasize again, however, that the correct way to tackle the radial force problem is through the full set of calculations defined in section 5.2. Of the two developed computing programs the

first one performs the double Fourier analysis of the kernel $K_{VR}(X',\xi)$ and the Fourier analysis of F(X'). It then solves the set of simultaneous equations (5.39) by matrix inversion in order to compute U_1^j and U_2^j of Eq. 5.34a. This program, called 'FORCE", is written in Fortran IV H-Extended version and can be operated on an IBM 370/3032. The second program, called "TEST", calculates the normalized forces and stiffness matrices of Eq. 5.35a,b as a function of inlet swirl circulation Γ over flow rate Q. It is written in Fortran IV and can be operated on a PDP-11. Finally both programs are reproduced in Appendix C.

Program FORCE. The final objective of 'FORCE" is the computation of U_1^j and U_2^j of Eq. 5.34a. The data provided consist of geometric quantities such as impeller radius (R2), blade leaving angle (BETA), tongue radius (DN), volute angle cotangent (ADN) and total angle subtended by the volute (TETMAX). Other inputs included flow rate (Q), design flow rate (QDES) and rotor speed (OMEGA). The number of harmonics used in the computations (previously N+1) is denoted by NHI. In view of the previous discussion we set NHI = 10. Throughout this program all numerical integrations are carried out using Romberg integration subroutines (for more information see Ref. [17]). Matrix inversion of Eq. 5.39 was carried out by a Caltech subroutine with initials 'EQSOV". This simultaneous equation solver with iterative improvement is included at the end of Appendix C for the convenience of the reader.

A brief description of the various steps followed is in order. The double Fourier cosine series (B_{lm}) of Eq. 5.38 is evaluated first through numerical double integration using two Romberg subroutines, "doubin" and "integ". The accuracy of integration could be varied by increasing the number of subdivisions defined by the input integer mMAX (note that Romberg subroutines use power of two subdivisions, i.e. in this case, 2^{mMAX} subdivisions were used). This is the most expensive part of the program and a compromise had to be made between

accuracy and cost. A value of mMAX = 7 was found to be satisfactory for NHI=10 and yielded estimated convergence accuracies of better than 0.1 percent. Printouts of all results were initiated for mMAX = 7 as well as for mMAX = 6 and mMAX = 5 in order to check this estimation. The total time required for these computations on an IBM 370/3032 was in the viscinity of 4500 seconds. The next step was the evaluation of coefficients C_k of Eq. 5.37 using Romberg subroutine "rinteg" with 2^{10} subdivisions (accuracies of better than 10 digits). Finally after the Glauert series were computed using Caltech subroutine 'EQSOV", U_1^i and U_2^i were evaluated using Romberg subroutines "ginteg" and "gintgg" with 2^{10} subdivisions (accuracies of better than 10 digits).

Program TEST. Program "TEST" accepts the values of the six integrals calculated by "FORCE" along with the ratio of the inlet swirl circulation over flow rate Q (denoted by R). It prints out the normalized radial forces (F_{OX}^* and F_{OY}^* of Eq. 5.35a) along with their slopes (with respect to $(Q_{des} - Q)/Q_{des}$) and the normalized stiffness matrices (K_{ij}^* of Eq. 5.35b). These results can then be readily compared to other experimental or theoretical data.

5.6. Numerical Results and Conclusions

A test case using the data of Impeller X and Volute A was computed in order to compare our theory with our experimental results. An impeller radius of 81 mm and rotor blade angle of 25 degrees were selected in addition to a volute tongue radius of 91 mm and volute angle of 81.9 degrees. The total angle subtended by the volute was assumed equal to 396 degrees. Flow conditions were set to be the same encountered by Impeller X during experimentation; a design flow coefficient of 0.092 was used with a rotor speed of 104.7 rad/sec (about 1000 rpm) and a design flow rate of 0.4 m^3/sec/m (equivalent to 99.7 gpm for Impeller X). Figures 5.6 a,b present data about the slopes of the normalized radial force components and stiffness matrix components. The linearity of such results with

respect to Γ/Q is predicted by Eqs. 5.35a,b. In a real pump inlet swirl circulation Γ is determined mainly by the presence of vanes at the inlet portions of the pump. In our experiments no such vanes were utilized; Γ/Q is then most probably zero.

We first compare the slopes of Fig. 5.6a with actual data presented in Fig. 4.8. The calculated values are found to be an order of magnitude larger than the measured ones; this effect might be due to our simplifying assumptions as the primary motive of this theory was the calculation of stiffness matrices. The correct way to get these forces is the one featured in section 5.2. This is beyond the scope of the present work.

The normalized stiffness matrix is plotted in Fig. 5.6b. For $\Gamma/Q = 0$ it is mainly a diagonal matrix. The diagonal elements K^*_{XX} and K^*_{YY} are around 0.5 which is four to five times less than what was measured. Their effect is to push the impeller towards the volute. The absence of "cross-coupling" terms is an indication that this potential flow theory failed to predict any inherent rotordynamic instability. Furthermore these data were somewhat similar to Colding-Jorgensen's simple source-vortex impeller model results [29].

In order to get a better comparison between theory and experiments we should subtract the effects of disk friction of section 4.6 (amounting to about 25 percent of the total stiffness matrix) from the experimental results; these effects cannot be recovered in the theory as we are treating a two-dimensional model. Furthermore rotational effects should be included in the impeller discharge flow in order to get better modelling of real flows. We have suggested in the past [19] a method dealing with the interaction of a moving cascade with a row of singularities. Vorticity was then assumed to be small enough to be carried on the mean flow streamlines and a method of solution was introduced accordingly. A similar type of calculation should be carried for the case of the

displaced impeller located inside a logarithmic volute in order to better the present theory.

Even though the present simplified potential flow model failed to duplicate the experimental results of Chapter 4, it is still perhaps useful in estimating trends of the stiffness matrix as a function of impeller and volute parameters. Here we separately vary rotor blade angle, volute angle and tongue radius. Figure 5.7 is a table showing the corresponding effects on the stiffness matrix coefficients for $\Gamma/Q = 0$. "Normal" condition represents the data given at the onset of this section. The main findings can be summarized as follows: no changes in the stiffness matrix components were detected when the rotor blade angle was increased from 20 to 25 to 30 degrees. However as the volute tongue radius was increased, the diagonal elements of the stiffness matrix decreased accordingly; this decrease was equal to 15 percent of the original values for a tongue gap $(\delta_o - r_2)$ of twice the original one and to 38 percent for a tongue gap of four times the original gap. These diagonal terms also decreased, as would be expected, when volute angle was decreased. Cross-coupling terms, however, remained small at all times.

In conclusion this theory failed to duplicate the experimental results on the stiffness matrix, as can be attested to by the absence of cross-coupling terms responsible for rotor whirl. Furthermore the diagonal elements were smaller by a ratio of four to five times. Their tendency is to push the impeller towards the walls of the volute which agrees with experimental findings. Future improvements should include entrance losses and rotational flows at the discharge using the same procedures described in reference [19].

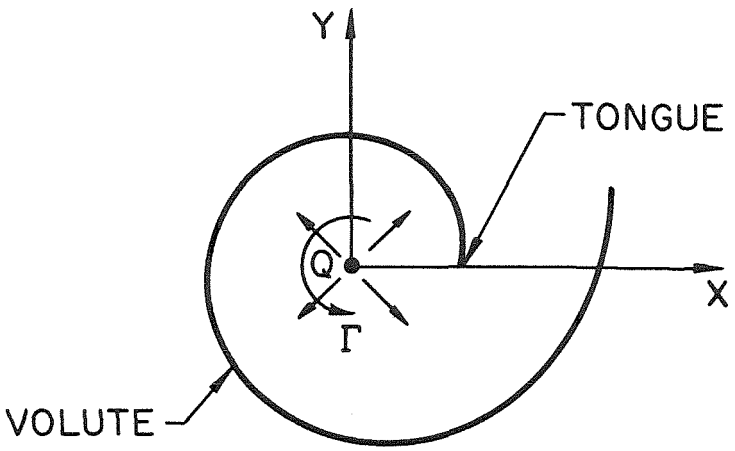

Fig. 5.1. Source-vortex model used by Csanady [31], Domm and Hergt [33] and Colding-Jorgensen [29] (see also text).

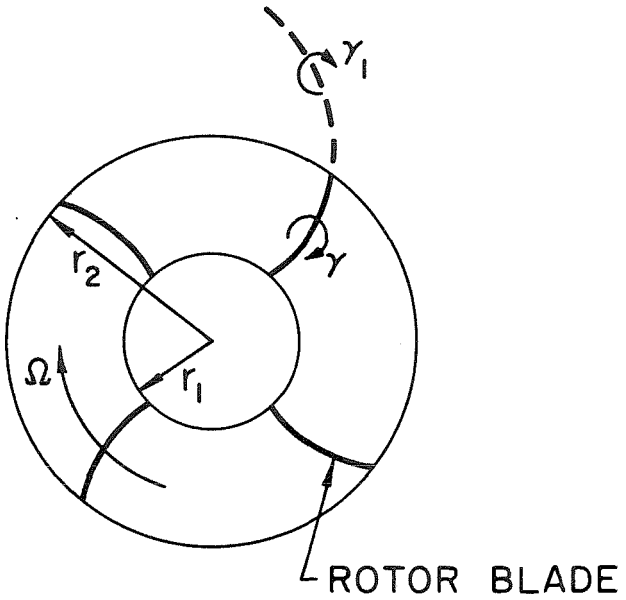

Fig. 5.2. Schematic of the rotor model used by Shoji and Ohashi [62] and Imaichi et al [43]. It has a finite number of blades (modeled by vortex sheet γ) and trailing wakes (modeled by vortex sheet γ_1).

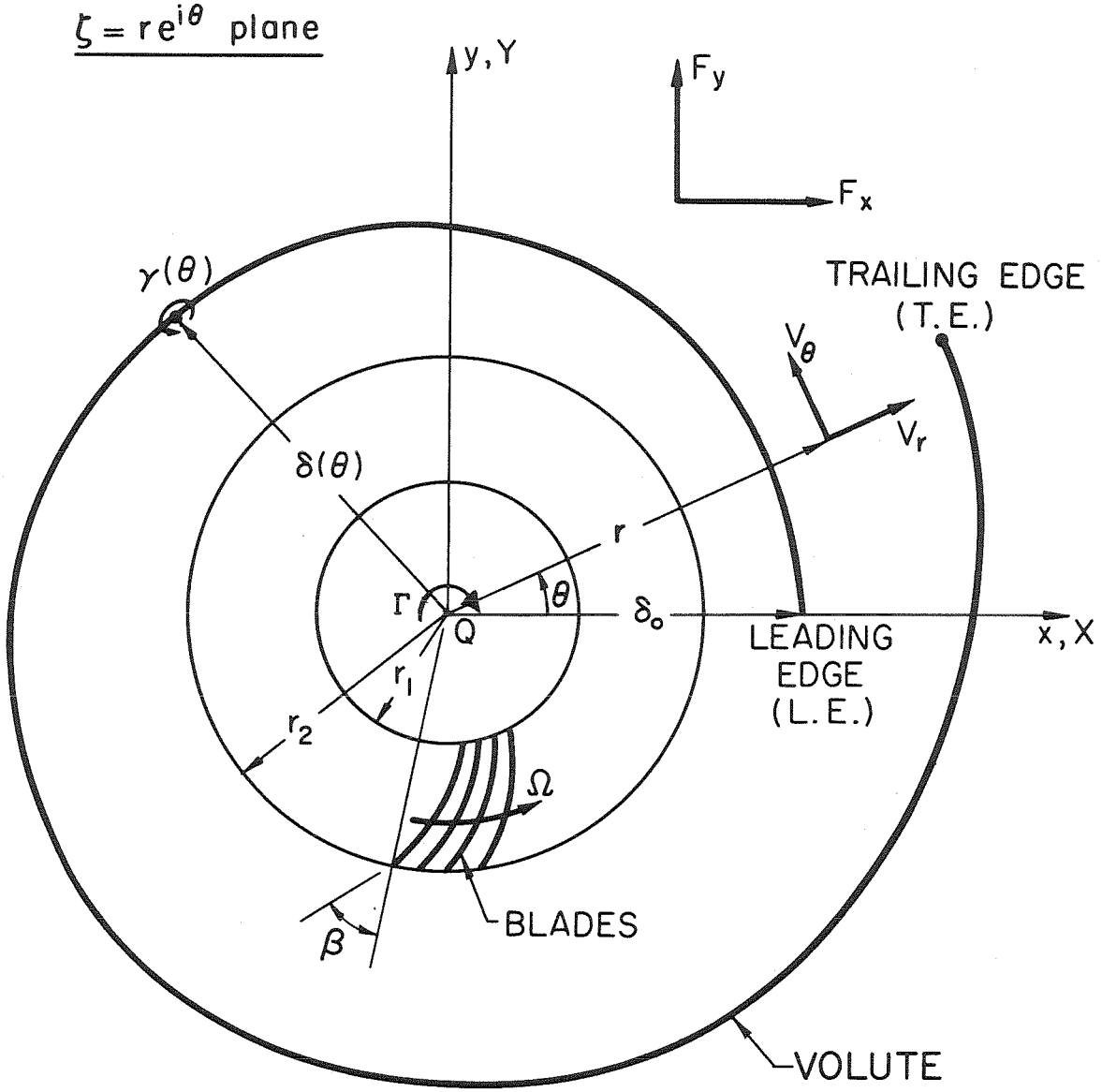

Fig. 5.3. Impeller and volute representation in the physical plane.

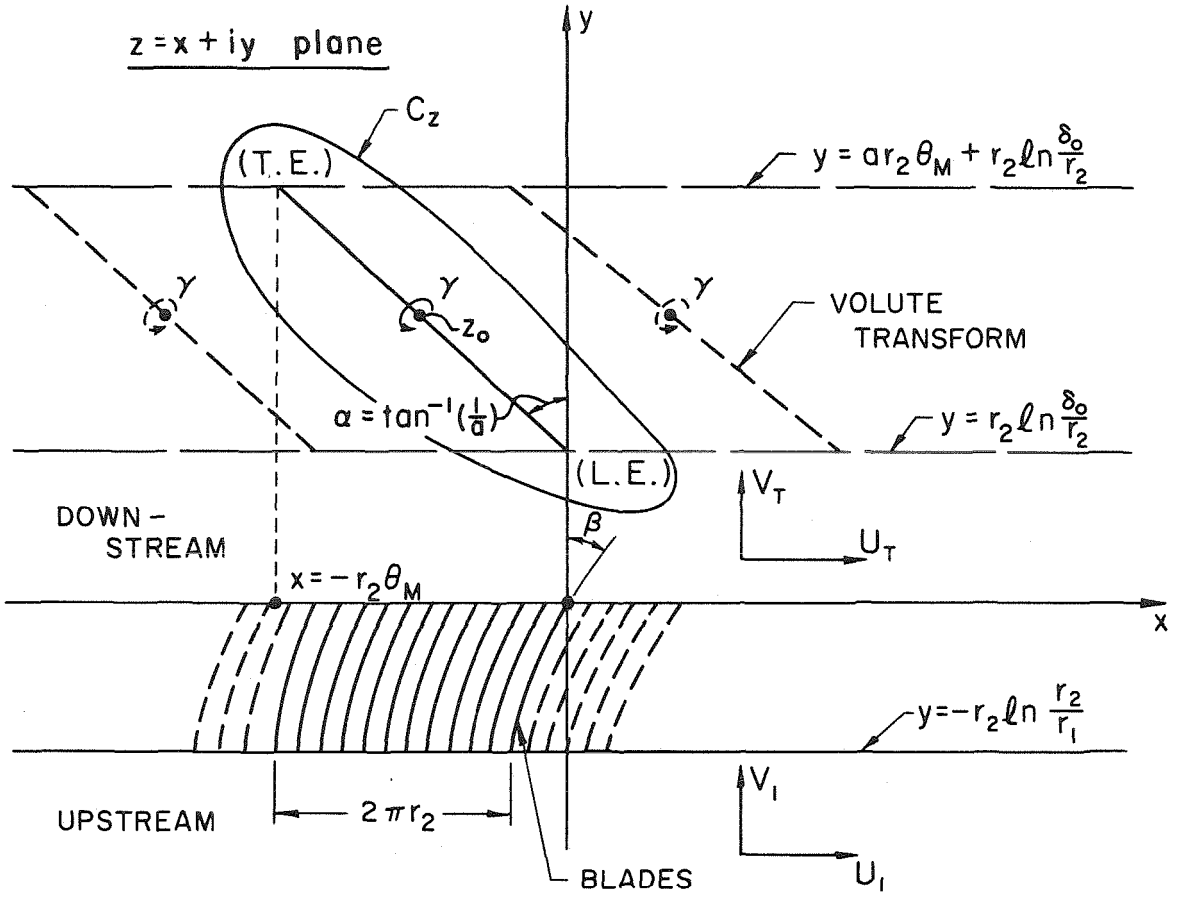

Fig. 5.4. Impeller and volute representation in the cascade plane.

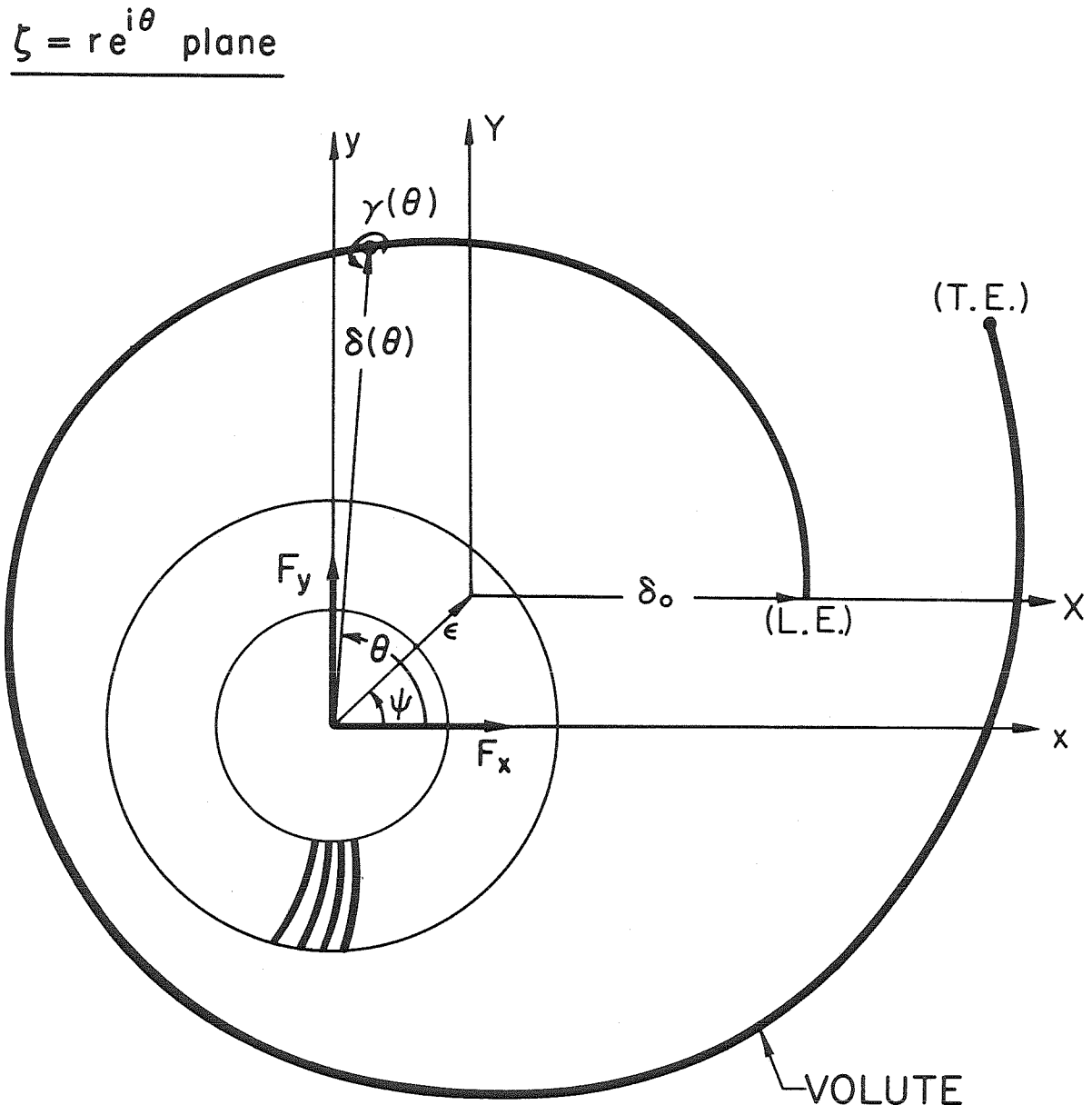

Fig. 5.5. The eccentric problem. The impeller is displaced from its original centered position to calculate the stiffness matrix.

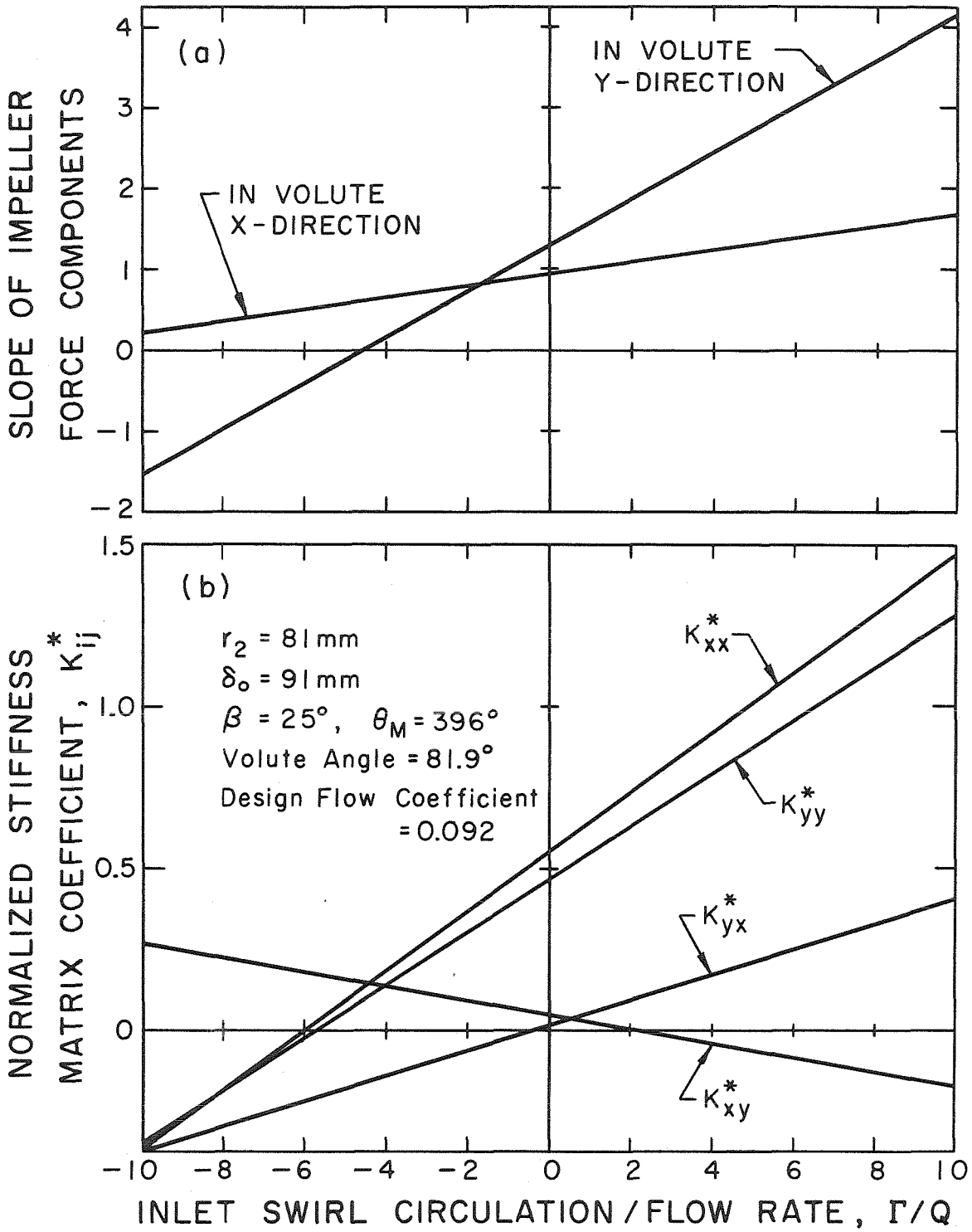

Fig. 5.6a. The slopes of the dimensionless radial force components are shown versus inlet swirl circulation over flow rate.

Fig. 5.6b. The normalized stiffness matrix coefficients are shown as a function of inlet swirl circulation over flow rate.

Impeller / Volute Parameters	K_{xx}^*	K_{yy}^*	K_{xy}^*	K_{yx}^*
Normal Case (*)	0.555	0.467	0.051	0.016
$\beta = 20°$ (**)	0.554	0.470	0.022	0.045
$\beta = 30°$ (**)	0.557	0.464	0.079	-0.012
$\delta_0 = 102$ mm (**)	0.475	0.393	0.026	0.030
$\delta_0 = 123$ mm (**)	0.351	0.285	0.001	0.040
Volute Angle = 74° (**)	0.422	0.261	-0.050	0.074

(*)

Normal Case depicts the test conditions used in Figs. 5.6 a,b where $r_2 = 81$mm, $\delta_0 = 91$mm, $\beta = 25°$, $\theta_M = 396°$, volute angle = 81.9° and design flow coefficient = 0.092.

(**)

Only parameter that was changed from Normal Case.

Fig. 5.7. Table showing impeller and volute parameter effects on the dimensionless stiffness matrix coefficients due to various geometric changes for $\Gamma/Q = 0$.

Chapter 6

SUMMARY AND CONCLUSIONS

A facility to measure steady and unsteady fluid forces acting on a whirling pump-rotor modelling one of the two double suction impellers of the HPFTP of the Space Shuttle was designed and constructed. The angular speed of the whirl as well as that of the impeller could be independently varied although the eccentricity of the whirling shaft was fixed. Only the steady-state vector forces arising from the quasi-static displacement of the rotor within the surrounding casing are measured herein. To accomplish this the whirl speed was maintained sufficiently slow to be equivalent to a quasi-steady change in rotor center position and to permit a continuous sampling of forces exerted on the impeller. These steady impeller forces are interpreted as an average volute force at the whirl center and a force proportional to this displacement from the center. The average volute forces are usually called radial forces. Experiments were made on two different types of volutes; the first is a "conventional" volute in which the collection area grows linearly with angular position around the impeller, and the second is a simple toroid or "circular" volute of constant cross-sectional area with tangential discharge.

Here we summarize our findings on radial forces:

i) the magnitudes of the radial forces scale with the square of rotor speed with some slight departure for the higher rotor speeds and low flow coefficients.

ii) the agreement with most past experience is good.

iii) for the conventional volute the magnitude of the radial force is found to vanish at the design flow coefficient. Above and below this design value a linear behaviour (with respect to flow coefficient) is detected. Values of the forces are in close agreement with the experimental results of Agostinelli et al [4] and Iversen et al [44] but not so much with the experimental results of Domm and Hergt [33]. The overall magnitudes of the radial forces were lower for the circular volute. A linear decrease in these magnitudes was observed towards shut-off but the force did not vanish there due to possible manufacturing imperfections.

iv) in order to minimize radial wear ring interference with the measurements of radial forces, two set of radial face seals were selected to control leakage flows from the volute into the inlet and the back of the pump housing. There was then no noticeable change in radial force magnitudes when the front and back face seal clearances were increased from 0.14 to a maximum possible value of 0.79 mm (inlet leakage flows of two and twelve percent respectively). No experiments were conducted, however, with the seals in contact.

v) potential flow theories [29,33] underestimate the radial forces up to a factor of two.

One of the major results concerns the force due to the displacement of the impeller from the center of the volute. This additional fluid force is interpreted in terms of a "stiffness" matrix multiplying the position vector of the displaced impeller; linearity of this relationship is assumed. These matrices have been measured for the first time and their main features can be summarized as follows:

vi) each component of the hydrodynamic stiffness matrix scales with the square of rotor speed.

vii) the new and most important finding is that for both volutes, the stiffness matrix is the sum of a diagonal and skew-symmetric matrix and the diagonal terms give a negative spring constant. This finding may have a bearing on the "rough running" reported in many pumps.

viii) a two dimensional flow model of an impeller and volute was made with the impeller being represented by an actuator having an infinite number of vanes. The flow is assumed to be irrotational as in earlier impeller-volute models. The diagonal terms of the stiffness matrix are underpredicted by a factor of four and the important properties of the off diagonal terms are not predicted. From this it seems clear that such theories must include the effects of flow rotationality known to be present in such flows.

ix) a solid impeller having the same geometric dimensions as the one tested was used to estimate disk friction effects for shut-off conditions. The stiffness matrix so found was 25 percent of that at the design flow coefficient for the case of the conventional volute.

x) detailed measurements of static pressure distributions around the circumference of the conventional volute were made for various locations of the impeller center (on the whirl orbit) in order to determine how much the static pressure forces are responsible for the radial forces and stiffness matrices. The static pressure force components were smaller than the radial force components and they do not exhibit the same sign for the X-direction; this was in disagreement with Iversen et al [44]. Furthermore the static

pressure matrix (defined similarly as the stiffness matrix using static pressure forces only) came up to about 20 percent of the total measured stiffness matrix. These results show that the steady hydrodynamic impeller force contains a substantial component due to the non-isotropy of the net momemtum flux leaving the impeller.

As a final comment, we have shown by direct measurements that the steady fluid dynamic impeller forces caused by the volute can induce rotor whirl. Additional measurements of forces at non-zero whirl are needed in the future to obtain damping and inertia forces so that stability criteria can be evaluated.

Appendix A

DYNAMIC FORCES ON A WHIRLING CENTRIFUGAL ACTUATOR IMPELLER IN AN UNBOUNDED MEDIUM-APPARENT MASS EFFECTS AND STABILITY ANALYSIS

A.1. Statement of the Problem

As an application on the many uses of the actuator disk as defined in Chapter V, we will introduce a simple calculation of the forces acting on a whirling impeller in an unbounded medium. The problem to be solved is shown in Fig. A.1. Here a rotor with an infinite number of vanes of arbitrary shape and blade angle β is assumed to whirl about a stationary point with a constant eccentricity ε and a constant whirl speed ω. Let us denote the rotor center's instantaneous coordinates by (ε, ψ), where $\psi = \omega t$, t being time. Flow passes through the rotor from a source Q located either at the rotor center (whirling) or at the center of whirl (stationary). There may also be a preswirl circulation Γ. The assumptions of incompressible and inviscid flow are postulated. The equations of motion for the fluid in a frame attached to the rotor are

$$\nabla \left[\int_{r_o}^{r} \frac{\partial \underline{W}}{\partial t} \, \underline{dr} + \frac{1}{2}(\underline{W}^2 - \Omega^2 r^2) + p/\rho \right] = \underline{W} \times (2\underline{\Omega} + \nabla \times \underline{W}) + \frac{\underline{F_B}}{\rho} - \underline{a_N} \qquad (A.1)$$

where $\underline{W}$ is the relative velocity, Ω is the impeller angular speed, p is the static pressure, ρ is the density, $\underline{F_B}$ is the body force representing the action of the vanes in a frictionless flow and a_N is the acceleration of the center of the rotor. It is assumed that there is no "shock loss" at the inlet of the impeller when the inlet relative flow angle does not match the vane angle there. We can identify three regions of the flow through the impeller sketched in Fig. A.1; in the inlet

region, I, the body force $\underline{F_B}$ is zero as we assume the flow to be irrotational there. Region II is defined as the area occupied by the impeller between its inner radius r_1 and its outer radius r_2. There the body force $\underline{F_B}$ is perpendicular to the blades and hence also to $\underline{W}$, the relative velocity. Region III is defined as the exit region for $r > r_2$. The flow there is inherently rotational. Progress is readily made however if we assume irrotationality in the exit region leaving the problem of entrance losses and outer vortical flows to a subsequent paper.

A.2. Problem Formulation

The flow in regions I and III is seen to be irrotational and incompressible hence

$$\nabla^2 \varphi' = 0 \tag{A.2}$$

there. φ' is the usual potential velocity. The flow must satisfy kinematic conditions of the moving, rotating blade row. In addition, it is assumed that the velocity leaving the blades in region III is parallel to them there; this is the equivalent of the Kutta condition. To solve the problem illustrated in Fig. A.1, it is convenient to solve two simpler ones indicated in Figs. A.2a,b. In this the kinematic problem is decomposed to that of determining the flow field and forces on the impeller due to the acceleration $\underline{a_N}$ of the center of a non-rotating wheel having zero through flow, and second that due to the rotating impeller with through flow moving at speed $\underline{V_N}$. Evidently (see Fig. A.1)

$$\underline{V_N} = i\omega\varepsilon e^{i\psi} \tag{A.3a}$$

and

$$\underline{a_N} = -\omega^2 \varepsilon e^{i\psi} \qquad \text{(A.3b)}$$

In the present problem all of the essential unsteady effects are due to the acceleration of the rotor center. It is convenient to solve both the acceleration and velocity fields relative to the center of the moving impeller.

Two cases concerning the position of the center of the source-vortex (Q,Γ) are treated; the first one involves having it coincide with the center of the impeller while in the second case the source-vortex center is stationary at the origin of the whirl coordinates. Both cases can also feature "shrouded" and "unshrouded" impellers. In the "shrouded" case we use the fact that real pumps have axial inlets. Therefore this inlet flow can contribute only to a momentum drag due to the presence of the source in the absence of preswirl. There the force on the impeller is

$$\underline{F} = \rho \int_{\text{vol.}} (\underline{a_B} - \underline{a_\infty})\, d(\text{vol.}) + \rho \int_{C_3} \underline{V}(\underline{V}.\underline{n})ds + \int_{C_3} p\underline{n}ds \qquad \text{(A.4a)}$$

where

vol. is the volume between $r = r_1$ and $r = r_2$

$\underline{a_\infty}$ is the acceleration far from the impeller $(=-\underline{a_N})$

$\underline{a_B}$ is the acceleration relative to the blades

$\underline{V}$ is the velocity relative to the reference frame xy of a rotating blade

p is the static pressure

C_3 is the contour enclosing the impeller at $r = r_2$

$\underline{n}$ is the normal vector to the contour C_3.

In the "unshrouded" case the inlet flow is assumed to be radial, i.e., a fully two-dimensional model is considered. There the force on the impeller is

$$\underline{F} = \rho \int_{vol.} (\underline{a_B} - \underline{a_\infty})\, d(vol.) + \rho \int_{C_3} \underline{V}(\underline{V}.\underline{n})ds + \int_{C_3} p\underline{n}ds$$

$$- \rho \int_{C_1} \underline{V}(\underline{V}.\underline{n})ds - \int_{C_1} p\underline{n}ds \ , \qquad \text{(A.4b)}$$

where C_1 is the contour at the impeller entrance ($r = r_1$). We will first calculate the forces due to the acceleration field for the various cases under consideration.

A.3. The Acceleration Field-Apparent Mass effect

It is somewhat more convenient to work with the acceleration potential

$$\Phi = -p/\rho \qquad \text{(A.5)}$$

since the equations of motion are then

$$\underline{a_I} = \nabla \Phi_I \text{ for } r < r_1$$

$$\underline{a_{II}} = \nabla \Phi_{II} + \underline{F_B}/\rho \ , \ r_1 < r < r_2$$

and

$$\underline{a_{III}} = \nabla \Phi_{III} \ , \ r > r_2 \qquad \text{(A.6)}$$

for the three regions shown if Fig. A.2a . The conditions to be satified are

$$\nabla \Phi_{III} \rightarrow \underline{a_\infty} \text{ as } r \rightarrow \infty \ , \tag{A.7a}$$

and continuity of the acceleration component in the radial direction at the boundaries of region II, i.e.,

$$a_{r_{III}}(r=r_2 \, , \, \theta) = a_{r_{II}}(r=r_2 \, , \, \theta) \tag{A.7b1}$$

$$a_{r_{II}}(r=r_1 \, , \, \theta) = a_{r_I}(r=r_1 \, , \, \theta) \ . \tag{A.7b2}$$

The force field of Eq. A.6 must be perpendicular to the acceleration field (this is the flow tangency condition) so that

$$a_{r_{II}}(r=r_1 \, , \, \theta+\Delta\theta) = a_{r_{II}}(r=r_2 \, , \, \theta) \cdot \left[\frac{r_2}{r_1}\right] \tag{A.7c}$$

where $\Delta\theta$ is the angular difference subtended by one blade.

An additional relation is necessary in order to solve for the acceleration potentials of Eq. A.5 . The pressure field must be finite at the origin. The acceleration potential Φ, since it is proportional to the physical pressure, must be single valued. This means that if the potential is got by integrating Eqs. A.6 around a closed contour as shown in Fig. A.2a, we must have

$$\Delta\Phi = \Phi_b - \Phi_a + \Phi_c - \Phi_b + \Phi_d - \Phi_c + \Phi_a - \Phi_d = 0 \ . \tag{A.8}$$

Each of these differences occurs within a different region of the flow. That portion within the impeller, region II, is integrated along a blade so that $\underline{F_B}$ makes no contribution there. We need solutions of Φ for regions III and I since these are

connected by the continuity relations of Eq. A.7. Clearly $\nabla^2\Phi = 0$ and hence possible solutions are of the form

$$\Phi_{III} = a_\infty r\cos(\theta - \psi) + \sum_{k=1}^{\infty} r^{-k} (a_k \cos k\theta + b_k \sin k\theta) \qquad (A.9a)$$

for $r > r_2$ and

$$\Phi_I = \sum_{k=1}^{\infty} r^{-k} (a'_k \cos k\theta + b'_k \sin k\theta) \qquad (A.9b)$$

for $r < r_1$. The coefficients a_k, b_k and a'_k, b'_k are connected by the matching conditions of Eq. A.7b and through Eq. A.8. The terms of Eq. A.8 within region II are evaluated readily by noting that

$$a_{r_{II}}(r,\theta) = \frac{r_2}{r_1} a_{r_{III}}(r_2, \theta) \ .$$

In this way we find that $a_k = b_k = a'_k = b'_k = 0$, $k \geq 2$ and that

$$\Phi_{III}(r,\theta) = a_\infty r\cos(\theta - \psi)\left[1 + \frac{r_2^2}{r^2}\frac{c}{2+c}\right] \qquad (A.10a)$$

and

$$\Phi_I(r,\theta) = a_\infty r \frac{r_2}{r}\left[\frac{2}{2+c}\right]\cos(\theta - \psi - \Delta\theta) \qquad (A.10b)$$

where

$$c = \int_{r_1}^{r_2} \frac{dr}{r\cos^2\beta(r)} \quad . \tag{A.10c}$$

Here $\beta(r)$ is the vane angle as a function of position on the blade. For a logarithmic blade, $\beta(r) = \beta$ = constant and

$$c = \frac{\ln(r_2/r_1)}{\cos^2(\beta)} \quad . \tag{A.10d}$$

It is perhaps worthwhile to mention that the acceleration in the inner region I is a linear one proportional to a_N but in general it is in a different direction by the amount $\Delta\theta$ except for a radial impeller where $\Delta\theta = \beta = 0$. Forces due to the centrifugal acceleration can now be found using parts of the momentum equation (Eqs. A.4a,b). Closed form solutions for logarithmic and radial impellers can then be expressed as

$$\underline{F_A} = -\varepsilon\omega^2 e^{i\psi} M_a \quad , \tag{A.11a}$$

that is a pure centripetal force. M_a represents the added mass effect and is equal to

$$M_a = \pi\rho r_2^2 \left\{ \frac{2c}{2+c} + 1 - (r_1/r_2)^2 \right\} \tag{A.11b}$$

in the case of an unshrouded impeller. Fig. A.3 shows this added mass normalized by $\pi\rho r_2^2$ plotted versus rotor blade angle β for various values of r_1/r_2. It is perhaps worthwhile to note the apparent mass to be three times the displaced mass of the impeller when $r_1 \to 0$. This result is valid for radial and logarithmic

impellers.

A.4. The Velocity Field for the Case of the Source-Vortex at the Origin of the Moving Impeller. Stability Analysis

Here we seek the velocity field of the rotating impeller immersed in the steady velocity field $\underline{V_\infty}$ of Fig. A.2 . The velocity potentials φ' in regions I and III have precisely the same form as Eqs. A.9a,b except that source and vortex terms are added; we have also the same continuity condition of Eq. A.7b wherein the radial velocities must conserve volume flow. Also far from the impeller

$$\nabla \varphi'_{III} \rightarrow \underline{V_\infty} \ . \tag{A.12}$$

There is one principal difference however which is the flow leaving the impeller is assumed to be tangent to the blades there. This requires

$$\left(r_2\Omega - \frac{\partial \varphi'_{III}}{r\partial\theta} \right) \cot\beta = \frac{\partial \varphi'_{III}}{\partial r} \quad \text{at } r = r_2 \ . \tag{A.13}$$

It is also understood that ε is such as the flow is outward there. For φ'_{III} we have

$$\varphi'_{III} = -V_\infty r\sin(\theta - \psi) + \frac{Q}{2\pi}\ln r + \frac{\Gamma_2}{2\pi}\theta + \sum_{k=1}^{\infty} r^{-k}\,(a_k\cos k\theta + b_k\sin k\theta) \tag{A.14}$$

We have then, by application of Eq. A.13

$$\Gamma_2 = 2\pi r_2^2\Omega - Q\tan\beta \ ,$$

and for an impeller of arbitrary blade shape

$$\varphi'_{III}(r,\theta) = \frac{Q}{2\pi}\ln r + \frac{\Gamma_2}{2\pi}\theta - V_\infty r\sin(\theta - \psi) + \frac{r_2^2}{r}V_\infty\sin(\theta - \psi - \beta) \quad . \qquad (A.15)$$

For a radial blade ($\beta = 0$) , the influence of the flow past the impeller is that of a simple doublet. The inner solution is readily found and consists of a uniform flow, the source and the original vortex at the center. For completeness,

$$\varphi'_I(r,\theta) = \frac{Q}{2\pi}\ln r + \frac{\Gamma}{2\pi}\theta - 2V_\infty r\frac{r_2}{r_1}\cos\beta\sin(\theta - \psi - \beta - \Delta\theta) \quad . \qquad (A.16)$$

Pressure may be calculated from the Bernouilli Equation in the steady reference frame of Fig. A.2b and with this the momentum equation (Eqs. A.4a,b) can be applied to obtain the resultant force due to the motion of the impeller. For axial inlets ("shrouded" case)

$$\underline{F'_V} = \rho V_\infty \Gamma_2 \, \underline{e_r} \qquad (A.17)$$

where $\underline{e_r}$ is a unit vector aligned with the axis of whirl O'O of Fig. A.1. $\underline{F'_V}$ is then merely a lift force that cannot contribute to rotor dynamic instability. However for an "unshrouded" impeller we must add the contributions of the pressure force and momentum flux on the inner contour, C_1 of Fig. A.1 . Then the force is

$$\underline{F'_V} = \left\{ \rho V_\infty \Gamma_2 - 2V_\infty \frac{r_2}{r_1}\cos\beta\left[Q\sin(\beta + \Delta\theta) + \Gamma\cos(\beta + \Delta\theta)\right] \right\} \underline{e_r}$$

$$+ \left\{ 2V_\infty \frac{r_2}{r_1}\cos\beta\left[Q\cos(\beta + \Delta\theta) - \Gamma\sin(\beta + \Delta\theta)\right] \right\} \underline{e_\psi} \quad . \qquad (A.18)$$

It is clear that the presence of a tangential component (terms in $\underline{e_\psi}$ may enhance rotor whirl. In fact for $|\beta| < 90°$ and for

$$Q\cos(\beta + \Delta\theta) > \Gamma\sin(\beta + \Delta\theta) \qquad (A.19)$$

self-excitation is achieved. Fig. A.4 shows the magnitude of the normalized tangential force (terms in $\underline{e_\psi}/\rho Q V_\infty$) for various logarithmic rotor blade angles β, Γ/Q ratios and for $r_1/r_2 = 0.5$. When this tangential force is positive, the theory predicts an unstable regime. This is even true for Impeller X ($\beta = 25°$) for $\Gamma/Q < 1$. The prediction that $\underline{F'_Y}$, a damping force, be destabilizing for such a simple case is contrary to what was observed experimentally by Ohashi and Shoji [57]. The main conclusion is that this theory is unsatisfactory unless vortex shedding and viscous losses are added to the analysis.

A.5. The Velocity Field for the Case of a Stationary Source-Vortex at the Center of Whirl

We wish now to investigate the case of a stationary inlet source. For simplicity we have neglected prerotation Γ. The problem can still be split into the two simpler ones of Figs. A.2a,b . The acceleration field is the same as in section A.3 with the force on the impeller due to the acceleration of the rotor center given by Eqs. A.11a,b. The outer velocity field of region III also remains unchanged with the force due to the motion of the impeller given by Eq. A.17 for the "shrouded" case. The only difference comes from the inner flow solution of region I as seen in Fig. A.2a. We will then have a different "unshrouded" impeller force resulting from the source seen as being displaced from the origin of the impeller by the given eccentricity ε (this is not shown in Fig. A.2). Solution of the inner flow field is achieved through use of the circle theorem to satisfy the proper boundary conditions at the impeller inlet ($r = r_1$). There the radial velocity is

$$V_{rI}(r_1,\theta) = \frac{Q}{2\pi r_1} - 2V_\infty \frac{r_2}{r_1}\cos\beta\sin(\theta - \psi - \beta - \Delta\theta) \quad . \tag{A.20a}$$

Then the tangential velocity at $r = r_1$ becomes

$$V_{\theta I}(r_1,\theta) = -\frac{Q}{\pi} \cdot \frac{\varepsilon\sin(\theta - \psi)}{\varepsilon^2 + r_1^2 + 2\varepsilon r_1\cos(\theta - \psi)}$$

$$- 2V_\infty \frac{r_2}{r_1}\cos\beta\sin(\theta - \psi - \beta - \Delta\theta) \quad . \tag{20b}$$

Contributions of the pressure and momentum flux on the inner contour C_1 can then be evaluated. These consist of a series of definite integrals somewhat hard to evaluate. Finally one finds

$$\underline{F'_Y} = \left\{ \rho V_\infty \Gamma_2 - \rho \frac{Q^2}{2\pi} \frac{\varepsilon}{r_1^2 - \varepsilon^2} - 2V_\infty \frac{r_2}{r_1} Q\cos\beta\sin(\beta + \Delta\theta) \right\} \underline{e_r}$$

$$+ \left\{ 2V_\infty Q \frac{r_2}{r_1}\cos\beta\cos(\beta + \Delta\theta) \right\} \underline{e_\psi} \quad . \tag{A.21}$$

It is interesting to note the similarity between Eqs. A.18 and A.21 for $\Gamma = 0$. They both exhibit the same tangential force and almost the same radial force except for the term involving Q^2. Therefore the same conclusions about the inadequacy of this theory apply. For completeness, we will refer to Fig. A.4 for the case $\Gamma/Q = 0$ to illustrate the tangential component of the preceding damping force.

A.6. Concluding Remarks

The forces on a whirling impeller in an unbounded medium are seen to consist of a "centrifugal" effect due to the apparent mass and an inwards "lift" force due to the circulation about the rotor for the case of an axial inlet, whether this inlet is stationary or whirling with the impeller.These are conservative forces which may be useful carrying out a vibration analysis, and they cannot lead to any form of unusual rotor vibration excitation. However when the inlet flow is purely radial, a tangential self-exciting or self-damping force can exist depending on blade geometry. It is perhaps interesting that the value of this tangential force does not depend on the relative position/motion of the inlet source. These findings, however, contradict known experimental results that show this force to be of a damping nature.

Certain improvements to the calculations can be readily imagined; for example, an incident angle-dependent shock loss would lead to a rotational outer flow having a different result from the present one. This will be the subject of future reports.

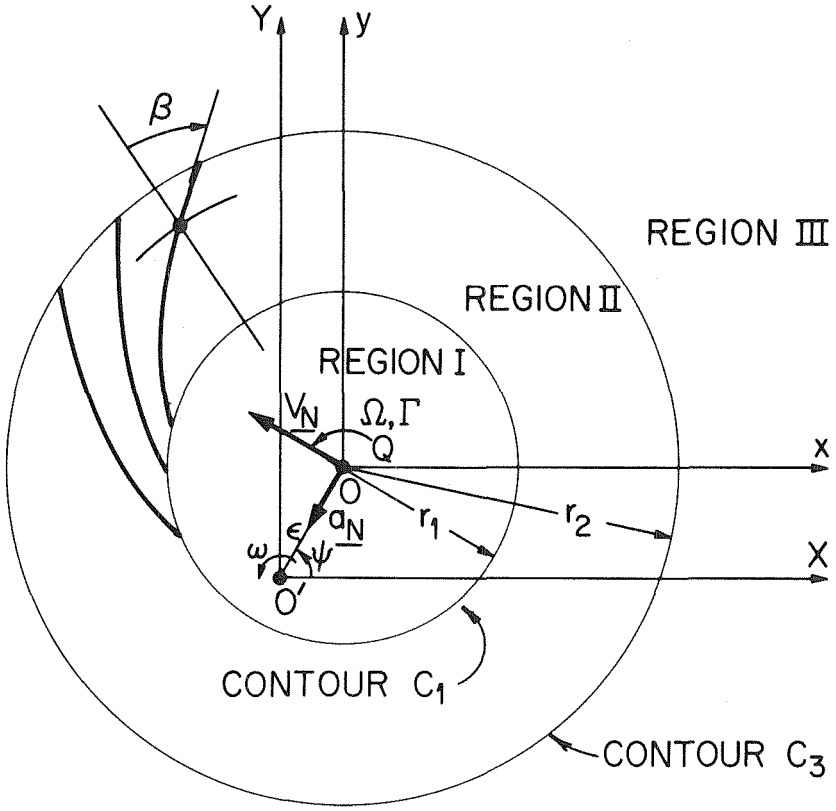

Fig. A.1. Sketch showing definitions of impeller parameters. The impeller blade coordinates are defined relative to the (xy) axes. The impeller rotates at angular velocity Ω in respect to the origin O of this system. This center, O, whirls at frequency ω about the center O' of a fixed coordinate system XY. Note that (xy) and (XY) axes do not rotate. The distance O' to O is ϵ and the angular position of O' is ψ. Q is the source strength and Γ is the circulation of the flow entering the impeller (region I). $\underline{V_N}$ and $\underline{a_N}$ are the tangential velocity and acceleration of the point O in respect to the fixed center O' respectively.

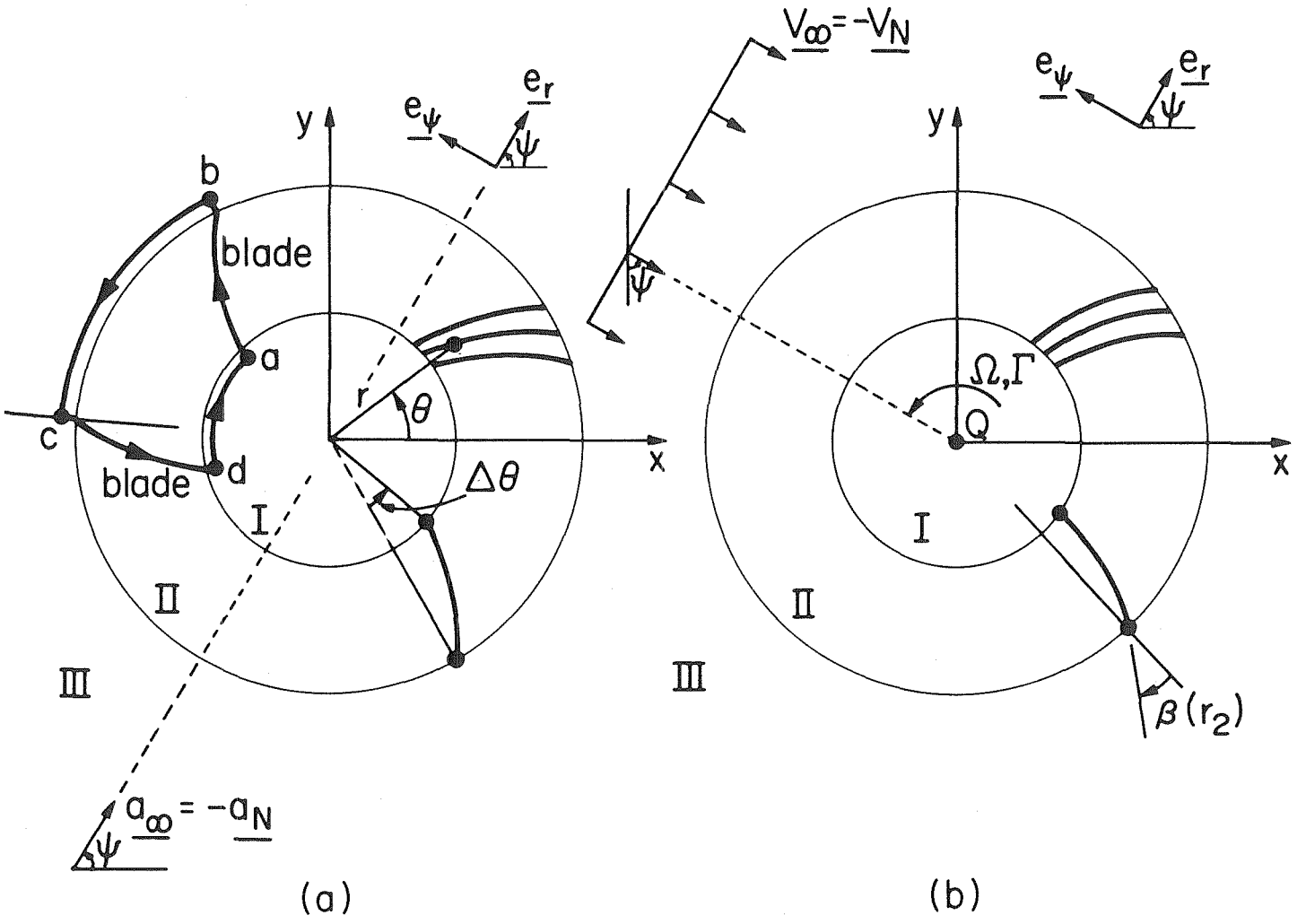

Fig. A.2. Sketch showing boundary conditions for the (a) acceleration field and (b) velocity field due to the motion of point O relative to O' of Fig. A.1.

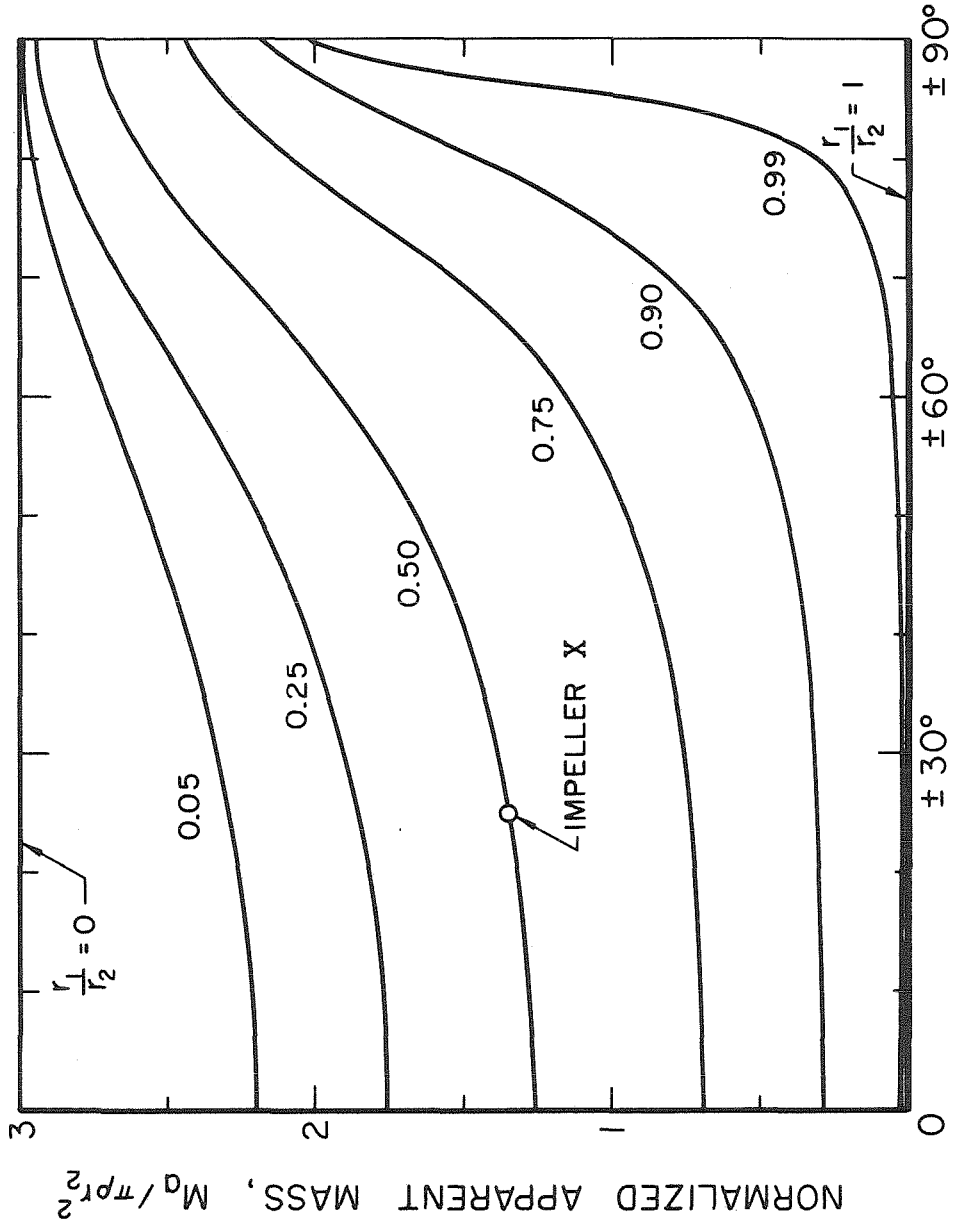

Fig. A.3. Normalized apparent mass of an accelerating actuator disk in an infinite medium plotted versus rotor blade angle β for various inlet over outlet radius ratios. A logarithmic blade shape is assumed.

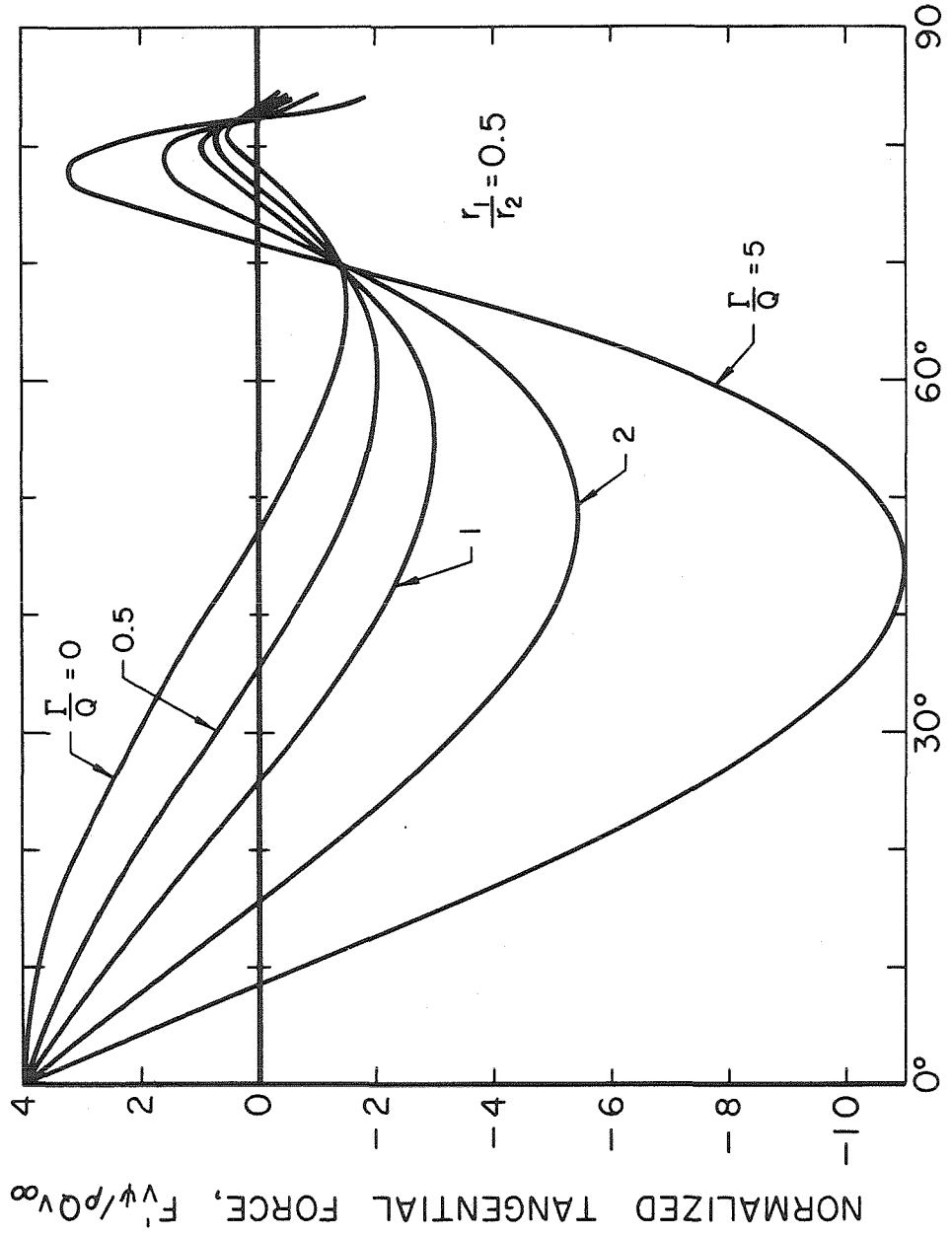

Fig. A.4. Magnitude of the normalized tangential force plotted versus rotor blade angle for various Γ/Q ratios and for $r_1/r_2 = 0.5$. An unstable regime exists for all positive values while a stable regime exits for all negative values. For comparison purposes, Impeller X has an exit blade angle of 25°.

Appendix B

EXPRESSIONS FOR S_3, S_4, S_5 AND S_6

We herein give the full expresions for S_3, S_4, S_5 and S_6 as defined in Equation 5.21. These are

$$S_3 = \int_0^{\pi}\int_0^{\pi} \left\{A_0(1 + \cos\lambda) + \sum_{k=1}^{\infty} A_k \sin\lambda \sin k\lambda\right\} d\lambda d\lambda'$$

$$\cdot \left\{A_0(1 + \cos\lambda') + \sum_{k=1}^{\infty} A_k \sin\lambda' \sin k\lambda'\right\} \cdot \exp\left\{\frac{a\Theta_M}{2}(\cos\lambda - 1) - \ln(\delta_o/r_2)\right\}$$

$$\cdot \frac{\sin[\frac{\Theta_M}{2}(\cos\lambda - 1)]\,\sin[\frac{\Theta_M}{2}(\cos\lambda - \cos\lambda')] + \cos[\frac{\Theta_M}{2}(\cos\lambda - 1)]\,\sinh[\frac{a\Theta_M}{2}(\cos\lambda - \cos\lambda')]}{\cosh[\frac{a\Theta_M}{2}(\cos\lambda - \cos\lambda')] - \cos[\frac{\Theta_M}{2}(\cos\lambda - \cos\lambda')]}$$

$$- \frac{4}{\Theta_M} \frac{\sin[\frac{\Theta_M}{2}(\cos\lambda - 1)] + a\cos[\frac{\Theta_M}{2}(\cos\lambda - 1)]}{(1 + a^2)(\cos\lambda - \cos\lambda')} \qquad \text{(B.1)}$$

and

$$S_4 = \int_0^{\pi}\int_0^{\pi} \left\{A_0(1 + \cos\lambda) + \sum_{k=1}^{\infty} A_k \sin\lambda \sin k\lambda\right\} d\lambda d\lambda'$$

$$\cdot \left\{A_0(1 + \cos\lambda') + \sum_{k=1}^{\infty} A_k \sin\lambda' \sin k\lambda'\right\} \cdot \exp\left\{\frac{a\Theta_M}{2}(\cos\lambda - 1) - \ln(\delta_o/r_2)\right\}$$

$$\cdot \frac{\cos[\frac{\Theta_M}{2}(\cos\lambda-1)]\sin[\frac{\Theta_M}{2}(\cos\lambda-\cos\lambda')] - \sin[\frac{\Theta_M}{2}(\cos\lambda-1)]\sinh[\frac{a\Theta_M}{2}(\cos\lambda-\cos\lambda')]}{\cosh[\frac{a\Theta_M}{2}(\cos\lambda-\cos\lambda')] - \cos[\frac{\Theta_M}{2}(\cos\lambda-\cos\lambda')]}$$

$$- \frac{4}{\Theta_M} \frac{\cos[\frac{\Theta_M}{2}(\cos\lambda-1)] - a\sin[\frac{\Theta_M}{2}(\cos\lambda-1)]}{(1+a^2)(\cos\lambda-\cos\lambda')} \qquad (B.2)$$

for S_3 and S_4 and

$$S_5 = \int_0^{\pi}\int_0^{\pi} \left\{A_0(1+\cos\lambda) + \sum_{k=1}^{\infty} A_k \sin\lambda \sin k\lambda\right\} d\lambda d\lambda'$$

$$\cdot \left\{A_0(1+\cos\lambda') + \sum_{k=1}^{\infty} A_k \sin\lambda' \sin k\lambda'\right\} \cdot \exp\left\{\frac{a\Theta_M}{2}(\cos\lambda-1) - \ln(\delta_o/r_2)\right\} \qquad (B.3)$$

$$\cdot \frac{\sin[\frac{\Theta_M}{2}(\cos\lambda-1)]\sin[\frac{\Theta_M}{2}(\cos\lambda-\cos\lambda')] + \cos[\frac{\Theta_M}{2}(\cos\lambda-1)]\sinh[\frac{a\Theta_M}{2}(\cos\lambda+\cos\lambda') - Y_1]}{\cosh[\frac{a\Theta_M}{2}(\cos\lambda+\cos\lambda') - Y_1] - \cos[\frac{\Theta_M}{2}(\cos\lambda-\cos\lambda')]}$$

and

$$S_6 = \int_0^{\pi}\int_0^{\pi} \left\{A_0(1+\cos\lambda) + \sum_{k=1}^{\infty} A_k \sin\lambda \sin k\lambda\right\} d\lambda d\lambda'$$

$$\cdot \left\{A_0(1+\cos\lambda') + \sum_{k=1}^{\infty} A_k \sin\lambda' \sin k\lambda'\right\} \cdot \exp\left\{\frac{a\Theta_M}{2}(\cos\lambda-1) - \ln(\delta_o/r_2)\right\} \qquad (B.4)$$

$$\cdot \frac{\cos[\frac{\theta_M}{2}(\cos\lambda-1)]\sin[\frac{\theta_M}{2}(\cos\lambda-\cos\lambda')]-\sin[\frac{\theta_M}{2}(\cos\lambda-1)]\sinh[\frac{a\theta_M}{2}(\cos\lambda+\cos\lambda')-Y_1]}{\cosh[\frac{a\theta_M}{2}(\cos\lambda+\cos\lambda')-Y_1]-\cos[\frac{\theta_M}{2}(\cos\lambda-\cos\lambda')]},$$

for S_5 and S_6 with $Y_1 = 2\ln(\delta_o/r_2) + a\theta_M$.

Appendix C

COMPUTER PROGRAMS

C.1. Program FORCE

```
c  This Program is the property of Dimitri S. CHAMIEH.
c           Subroutines written by P. C. CHEN.
c  It computes all the numbers needed for the calculation of forces
c  acting on an actuator disk impeller eccentrically located within
c  a logarithmic spiral volute with the assumptions of irrotational
c  inviscid flows, small eccentricities and flow rates close to
c  design. Along with program TEST it computes dimensionless impeller
c  force components and dimensionless stiffness matrix components.
c  For use on IBM 370/3032
c
c.....................MAIN PROGRAM.........................
c
//FORCE  JOB(*****,***,***),'FORCE',TIME=120,CLASS=X
/*JOBPARM REGION=500K
/*JOBPARM LINES=15
//   EXEC FORTXCLG,PARM.FORT='OPTIMIZE(2)'
//FORT.SYSIN DD *
        IMPLICIT REAL*8(A-H,O-Z)
        REAL*4 DDZERO(21),DDCC(21),DDCS(21),
     .         GZ(21),GZ1(21),GZ2(21),
     .         GC(21),GC1(21),GC2(21),
     .         GS(21),GS1(21),GS2(21),
     .         DDBXB(50,21),DDBXB1(50,21),DDBXB2(50,21)
c
        DIMENSION BFOUR(21,22),B1(21,22),B2(21,22),
     .            BXB(21,21),BXB1(21,21),BXB2(21,21),
     .            CZFOUR(21),CCFC(21),CSFS(21)
c
        COMMON/CF/DN,R2,ADN,TETMAX,BETA,PI,TAU2
        common ih
        common /bcf/ib,jb
        common limn
c
c  Impeller and volute geometric data and flow conditions data.
c
        DATA OMEGA,Q,QDES/104.7D0,4.1D0,4.3D0/
        DN=0.3D0
        ADN=0.1418D0
        R2=0.265D0
        BETA=0.436D0
        PI=DARCOS(-1.0D0)
        TETMAX=2.2D0*PI
        QH=(QDES-Q)/QDES
        TAU2=2.0D0*PI*OMEGA*R2*R2-Q*DTAN(BETA)
c
c  Enter number of harmonics and Romberg integration number.
c
        NHI=10
        mMAX=7
        limn=NHI
        NHI2=NHI+1
c
        WRITE(6,2000)DN,R2,ADN,TETMAX,BETA,PI,TAU2,OMEGA,Q,QDES,
     .               QH,NHI,NHI2,mMAX
 2000   FORMAT(1X/1X,'DN=',D14.7/1X,'R2=',D14.7/1X,'ADN=',D14.7/
     .         1X,'TETMAX=',D21.14/1X,'BETA=',D14.7/1X,'PI=',D21.14/
     .         1X,'TAU2=',D21.14/1X,'OMEGA=',D14.7/1X,'Q=',D14.7/
     .         1X,'QDES=',D14.7/1X,'QH=',D21.14/1X,'NHI=',I3/1X,
     .         'NHI2=',I3/1X,'mMAX=',I3//)
```

```
c
c  Evaluation of the double Fourier serie expansions of the kernel.
c  BFOUR(ib,jb) corresponds to mMax, B1(ib,jb) to mMax-1 and
c  B2(ib,jb) to mMAX-2.
c
      WRITE(6,2005)
 2005 FORMAT(1X,'BFOUR(L,M); Left to Right decreasing mMAX'/)
      do 20 ib=1,NHI
        do 10 jb=1,NHI2
          call doubin(ssg,ib,jb,mMAX)
          call doubin(ssg1,ib,jb,mMAX-1)
          call doubin(ssg2,ib,jb,mMAX-2)
          write(6,2010) ib,jb,ssg,ssg1,ssg2
 2010     format(1x,I2,2x,I2,3x,d21.14,3x,d21.14,3x,d21.14)
          BFOUR(ib,jb)=ssg
          B1(ib,jb)=ssg1
          B2(ib,jb)=ssg2
 10     continue
 20   continue
c
c  Evaluation of the Cosine Fourier serie expansion of the right
c  hand side of the integral equation. CZFOUR corresponds to Eq.
c  5.32a, CCFC to Eq. 5.32b and CSFS to Eq.5.32c. These results
c  are automatically divided by PI as they appear in Eq. 5.39.
c
      WRITE(6,2015)
 2015 FORMAT(//1x,'Right Hand Side Fourier Decompositions'/)
      do 30 ih=1,NHI
        CZFOUR(ih)=0.0d0
        if(ih.eq.1)CZFOUR(1)=4.0D0*QH*TAU2/(R2*TETMAX*PI)
        call rinteg(sfc,sfs)
        CCFC(ih)=sfc*4.0d0*(1.0d0+ADN*ADN)*TAU2/(TETMAX*DN*PI)
        CSFS(ih)=sfs*4.0d0*(1.0d0+ADN*ADN)*TAU2/(TETMAX*DN*PI)
      WRITE(6,2020)ih,CZFOUR(ih),ih,CCFC(ih),ih,CSFS(ih)
 2020 FORMAT(1X,'CZFOUR(',I2,')=',D21.14,5X,'CCFC(',I2,')=',
     .       D21.14,5X,'CSFS(',I2,')=',D21.14)
      DDZERO(ih)=CZFOUR(ih)
      DDCS(ih)=CSFS(ih)
      DDCC(ih)=CCFC(ih)
 30   CONTINUE
c
c  Simultaneous equation matrix as defined by Eq. 5.39.
c
      DO 40 I=1,NHI
c
      BXB(I,1)=BFOUR(I,1)+BFOUR(I,2)/2.0D0
      BXB1(I,1)=B1(I,1)+B1(I,2)/2.0D0
      BXB2(I,1)=B2(I,1)+B2(I,2)/2.0D0
      IF(I.EQ.1)BXB(I,1)=BXB(I,1)-4.0D0/TETMAX
      IF(I.EQ.1)BXB1(I,1)=BXB1(I,1)-4.0D0/TETMAX
      IF(I.EQ.1)BXB2(I,1)=BXB2(I,1)-4.0D0/TETMAX
c
      BXB(I,2)=BFOUR(I,1)/2.0D0-BFOUR(I,3)/4.0D0
      BXB1(I,2)=B1(I,1)/2.0D0-B1(I,3)/4.0D0
      BXB2(I,2)=B2(I,1)/2.0D0-B2(I,3)/4.0D0
      IF(I.EQ.2)BXB(I,2)=BXB(I,2)+4.0D0/TETMAX
      IF(I.EQ.2)BXB1(I,2)=BXB1(I,2)+4.0D0/TETMAX
      IF(I.EQ.2)BXB2(I,2)=BXB2(I,2)+4.0D0/TETMAX
c
      DO 40 J=3,NHI
      BXB(I,J)=(BFOUR(I,J-1)-BFOUR(I,J+1))/4.0D0
      BXB1(I,J)=(B1(I,J-1)-B1(I,J+1))/4.0D0
      BXB2(I,J)=(B2(I,J-1)-B2(I,J+1))/4.0D0
      IF(I.EQ.J)BXB(I,J)=BXB(I,J)+4.0D0/TETMAX
      IF(I.EQ.J)BXB1(I,J)=BXB1(I,J)+4.0D0/TETMAX
      IF(I.EQ.J)BXB2(I,J)=BXB2(I,J)+4.0D0/TETMAX
```

```
c
 40     CONTINUE
        WRITE(6,2030)
 2030   FORMAT(1X//1X,'I , J',15X,'BXB',24X,'BXB1',24X,'BXB2'/)
        DO 50 I=1,NHI
        DO 50 J=1,NHI
        DDBXB(I,J)=BXB(I,J)
        DDBXB1(I,J)=BXB1(I,J)
        DDBXB2(I,J)=BXB2(I,J)
        WRITE(6,2040)I,J,BXB(I,J),BXB1(I,J),BXB2(I,J)
 2040   FORMAT(1X,I2,',',I2,5X,D21.14,4X,D21.14,4X,D21.14)
 50    CONTINUE
c
c  Evaluate Glauert series terms. EQSOV is a simultaneous equation
c  solver with iterative improvement and is a CALTECH subroutine.
c  GZ, GZ1 and GZ2 belong to Eq. 5.32a for mMAX, mMAX-1 and mMax-2.
c  GC, GC1 and GC2 belong to Eq. 5.32b for mMAX, mMAX-1 and mMax-2.
c  GS, GS1 and GS2 belong to Eq. 5.32c for mMAX, mMAX-1 and mMax-2.
c
        CALL EQSOV(NHI,DDBXB,DDZERO,10,0.00001,GZ,IT1,2)
        CALL EQSOV(NHI,DDBXB1,DDZERO,10,0.00001,GZ1,IT2,2)
        CALL EQSOV(NHI,DDBXB2,DDZERO,10,0.00001,GZ2,IT3,2)
        CALL EQSOV(NHI,DDBXB,DDCC,10,0.00001,GC,IT4,2)
        CALL EQSOV(NHI,DDBXB1,DDCC,10,0.00001,GC1,IT5,2)
        CALL EQSOV(NHI,DDBXB2,DDCC,10,0.00001,GC2,IT6,2)
        CALL EQSOV(NHI,DDBXB,DDCS,10,0.00001,GS,IT7,2)
        CALL EQSOV(NHI,DDBXB1,DDCS,10,0.00001,GS1,IT8,2)
        CALL EQSOV(NHI,DDBXB2,DDCS,10,0.00001,GS2,IT9,2)
c
        WRITE(6,2050)IT1,IT2,IT3,IT4,IT5,IT6,IT7,IT8,IT9
 2050   FORMAT(1X//1X,'Conversion Iterations in order (1 to 9):',
     .          9I5//1X,' GLAUERT COEFFICIENTS : ZEROTH, COSINE ',
     .          'AND SINE BLOCKS'/3x,'From left to right, mMAX, ',
     .          'mMAX-1 and mMAX-2 Blocks'//)
        DO 60 I=1,NHI
        WRITE(6,2060)I,GZ(I),GZ1(I),GZ2(I)
 2060   FORMAT(1X,I3,5X,E14.7,5X,E14.7,5X,E14.7)
 60     CONTINUE
        DO 70 I=1,NHI
        WRITE(6,2070)I,GC(I),GC1(I),GC2(I)
 2070   FORMAT(1X,I3,5X,E14.7,5X,E14.7,5X,E14.7)
 70     CONTINUE
        DO 80 I=1,NHI
        WRITE(6,2080)I,GS(I),GS1(I),GS2(I)
 2080   FORMAT(1X,I3,5X,E14.7,5X,E14.7,5X,E14.7)
 80     CONTINUE
c
c  Evaluation of U1 and U2 according to Eq. 5.34a.
c
        call ginteg(sgz,GZ)
        call ginteg(sgz1,GZ1)
        call ginteg(sgz2,GZ2)
        call ginteg(sgc,GC)
        call ginteg(sgc1,GC1)
        call ginteg(sgc2,GC2)
        call ginteg(sgs,GS)
        call ginteg(sgs1,GS1)
        call ginteg(sgs2,GS2)
c
        call gintgg(suz,GZ)
        call gintgg(suz1,GZ1)
        call gintgg(suz2,GZ2)
        call gintgg(suc,GC)
        call gintgg(suc1,GC1)
        call gintgg(suc2,GC2)
        call gintgg(sus,GS)
        call gintgg(sus1,GS1)
        call gintgg(sus2,GS2)
```

```
c
      write(6,2090)sgz,sgz1,sgz2,sgc,sgc1,sgc2,sgs,sgs1,sgs2,
     .             suz,suz1,suz2,suc,suc1,suc2,sus,sus1,sus2
 2090 Format(//1X,'FROM LEFT TO RIGHT DECREASING mMAX BLOCKS'/
     .       1X,'U1ZERO'/1X,D21.14,5X,D21.14,5X,D21.14//
     .       1X,'U1COS'/1X,D21.14,5X,D21.14,5X,D21.14//
     .       1X,'U1SIN'/1X,D21.14,5X,D21.14,5X,D21.14//
     .       1X,'U2ZERO'/1X,D21.14,5X,D21.14,5X,D21.14//
     .       1X,'U2COS'/1X,D21.14,5X,D21.14,5X,D21.14//
     .       1X,'U2SIN'/1X,D21.14,5X,D21.14,5X,D21.14//)
c
      STOP
      END
c
c.....................SUBROUTINES.............................
c
c  Double Fourier decomposition subroutine
c
      subroutine doubin(ssf,ib,jb,m)
      IMPLICIT REAL*8(A-H,O-Z)
      double precision t(20,20)
      double precision ssf
      pi=darcos(-1.0d0)
      a=0.0d0
      b=pi
      call integ(a,fa,ib,jb,m)
      call integ(b,fb,ib,jb,m)
        m1=m+1
      do 200 k=1,m1
        t(1,k)=(fa+fb)*(b-a)/(2**k)
        if (k.eq.1) go to 200
           m12=2**(k-1)-1
        do 210 n=1,m12
          call integ(a+n*(b-a)/2**(k-1),fyc,ib,jb,m)
          t(1,k)=t(1,k)+(b-a)*fyc/(2**(k-1))
 210    continue
 200  continue
      do 220 i=1, m
          mi=m-i+1
        do 230 jj=1,mi
           j=jj-1
          t(i+1,j+1)=((4**i)*t(i,j+2)-t(i,j+1))/((4**i)-1)
 230    continue
 220  continue
      ssf=t(m+1,1)
      return
      end
c
c  Subroutine of the double Fourier decomposition subroutine
c
      subroutine integ(yc,sf,ib,jb,m)
      IMPLICIT REAL*8(A-H,O-Z)
      double precision t(20,20)
      double precision sf
      pi=darcos(-1.0d0)
      a=0.0d0
      b=pi
        m1=m+1
      do 310 k=1,m1
        t(1,k)=(fnk(a,yc)+fnk(b,yc))*(b-a)/(2**k)
        if (k.eq.1) go to 310
           m12=2**(k-1)-1
        do 300 n=1,m12
          t(1,k)=(b-a)*fnk(a+n*(b-a)/2**(k-1),yc)/(2**(k-1))
    *+t(1,k)
 300    continue
 310  continue
      do 330 i=1, m
         mi=m-i+1
```

```
          do 320 jj=1,mi
             j=jj-1
            t(i+1,j+1)=((4**i)*t(i,j+2)-t(i,j+1))/((4**i)-1)
 320      continue
 330    continue
        sf=t(m+1,1)
        return
        end
c
c  Single Fourier decomposition subroutine
c
        subroutine rinteg(sfc,sfs)
        IMPLICIT REAL*8(A-H,O-Z)
        double precision tc(20,20),ts(20,20)
        common ih
        pi=darcos(-1.0d0)
        a=0.0d0
        b=pi
        m=10
        do 100 k1=1,20
          do 110 k2=1,20
            tc(k1,k2)=0
            ts(k1,k2)=0
 110      continue
 100    continue
          m1=m+1
        do 120 k=1,m1
          tc(1,k)=(fnc(a,ih)+fnc(b,ih))*(b-a)/(2**k)
          ts(1,k)=(fns(a,ih)+fns(b,ih))*(b-a)/(2**k)
          if (k.eq.1) go to 120
           m12=2**(k-1)-1
          do 130 n=1,m12
            tc(1,k)=(b-a)*fnc(a+n*(b-a)/2**(k-1),ih)/(2**(k-1))
     *+tc(1,k)
            ts(1,k)=(b-a)*fns(a+n*(b-a)/2**(k-1),ih)/(2**(k-1))
     *+ts(1,k)
 130      continue
 120    continue
        do 140 i=1, m
             mi=m-i+1
          do 150 jj=1,mi
             j=jj-1
            tc(i+1,j+1)=((4**i)*tc(i,j+2)-tc(i,j+1))/((4**i)-1)
            ts(i+1,j+1)=((4**i)*ts(i,j+2)-ts(i,j+1))/((4**i)-1)
 150      continue
 140    continue
        sfc=tc(m+1,1)
        sfs=ts(m+1,1)
        return
        end
c
c  Subroutine for the evaluation of Ul.
c
        subroutine ginteg(sf,XMAT)
        IMPLICIT REAL*8(A-H,O-Z)
        REAL*4 XMAT(21)
        double precision t(20,20)
        double precision sf
        pi=darcos(-1.0d0)
        a=0.0d0
        b=pi
        m=10
          m1=m+1
        do 400 k=1,m1
          t(1,k)=(fng(a,XMAT)+fng(b,XMAT))*(b-a)/(2**k)
          if (k.eq.1) go to 400
             m12=2**(k-1)-1
          do 410 n=1,m12
            t(1,k)=(b-a)*fng(a+n*(b-a)/2**(k-1),XMAT)/(2**(k-1))
     *+t(1,k)
```

```
410       continue
400     continue
        do 430 i=1, m
            mi=m-i+1
          do 420 jj=1,mi
              j=jj-1
            t(i+1,j+1)=((4**i)*t(i,j+2)-t(i,j+1))/((4**i)-1)
420       continue
430     continue
        sf=t(m+1,1)
        return
        end
c
c  Subroutine for the evaluation of U2.
c
        subroutine gintgg(sf,XMAT)
        IMPLICIT REAL*8(A-H,O-Z)
        REAL*4 XMAT(21)
        double precision t(20,20)
        double precision sf
        pi=darcos(-1.0d0)
        a=0.0d0
        b=pi
        m=10
          m1=m+1
        do 440 k=1,m1
          t(1,k)=(fgg(a,XMAT)+fgg(b,XMAT))*(b-a)/(2**k)
          if (k.eq.1) go to 440
             m12=2**(k-1)-1
          do 450 n=1,m12
            t(1,k)=(b-a)*fgg(a+n*(b-a)/2**(k-1),XMAT)/(2**(k-1))
     *+t(1,k)
450       continue
440     continue
        do 470 i=1, m
            mi=m-i+1
          do 460 jj=1,mi
              j=jj-1
            t(i+1,j+1)=((4**i)*t(i,j+2)-t(i,j+1))/((4**i)-1)
460       continue
470     continue
        sf=t(m+1,1)
        return
        end
c
c.........................FUNCTIONS.............................
c
c  Regular part of the kernel function (see Eq. 5.36).
c
        function fnk(tet,dlan)
        IMPLICIT REAL*8(A-H,O-Z)
        COMMON/CF/DN,R2,ADN,TETMAX,BETA,PI,TAU2
        common/bcf/ib,jb
c
        Y1=2.0D0*DLOG(DN/R2)+ADN*TETMAX
        SX=DCOS(TET)
        SZ=DCOS(DLAN)
        XMZ=TETMAX*(SX-SZ)/2.0D0
        XPZ=ADN*TETMAX*(SX+SZ)/2.0D0-Y1
        DEN01=DCOSH(ADN*XMZ)-DCOS(XMZ)
        DEN02=DCOSH(XPZ)-DCOS(XMZ)
        CPS=DCOS(2.0D0*BETA)+ADN*DSIN(2.0D0*BETA)
        CMS=ADN*DCOS(2.0D0*BETA)-DSIN(2.0D0*BETA)
        FKV=(CPS*DSIN(XMZ)+CMS*DSINH(XPZ))/DEN02-DSIN(2.0D0*BETA)-
     .      ADN*(1.0D0-DCOS(2.0D0*BETA))
c
```

```
c   Test singular part
c
        IF(DABS(SX-SZ).LE.1.0D-3) GO TO 1
        CBC=(DSIN(XMZ)+ADN*DSINH(ADN*XMZ))/DENO1-2.0D0/XMZ
        FKV=FKV+CBC
        GO TO 2
c
    1   ZZ1=1.0D0+ADN*ADN*ADN*ADN*ADN*ADN
        ZZ1=ZZ1/((1.0D0+ADN*ADN)*90.0D0)
        ZZ1=ZZ1-(1.0D0-ADN*ADN)*(1.0D0-ADN*ADN)/72.0D0
        TLEB=ZZ1*XMZ*XMZ*XMZ
        TLEB=TLEB-(1.0D0-ADN*ADN)*XMZ/6.0D0
        FKV=FKV+TLEB
    2   CONTINUE
c
         if((ib.eq.1).and.(jb.eq.1))fnk=FKV/(PI*PI)
         if((ib.eq.1).and.(jb.ne.1))fnk=(2.0d0*FKV/(PI*PI))
     .                               *dcos((jb-1)*DLAN)
         if((ib.ne.1).and.(jb.eq.1))fnk=(2.0d0*FKV/(PI*PI))
     .                               *dcos((ib-1)*TET)
         if((ib.ne.1).and.(jb.ne.1))fnk=(4.0d0*FKV/(PI*PI))
     .                    *dcos((ib-1)*TET)*dcos((jb-1)*DLAN)
        RETURN
        END
c
c   Function of right hand side of Eq. 5.32b.
c
        double precision function fnc(tet,nh)
        IMPLICIT REAL*8(A-H,O-Z)
        COMMON/CF/DN,R2,ADN,TETMAX,BETA,PI,TAU2
        X=DCOS(TET)
        FC=DEXP(ADN*TETMAX*(X-1)/2.0D0)*DSIN(TETMAX*(X-1)/2.0D0)
        if (nh.eq.1) fnc=(1/pi)*fc
        if (nh.ne.1) fnc=(2/pi)*fc*dcos((nh-1)*tet)
        RETURN
        END
c
c   Function of right hand side of Eq. 5.32c.
c
        double precision function fns(tet,nh)
        IMPLICIT REAL*8(A-H,O-Z)
        COMMON/CF/DN,R2,ADN,TETMAX,BETA,PI,TAU2
        X=DCOS(TET)
        FS=DEXP(ADN*TETMAX*(X-1)/2.0D0)*DCOS(TETMAX*(X-1)/2.0D0)
        if (nh.eq.1) fns=(1/pi)*fs
        if (nh.ne.1) fns=(2/pi)*fs*dcos((nh-1)*tet)
        RETURN
        END
c
c   Function of U1.
c
        double precision function fng(x,XMAT)
        IMPLICIT REAL*8(A-H,O-Z)
        REAL*4 XMAT(21)
        COMMON/CF/DN,R2,ADN,TETMAX,BETA,PI,TAU2
        common limn
        sx=DCOS(x)
        ex1=ADN*TETMAX*(sx-1.0D0)/2.0d0-DLOG(DN/R2)
        fac1=DEXP(ex1)*DCOS(TETMAX*(sx-1.0D0)/2.0D0)
        fac2=XMAT(1)*(1.0d0+sx)
        do 500 k=2,limn
          fac2=fac2 + XMAT(k)*DSIN(x)*DSIN((k-1)*x)
  500   continue
        fng=fac1*fac2
        RETURN
        END
```

```
c
c  Function of U2.
c
      double precision function fgg(x,XMAT)
      IMPLICIT REAL*8(A-H,O-Z)
      REAL*4 XMAT(21)
      COMMON/CF/DN,R2,ADN,TETMAX,BETA,PI,TAU2
      common limn
      sx=DCOS(x)
      ex1=ADN*TETMAX*(sx-1.0D0)/2.0d0-DLOG(DN/R2)
      fac1=(DEXP(ex1))*DSIN(TETMAX*(sx-1.0D0)/2.0D0)
      fac2=XMAT(1)*(1.0d0+sx)
      do 600 k=2,limn
        fac2=fac2 + XMAT(k)*DSIN(x)*DSIN((k-1)*x)
 600  continue
      fgg=fac1*fac2
      RETURN
      END
/*
//
```

C.2. Program TEST

```
c  This program is the exclusive property of Dimitri S. CHAMIEH.
c  It takes the values of the six integrals (U1 and U2) defined by
c  Eq. 5.34a and computed by program FORCE then computes the
c  dimensionless average impeller force components along with the
c  dimensionless impeller stiffness matrix, all as a function of
c  of geometries, flow rate, rotor speed and inlet prerotation
c  (swirl) over flow rate ratio.
c
      IMPLICIT REAL*8(A-H,O-Z)
      REAL*8 KXX,KXY,KYX,KYY
      PI=DACOS(-1.0D0)
      TETMAX=2.2D0*PI
      BETA=0.436D0
      OMEGA=104.7D0
      Q=4.1D0
      QDES=4.3D0
      QH=(QDES-Q)/QDES
      R2=0.265D0
      TYPE 10
 10   FORMAT(//' Ratio of inlet swirl/flow rate (TAU/Q) = ',$)
      ACCEPT *,R
      WRITE(6,100)R2,BETA,TETMAX,OMEGA,Q,QDES,QH
 100  FORMAT(/1X,'Radius of impeller (ft) = ',D14.7/1X,'Blade '
     .       'leaving angle (rad) = ',D14.7/1X,'Total angle subte',
     .       'nded by volute (rad) = ',D14.7/1X,'Rotor speed (rad',
     .       '/sec) = ',D14.7/1X,'Flow rate Q (cubic ft/sec/ft) = ',
     .       D14.7/1X,'Design flow rate QDES (cubic ft/sec/ft) = ',
     .       D14.7/1x,'h = ',d14.7)
c
c  Write values of integrals as defined by Eq. 5.34a. These integrals
c  are the end product of the previous program with initials "FORCE".
c
      U1ZERO=-1.35855695d0
      U2ZERO=1.64210806d0
      U1COS=15.6695486d0
      U2COS=0.539614429d0
      U1SIN=2.27123174029d0
      U2SIN=-13.06792545d0
c
c  Define L and M of Eq. 5.34b.
c
      XL=Q*(DTAN(BETA)+DSIN(2.0D0*BETA)-R*(1.0D0+DCOS(2.0D0*BETA)))
     .   /(2.0D0*PI*R2)-OMEGA*R2
      XM=-Q*(COS(2.0D0*BETA)+R*SIN(2.0D0*BETA))/(2.0D0*PI*R2)
c
```

```
c  Calculate dimensionless force and slope.
c
      FN=2.0D0*PI*OMEGA*OMEGA*R2*R2
      FIOX=TETMAX*(XL*U1ZERO+XM*U2ZERO)/FN
      FIOY=TETMAX*(XM*U1ZERO-XL*U2ZERO)/FN
      SX=FIOX/QH
      SY=FIOY/QH
      AX=180.0D0*DATAN(SX)/PI
      AY=180.0D0*DATAN(SY)/PI
c
c  Calculate dimensionless stiffness matrix.
c
      KXX=-TETMAX*(XL*U1COS+XM*U2COS)/FN
      KXY=-TETMAX*(XL*U1SIN+XM*U2SIN)/FN
      KYX=-TETMAX*(XM*U1COS-XL*U2COS)/FN
      KYY=-TETMAX*(XM*U1SIN-XL*U2SIN)/FN
c
      WRITE(6,110)FIOX,FIOY,SX,AX,SY,AY,KXX,KXY,KYX,KYY
 110  FORMAT(/30X,'IN X-DIR :  ',D14.7/1X,'NORMALIZED FORCE ',
     .       'COMPONENTS'/30X,'IN Y-DIR :  ',D14.7/1X,
     .       'SLOPE AND SLOPE ANGLE (DEGREES) IN X-DIR : ',D14.7,4X,
     .       D14.7/1X,'SLOPE AND SLOPE ANGLE (DEGREES) IN Y-DIR : ',
     .       D14.7,4X,D14.7//32X,
     .       '*********************************************'/32X,
     .       '*  KXX=',D14.7,5X,'KXY=',D14.7,'  *'/1X,
     .       'NORMALIZED STIFFNESS MATRIX=  ********************',
     .       '*************************'/32X,'*  KYX=',
     .       D14.7,5X,'KYY=',D14.7,'  *'/32X,'*****************',
     .       '*********************************'//)
      STOP
      END
```

C.3. Subroutine EQSOV

```
      SUBROUTINE EQSOV(M,BDMTX,V,ITER,EPS,F,IT,INEW)

C WRITTEN BY KIKU MATSUMOTO, CALIFORNIA INSTITUTE OF TECHNOLOGY
C EQSOV                                   DATE OF OBJECT DECK 04-11-72
C      M = ORDER OF MATRIX
C  BDMTX = TWO- DIMENSIONAL ARRAY OF COEFFICIENTS
C      V = RIGHT-HAND VECTOR
C     ITER = MAXIMUM NUMBER OF ITERATIONS DESIRED
C      EPS = TOLERANCE FOR CONVERGENCE (.GE. 1.E-7)
C      F = RESULTING VECTOR
C      IT = OUTPUT FROM ROUTINE SPECIFYING NUMBER OF ITERATIONS ACTUALLY
C      INEW (FIRST CALL) SET INEW .NE. 1
C           (LATER CALLS) IF THE MATRIX IS UNCHANGED AND ONLY THE
C           COLUMN VECTOR B IS CHANGED, THEN SET INEW = 1
      COMMON/EQSVB/SG1
      DIMENSION BDMTX(50,50), V(50), F(50),        X(50),
     1 A(50,50),IDX(50),XT(50)
      DOUBLE PRECISION R
      IF(M.EQ.1) GO TO 210
      N = M
      IT = 0
      DO 9 I = 1,N
      X(I) = V(I)
      F(I) = 0.0
   9  CONTINUE
      N1 = N - 1
      IF (INEW .EQ. 1) GO TO 181
      DO 10 I = 1, N
      DO 10 J = 1, N
      A(I,J) = BDMTX(I,J)
  10  CONTINUE
```

```
      DO 12 I = 1,N
   12 IDX(I) = I
      SG1 = 0
      DO 60 I = 2, N
C     PARTIAL PIVOTING, CHECK FOR MAX ELEMENT IN (I-1)ST COLUMN.
      AMX = ABS(A(I-1,I-1))
      IM1 = I - 1
      JMX = IM1
      DO 16 J = I,N
      ABSA = ABS(A(J,I-1))
      IF(AMX .GE. ABSA) GO TO 16
      AMX = ABSA
      JMX = J
   16 CONTINUE
      IF(JMX .EQ. IM1) GO TO 20
C     MOVE THE ROW WITH MAX A(J,I-1) TO (I-1)ST ROW.
       DO 18 K = 1,N
      T = A(I-1,K)
      A(I-1,K) = A(JMX,K)
   18 A(JMX,K) = T
      II = IDX(I-1)
      IDX(I-1) = IDX(JMX)
      IDX(JMX) = II
      XI = X(I-1)
      X(I-1) = X(JMX)
      X(JMX) = XI
      SG1 = 1.0
   20 CONTINUE
      IF(A(I-1,I-1) .EQ. 0.) GO TO 200
      DO 55 J = I, N
      CX = A(J,I-1) / A(I-1,I-1)
      K2 = I
      DO 50 K = I, N
      A(J,K2) = A(J,K2) - CX * A(I-1,K2)
      K2 = K2 + 1
   50 CONTINUE
      A(J,I-1) = CX
   55 CONTINUE
   60 CONTINUE
C  FORWARD PASS - OPERATE ON RIGHT HAND SIDE AS
C  ON MATRIX
   62 CONTINUE
      DO 70 I = 2, N
      DO 65 J = I, N
      X(J) = X(J) - X(I-1) * A(J,I-1)
   65 CONTINUE
   70 CONTINUE
C
C  BACKWARD PASS - SOLVE FOR AX = B
       X(N) = X(N) / A(N,N)
      DO 80 I = 1, N1
      SUM = 0.0
      I2 = N - I + 1
      DO 75 J = I2, N
      SUM = SUM + A(I2-1,J) *  X(J)
   75 CONTINUE
       X(I2-1) = (X(I2-1)-SUM) / A(I2-1,I2-1)
   80 CONTINUE
      DO 90 I = 1, N
      F(I) = F(I) +  X(I)
   90 CONTINUE
      IF(IT.EQ.ITER) RETURN
      IT = IT + 1
      DO 95 I = 1, N
      IF(ABS(F(I)).LT.1.0E-10)  GO TO 95
      IF(ABS( X(I)/F(I)) .GT. EPS) GO TO 150
   95 CONTINUE
C  FINISHED
      RETURN
```

```
C  DOUBLE PRECISION MATRIX MULTIPLICATION
  150 CONTINUE
      DO 170 I = 1, N
      R    = 0.0D0
      DO 160 J = 1, N
      R    =  R   + BDMTX(I,J) * F(J)
  160 CONTINUE
      X(I) = V(I) - R
  170 CONTINUE
  181 IF(SG1 .EQ. 0.0) GO TO 62
C     IF SG1 .NE. 0, PERMUTE X BEFORE PERFORMING FORWARD PASS.
      DO 182 I=1,N
  182 XT(I) = X(I)
      DO 184 I = 1,N
      K = IDX(I)
  184 X(I) = XT(K)
      GO TO 62
  200 I1 = I - 1
      WRITE (6,510) I1
  510 FORMAT(/1X 25HERROR RETURN FROM SEQSOV    I10,
     1 35HDIAGONAL TERM REDUCED TO ZERO    / )
      RETURN
 210   CONTINUE
       IT = 0
       F(1) = V(1)/BDMTX(1,1)
      RETURN
       END
```

REFERENCES

1. Acosta, A. J., and Bowerman, R. D., "An Experimental Study of Centrifugal Pump Impeller", Trans. ASME, Vol. 79, pp. 1821-1839, November 1957.

2. Adams, M. L., and Makay, E., "Development of Advanced Rotor- Bearing Systems for Feedwater Pumps, Phase 2", EPRI CS-2027, Project 1266-7-1, Final Report, September 1981.

3. Adams, M. L., and Padovan, J., "Insights into Linearized Rotor Dynamics", J. of Sound and Vibration, Vol. 76, pp. 129-142, 1981.

4. Agostinelli, A., Nobles, D., and Mockridge, C. R., "An Experimental Investigation of Radial Thrust in Centrifugal Pumps", Trans. ASME, J. of Eng. for Power, Vol. 82, pp. 120-126, April 1960.

5. Alford, J. S., "Protecting Turbomachinery from Self-Excited Rotor Whirl", J. of Eng. for Power, Vol. 87, pp. 333-344, Oct. 1965.

6. Allaire, P. E., Branagan, L. A., and Kocur, J. A., "Aerodynamic Stiffness of an Unbounded Eccentric Whirling Centrifugal Impeller with an Infinite Number of Blades", 2nd Workshop on Rotordynamic Instability Problems in High Performance Turbomachinery,Texas A&M University, to be presented in a NASA Conf. Pub., May 10-12 1982.

7. Balje, O. E., "Turbomachines", Wiley, New York, 1981.

8. Bently, D. E., "Forced Subrotative Speed Dynamic Action of Rotating Machinery", ASME Paper No. 74-PET-16, 1974.

9. Bevan, T., "The Theory of Machines", Third Edition, William Clowes and Sons, London, pp. 565-568, 1960.

10. Biheller, H. J., "Radial Force on the Impeller of Centrifugal Pumps with Volute, Semivolute and Concentric Casings", J. of Eng. for Power, Vol. 87, pp. 319-323, July 1965.

11. Binder, R. C., and Knapp, R. T., "Experimental Determinations of the Flow Characteristics in the Volutes of Centrifugal Pumps", Trans. ASME, Vol. 58, pp. 649-661, 1936.

12. Bowerman, R. D., and Acosta, A. J., "Effect of the Volute on Performance of a Centrifugal Pump Impeller", Trans. ASME, Vol. 79, pp. 1057-1069, July 1957.

13. Braisted, D. M., "Cavitation Induced Instabilities Associated with Turbomachines", Ph. D. Thesis, Division of Engineering and Applied Sciences, California Institute of Technology, 1979.

14. Brennen, C. E., Acosta, A. J., and Caughey, T. K., "A Test Program to Measure Fluid Mechanical Whirl-Excitation Forces in Centrifugal Pumps", First Workshop on Rotordynamic Instability Problems in High-Performance Turbomachinery, Texas A&M university, NASA Conf. Pub. 2133, pp. 229-

235, 1980.

15. Brennen, C. E., Meissner, C., Lo, E. Y., and Hoffmann, G.W., "Scale Effects in the Dynamic Transfer Functions for Cavitating Inducers", ASME Paper No. AT-WA/HT-51, to appear shortly in the J. of Fluids Eng., 1980.

16. Caignaert, G., "Contribution a l'Etude des Interactions entre le Bec de la Volute et la Roue d'une Pompe Centrifuge", Thesis Dissertation, Universite des Sciences et Techniques de Lille, France, February 1978.

17. Carnahan, B., Luther, H. A., and Wilkes, J. O., "Applied Numerical Methods", Wiley, New York, pp. 90-99, 1969.

18. Chamieh, D. S., and Acosta, A. J., "Dynamic Forces on a Whirling Centrifugal Rotor", Proc. 6th Conf. on Fluid Machinery, Akademiai Kiado, Budapest, Hungary, pp. 210-219, 1979.

19. Chamieh, D. S., Acosta, A. J., Brennen, C. E., and Caughey, T. K., "A Brief Note on the Interaction of an Actuator Cascade with a Singularity", First Workshop on Rotordynamic Instability Problems in High-Performance Turbomachinery, Texas A&M university, NASA Conf. Pub. 2133, pp. 237-247, 1980.

20. Chamieh, D. S., "Calculation of the Stiffness Matrix of an Impeller Eccentrically Located within a Volute", Cavitation and Polyphase Flow Forum, Joint ASME/ASCE Conf., Boulder, Colorado, pp. 51-53, 1981.

21. Chamieh, D. S., Acosta, A. J., Brennen, C. E., Caughey, T. K., and Franz, R., "Experimental Measurements of Hydrodynamic Stiffness Matrices for a Centrifugal Pump Impeller", 2nd Workshop on Rotordynamic Instability Problems in High Performance Turbomachinery, Texas A&M University, to be presented in a NASA Conf. Pub., May 10-12 1982.

22. Cheng, H. K., and Rott, N., "Generalizations of the Inversion Formula of Thin Airfoil Theory", J. of Rational Mechanics and Analysis, Vol. 3, pp. 357-382, 1954.

23. Childs, D. W., "Rub-Induced Parametric Excitation in Rotors", J. of Mechanical Design, Vol. 101, pp. 640-644, October 1979.

24. Childs, D. W., Dressman, J. B., and Childs, S. B., "Testing of Turbulent Seals for Rotordynamic Coefficients", First Workshop on Rotordynamic Instability Problems in High-Performance Turbomachinery, Texas A&M university, NASA Conf. Pub. 2133, pp. 121-138, 1980.

25. Childs, D. W., Hendricks, R. C., and Vance, J. M., (eds.) Introductory Comments At the First Workshop on Rotordynamic Instability Problems in High-Performance Turbomachinery, Texas A&M University, NASA Conf. Pub. 2133, Preface, 1980.

26. Childs, D. W., "Fractional-Frequency Rotor Motion Due to Nonsymmetric Clearance Effects", ASME Paper No. 81-GT-145, 1981.

27. Childs, D. W., Nelson, C., Noyes, T., and Dressman, J. B., "A High-Reynolds-Number Seal Test Facility: Facility Description and Preliminary Test Data", 2nd Workshop on Rotordynamic Instability Problems in High Performance Turbomachinery,Texas A&M University, to be presented in a NASA Conf. Pub., May 10-12 1982.

28. Chow, S. K., Hou, A. Y., and Landweber, L., "Calculation of Flow through a Two-Dimensional Centrifugal Impeller by the Method of Hydrodynamic Singularities", Chapter 6, "Pumps: Analysis Design and Application", Worthington Pump Inc., Vol.1, pp. 113-133, 1978.

29. Colding-Jorgensen, J., 'The Effect of Fluid Forces on Rotor Stability of Centrifugal Compressors and Pumps", Ph. D. Thesis, Dept. of Machine Design, Technical University of Denmark, 1979.

30. Crandall, S. H., and Brosens, P. J., "On the Stability of Rotation of a Rotor with Rotationally Unsymmetric Inertia and Stiffness Properties", J. of Applied Mechanics, Vol. 28, pp. 567-570, December 1961.

31. Csanady, G. T., 'Radial Forces in a Pump Caused by Volute Casing", Trans. ASME, J. of Eng. for Power, Vol. 84, pp. 337-340, October 1962.

32. Den Hartog, J. P., 'Mechanical Vibrations", Fourth Edition, McGraw-Hill, New York, 1956.

33. Domm, H., and Hergt, P., 'Radial Forces on Impeller of Volute Casing Pumps", Flow Research on Blading (L. S. Dzung, ed.), Elsevier Pub. Co., The Netherlands, pp. 305-321, 1970.

34. Doyle, H. E., 'Field Experiences with Rotodynamic Instability in High-Performance Turbomachinery", First Workshop on Rotordynamic Instability Problems in High-Performance Turbomachinery, Texas A&M University, NASA Conf. Pub. 2133, pp. 3-13, 1980.

35. Ehrich, F. F., 'The Dynamic Stability of Rotor/Stator Radial Rubs in Rotating Machinery", J. of Eng. for Industry, Vol. 91, pp. 1025-1028, Nov. 1969.

36. Ek, M. C., 'Solution of the Subsynchronous Whirl Problem in the High Pressure Hydrogen Turbomachinery of the Space Shuttle Main Engine", Paper No. 78-1002, AIAA/SAE 14th Joint Propulsion Conf., Las Vegas, Nevada, July 25-28 1978.

37. Giberson, M. F., 'Time Transient Non-Synchronous Rotor Response", Shock and Vibration Computer Programs-Reviews and Summaries, Shock and Vibration Monograph-10, Naval Research Laboratory, Wasington, D. C., pp. 465-466, 1975.

38. Goggin, D. G., 'Field Experiences with Rub Induced Instabilities in Turbomachinery", 2nd Workshop on Rotordynamic Instability Problems in High-Performance Turbomachinery, Texas A&M University, to be presented in a NASA Conf. Pub., May 10-12 1982.

39. Hergt, P., and Krieger, P., 'Radial Forces in Centrifugal Pumps with Guide Vanes", Advance Class Boiler Feed Pumps, Proc. Inst. of Mechanical

Engineers, Vol. 184, Pt 3N, pp. 101-107, 1969-1970.

40. Hess, J. L., "Numerical Solution of Inviscid Subsonic Flows", Von Karman Institute for Fluid Dynamics, Lecture Series No. 34, March 1971.

41. Hoffmeister, M., Die Entwicklung von Radialen Laufschaufeln unter Benutzung des Singularitatenverfahrens", Maschinenbau Technik, 8(2), 1959.

42. Hori, Y., "A Theory of Oil Whip", ASME J. of Applied Mechanics, Vol. 26, pp. 189-198, June 1959.

43. Imaichi, K., Tsujimoto, Y., and Yoshida, Y., "A Two Dimensional Analysis of the Interaction Effects of Radial Impeller in Volute Casing", IAHR/AIRH Symposium, Tokyo, Japan, pp. 635-647, 1980.

44. Iversen, H. W., Rolling, R. E., and Carlson, J. J., "Volute Pressure Distribution, Radial Force on the Impeller and Volute Mixing Losses of a Radial Flow Centrifugal Pump", Trans. ASME, J. of Eng. for Power, Vol. 82, pp. 136-144, April 1960.

45. Japikse, D., 'Review-Progress in Numerical Turbomachinery Analysis", Trans. ASME, J. of Fluids Eng., Vol. 98, pp.592-606, December 1976.

46. Kamimoto, G., Ohshima, T., Mizutani, M., and Mizutani, H., "Application of Singularity Method in Turbomachinery", IAHR/AIRH Symposium, Tokyo, Japan, pp. 649-660, 1980.

47. Kimball, A. L., Jr., 'Internal Friction Theory of Shaft Whirling", General Electric Review, Vol. 27, pp. 244-251, April 1924.

48. Kovats, A., 'Design and Performance of Centrifugal and Axial Flow Pump and Compressors", Macmillan, New York, 1964.

49. Kurokawa, J., 'Theoretical Determinations of the Flow Characteristics in Volutes", IAHR/AIRH Symposium, Tokyo, Japan, pp. 623-634, 1980.

50. Lawaczek, F., 'Turbinen und Pumpen", Julius Springer Verlag, Berlin, Germany, pp. 152-157, 1932.

51. Lazarkiewicz, S., and Troskolanski, A. T., 'Impeller Pumps", Pergamon Press, Translated by D. K. Rutter (Polish Ed. Title : Pompy Wirowe), 1965.

52. Loret, G., 'Pressure Distribution in Volutes", Presented Unpublished at Symposium on Flow through Centrifugal Impellers, ASME, New Orleans, March 1980.

53. Mani, R., "A Method of Calculating Quasi Two-Dimensional Flows through Cascades", Office of Naval Research, Report No. E-79.10, Engineering Division, California Institute of Technology, July 1967.

54. Newkirk, B. L., "Shaft Whipping", General Electric Review, Vol. 27, pp. 169-178, March 1924.

55. Ng, S. L., 'Dynamic Response of Cavitating Turbomachines", Ph. D. Thesis, Division of Engineering and Applied Sciences, California Institute of Technology, 1976.

56. Ng, S. L., and Brennen, C. E., 'Experiments on the Dynamic Behaviour of Cavitating Pumps", J. of Fluid Engineering, Vol. 100, pp. 166-176, June 1978.

57. Ohashi, H., Shoji, H., Yanagisawa, S., and Tomita, K., 'Experimental Study of Fluid Forces on Whirling Centrifugal Impeller in Vaneless Diffuser", Symp. Fluid/ Structures Interactions in Turbomachinery, W. E. Thompson Ed., pp. 57-62, ASME Winter Annual Meeting, 1981.

58. Pollman, E., Schwerdtfeger, H., and Termuehlen, H., 'Flow Excited Vibrations in High Pressure Turbines (Steam Whirl)", J. of Eng. for Power, Vol. 100, pp. 219-228, April 1978.

59. Sabersky, R. H., Acosta, A. J., and Hauptmann, E. G., 'Fluid Flow, A First Course in Fluid Mechanics", 2nd Edition, Macmillan, New York, 1971.

60. Sato, C., and Allaire, P., "Aerodynamic Forces on an Unbounded Centrifugal Impeller Undergoing Synchronous Whirl", Report No. UVA/643092/MAE82/196, School of Engineering and Applied Science, University of Virginia, June 1982.

61. Schlichting, H., 'Berechnung der Reibungslosen Inkompressiblen Stromung fur ein Vorgebenes Ebenes Schaufelgitter", VDI-Forschungsh. 447, 1955.

62. Shoji, H, and Ohashi, H., 'Fluid Forces on Rotating Centrifugal Impeller with Whirling Motion", First Workshop on Rotordynamic Instability Problems in High-Performance Turbomachinery, Texas A&M University, NASA Conf. Pub. 2133, pp. 317-328, 1980.

63. Stepanoff, A. J., 'Centrifugal and Axial Flow Pumps", 2nd Edition, Wiley, New York, 1957.

64. Thompson, W. E., 'Fluid Dynamic Excitation of Centrifugal Compressor Rotor Vibrations", J. Fluid Engineering, Vol. 100, pp. 73-78, March 1978.

65. Vance, J. M., and Laudalio, F. J., 'Rotordynamic Instability in Centrifugal Compressors - Are All the Excitations Understood?", ASME Paper No. 80-GT-149, 1980.

66. Wislicenus, G. F., 'Fluid Mechanics of Turbomachinery", McGraw-Hill, New York, 1947.

67. Worster, R. C., 'The Flow in Volutes and its Effect on Centrifugal Pump Performance", Proc. Institution of Mechanical Engineers, Vol. 177, No. 31, pp. 843-875, 1963.